

The University of Adelaide

Department of Mechanical Engineering

**A STUDY OF POWER TRANSMISSION
IN ACTIVELY CONTROLLED SIMPLE
STRUCTURES**

Xia Pan

Submitted for the Degree of Doctor of Philosophy

August 1996

Contents

Abstract	vi
Statement of originality	vii
Acknowledgments	viii
List of symbols	ix
1 Overview	1
1.1 Introduction	1
1.2 Literature review	2
1.2.1 Analysis of vibration in simple structures	2
1.2.2 Active control	3
1.2.3 Measurement of vibratory intensity in simple structures	8
1.3 New work	10
2 Minimizing the forced response and vibratory power transmission in an infinite beam	11
2.1 Introduction	11
2.2 Theory	12
2.2.1 Minimizing acceleration	12
2.2.2 Minimizing power transmission	13
2.3 Numerical results	16
2.3.1 Comparison of acceleration and power transmission control	16
2.3.2 Effect of error sensor and control force location	18

2.4	Comparison of theory with experiment	26
2.5	Summary	28
3	Minimizing the forced response of a finite beam	29
3.1	Introduction	29
3.2	Theory	30
3.2.1	Minimizing acceleration	30
3.3	Numerical results	33
3.3.1	Effect of boundary impedance	33
3.3.2	Effect of control force location	37
3.3.3	Effect of error sensor location	39
3.3.4	Effect of forcing frequency	43
3.3.5	Comparison with control of semi-infinite beam	46
3.4	Summary	51
4	Minimizing acceleration and power transmission in a semi-infinite plate	52
4.1	Introduction	52
4.2	Theory	53
4.2.1	Minimization of acceleration with a line of in-phase control forces	53
4.2.2	Minimization of acceleration with a line of three independently driven control forces	54
4.2.3	Power transmission	55
4.2.4	Minimization of power transmission with a line of in-phase point control forces	56
4.2.5	Minimization of power transmission with a line of three independently driven point control forces	58
4.3	Numerical results	59
4.3.1	One primary and one control force	60
4.3.2	A row of in-phase, uniform amplitude control forces and a single primary force	67
4.3.3	A row of in-phase, uniform amplitude control forces and a row of in-phase, uniform amplitude primary forces	69

4.3.4	Effect of forcing frequency on performance with in-phase control forces	71
4.3.5	A row of three in-phase primary forces and a row of three independently driven control forces	72
4.3.6	Effect of error sensor type and location	76
4.4	Summary	81
5	An experimental study of active control of power transmission characteristics in a semi-infinite plate	82
5.1	Introduction	82
5.2	Experimental arrangement	83
5.3	Test procedure	84
5.4	Numerical and experimental results	86
5.4.1	Active control of power transmission	91
5.4.2	Intensity vortices	93
5.5	Discussion and summary	98
6	Piezoelectric actuator vs point force excitation of a beam and a plate	100
6.1	Introduction	100
6.2	Response of infinite beam excited by a pair of piezoelectric actuators	101
6.3	Response of semi-infinite plate driven by a pair of piezoelectric actuators	105
6.4	Power transmission along a semi-infinite plate excited by a pair of piezoelectric actuators	109
6.5	Discussion and summary	111
7	Minimizing acceleration and power transmission in a semi-infinite cylinder	113
7.1	Introduction	113
7.2	Theory	114
7.2.1	Minimization of acceleration with a line of in-phase control forces	114
7.2.2	Minimization of acceleration with a line of three independently driven control forces	116
7.2.3	Power transmission	117

7.2.4	Minimization of power transmission with a line of in-phase point control forces	118
7.2.5	Minimization of power transmission with a line of three independently driven point control forces	120
7.3	Numerical results	122
7.3.1	Definition of the near field	122
7.3.2	Power transmission reduction	123
7.3.3	Effect of error sensor type, location and number	125
7.3.4	Effect of control force type and location	132
7.3.5	Effect of thickness, radius and frequency	134
7.4	Summary	136
8	An experimental study of active control of power transmission in a semi-infinite cylinder	137
8.1	Introduction	137
8.2	Experimental arrangement	137
8.3	Test procedure	142
8.4	Numerical and experimental results	143
8.5	Summary	147
9	Conclusions and recommendations	149
A	Classification of beam boundary conditions	152
A.1	Beam boundary impedance	152
A.2	Equivalent boundary impedance of an infinite beam	157
B	Response of a finite beam to a point force	159
C	Response of a semi-infinite plate to a line of point forces driven in phase	162
D	Modal decomposition method in a semi-infinite plate	167
E	Measurement of amplitude reflection coefficient in a semi-infinite plate	169

F	Response of a semi-infinite cylinder to a line of point forces driven in phase	171
F.1	Determining the wavenumbers and constants α and β	172
F.2	Determining the flexural wavelength	175
F.3	Simply supported end conditions	175
F.4	Equilibrium conditions at the point of an applied force	176
F.5	Determination of the eigenvector	177
G	Modal decomposition method in a semi-infinite cylinder	180
H	Measurement of vibratory intensity in simple structures	181
H.1	Measurement of vibratory intensity in an infinite beam	181
H.2	Measurement of vibratory intensity in a semi-infinite plate	182
H.3	Measurement of vibratory intensity in a semi-infinite cylinder	184
	References	189
	Publications originating from this thesis work	196

Abstract

Feedforward active control of harmonic vibratory power transmission in simple structures is investigated theoretically and experimentally. The structures investigated are a beam, a plate and a cylinder. Primary excitation is used to represent unwanted noise or vibration. Secondary excitation is introduced using control sources which are adjusted to minimize acceleration or power transmission in the structures. The primary and secondary excitation is produced by either electromagnetic force actuators (shakers) or piezoelectric ceramics.

The theoretical predictions are compared to the experimental test results. In addition, vibratory intensity distributions before and after control are investigated.

Both the theoretical and experimental results demonstrate that it is possible to minimize vibratory power transmission in the test simple structures using a maximum of three control sources in the test frequency range. The study also indicates that, in most cases, the harmonic vibratory power transmission in simple structures can be measured by using a maximum of two accelerometers in the test frequency range.

Statement of originality

This thesis contains no material which has been accepted for the award of any other degree or diploma in any University. To the best of the author's knowledge and belief, this thesis contains no material previously published or written by another person, except where due reference is made in the text. If accepted for the award of the degree of Doctor of Philosophy, I consent that this thesis be made available for loan and photocopying.

20 December, 1996

Xia Pan

Acknowledgments

The work presented in this thesis would not be possible without the support and encouragement of many people. Firstly, thanks to my supervisor Dr Colin Hansen, for attracting my interest in this field, for his advice, guidance, encouragement, for improving my English writing skills and, for always making sure everything I needed was available.

Thanks to all the staff in the Mechanical Engineering Department who contributed in some way to this work. In particular, my thanks to Ron Jager for his excellent technical support, and Herwig Bode and George Osborne for their assistance.

My thanks are also extended to the postgraduate students and research officers who were part of the Active Noise and Vibration Control Group for their questions and suggestions. Particular thanks must go to Neil Mackenzie, Dr Scott Snyder, Dr Anthony Zander, Carl Howard and Ben Cazzolato for their advice on my experimental work.

Special thanks are due to Dr Ray Peterson and Les Gray for their help with my English.

Support for this research from Overseas Postgraduate Research Scholarship is also gratefully acknowledged.

I would like to thank Vera Melissaratos, Dr David Bies and Dr Allan Shaw for sharing my frustrations and successes, for helping with motivation and ideas and, for being my friends. Also, I would like to thank my host family for their kindness and support.

Finally, my heart-felt thanks go to my mother Hongxiu Diao and my brother Dr Jie Pan, for their support and patience. In particular, I would like to thank Pan, for guiding my interest in the engineering area, for his encouragement and advice and, for financial support in my first year of overseas study. I would not have been able to start my research without his support. Also, I wish to thank my deceased father Liyou Pan for his encouragement and the love he gave me throughout his life.

List of symbols

$[A]$	modal amplitude vector
A	matrix term
A_n	modal amplitude for the n th mode
A_n^{in}	amplitude of the incident wave for the n th mode
A_n^{ref}	amplitude of the reflected wave for the n th mode
c_f	flexural wave speed
D_e	extensional rigidity, $= \frac{Eh}{1-\nu^2}$
D_h	flexural rigidity, $= \frac{Eh^3}{12(1-\nu^2)}$
E	Young's modulus
f	applied frequency
F	point force
F_c	control point force
F_0	complex point force amplitude, or point force applied at $x = x_0$
F_p	primary point force
F_r	radial force per unit surface area
F_x	axial force per unit surface area
F_ϕ	tangential force per unit surface area
h	thickness of beams, plates and cylinders
Im	imaginary component of a complex value
I_{xa}	plate vibratory intensity
I_{yy}	beam moment of inertia of a cross section about the Y-axis
j	complex unit, $= \sqrt{-1}$
k	number of point moments in the plate

K	cylinder bending stiffness, $= \frac{Eh^3}{12(1-\nu^2)}$
k_f	flexural wavenumber: for the beam $= \sqrt{\omega(\rho S)^{\frac{1}{4}}(EI_{yy})^{-\frac{1}{4}}}$ for the plate $= \pm \sqrt{\left(\frac{n\pi}{L_y}\right)^2 \pm \sqrt{\frac{\rho h \omega^2}{D_h}}}$ for the cylinder $= \omega\left(\frac{\omega^2 E h^2}{12\rho(1-\nu^2)r^4}\right)^{-\frac{1}{4}}$
k_{in}	plate modal wavenumbers for nth mode
k_{sn}	cylinder modal wavenumbers for nth circumferential mode
L_y	plate width
m	number of forces, or mass per unit area of the plate
M	beam bending moment
M_p	plate applied moment
M_{px}	plate line moment generated by a piezoceramic actuator acting along the y-axis
M_{py}	plate line moment generated by a piezoceramic actuator acting along the x-axis
M_x	plate bending moment (in Chapter 4), counteracting line moments parallel to the y-axis (in Chapter 6), moment about the ϕ -axis (in Chapter 7)
M_{xy}	plate twisting moment
M_y	counteracting line moments parallel to the x-axis in the plate
n	integer 1, 2, 3 ..., or mode number
N	number of measurement points
N_x	axial force
$N_{x\phi}$	tangential shear force
P	beam power transmission
P_a	active power transmission
P_{co}	controlled power transmission
P_e	extensional wave power transmission
P_f	flexural wave power transmission
P_r	reactive power fluctuation
P_{red}	reduction of power transmission
P_s	cylinder power transmission
P_t	torsional wave power transmission

P_{un}	uncontrolled power transmission
P_{xa}	plate power transmission
$P.T.$	power transmission
Q	beam shear force
Q_x	transverse shear in a plate and a cylinder
$q(x, y)$	plate applied force
r	cylinder mean radius
Re	real component of an complex value
S	cross-sectional area of the beam
t	time
T	period of vibration
u	axial displacement
v	tangential displacement
x_c	control force location
x_e	error sensor location
x_p	primary force location
$[\mathbf{X}_c]$	boundary eigenvector for the control force
$[\mathbf{X}_p]$	boundary eigenvector for the primary force
w	flexural displacement
\dot{w}	flexural velocity
w_{c-f}	flexural response due to unit control force excitation
w_{p-f}	flexural response due to unit primary force excitation
$[Z]$	impedance matrix
$[Z_L]$	left finite beam impedance matrix
$[Z_{L,inf}]$	left infinite beam impedance matrix
$[Z_R]$	right finite beam impedance matrix
$[Z_{R,inf}]$	right infinite beam impedance matrix
α	eigenroot coefficient, or constant (in Chapter 6)
β	eigenroot coefficient
γ^2	$= \frac{\rho r^2(1-\nu^2)}{E}$

η	loss factor of the beam
$\dot{\theta}$	rotational velocity
θ_x	angular rotation about the ϕ -axis
λ_f	flexural wavelength
ν	Poisson's ratio
ξ	$= \frac{h^2}{12r^2}$
ρ	mass density
ϕ	circumferential coordinate
ϕ_c	phase of control force
ϕ_p	phase of primary force
ω	angular frequency of vibration
Δ	distance between two closely spaced accelerometers

Superscripts

H	complex conjugate and transpose of a matrix
T	transpose of a matrix
\cdot	derivative with respect to t , or derivative with respect to ϕ (in Chapter 7 and Appendix F)
$'$	derivative with respect to x , or derivative with respect to the dimensionless coordinate $\frac{x}{r}$ (in Chapter 7 and Appendix F)
$-$	time averaged
$*$	complex conjugate

Subscripts

c	control force only
f	force only, or flexural wave only (in Chapter 7)
m	moment only
p	primary force only



Chapter 1

Overview

1.1 Introduction

In this thesis, the feed-forward active control of power transmission in simple structures (a beam, plate and cylinder) is studied both experimentally and theoretically. Prior work has included a direct comparison of theoretical results and experimental data for active control of power transmission in a beam; however, to the author's knowledge, there has been little consideration of the active control of power transmission in a plate or a cylinder. Also very little previous work has been carried out on the measurement of vibratory intensity in simple structures. This earlier work was limited to a beam and plate, and required complex measurement methods. For example, two (in the far field of a source) or four (in the near field of a source) accelerometers were required for measuring vibratory intensity in a beam, and four (in the far field of a source) or eight (in the near field of a source) accelerometers were required for a plate. The earlier work did not extend to measurement of vibratory intensity in a cylinder.

The primary purpose of the work in this thesis is to evaluate the constraints associated with actively reducing power transmission in simple structures. A secondary purpose is to develop a practical means for the measurement of intensity in simple structures. The evaluation includes investigation of the use of single or multiple control sources with two alternative cost functions: vibration acceleration amplitude at the error sensor or power transmission passing the error sensor. Methods for the measurement of vibratory intensity in

a beam, plate and cylinder are also investigated. This includes assessment of the possibility of simplifying the measurement of intensity by using a maximum of two accelerometers for simple structures. As the simple structures may be very large, the results of this work could be applied to suppressing hull vibration of ships and submarines.

1.2 Literature review

1.2.1 Analysis of vibration in simple structures

The equation of motion for a thin beam is used by many authors, such as Cremer et al. (1973), Graff (1975) and Fahy (1985). A general solution for the equation of motion given by the above authors, consists of incident and reflected wave terms for both near and far fields. As this solution can be applied easily for active vibration control in a thin beam with a wide array of geometries and boundary conditions, this solution is used in this thesis.

The basics of free vibration in a plate were discussed by Leissa (1969), Graff (1975), Fahy (1985) and others. Leissa (1969) prepared comprehensive summaries of the analysis of free vibration to that time. Leissa's work presents results for the free vibration frequencies and mode shapes with a wide array of geometries and boundary conditions. Therefore, the solutions to the equation of motion shown by Leissa (1969) are developed for active vibration control predictions in this thesis.

Flügge (1973) described the three dimensional equations of motion for the vibration of a cylindrical shell. Leissa (1973) carried out a numerical analysis which showed that similar results were obtained by the use of Flügge's equations, and the equations of various authors including Forsberg (1964, 1966). Subsequently Flügge has been recognized as the pre-eminent author in this field. However, little experimental work has been carried out to test the validity of Flügge's equations in practical active vibration control applications. In particular, it should be noted that Flügge's model includes a simplifying assumption which does not take into account the linear inertia of the cylinder, and the assumption can cause inaccurate results. Thus, Flügge's model could not be used directly for the active control applications addressed in this thesis. It was necessary to develop a more fundamental approach to the model, taking account of cylinder linear inertia. The extension of Flügge's

equations with the linear inertia terms included, is considered in this current thesis.

1.2.2 Active control

Feedback control methods

Most early active control theory considered modal feedback control of large structures. Meirovitch et al. (1983 and 1986) and Venkatraman et al. (1990) reviewed various modal feedback control techniques for large flexible systems and demonstrated the advantage of independent modal space control (IMSC) where a coordinate transformation is used to decouple a complicated system into a set of independent second order systems in terms of modal coordinates. However, the IMSC has a disadvantage which requires one controller for each mode. The IMSC may result in undesirable modes called control spillover when the number of control sources is less than the number of modes. Baz and Poh (1987) developed a modification of the IMSC termed MIMSC which minimizes control spillover.

In 1986 von Flotow presented another feedback control solution based on a wave control concept, in which structural vibration is described in terms of waves traveling in various directions. In this case vibration attenuation required control of the propagation of these waves by minimizing the wave amplitude. In this present thesis, the traveling wave concept is used for the numerical analysis in simple structures, however feed-forward rather than feed-back control is used.

Feedback control methods like those discussed above are suited to the control of vibration in very large structures with many structural members and in situations where it is difficult to obtain a suitable reference signal (Young, 1995). In feedback systems, design of the control system is dependent on the physical system (control source and error sensor configuration). In feed-forward control systems, the design of the physical system may be separated from the design of the electronic controller. In recent years, much research has been concerned with feed-forward control. The subject of this thesis is the physical system design needed for the feed-forward active control of harmonic power transmission in simple structures. When the excitation is harmonic, it is usually feasible to obtain a useful reference signal which makes feed-forward control the preferred option. It should be noted that the results relating to the performance of the control actuators are also relevant to

feedback control systems.

Actuators for active control

Noiseux (1970) used electro-magnetic shakers as actuators in his experimental work on active control. Although electro-magnetic shakers are useful tools in experimental work, their usefulness in practical applications is limited by their size and mass.

Alternative actuators are piezoelectric actuators which can be small and light. Crawley and de Luis (1987) presented an analytical and experimental investigation of piezoelectric actuators as vibration sources. Clark et al. (1991) made tests on a beam excited by pairs of piezoelectric actuators bonded to each of two opposite surfaces. They modeled the actuator pair as a pair of counteracting moments.

Dimitriadis et al. (1991) made a two-dimensional extension of Crawley and de Luis' work, applying pairs of laminated piezoelectric actuators to a plate. They demonstrated that the location and shape of the actuator pairs dramatically affected the vibration response of the plate. However, Kim and Jones (1991) indicated that Dimitriadis et al. (1991) made a simplifying assumption for zero bonding layer thickness (i.e. perfect bonding). Kim and Jones (1991) then developed expressions relating the applied moment to piezoelectric driving voltage in a plate including bonding layer thickness. They concluded that, in some cases, comparisons between their study and the investigation of Dimitriadis et al. (1991) showed noticeable discrepancies. Therefore, it is suggested to take into account the bonding layer thickness.

Lester and Lefebvre (1993) demonstrated a three-dimensional extension of the work of Dimitriadis et al. (1991). They performed two models: firstly a pair of piezoelectric actuators acted on the cylinder through line moments along the each edge of the actuator, secondly a pair of piezoelectric actuators acted on the cylinder through in-plane forces along each edge of the actuator.

Many other authors (Fansen and Chen, 1986; Baz and Poh, 1988, 1990) have used piezoelectric actuators in active vibration control experiments. Clearly there is a need for a vibration actuator that can be used in practical situations, where the large reaction mass of an electro-magnetic shaker is unsuitable (Rivory, 1992). The laminated piezoelectric actuator pair has become the popular alternative, but this type of actuator pair is fragile

and is not capable of generating great amounts of force (Young, 1995). Also it is difficult to ensure that each element in each actuator pair produces the same force. To the author's knowledge, no research has been performed considering the conditions under which the piezoelectric actuator pair can be considered as a point force. However, this is investigated in this thesis (Chapter 6).

Error sensors for active control

Young (1995) investigated active control of flexural vibration in a beam using a control source which consisted of a piezoceramic actuator placed between a stiffener flange and the beam surface. Young (1995) concluded that for a beam the use of a second error sensor gave no overall improvement in acceleration attenuation. In particular, it was claimed that, with the use of a second error sensor, it may not be possible to improve the relatively poor attenuation when the first error sensor was located at a standing wave node. However, it should be noted that Young (1995) considered only the minimization of the sum of the displacement at each error sensor. However, minimization of the sum of the mean squared displacement at each error sensor is the preferred method and it is the normal method in noise control applications. In the current thesis, the preferred minimization method is used to evaluate the maximum achievable attenuation for introducing a second error sensor in a beam (Chapter 3).

Feed-forward active control of acceleration and power transmission in a beam

Mace (1987) demonstrated theoretically the active control of harmonic flexural vibration in a beam by using the modulus squared of acceleration as the cost function. He discussed the excitation and control of vibration from two types of actuators: point force and point moment. Mace treated the point force and point moment as discontinuities in the shear force and bending moment in the beam, with resulting discontinuities in the displacement solution for the beam equation, at the point of application of the force or moment. This method is followed in the current thesis for the control of vibration in a beam (Chapter 2). In Mace's work, there is no mention of the effect of various parameters, including control

source location, error sensor location, beam termination type and frequency, on the level of attenuation of vibration. However, these parameters are discussed in this thesis (Chapter 2 and 3).

Gonidou (1988), Fuller and Gonidou (1988), and Fuller et al. (1990) investigated feed-forward active control of harmonic flexural power transmission in a beam resulting from a point force input. They demonstrated that power transmission can be attenuated with a small number of control sources. In all three cases, the cost function used was the flexural power transmission at the error sensor. The results presented by Fuller and Gonidou (1988) demonstrated that when the error sensor measuring power transmission is located in the far field, the bending near field contributions are negligible. However, no detailed discussion of near field effects was included and there was no comparison of power transmission control and acceleration control.

Pan and Hansen (1990) gave an expression for the power transmission resulting from an arbitrarily distributed point excitation force and an arbitrarily distributed point control force, which was chosen to minimize the power transmission in a beam. They demonstrated that when controlling power transmission, it does not matter whether the power transmission sensor is located in the near field or in the far field of the primary or control sources, but they made no mention of acceleration as a cost function and they made no comparison of power transmission control and acceleration control.

On reviewing previous work on the active control of beam vibration, it is apparent that both beam acceleration (Mace, 1987) and power transmission (Fuller et al. 1988, 1990; Pan and Hansen, 1990) have been used by other authors as cost functions for control. Use of either cost function has advantages and disadvantages in terms of transducer design and power transmission observability which have not been discussed elsewhere but which are addressed in the current thesis (Chapter 2).

Feed-forward active control of acceleration and power transmission in a plate

Dimitriadis et al. (1991) solved the two dimensional plate displacement equation in their study of control of harmonic flexural vibration in a plate. They showed that the location of the control actuators and the excitation frequency are important factors in the effectiveness

of the control achieved. They did not investigate in any depth the dependency of control effectiveness on control actuator location, error sensor location and frequency. In the current thesis, the dependency of reduction of power transmission on control actuator location, error sensor location and frequency are investigated in detail (Chapter 4).

Fuller (1990) and Metcalf et al. (1992) made an experimental and theoretical investigation of active feed-forward active control of sound transmission and radiation from a plate using point control sources. Although active noise control and active vibration control have much in common, the purpose of this thesis is to investigate control of power transmission, not control of radiated sound.

To this author's knowledge, examining the control of power transmission along a large plate has not been studied by earlier authors. In this thesis, this topic is investigated in detail (Chapter 4 and 6). This approach is one step along the path towards the development of active systems to control vibration transmission in large structures.

Feed-forward active control of acceleration and power transmission in a cylinder

Recently, attention has been given to the feed-forward active control of noise in a cylinder which represents an aircraft fuselage. However, the research is mainly directed at reducing the noise radiated from a cylindrical shell or transmitted through it rather than reducing vibratory power transmission along it. In 1987 Fuller and Jones presented an experimental investigation on the control of interior noise in a cylinder using a single point vibration control source to reduce noise transmission. Jones and Fuller (1989) extended this work to include more control sources. They showed that significant reduction can be achieved for harmonic excitation. Elliott et al. (1989) demonstrated successful experiments on the control of the noise field in a cabin of an aircraft, by using acoustic rather than vibration control sources.

Young (1995) investigated feed-forward active control of acceleration in a cylinder using piezoelectric stack actuators and an angle stiffener at a circumference of the cylinder. He demonstrated the piezoelectric stack actuators can be used as control sources to significantly reduce vibration in a cylinder. He discussed the effects of excitation frequency, number of control sources, control source location and error sensor location on the attenuation of

acceleration. He indicated these effects may be considered to establish trends that can be significant when taking the next step in practical implementation. Young's work considered only the control of individual wave (flexural, extensional or torsional) acceleration and did not consider total power transmission caused by coupling of the three wave types.

Feed-forward active control of power transmission in a pipe i.e. a cylinder with small diameter, has been the subject of increasing attention in recent years. Fuller and Brevart (1995) demonstrated the active control of vibratory power transmission in a pipe by using point control sources to minimize the acceleration of the shell around its circumference at several axial locations. However, they considered mainly the low frequency range (well below the ring frequency) where, based on earlier work by Pinnington and Briscoe (1994), the pipe behaves as a beam. Their method may be difficult to apply to a cylinder with a large diameter and over a wide frequency range. To this author's knowledge, there has been little consideration of active control of power transmission in a cylinder with a relatively large diameter to thickness ratio. Hence in the present thesis, feed-forward active control of power transmission in a cylinder including a wide range of diameters and a wide range of applied frequencies is considered (Chapter 7 and 8). This cylinder represents a very approximate model of either a large aircraft or a submarine.

1.2.3 Measurement of vibratory intensity in simple structures

Measurement of vibratory intensity (vibratory power transmission per unit width of cross section) has attracted more and more attention in recent years. Noiseux (1970) carried out the first definitive work on intensity measurement in a beam and a plate.

A landmark paper on intensity in a beam and a plate was written by Pavic (1976). He discussed methods for the measurement of intensity by using accelerometers and showed that by using finite difference approximations, all derivatives relating to intensity can be calculated. He used two (in the far field of a source) or four (in the near field of a source) accelerometers to measure intensity in a beam, and eight accelerometers (in both far and near fields of a source) to measure intensity in a plate. However in a large plate, it is very complicated in practice to use eight accelerometers per measurement point. Pavic's work did not extend to the measurement of intensity in a cylinder.

Much of the recent work on structural intensity (Pavic 1986, Carniel et al. 1985, Rasmussen 1985 and Williams 1988) has been based on Pavic's 1976 paper. Hirata et al. (1990) have developed Pavic's technique and presented the method of measurement of plate intensity by using four accelerometers in the far field of a source. However, eight accelerometers were still required in the near field of a source. Wagstaff et al. (1995) suggested that it would be possible to use only two accelerometers to measure intensity in a finite plate. Some experimental work was carried out, however no numerical analysis was completed and, hence his results were not verified. The current thesis has carried out the numerical analysis and experimental work for simplifying the measurement of intensity by using a maximum of two accelerometers for simple structures (a beam, plate and cylinder).

Work has also been carried out by Taylor (1990a) to quantify the errors associated with intensity measurement discussed in earlier studies. He concluded that, for most cases, the limitation of intensity measurement in the near field of a vibration source is the phase tolerance of accelerometer pairs. The work by Taylor (1990a) and others indicates that obtaining reliable structural intensity measurement is very difficult in the near field, and still somewhat difficult in the far field. In many practical cases, a knowledge of power transmission in the far field is more important.

Structural intensity may be considered in terms of a vector. The directions of the vectors (at many measurement points) may vary over the surface of a structure and in some cases may indicate energy circulation. The existence of intensity vortices on a simply supported plate was first reported by Tanaka et al. (1993). They found that the path of power transmission is a combination of linear transmission and rotation, the latter being induced by the interference of two modes producing a "vortex generating block". A qualitative formula for predicting the number of power transmission vortices, as well as the geometric arrangement, was put forward. It was concluded that it is straightforward to produce a power transmission vortex on a vibrating simply supported plate, and this could have a practical application to control the path of power transmission in large systems. However, there is no discussion in other work of power transmission vortices in a semi-infinite plate, and this is addressed in this thesis (Chapter 5).

1.3 New work

The following work is presented in this thesis:

1. Study of the active control of vibratory power transmission in simple structures (a beam, plate and cylinder). This demonstrated that significant power transmission reduction can be obtained by using single or/and multiple control sources.
2. Investigation of the effect of error sensor location and cost function type in actively controlled simple structures. This demonstrated that it is possible to use far field acceleration as the cost function to achieve satisfactory control of power transmission to a remote measurement location.
3. Demonstration that for simple structures, in most cases, vibratory intensity can be measured by using a maximum of two accelerometers.
4. Discussion of the effect of end conditions on the active control of beam vibration. This demonstrated that the end conditions of finite and infinite beams can be described in terms of impedances, and that the behavior of infinite beams can be simulated by choosing impedance values which produce no reflections.
5. Confirmation of the existence of intensity vortices on a semi-infinite plate under primary excitation, and discussion of the relationship between vortices and power transmission. This demonstrated that the addition of control actuators, driven to minimize power transmission, largely eliminates the vortices.
6. Investigation of the effect of a piezoelectric actuator pair versus a point force excitation of a beam and a plate. This demonstrated the conditions under which the piezoelectric actuator pair can be approximated as a point force excitation.

Chapter 2

Minimizing the forced response and vibratory power transmission in an infinite beam

2.1 Introduction

This chapter is concerned with a theoretical analysis of the physical system for the control of power transmission in an infinite thin beam using a single control force and a single error sensor. Physical system conditions which may be varied include error sensor type, as defined below, error sensor location and control force location. The simplest error sensor type uses a single accelerometer, in which case acceleration amplitude is used as the error sensor cost function. An alternative error sensor type uses two accelerometers (Pavic, 1976) in which case power transmission is used as the error sensor cost function. Among other things, the analysis in this chapter determines, for minimization of power transmission passing the error sensor, under what conditions it is acceptable to use a simple measurement of acceleration amplitude, rather than power transmission at the error sensor.

2.2 Theory

2.2.1 Minimizing acceleration

The coordinate system for an infinitely long (i.e. without reflective boundaries) aluminum thin beam of width 50 mm and depth 25 mm is shown in Figure 2.1. The point forces are always in the x, y plane and act in the z direction. A primary point force of magnitude F_p and zero relative phase acts on the $x = 0$ plane. At any particular frequency, using the control force required to minimize a flexural wave displacement amplitude is equivalent to minimize acceleration. The results of the following analysis are non-dimensional and apply to a thin beam with any cross-section.

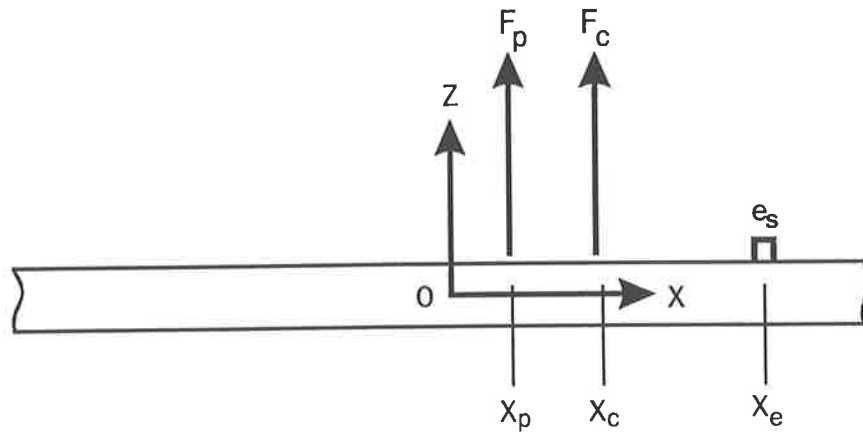


Figure 2.1: Beam model.

The displacement amplitude of an infinite beam (in the z direction) at location x is defined by Junger (1972) and Pan and Hansen (1990), as

$$w(x) = \frac{1}{4EI_{yy}k_f^3}(F_p\beta_p + F_c\beta_c), \quad (2.1)$$

where the factors β_p and β_c are defined as

$$\beta_{p,c} = -(je^{-jk_f|x-x_{p,c}|} + e^{-k_f|x-x_{p,c}|}), \quad (2.2)$$

of which the first term is a propagating wave component and the second term is a non-propagating (or near field which will be defined in Section 2.3.1) component. F_p is the primary force located at x_p , F_c is a control force located at x_c .

The control force which minimizes the displacement at x_e is obtained from equation (2.1) by requiring $w(x_e)$ to be zero: i.e.

$$F_c = -F_p \frac{\beta_p}{\beta_c}. \quad (2.3)$$

The ratio of controlled to uncontrolled displacement amplitude downstream of the control force is

$$R = \left| \frac{(F_p \beta_p + F_c \beta_c)}{F_p \beta_p} \right| = \left| 1 + \frac{F_c \beta_c(x)}{F_p \beta_p(x)} \right|. \quad (2.4)$$

By substituting equation (2.3) into this, one obtains

$$R = \left| 1 - \frac{\beta_p(x_e) \beta_c(x)}{\beta_c(x_e) \beta_p(x)} \right|. \quad (2.5)$$

The β_p and β_c factors can then be replaced by their definitions and the limit as x approaches infinity is taken so that the expression for the reduction in far field residual vibration is

$$\lim_{x \rightarrow \infty} R = \frac{|1 - e^{-k_f(x_c - x_p)(1-j)}|}{|j e^{k_f(x_e - x_c)(1+j)} + 1|}. \quad (2.6)$$

From the equation it is clear that the reduction in far field acceleration level depends on the separation between the control force and the primary force as well as the separation between control force and the error sensor (at which acceleration is minimized). If the distance between the primary and control force is large compared with a wavelength, that is, if $k_f(x_c - x_p) \gg 1$, the numerator of equation (2.6) approaches unity. If, in addition the distance between the error sensor and the control force is large compared with a wavelength, that is, if $k_f(x_e - x_c) \gg 1$, the final expression for the downstream residual vibration becomes

$$\lim_{x \rightarrow \infty} R \approx e^{-k_f(x_e - x_c)}. \quad (2.7)$$

2.2.2 Minimizing power transmission

Power transmission associated with flexural vibration can be thought of as having two components. The first is associated with the product of the internal shear force and transverse velocity, and the second is associated with the product of the bending moment about the neutral axis and rotational velocity. This instantaneous harmonic power transmission $P(x, t)$ can be written as

$$P(x, t) = -Re[Q(x, t)]Re[\dot{w}(x, t)] - Re[M(x, t)]Re[\dot{\theta}(x, t)]. \quad (2.8)$$

To simplify future notation we will set $w = w(x, t)$ and $\bar{w} = \bar{w}(x)$, and we will use similar equivalents for Q , M and θ . By adopting the approach of Skudrzyk (1965) and Fahy (1989), the active (or time averaged) harmonic power transmission becomes

$$P_a = -\frac{1}{2} \text{Re}[\bar{Q}^* \dot{\bar{w}} + \bar{M}^* \dot{\bar{\theta}}], \quad (2.9)$$

and the amplitude of the harmonic reactive power is

$$P_r(x) = -\frac{1}{2} \text{Im}[\bar{Q}^* \bar{w} + \bar{M}^* \bar{\theta}], \quad (2.10)$$

where each variable on the right-hand side of equations (2.9) and (2.10) is a complex amplitude, constant in time for any given location x . Conservation of energy requires that the active power transmission is independent of location x along the beam, but the reactive power remains a function of x . To simplify future expressions, we use the terms “power transmission” for active harmonic power transmission and “reactive power fluctuation” for reactive harmonic power in most cases.

For simple harmonic excitation, the flexural displacement $w(x, t)$ in the right-hand far field of the control force is proportional to $e^{j(\omega t - k_f x)}$. This gives $\dot{w} = j\omega w$, and $\dot{\theta} = -j\omega \frac{\partial w}{\partial x}$. Simplifying equation (2.9), by using Graff's approach,

$$\bar{Q} = -EI_{yy} \frac{\partial^3 \bar{w}}{\partial x^3} \quad \text{and} \quad \bar{M} = -EI_{yy} \frac{\partial^2 \bar{w}}{\partial x^2}, \quad (2.11)$$

produces

$$P_a = EI_{yy} k_f^3 \omega |\bar{w}|^2. \quad (2.12)$$

By replacing \bar{w} with R in equation (2.12) and substituting equation (2.7) into (2.12), it can be shown that the power transmission reduction is proportional to $\frac{20}{\log_e 10} k_f (x_e - x_c)$ dB. The expression for power transmission in the left-hand far field of the primary force is the same except that the sign (i.e. direction of power transmission) is changed. This proportionality of power transmission and displacement magnitude squared implies that controlling power transmission produces the same result as obtained by controlling acceleration. However, in the near field, the expression for the displacement contains a near field term and, so power transmission cannot be represented as $P_a \propto |\bar{w}|^2$. Thus, if the error sensor is placed in a force near field, controlling acceleration produces different results from those obtained by controlling power transmission. This will be discussed in more detail (Section 2.3.2).

Pan and Hansen (1990) have shown that the complex power, defined in a similar way to the complex intensity defined by Fahy (1989) and resulting from a single generalized primary excitation force and single generalized control force acting on an infinite beam is

$$P(x) = P_a + jP_r(x) = [F_c^* a_B F_c + b_{1B} F_c + F_c^* b_{2B} + c_B], \quad (2.13)$$

where a_B , b_{1B} , b_{2B} and c_B are complex numbers depending on the location of the primary and control forces. The value of the control force required to minimize the active power transmission for both near field (defined below in Section 2.3.1) and for far field conditions is (Pan and Hansen, 1990)

$$F_c = -\frac{1}{2\text{Re}[a_B]}(b_{1B}^* + b_{2B}). \quad (2.14)$$

Substituting expressions for a_B , b_{1B} and b_{2B} (Pan and Hansen, 1990) into equation (2.14) gives the following simple result for the control force:

$$F_c = -F_p e^{-jk_f(x_c - x_p)}. \quad (2.15)$$

This shows that the control force has the same amplitude as the primary force and has a relative phase which depends only on the separation between the primary and control force. In equation (2.13), assuming $F_c = 0$, the uncontrolled power transmission (c_B) can be simplified as

$$P_{un} = F_p^2 \frac{\omega}{16EI_{yy}k_f^3}. \quad (2.16)$$

The ratio of controlled to uncontrolled power transmission on the left side of the primary force ($x < x_p$) under optimally controlled conditions is

$$\frac{P_{aL}}{P_{un}} = 2(\cos(2k_f(x_c - x_p)) - 1); \quad (2.17)$$

the corresponding power transmission ratio between the primary and control force ($x_p < x < x_c$) is

$$\frac{P_{aR}}{P_{un}} = 2 \sin(k_f(x_c - x_p)) e^{-k_f(x_c - x_p)}; \quad (2.18)$$

the power transmission ratio is zero to the right of the control force ($x_c < x$).

In the ideal case where equations (2.17) and (2.18) are zero,

$$x_c - x_p = n \frac{\pi}{k_f} = n \frac{\lambda_f}{2}. \quad (2.19)$$

Therefore, power transmission upstream of the control force is zero if the distance between control and primary forces is an integer multiple of half of the flexural wavelength.

2.3 Numerical results

For the results presented in this chapter, the applied frequency is at 1000 Hz and the flexural wave length is $\lambda_f = 0.4823$ m. The primary force is $x_p = 0$ m. These values are adhered to unless otherwise stated. The dB reference level in the following figures of this chapter is the far field uncontrolled acceleration (or power transmission, as appropriate) produced by the primary force.

2.3.1 Comparison of acceleration and power transmission control

Definition of the near field

The near field of an isolated vibration force is the region near the force in which the amplitude of the reactive power fluctuation is not negligible. As shown in Figure 2.2, the boundary between near and far fields is arbitrarily taken to be the point at which the amplitude of the reactive power fluctuation is 20 dB less than the corresponding active power transmission. The dB reference level in this and subsequent figures is the far field uncontrolled acceleration (or power transmission, as appropriate) produced by the primary force. The radius of the near field is then $x/\lambda_f = 0.73$; that is, points further than 0.73 from the primary force are considered to be in the far field. It should be noted that the transition from near to far field is gradual and a definite location is chosen only for convenience.

Comparison of control forces

From equation (2.15) the control force which minimizes power transmission is clearly different from the control force required to minimize acceleration (equation (2.3)). However, the numerical example in Figure 2.3 shows that if the error sensor is placed in the far field of the primary and control excitation forces, the control force F_c required to minimize power transmission is the same as that required to minimize acceleration. The resulting distribution of power transmission and acceleration along the beam are also the same. However, if the error sensor is in the near field of the control force, the two control forces required in each case are different. In the case of acceleration control, the magnitude of the control

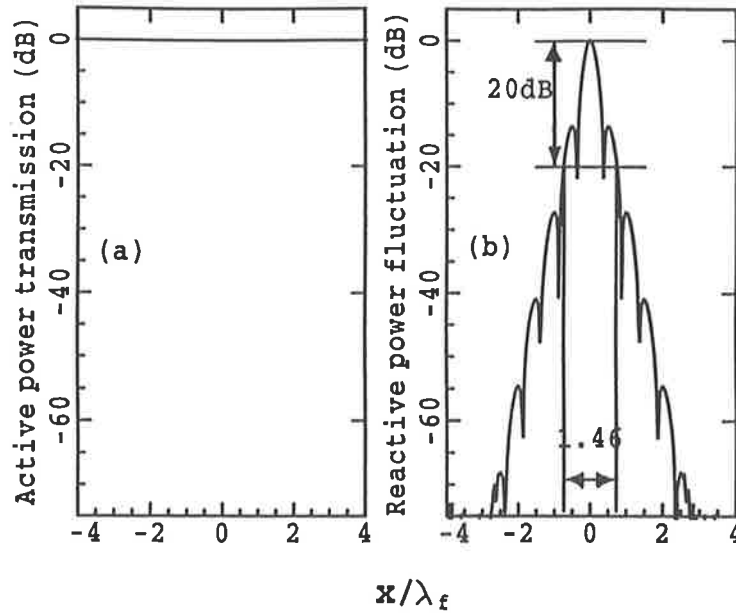


Figure 2.2: Amplitude of the reactive power. At the primary force the active power transmission is equal to the amplitude of the reactive field. The near field is considered to end where the amplitude of the reactive power amplitude is 20 dB less than the active power. (a) Active power transmission at the primary force; (b) Amplitude of the reactive power fluctuation at the primary force.

force has a maximum value of about 1.014 at $(x_e - x_c)/\lambda_f = 0.64$ and then decreases rapidly to approximately $1/\sqrt{2}$ as the control force approaches the error sensor. When the error sensor is in the near field of the control force, the vibration level it measures is a result of both the active power transmission and reactive power fluctuation, and minimization of acceleration level minimizes the sum of the two instead of just the active power transmission. For control of power transmission, the magnitude of the optimum control force is the same as the primary force magnitude and the optimum relative phase is proportional to the separation between the control and primary forces, as may be deduced by inspection of equation (2.15).

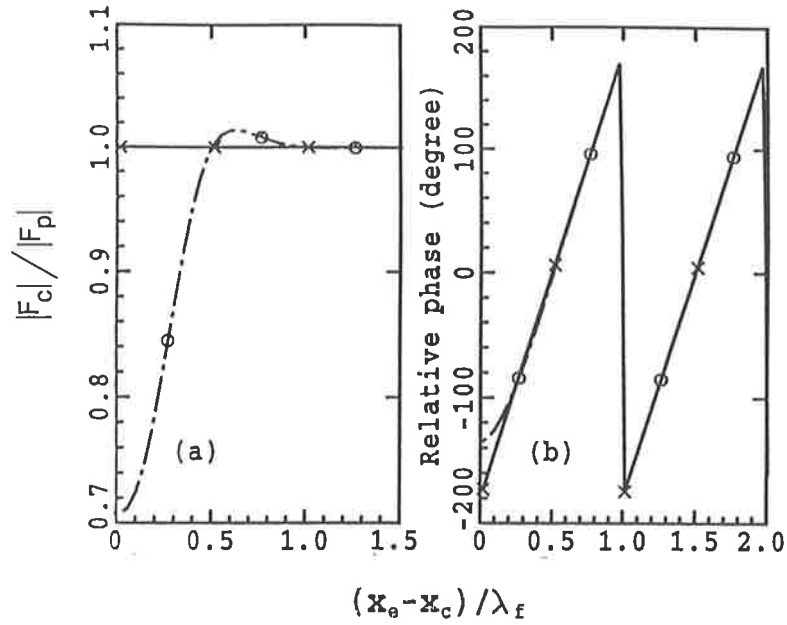


Figure 2.3: Comparison of control forces required to minimize power transmission and to minimize acceleration, for $x_e/\lambda_f = 4.0$. (a) Amplitude of control force; (b) Phase between the control force and the primary force. \times — \times — \times — \times minimized power transmission; o — o — o — o minimized acceleration.

2.3.2 Effect of error sensor and control force location

Power transmission

An example of power transmission distribution along a beam for optimally controlled power transmission and also for optimally controlled acceleration is shown in Figure 2.4. As required by simple conservation of energy, the active power transmission is piecewise constant with discontinuities at the two vibration forces.

Figure 2.5 shows the active power transmission at three distinct observation points on the beam as a function of the separation x_c between the control and primary forces. The observation points are in the left far field of the primary force, half way between the forces, and on the right of the error sensor and data for both acceleration and power transmission control are included. Acceleration control and power transmission control produce different power transmissions upstream of the primary force only if the error sensor is in the near field of the control force ($(x_e - x_c)/\lambda_f < 0.73$). For $(x_e - x_c)/\lambda_f < 2.0$ or $(x_e - x_c)/\lambda_f > 2.0$, the active power transmission between the primary and control forces is essentially independent of whether the cost function determined by the error sensor is

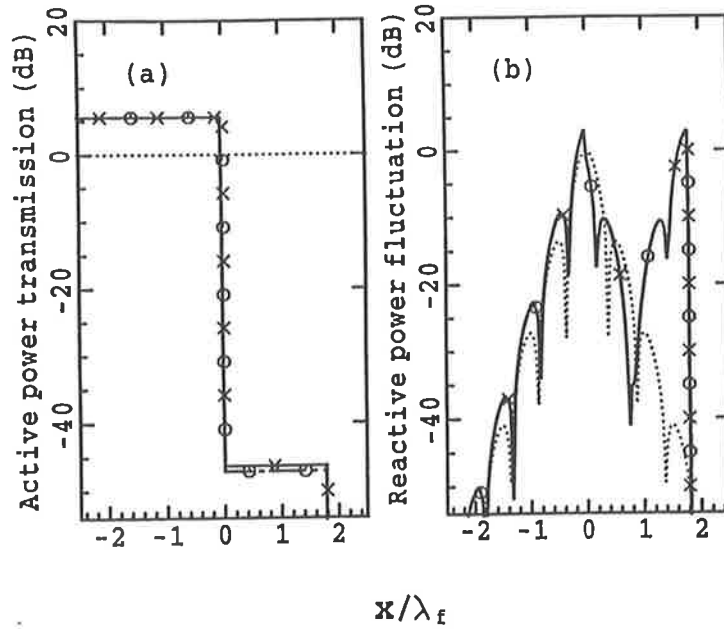


Figure 2.4: The distribution of (a) active power transmission and (b) reactive power amplitude along the beam, with $x_c/\lambda_f = 1.8$ and $x_e/\lambda_f = 4.0$. \times — \times — \times — \times minimized power transmission at the error sensor; o — o — o — o minimized acceleration at the error sensor; $\dots\dots\dots$ uncontrolled.

power transmission or acceleration level. For $(x_c - x_p)/\lambda_f > 2.0$ or $(x_e - x_c)/\lambda_f < 2.0$ power transmission control continues to reduce power transmission as $(x_c - x_p)$ increases according to equation (2.18), but for acceleration control, the effect of error sensor proximity is to reverse the trend and so increase the power transmission as $(x_c - x_p)$ increases and exceeds $(x_e - x_c)$. The residual power transmission downstream of the control force is shown for acceleration control as a solid line. This is clearly an exponentially increasing function of the form $Ke^{(x_c - x_e)}$. However, if the error sensor is not in the near field of the control force (i.e. $(x_e - x_c)/\lambda_f < 0.73$), more than 40 dB of attenuation is achieved. The downstream residual power produced by optimal power transmission control is zero and, so is not shown in the figure. It is shown in Figure 2.5 that proximity of the control force to the error sensor affects the acceleration control case but not the power transmission control case. For a sensor located in the near field of the control force, acceleration amplitude level is a much poorer choice of cost function than power transmission for achieving power transmission control on the downstream side of the control force and, also for reducing power transmission between the control force and primary force. As has been indicated in Section 2.3.1, minimization of acceleration level does not minimize the active power

transmission.

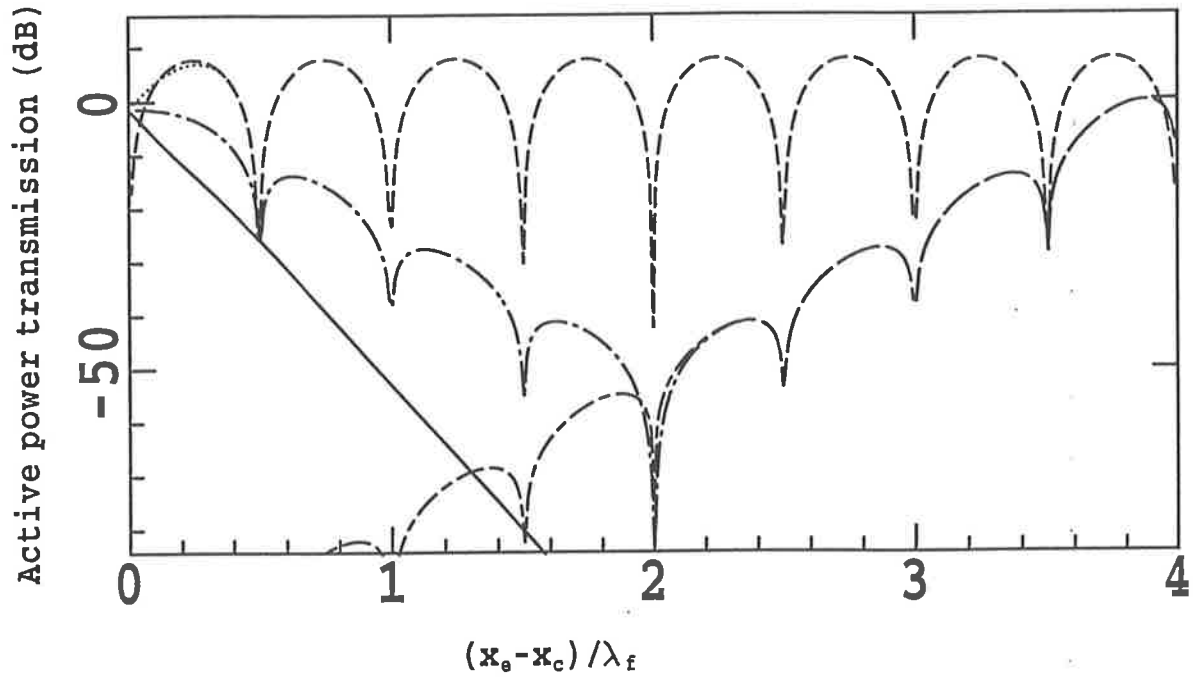


Figure 2.5: Active power transmission at three points on the beam as a function of distance between the error sensor and the control force $(x_e - x_c)/\lambda_f$, with $x_e/\lambda_f = 4.0$.
 - - - - upstream of the primary force and - - - - between the primary and control forces with active power transmission as the control cost function; upstream of the primary force, - · - · between the primary and control forces and - - - - downstream of error sensor, with acceleration amplitude as the control cost function.

It can also be seen from Figure 2.5 that there are preferred spacings between the primary and control forces which minimize power transmission on the primary force side of the control force. These spacings are at half wavelength intervals as shown in equation (2.19). The extreme sensitivity of these minima to control force location implies that it would not be possible in practice to locate a control force with sufficient precision to achieve the level of control shown.

Acceleration

The acceleration distribution along the beam may be calculated from equation (2.1) for both the controlled condition where the control force is given by equation (2.3) and the uncontrolled condition. In the example shown in Figure 2.6(a), the error sensor is placed in the far field of the control force and the control force is also in the far field of the primary force. Clearly the (constant) residual acceleration level on the right of the error sensor (x_e) is very much smaller than the uncontrolled level.

For this particular case, the reduction in vibration level is about 110 dB. It is not greater than this due to a very slight near field effect. This is similar to the results shown by Young (1995). It would not be feasible to achieve this reduction with a practical control system in which the control amount is dependent on a controller. Nevertheless, the calculation does indicate the possible maximum theoretical reduction. Between the control force location and the error sensor, the vibration level decreases exponentially from the uncontrolled level to the residual level. As required in the analysis, the vibration amplitude at the error sensor ($x_e/\lambda_f = 4.0$) is zero ($-\infty$ dB). When the control force is placed in the near field of the primary force, the resulting reduction in vibration level downstream of the error sensor is slightly greater, as expected by inspection of equation (2.6).

In the example shown in Figure 2.6(b), the error sensor is in near field of the control force ($(x_e - x_c)/\lambda_f = 0.1$). The residual acceleration level on the right of the error sensor is only 9 dB lower than the uncontrolled level. This is much larger than that shown in Figure 2.6(a) and indicates the importance of placing a vibration error sensor in the far field of the control force if the acceleration downstream of the error sensor is to be controlled adequately.

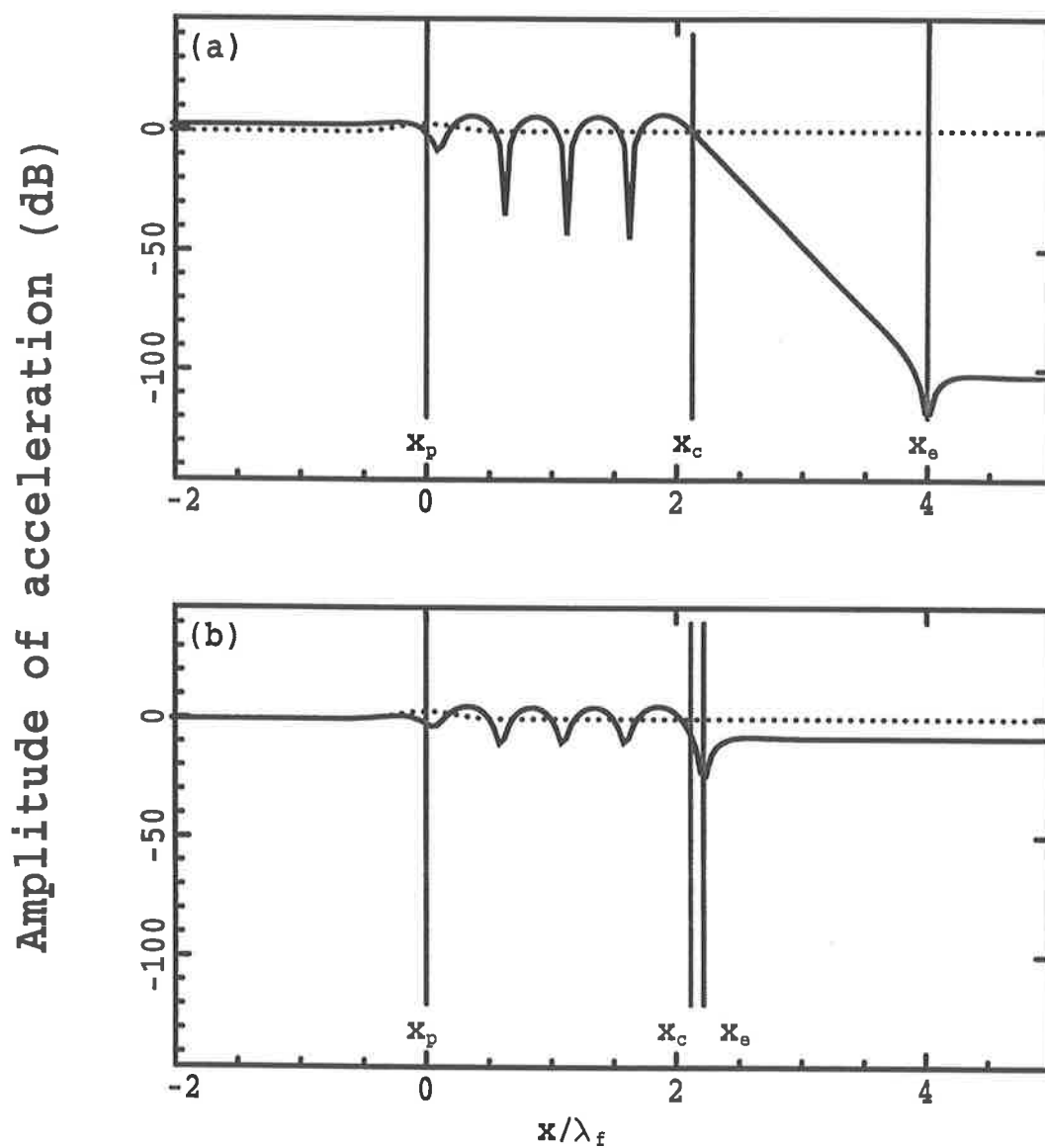


Figure 2.6: Distribution of acceleration amplitude for minimization of acceleration level at the error sensor, with $x_c/\lambda_f = 2.12$. (a) With $x_e/\lambda_f = 4.0$; (b) with $x_e/\lambda_f = 2.22$.

————— controlled; uncontrolled.

Between the primary and control forces there is a standing wave pattern in both figures. As the applied forces represent structural discontinuities with finite rather than infinite or zero impedance, the primary and control forces appear at neither the nodes nor the anti-nodes of these standing wave patterns.

Acceleration distributions along the beam for optimally controlled acceleration and for optimally controlled power transmission are shown in Figure 2.7. Figure 2.7(a) shows the case for the control force located in the near field of the primary force, with the error sensor in the far field of the control force. Clearly, there is no difference in using power transmission control and acceleration control for this case. Figure 2.7(b) shows the case for the control force in the far field of the primary force and the error sensor in the far field of the control force. Note the standing wave set-up between the control force and the primary force. However, the attenuation downstream of the control force is identical to that shown in Figure 2.7(b). Figure 2.7(c) shows the case in which the error sensor is on the border of the control force near field: it is indicated that the near field is beginning to affect the performance of acceleration control case, as shown by the increase in acceleration level downstream of the error sensor. In Figure 2.7(d), where the error sensor is clearly in the near field of the control force, this effect is even more pronounced, with the performance of acceleration control being very poor indeed.

As expected, the beam accelerations resulting from power transmission control and acceleration control are the same when the error sensor is in the far field of the control force. In the far field, upstream of the primary force and downstream of the error sensor, acceleration level is constant. Both types of cost function result in poor control of acceleration level between the primary force and control force. In fact, acceleration levels generally increase in this region for all control force locations. Between the control force and error sensor locations, the acceleration level decreases exponentially from the uncontrolled level to the residual level. Figure 2.8 shows the acceleration level in the far field, upstream of the primary force and far downstream of the error sensor. The figure includes data for both acceleration and power transmission control. Acceleration control and power transmission control produce different acceleration levels upstream of the primary force only if the error sensor is in the near field of the control force; thus the two curves overlap, except at high values of x_c/λ_f . Acceleration upstream of the primary force is zero if the control

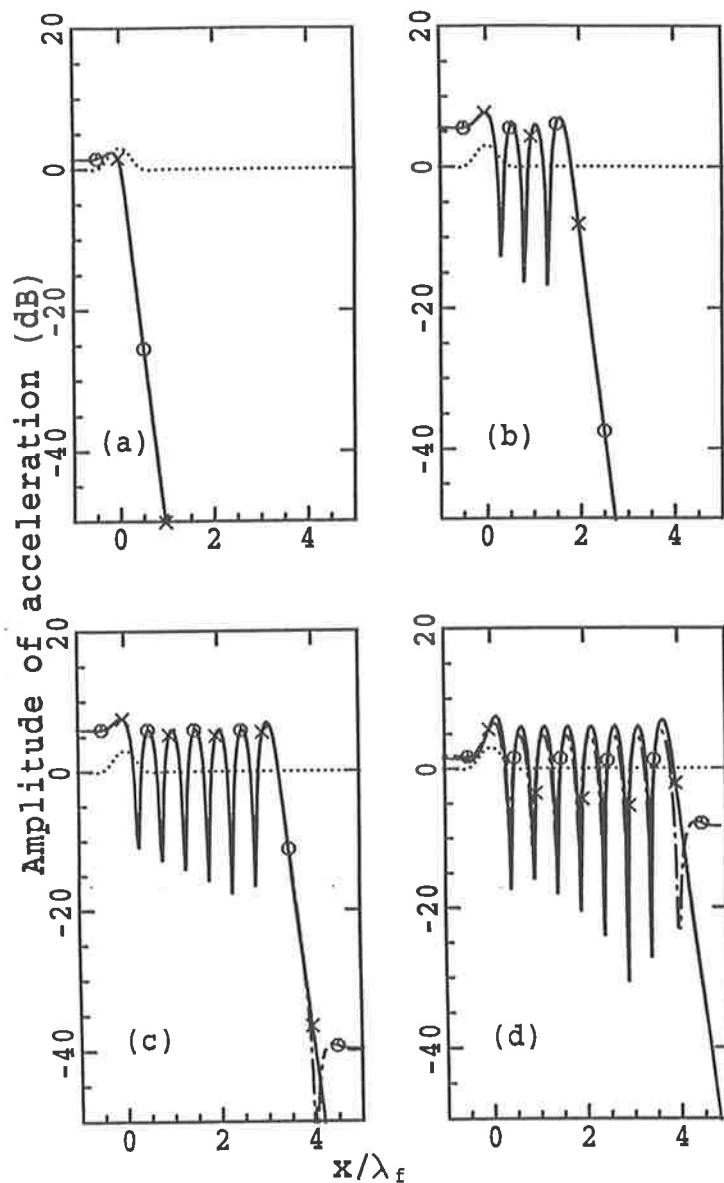


Figure 2.7: Comparison of the effect of power transmission control and acceleration control on the distribution of acceleration level along the beam ($x_e/\lambda_f = 4.0$). $(x_e - x_c)/\lambda_f =$ (a) 3.9, (b) 2.2, (c) 0.73, (d) 0.1. \times — \times — \times — \times minimized power transmission at the error sensor; \circ — \circ — \circ — \circ minimized acceleration at the error sensor; uncontrolled.

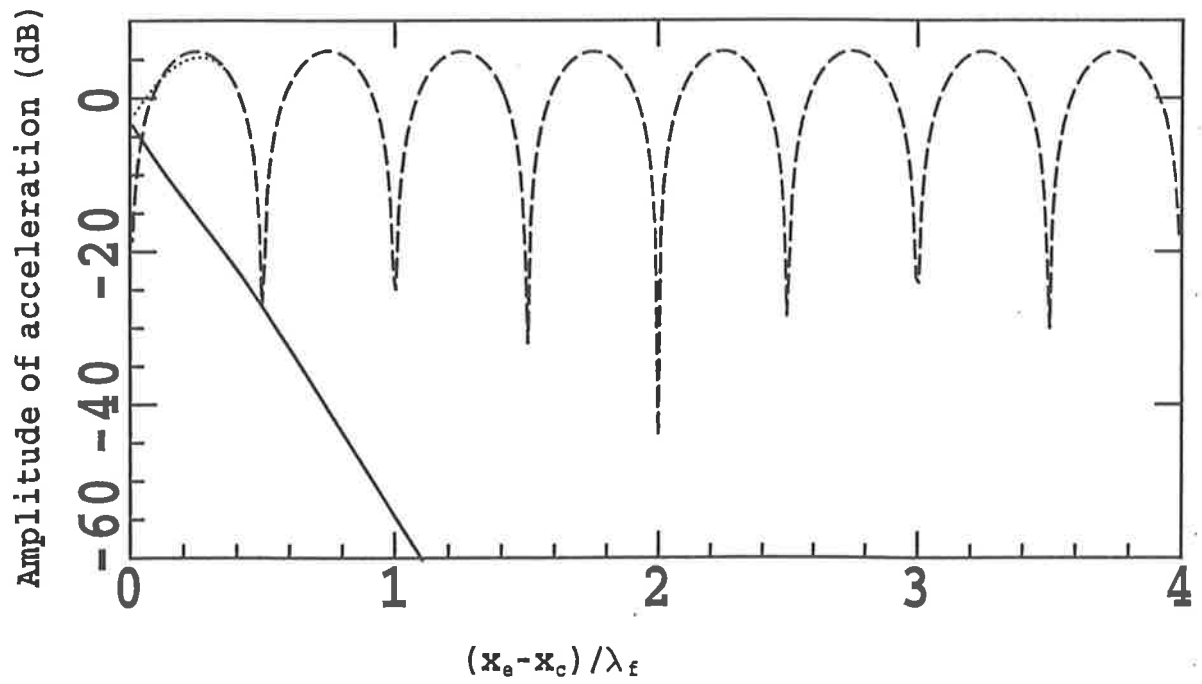


Figure 2.8: Upstream far field and residual downstream acceleration amplitude as a function of the distance between the control force and the error sensor. **---** upstream of the primary force with active power transmission as the control cost function; **.....** upstream of the primary force and **—** downstream of the error sensor with acceleration as the control cost function.

and primary force separation is an integer multiple of the half flexural wavelength. A numerical analysis shows that the minima occur at control and primary force separations of $(d + n\lambda_f/2)$ where d is a constant dependent on frequency and termination type and n is an integer (Young, 1995). The residual acceleration downstream of the control force (solid line) is clearly an exponentially increasing function of the form $Ke^{(x_c-x_e)}$. The residual acceleration for power transmission control is not shown because it is zero. For a sensor located in the near field of the control force, acceleration amplitude level is also a poorer cost function than power transmission for achieving acceleration control on the downstream side of the control force, as power transmission control is unaffected by the proximity of the control force and error sensor.

2.4 Comparison of theory with experiment

The results from experiment and from the analysis of Section 2.2.1 in which acceleration level was minimized at the error sensor location, are compared in Figure 2.9. The excitation frequency was 980 Hz and the beam cross-section dimensions were $50 \times 25(\text{mm})^2$ in both cases, giving a flexural wavelength $\lambda_f = 0.4872 \text{ m}$. In Figure 2.9(a), the error sensor is in the far field of the control force. It is clear from the standing wave shown in the measured data that the anechoic termination used for the experimental work was imperfect and produced a weak standing wave. If this is ignored (as in the theory an anechoic termination is assumed), then the figure shows good agreement between theory and experiment. Of course, the minimum calculated acceleration level is a little lower than that which could be measured, due to the difficulty involved in adjusting the control force phase and magnitude with sufficient accuracy and because of the background noise level. The result of placing the error sensor in the near field of the control force is shown in Figure 2.9(b). The primary and control force locations and forcing frequency are the same as for Figure 2.9(a). In this case, the agreement between the theory and experiment is very good and better than when the error sensor is in the far field. This is due to limitations in the controller capability. Better control is achieved with the error sensor in the far field of the control force than in its near field, because acceleration rather than power transmission was used as the cost

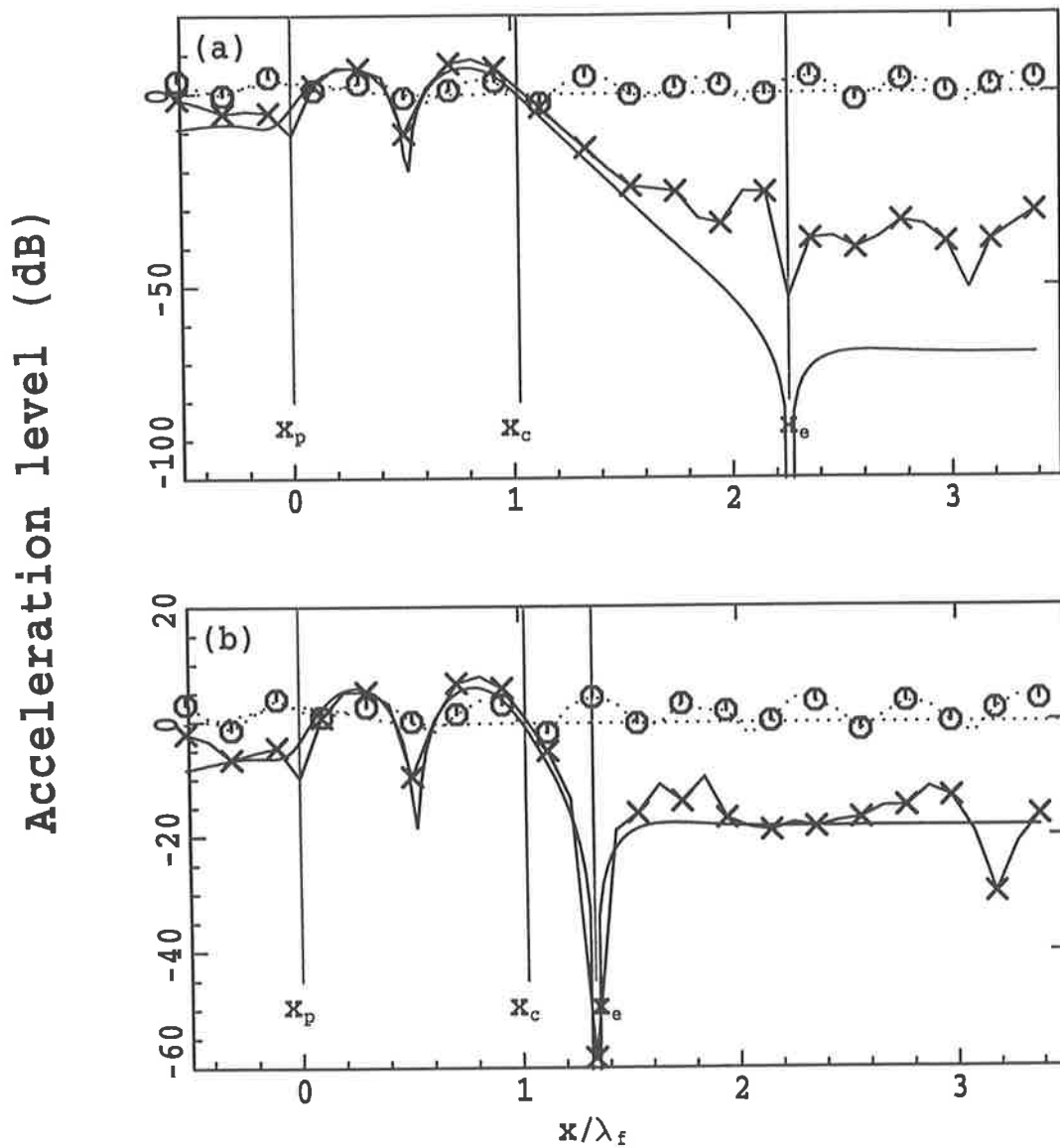


Figure 2.9: Comparison of theoretical with experimental acceleration distributions for optimally controlled acceleration with $x_c/\lambda_f = 1.02$. (a) With $x_e/\lambda_f = 2.25$; (b) with $x_e/\lambda_f = 1.33$. $\cdots\cdots\cdots$ theoretical uncontrolled excitation; ----- theoretical controlled; ---o---o---o experimental uncontrolled; ---x---x---x experimental controlled.

function.

2.5 Summary

It has been shown that when active control is used to minimize power transmission along an infinite beam, minimization of acceleration and minimization of power transmission give identical results provided the point of minimization, i.e. the error sensor, is in the far field of the primary and control forces. However, when the point of minimization is in the near field of the primary and control forces, a control method which minimizes acceleration produces very poor results, whereas a control method which minimize power transmission is not degraded by near field effects. This is because near field reactive power fluctuations affect the ability of an acceleration error sensor to properly observe the propagating part of power transmission. Minimization of the acceleration does not minimize the power transmission. This must be taken into consideration in the design of an active control system.

The relative proximity of the control force to the primary force is not important when considering the reduction of power transmission downstream from the control force. However, the reduction of power transmission upstream of the control force is affected significantly by the relative locations of the two forces, with a separation of an integer multiple of half of a flexural wavelength corresponding to a total reduction in power transmission.

Chapter 3

Minimizing the forced response of a finite beam

3.1 Introduction

In practice, most beams are of finite length and are associated with various boundary conditions. This chapter describes a theoretical investigation of the effect of the boundary conditions on the controllability of the beam acceleration amplitude using a single control force and a single error sensor. The primary purpose of the analysis is to compare the controllability of a finite beam having various boundary conditions, with the controllability of semi-infinite and infinite beams.

The distribution of the beam acceleration amplitude can be explained in terms of propagating flexural waves. The nature of waves in a beam is determined by its geometry, material properties and boundary conditions. For an infinite beam (as described in Chapter 2), the acceleration amplitude distribution may be modeled by considering a single wave traveling in one direction and having no reflection from the boundaries. However, for a finite beam, the acceleration amplitude distribution may be modeled by considering two waves traveling in opposite directions with reflection from the boundaries. In this chapter, the boundary conditions of the beams are arbitrary and described in terms of a force impedance and a moment impedance. The boundary impedance concept is introduced in Appendix A where all the possible boundary conditions have been described in terms of a coupled force and

moment impedance matrix.

3.2 Theory

3.2.1 Minimizing acceleration

In the following analysis, a primary point force, a control point force and an error sensor are shown in Figure 3.1(b). The cost function to be minimized is acceleration amplitude at the location of the error sensor. The total beam response may be considered as the sum of the responses due to the primary and control forces, each of which may be calculated separately.

The boundary condition equation for the primary force is (Appendix B)

$$[\alpha_p][\mathbf{X}_p] = [\mathbf{F}_p] \quad (3.1)$$

or

$$[\mathbf{X}_p] = [\alpha_p]^{-1}[\mathbf{F}_p], \quad (3.2)$$

where the primary force vector $[\mathbf{F}_p] = [0, 0, 0, 0, 0, 0, 0, \frac{F_p}{Q_3}]^T$, $Q_3 = EI_{yy}k_f^3$ and $[\alpha_p]$ is the matrix of boundary condition coefficients for the primary force. The boundary condition equation for the control force is (Appendix B)

$$[\alpha_c][\mathbf{X}_c] = [\mathbf{F}_c] \quad (3.3)$$

or

$$[\mathbf{X}_c] = [\alpha_c]^{-1}[\mathbf{F}_c], \quad (3.4)$$

where the control force vector $[\mathbf{F}_c] = [0, 0, 0, 0, 0, 0, 0, \frac{F_c}{Q_3}]^T$ and $[\alpha_c]$ is the matrix of boundary condition coefficients for the control force.

At the error sensor x_e , the displacement due to the primary force is

$$w_p = [\mathbf{X}_p]^T[\mathbf{E}] \quad (3.5)$$

and the displacement due to the control force is

$$w_c = [\mathbf{X}_c]^T[\mathbf{E}] \quad (3.6)$$

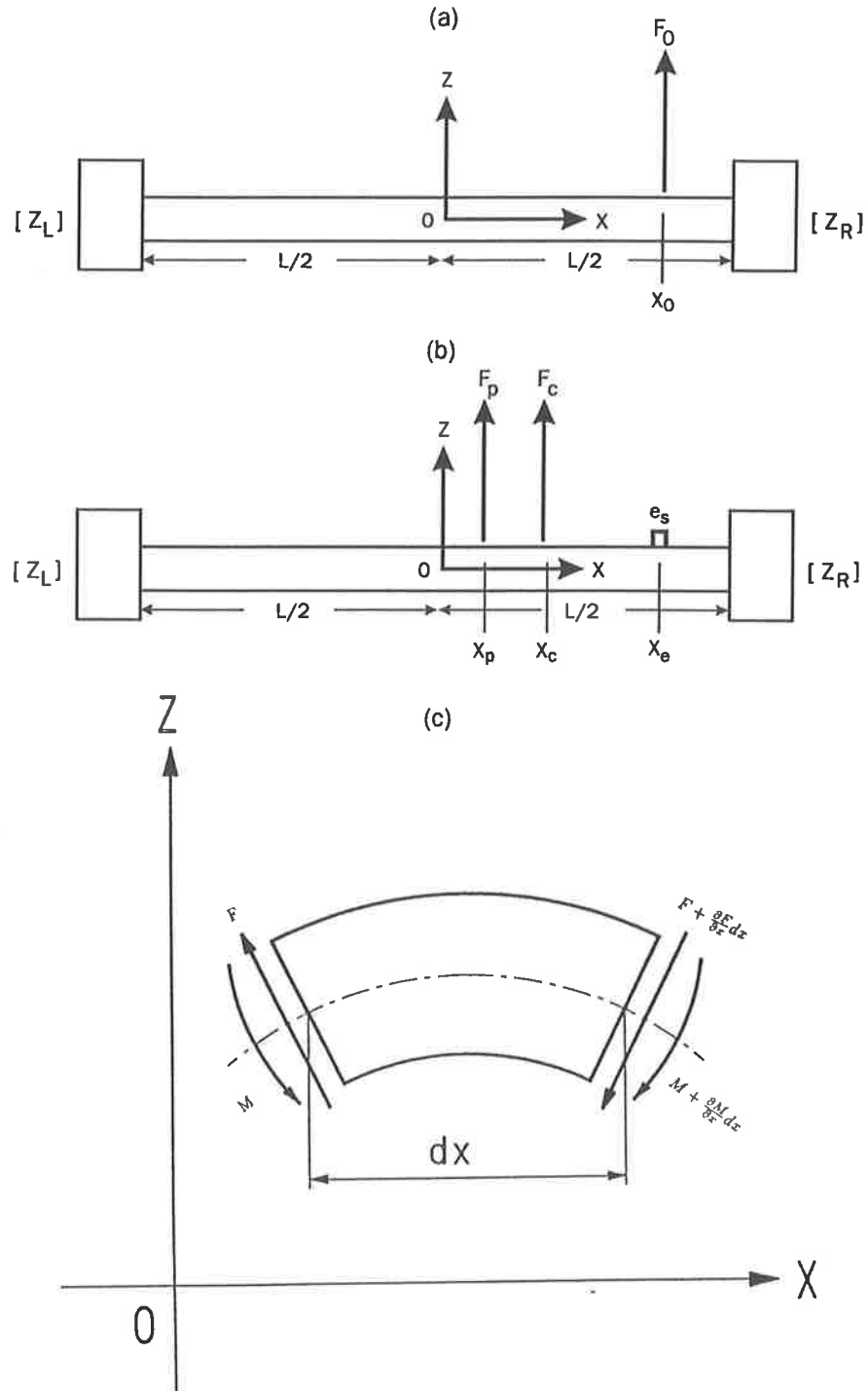


Figure 3.1: Finite beam model: (a) with point force excitation; (b) with a point force excitation and an applied point controlled force; (c) bending moment and shear force sign conventions.

and

$$[\mathbf{E}] = \begin{bmatrix} 0 \\ 0 \\ 0 \\ 0 \\ e^{k_f x_e} \\ e^{-k_f x_e} \\ e^{jk_f x_e} \\ e^{-jk_f x_e} \end{bmatrix}. \quad (3.7)$$

By adding equations (3.5) and (3.6), the total displacement is

$$\begin{aligned} w &= w_p + w_c \\ &= [\mathbf{X}_p]^T [\mathbf{E}] + [\mathbf{X}_c]^T [\mathbf{E}], \end{aligned} \quad (3.8)$$

and by substituting equations (3.2) and (3.4) into equation (3.8) one obtains

$$\begin{aligned} w &= ([\alpha_p]^{-1} [\mathbf{F}_p])^T [\mathbf{E}] + ([\alpha_c]^{-1} [\mathbf{F}_c])^T [\mathbf{E}] \\ &= \frac{F_p}{Q_3} ([\alpha_p]^{-1})_{i,8}^T [\mathbf{E}] + \frac{F_c}{Q_3} ([\alpha_c]^{-1})_{i,8}^T [\mathbf{E}]. \end{aligned} \quad (3.9)$$

The optimal control force F_c for the primary force F_p may be found by setting $w = 0$ in equation (3.9). By writing the transpose of the eighth column of the inverse of $[\alpha_p]$ as $[\mathbf{P}] = ([\alpha_p]^{-1})_{i,8}^T$, and the transpose of the eighth column of the inverse of $[\alpha_c]$ as $[\mathbf{C}] = ([\alpha_c]^{-1})_{i,8}^T$, the optimal control force can be written as

$$F_c = - \frac{[\mathbf{P}][\mathbf{E}]}{[\mathbf{C}][\mathbf{E}]} F_p \quad (3.10)$$

for an error sensor in either the near field or the far field of the control force. If the infinite beam impedances from equations (A.18) and (A.19) in Appendix A are substituted into equation (3.10), the numerical result is the same as equation (2.3) obtained for an infinite beam. In equation (2.3), the factors β_p and β_c (equation(2.2)) are functions of the distances between the excitation forces (primary and control) and the error sensor. Equation (3.10) is clearly more complicated than equation (2.3) because it takes into account not only the boundary conditions (boundary impedances), but also the relative locations of the primary and control forces, and the error sensor in relation to the ends of the beam.

If a second error sensor is introduced at some location x'_e downstream from the first error sensor x_e and a single control force driven in a way so as to optimally reduce vibration at both locations, the optimal control force can be obtained by minimizing the sum of mean squares of displacement at two locations. This is achieved by setting the partial derivatives of the sum with respect to each of the real and imaginary components of the control force equal to zero. The optimal control force can be written as

$$F_c = -\frac{1}{2} \left(\frac{[\mathbf{P}][\mathbf{E}]}{[\mathbf{C}][\mathbf{E}]} + \frac{[\mathbf{P}][\mathbf{E}']}{[\mathbf{C}][\mathbf{E}']} \right) F_p \quad (3.11)$$

where $[\mathbf{E}']$ is obtained by replacing x_e with x'_e on the right hand side of equation (3.7).

3.3 Numerical results

In this chapter, the cross section of the beam is the same as shown in Figure 2.1. Harmonic excitation is at 1000 Hz which does not correspond to a beam resonance. The flexural wavelength is $\lambda_f = 0.4824 \text{ m}$. Acceleration level is minimized at the error sensor ($x_e - x_p$)/ $\lambda_f = 4.48$, with $x_p/\lambda_f = 0$ and $(x_c - x_p)/\lambda_f = 2.24$. The beam extends from $(x - x_p)/\lambda = -10$ to $(x - x_p)/\lambda_f = 10$. These values are adhered to unless otherwise stated. For the dB ordinate scale in the following figures of this chapter, the reference level is the far field uncontrolled infinite beam acceleration produced by the primary force.

3.3.1 Effect of boundary impedance

Acceleration distributions along the beam for both optimally controlled and uncontrolled cases for a range of boundary impedances are shown in Figures 3.2 and 3.3. By optimally controlled, it means that the single control force has been driven in such a way as to obtain the maximum achievable acceleration reduction at the error sensor. As the error sensor is not near the point of application of a force or a discontinuity, near field effects on the beam response at the error sensor are expected to be numerically negligible.

For convenience, we start with a number of simple boundary conditions. The results are shown in Figure 3.2. In each case of Figure 3.2, the calculated reduction in acceleration amplitude downstream of the error sensor is over 100 dB. From these figures, it can be seen that the free-free beam has the same acceleration distribution and potential for acceleration

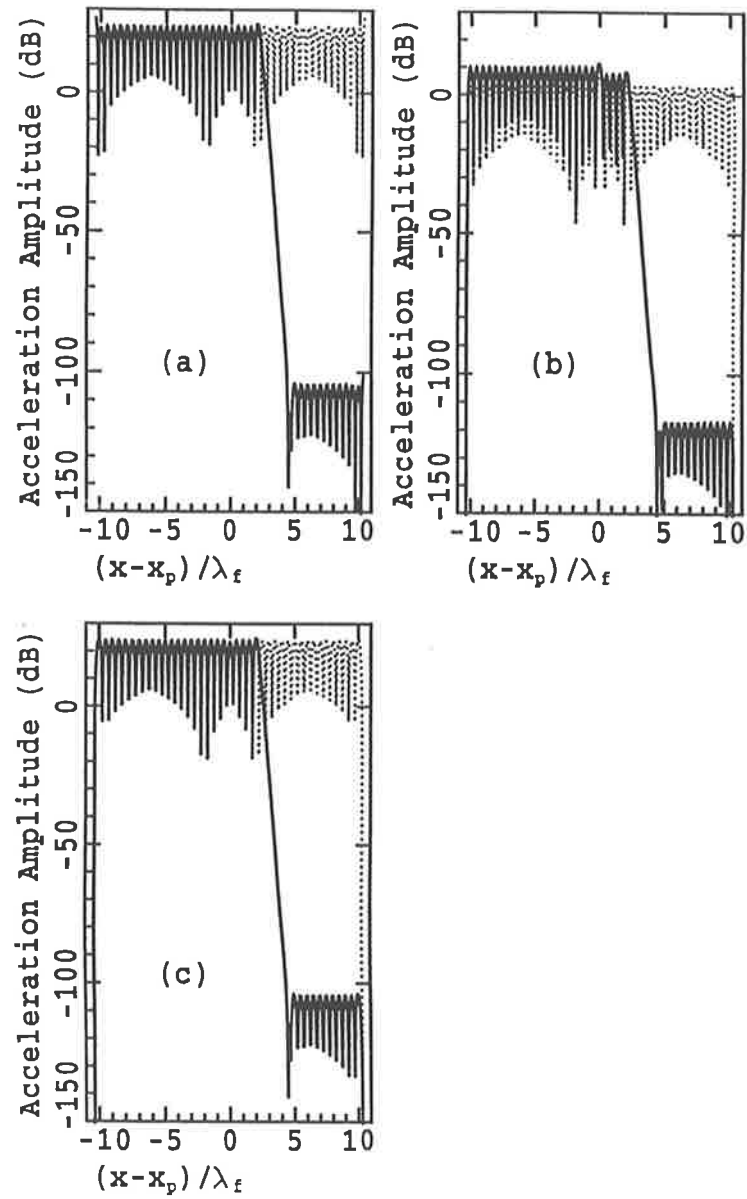


Figure 3.2: Controlled and uncontrolled distribution of beam acceleration amplitude as a function of boundary impedances. Three standard boundary conditions are: (a) $Z_{f\dot{w}} = 0$ and $Z_{m\dot{\theta}} = 0$ (free-free); (b) $Z_{f\dot{w}} = \infty$ and $Z_{m\dot{\theta}} = 0$ (pinned-pinned); (c) $Z_{f\dot{w}} = \infty$ and $Z_{m\dot{\theta}} = \infty$ (fixed-fixed). — controlled; uncontrolled.

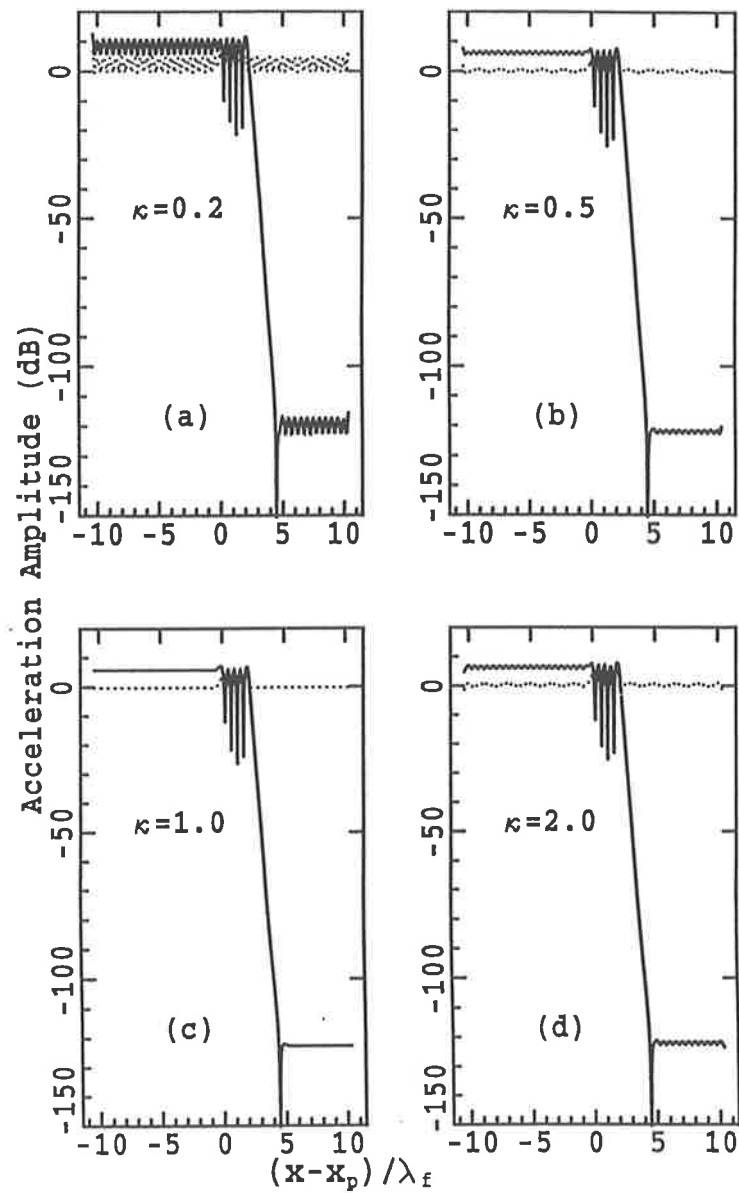


Figure 3.3: Effect of varying the boundary impedance. Boundary impedances are $[Z_L] = \kappa[Z_{L,inf}]$ and $[Z_R] = \kappa[Z_{R,inf}]$. (a) $\kappa = 0.2$; (b) $\kappa = 0.5$; (c) $\kappa = 1.0$; (d) $\kappa = 2.0$. ——— controlled; uncontrolled.

reduction as the fixed-fixed beam except within approximately half a wavelength of the ends of the beam, which are at $(x - x_p)/\lambda_f = \mp 10.32$ respectively. For the free-free beam, the increase in acceleration level near the end of the beam is the result of a near field effect caused by reflection from the boundary. For the fixed-fixed beam, the decreased acceleration level near each end of the beam is caused by the fixed nature of the boundary. The pinned-pinned beam has a different acceleration distribution from those of the free-free and fixed-fixed beam. In particular, between each end and the adjacent force, the acceleration level is about 15 dB lower. Also, the acceleration level of the controlled beam between the primary and control forces is about 5 dB lower than on the left of the primary force. These differences occur because the harmonic excitation is “off-resonance” for the pinned-pinned beam, and near a resonance frequency for the free-free and fixed-fixed beam. It is obvious that the extent of the reductions shown in the figures will not be realized in practice. However, it is necessary to present them to gain insight into the effect of the termination impedances on the beam controllability.

Acceleration amplitude distributions for various left and right boundary impedances which are a (real scalar) multiple κ of the left and right infinite beam impedances ($[Z_{L,inf}]$ and $[Z_{R,inf}]$) are presented in Figure 3.3. The purpose of this is to examine the effect on controllability of the boundary impedance approaching the infinite beam impedance. The use of the factor κ to change the boundary impedances is somewhat arbitrary, but it overcomes the difficulty of selecting a best “direction of approach” to the infinite beam impedance values. The characteristic standing wave distribution of acceleration shown in Figures 3.3(a), (b) and (d) is due to reflections from the boundaries. This variation in acceleration amplitude along the beam decreases as the boundary impedances approach the infinite beam impedance. For $\kappa < 1$ the increase in acceleration levels at each end of the beam are the result of a near field effect caused by reflections from the boundary. For $\kappa > 1$ the decreased acceleration level in the boundary near fields is caused by larger dissipation by the boundary impedances. The result for boundary impedances equal to the infinite beam impedances is shown in Figure 3.3(c).

From Figure 3.3 it can be observed that on the error sensor side of the control force, the acceleration level of the controlled beam (solid line) decreases as the boundary impedances approach the infinite beam impedances. From the control force location to the error sensor

location, the acceleration level decays exponentially to zero at the error sensor, with an average reduction of about 120 dB to the right of the error sensor. Except in the near field of the boundary, the controlled acceleration level at the anti-nodes on the right-hand side of the error sensor is essentially constant and only weakly dependent upon the beam termination impedance. It may be concluded that acceleration amplitude of a beam excited harmonically off-resonance and terminated by arbitrary impedances can be controlled by using only one control force and one error sensor.

3.3.2 Effect of control force location

Figure 3.4(a), (c) and (e) show the mean attenuation of acceleration level in the far field upstream of the primary force for free-free, pinned-pinned and infinite-infinite beams, respectively. Control of the fixed-fixed beam produces attenuation similar to that of the free-free beam, so the results for the fixed-fixed beam are not shown here. In these examples, the mean attenuation of acceleration is shown as a function of the distance between the primary and control forces ($x_c - x_p$). From these figures, it can be seen that acceleration upstream of the primary force is maximally reduced if the separation between the primary and control forces is an integer multiple of half a wavelength. The attenuation minima occur due to the difficulty in controlling the flexural vibration when the control force location is at a node of the the standing wave caused by reflection from the termination.

Figure 3.4(b), (d) and (f) show the corresponding maximum achievable mean attenuation downstream of the error sensor, for an ideal feed-forward controller. For the free and pinned beams, the maxima occur if the separation between the primary and control forces is an integer multiple of half a wavelength. The minima (every second minima for the pinned beam) occur at control and primary force separations of $(d + n\lambda_f/2)$, where d is a constant dependent on frequency and termination type (Young, 1995). The infinite beam (Figure 3.4(f)) produces a constant maximum achievable mean attenuation of about 110 dB. The reduction does not depend on the control force and primary force separation location in this case. However, the attenuation should depend on $x_e - x_c$ as there will be a small near field effect which decreases as $x_e - x_c$ increases. This will be discussed in more detail in Section 3.3.3. In the case of the infinite beam (or, alternatively a long, well

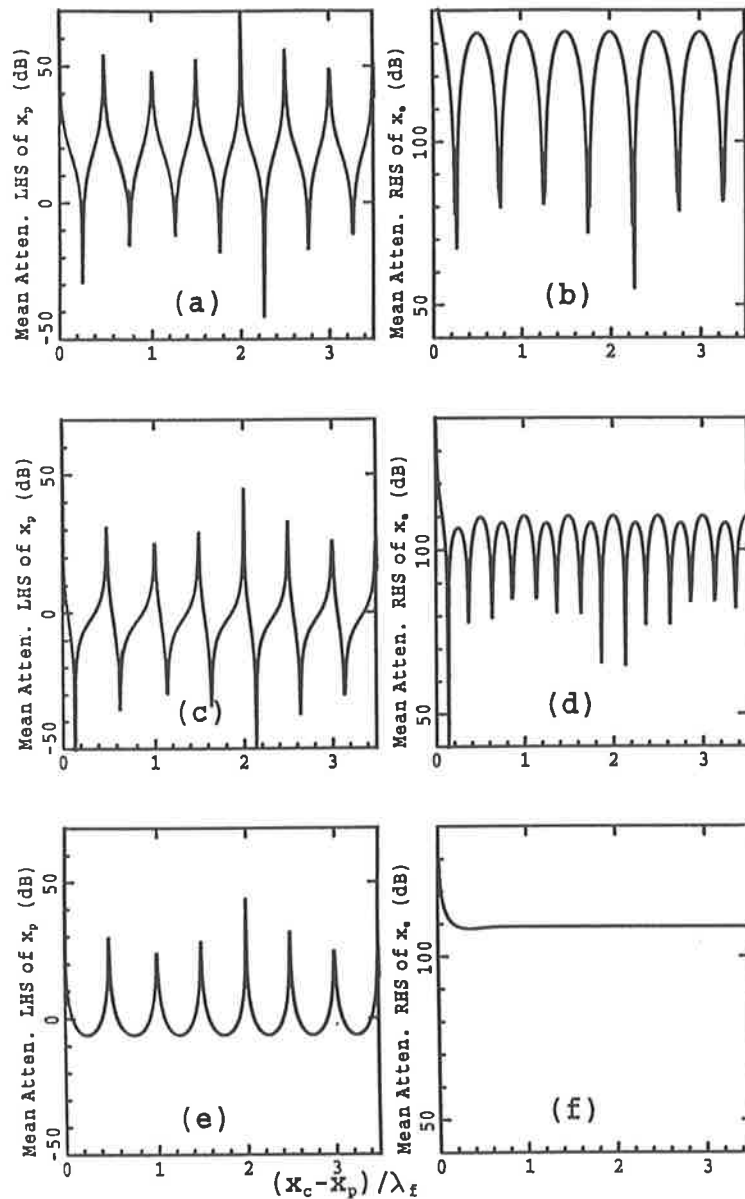


Figure 3.4: Effect of control force location x_c/λ_f on the mean attenuation of acceleration with fixed $(x_e - x_p)/\lambda_f = 2.0$. (a) Mean attenuation of acceleration upstream of the primary force (free-free); (b) mean attenuation of acceleration downstream of the error sensor (free-free); (c) mean attenuation of acceleration upstream of the primary force (pinned-pinned); (d) mean attenuation of acceleration downstream of the error sensor (pinned-pinned); (e) mean attenuation of acceleration upstream of the primary force (infinite-infinite); (f) mean attenuation of acceleration downstream of the error sensor (infinite-infinite).

damped beam), this independence from control force location ensures that good control is possible. In contrast, the extreme sensitivity of the finite beams to control force location indicates that it would be far more difficult to achieve satisfactory control if the primary force location or excitation frequency are not fixed. This implies that good control of a broadband signal would only occur over narrow bands, separated by very narrow bands where control is poor.

The level of the peaks in Figures 3.4(a), (c) and (e) and troughs in Figures 3.4(a) to (d) vary within a particular figure because the plotted points may not occur at the actual maximum or minimum value. If the plotted points were closer together it is more likely that the maximum and minimum values would be similar in any particular figure.

According to earlier work, a second control force can be used to overcome the difficulty in controlling acceleration when the first control force is located at a standing wave node (Young, 1995). Therefore, by the introduction of the second control force the depth of the troughs in Figures 3.4 would be reduced. Alternatively, it is suggested that the minima in the curves in Figures 3.4 can be higher if significant damping were added to the system.

3.3.3 Effect of error sensor location

Figure 3.5(a) shows the mean attenuation of acceleration level of the free-free beam in the far field upstream of the primary force as a function of both control force and error sensor locations. Each curve in the figure indicates the attenuation for a fixed but different value of control force location. This figure shows that the attenuation depends on $x_e - x_p$ but not on the error sensor position, provided that the error sensor is in the far field of the control and primary forces. The corresponding maximum achievable mean attenuation downstream of the error sensor is shown in Figure 3.5(b). The average reduction in dB is clearly a linearly increasing function of $(x_e - x_c)/\lambda_f$ because of the corresponding decreasing effect of the near field.

Figures 3.5(c), (e) and (g) show the mean attenuation of acceleration level on the left-hand side of the primary force for free-free, pinned-pinned and infinite-infinite beams. These figures show that the mean attenuation is different for each of the different boundary conditions, because the control force is located at a different position on a standing wave

for each boundary condition. As in Figure 3.5(a), the attenuation upstream of primary force in all three beams does not depend on the error sensor position if the error sensor is in the far field of the control and primary forces. The corresponding mean attenuation downstream of the error sensor is shown in Figures 3.5(d), (f) and (h). The minima in the curves, for free and simply supported beams, correspond to separations in the error sensor and control force location of $(d + n\lambda_f/2)$, where d is a constant dependent on frequency and termination type as previously defined (Section 3.3.2). In the control force far field of the infinite beam (Figure 3.5(h)), the attenuation is simply (in dB) proportional to the distance between the error sensor and the control force.

The troughs in the curves in Figures 3.5(b), (d) and (f) are represented correctly, and finer frequency resolution would not cause them to be much lower.

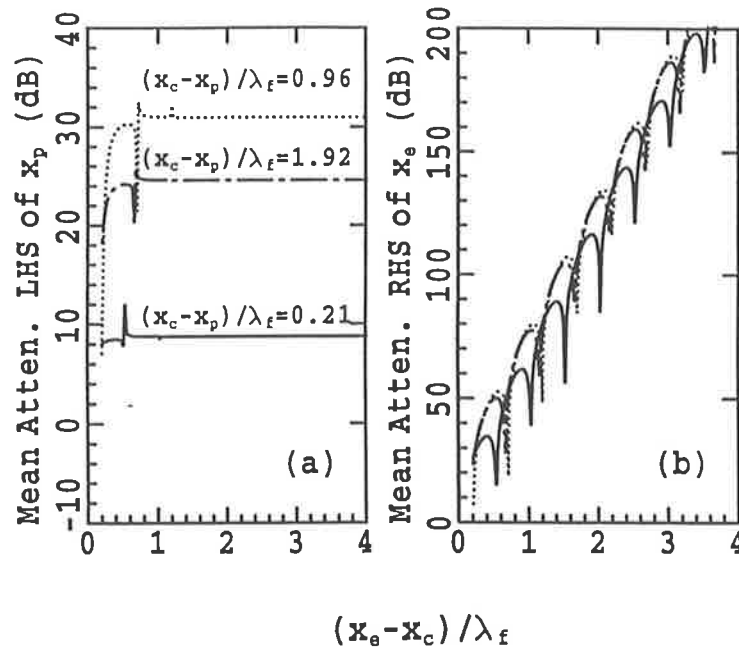
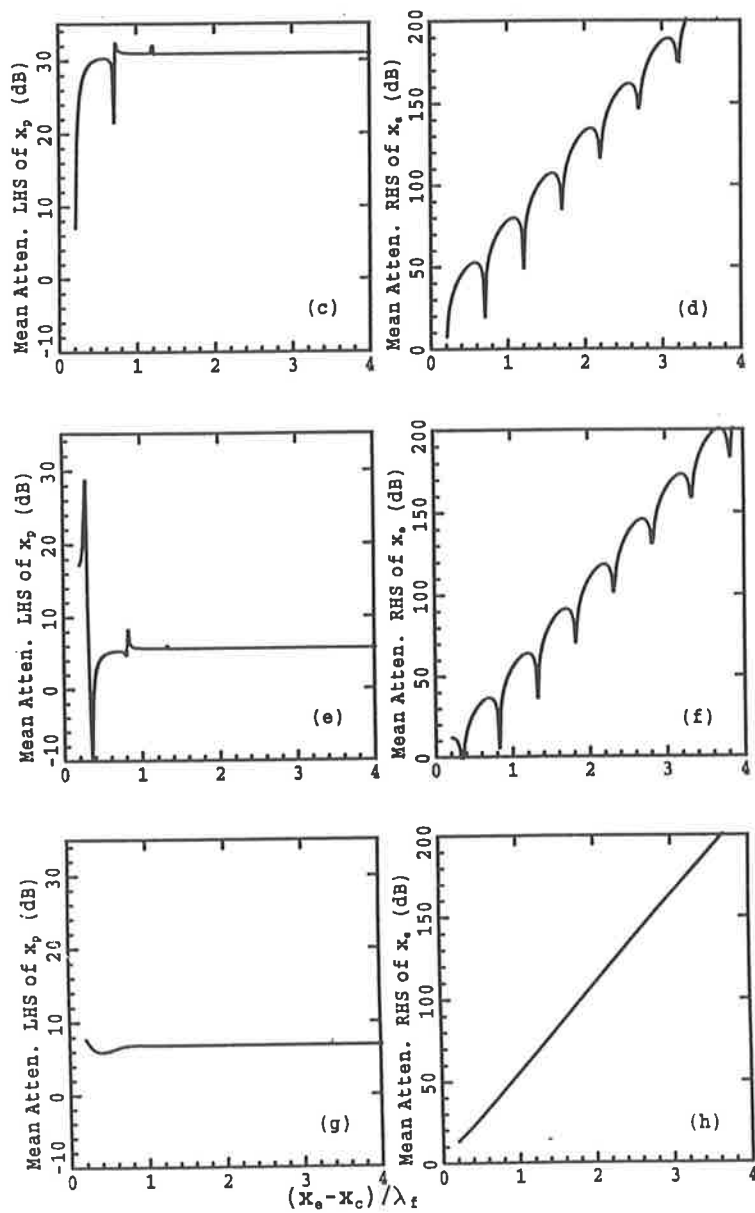


Figure 3.5: Effect of error sensor location $(x_e - x_c) / \lambda_f$ on the mean attenuation of acceleration for various separations between the primary and control forces. (a) Mean attenuation of acceleration upstream of the primary force with varying $(x_c - x_p) / \lambda_f$ (free-free); (b) mean attenuation of acceleration downstream of the error sensor with varying $(x_c - x_p) / \lambda_f$ (free-free); (c) mean attenuation of acceleration upstream of the primary force (free-free), in (c) to (h) $(x_c - x_p) / \lambda_f = 0.96$; (d) mean attenuation of acceleration downstream of the error sensor (free-free); (e) mean attenuation of acceleration upstream of the primary force (pinned-pinned); (f) mean attenuation of acceleration downstream of the error sensor (pinned-pinned); (g) mean attenuation of acceleration upstream of the primary force (infinite-infinite); (h) mean attenuation of acceleration downstream of the error sensor (infinite-infinite).

Figure 3.5—continued



3.3.4 Effect of forcing frequency

The acceleration distribution along the controlled and the uncontrolled beam (free-free beam) near a resonance frequency at 76.9 Hz is shown in Figure 3.6(a). From this figure, it can be seen that optimal control (solid line) decreases the acceleration level both upstream of the primary force and downstream of the error sensor but by a much smaller amount than shown in Figure 3.2 for 1000 Hz excitation because the error sensor is now in the near field of the control force. The acceleration level to the right of the error sensor is about 50 dB lower than that from the uncontrolled level. The forced response at a lower “off-resonance” frequency of 68.7 Hz is shown in Figure 3.6(b). This figure shows the upstream controlled acceleration is the same as the uncontrolled acceleration, and the downstream level is 30 dB lower. Clearly, better control is achieved at a resonance forcing frequency than at an “off-resonance” forcing frequency. This can be explained by considering the forced response of the controlled beam to be a weighted sum of modal components. Controlling the beam at a resonance frequency means controlling just one mode. As explained by the advocates of IMSC, this is easily achieved with one control force and one error sensor. However, at the “off-resonance” forcing frequency two modes are present in approximately equal strength and, so control at this frequency means simultaneous control of more than one mode by a single control force. Venkatraman and Narayanan (1990) reported that this is likely to induce spillover. However, the maximum achievable acceleration reduction in the beam is still large in both cases, although it is better at resonance than off-resonance.

For the controlled case, the level of the peaks and troughs vary within a particular figure, because the control force is located at a different position on a standing wave for each forcing frequency. For example, the control force is located at an anti-node in Figure 3.6(a) and at a node in Figure 3.6(b). The distance between two peaks or troughs in Figure 3.6 is half a wavelength, except for the range near the control force as this force created a discontinuity to produce a near field effect.

Figure 3.7(a) shows the mean attenuation of acceleration level in the far field upstream of the primary force as a function of the forcing frequency for the free-free beam. The corresponding maximum achievable mean attenuation downstream of the error sensor is shown in Figure 3.7(b). In both cases, acceleration is reduced maximally at frequencies for

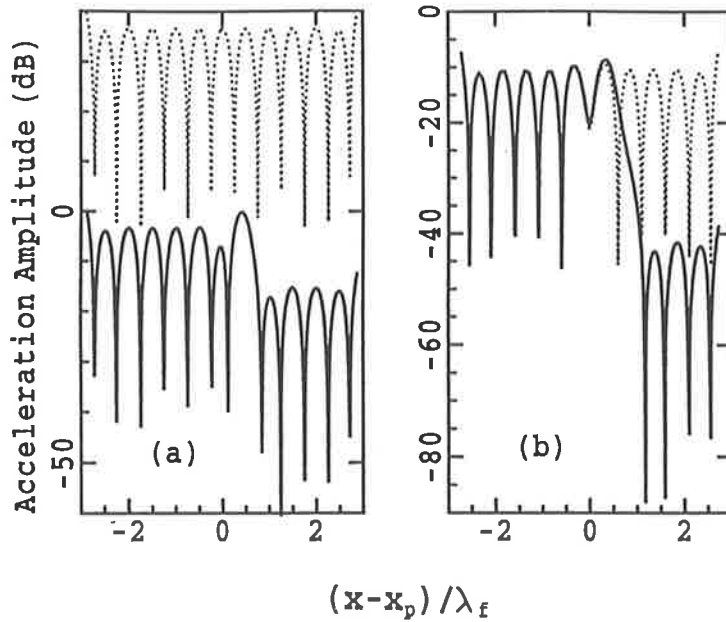


Figure 3.6: Effect of forcing frequency on the beam acceleration distribution for free-free beam. (a) Excitation near a beam resonance frequency at 76.9Hz , with force and error sensor locations of $\frac{x_c - x_p}{\lambda_f} = 0.62$, $\frac{x_e - x_p}{\lambda_f} = 1.24$; (b) excitation “off-resonance” at 68.7Hz , with $\frac{x_c - x_p}{\lambda_f} = 0.58$, $\frac{x_e - x_p}{\lambda_f} = 1.17$. ——— controlled; uncontrolled.

which the separation between the primary and control forces is an integer multiple of half of a wavelength. In Figure 3.7(b), the average attenuation clearly increases with increasing frequency. The performance is poor at low frequencies because the error sensor is in the near field of the control force.

The maximum achievable mean attenuation of acceleration in an infinite beam is shown as a function of frequency in Figures 3.7(c) and (d). There are six sharp peaks in Figure 3.7(c). At each of these peaks, the distance between control and primary forces is an integer multiple of the half wavelength. The number of peaks is limited to six because there are no reflections from boundaries (i.e. no resonances). In Figure 3.7(d), the attenuation is proportional to the square root of frequency because the attenuation is proportional to $(x_e - x_c)/\lambda_f$ and $\lambda_f \propto \frac{1}{\sqrt{f}}$.

The peaks and troughs in the curves are represented correctly in Figure 3.7(a) to (c). Finer frequency resolution would not cause them to be significantly higher or lower. These peaks and some of the troughs are caused by the reasons described in Section 3.3.2 and 3.3.3. In Figure 3.7(b), some of the troughs are also considered likely to occur when

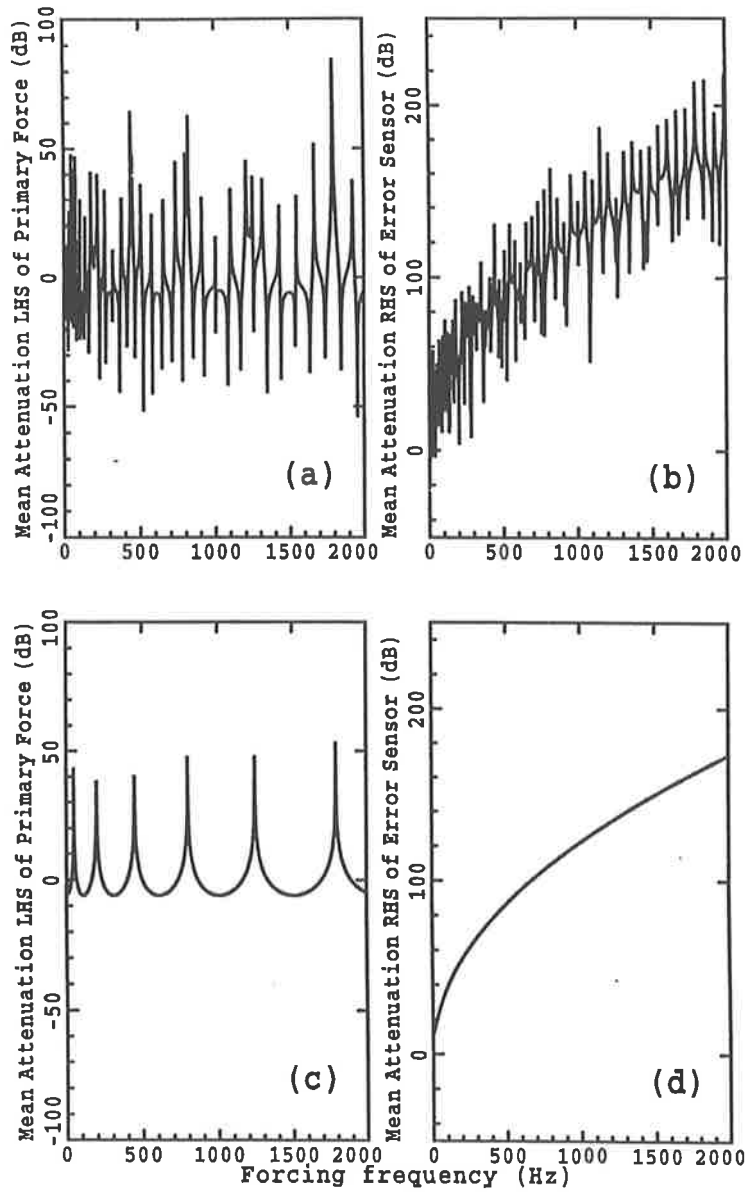


Figure 3.7: Mean attenuation of acceleration as a function of forcing frequency. (a) Mean attenuation of acceleration upstream of the primary force (free-free); (b) mean attenuation of acceleration downstream of the error sensor (free-free); (c) mean attenuation of acceleration upstream of the primary force (infinite-infinite); (d) mean attenuation of acceleration downstream of the error sensor (infinite-infinite).

the error sensor is at a standing wave node where it cannot work effectively.

The introduction of a second error sensor would be expected to result in improved attenuation in the situation where the first error sensor is located at a node. Figure 3.8 shows after adding a second error sensor, the mean attenuation of acceleration in the free-free beam is a function of forcing frequency. The second error sensor is located 0.1 m downstream from the first. The mean attenuation for a single error sensor is also shown in Figure 3.8 for comparison. From Figure 3.8(a), it can be seen that there is no improvement in attenuation upstream of the primary force by adding a second error sensor. This was expected because the attenuation upstream of the primary force depends on the separation between the primary and control force, but not on the error sensor location when the error sensor is in the far field of a control force (Section 3.3.3). However in Figure 3.8(b), it can be seen that there is an overall improvement in attenuation resulting from the introduction of the second error sensor. Particularly, the original minima in attenuation using one error sensor are generally higher or even eliminated by the introduction of the second error sensor.

3.3.5 Comparison with control of semi-infinite beam

The behavior of the semi-infinite beam shown in Figure 3.9 can be investigated by making the boundary impedance of the right end equal to the infinite beam impedance (so that no reflections are produced). A variety of impedances can be selected for the left-hand boundary. The following examples are for the use of one error sensor only. In Figures 3.10(a)—(c) the uncontrolled and optimally controlled responses of these “semi-infinite” beams for the same simple left-hand boundary conditions as in Figure 3.2 are shown.

In Figures 3.10(d)—(g) the uncontrolled and optimally controlled responses of semi-infinite beams with the same left boundary impedances as in Figure 3.3 are shown. In each of these four cases, reflections from the left boundary produce standing wave patterns on the left of the primary force. This acceleration amplitude along the beam decreases as the boundary impedances approach the infinite beam impedance. On the right side of the primary force there is no evidence of far field reflections and the beam behaves as if it were of infinite length.

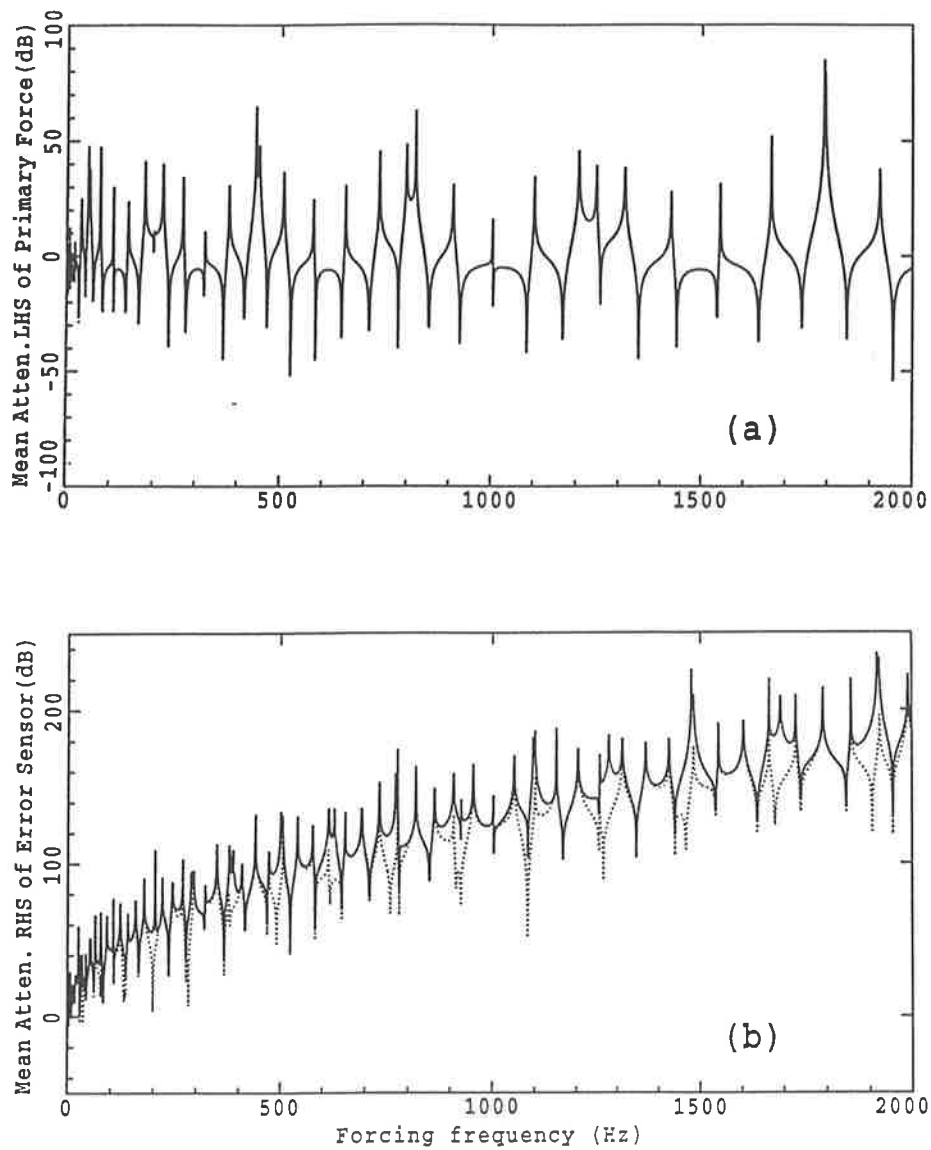


Figure 3.8: Mean attenuation of acceleration as a function of a forcing frequency. (a) Mean attenuation of acceleration upstream of the primary force (free-free), note that at all frequency above 80 Hz, the two lines are overlap; (b) Mean attenuation of acceleration downstream of the error sensors (free-free). one error sensor; — two error sensors.

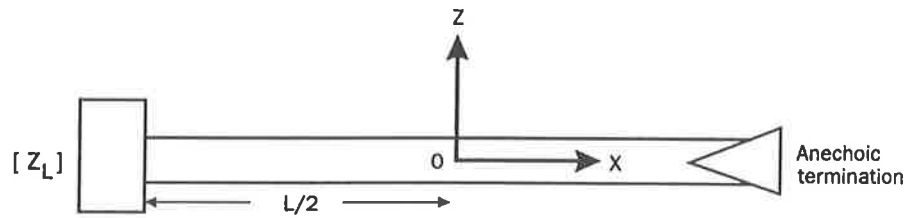


Figure 3.9: Semi-infinite beam model.

By comparing Figures 3.2 and 3.3 with Figure 3.10, it can be seen that acceleration downstream of the error sensor for the finite beams are similar to the semi-infinite beam.

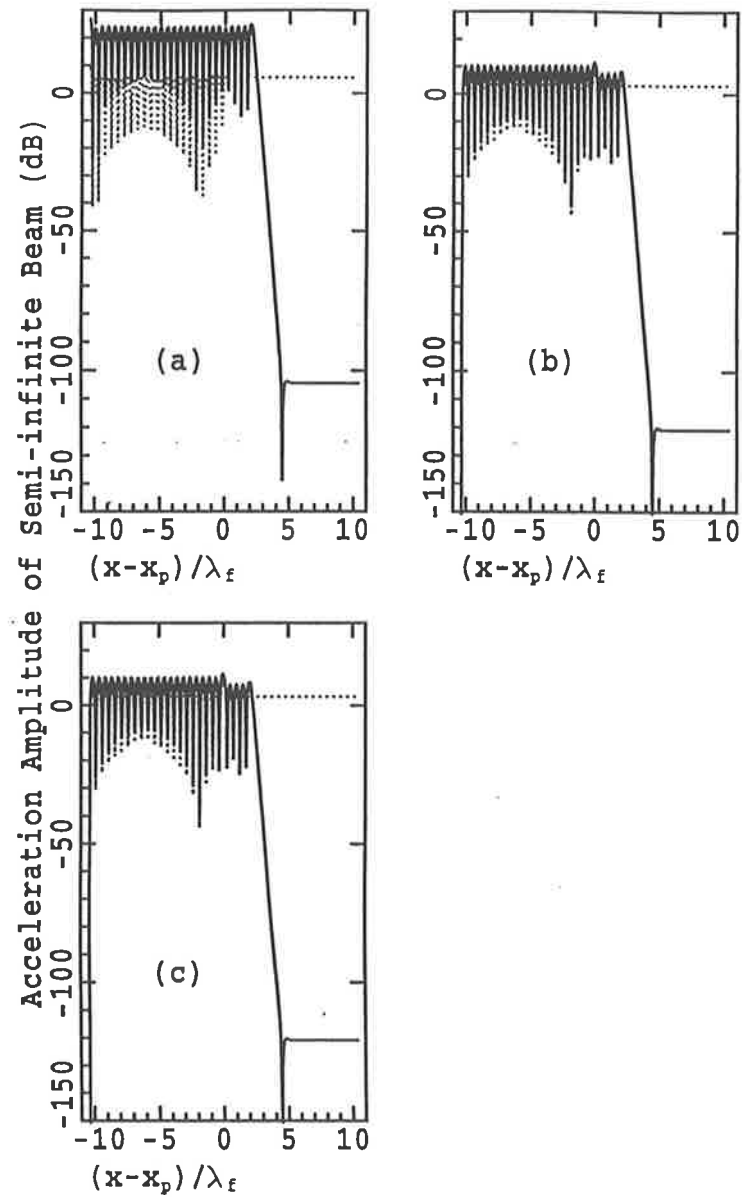
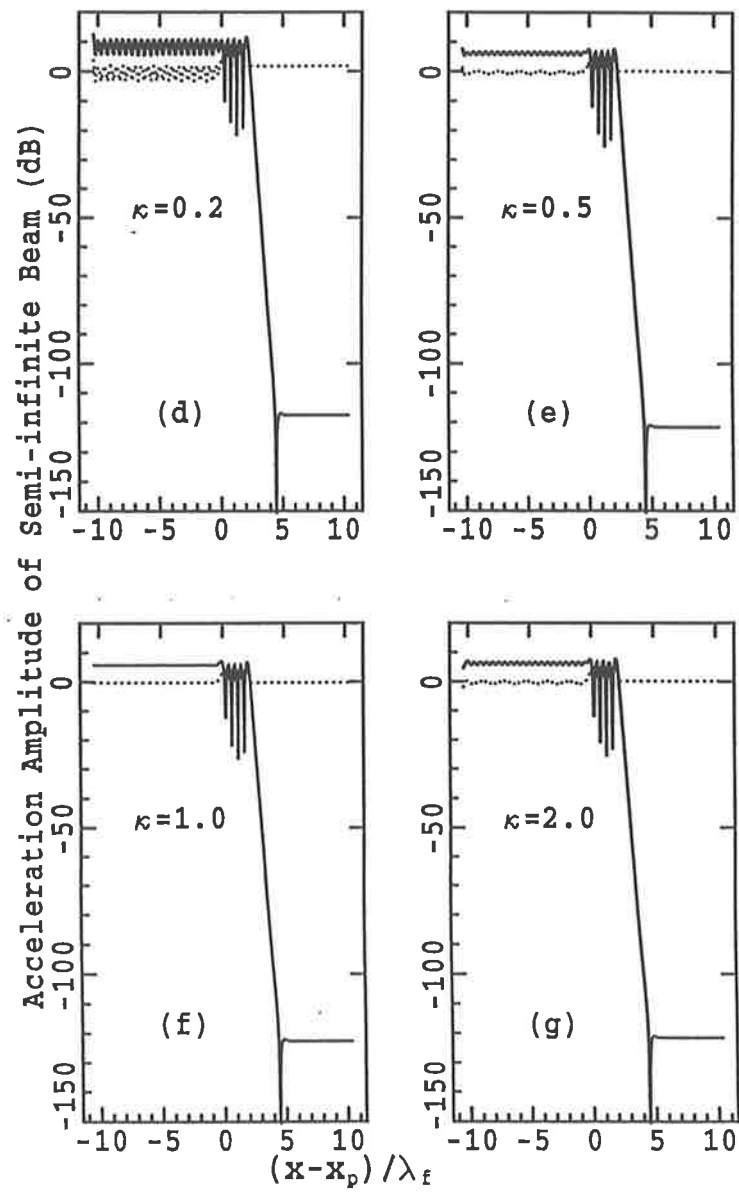


Figure 3.10: Effect of an infinite beam extending to the right of the primary excitation force, with the beam on the left side of the primary force being finite. The force and the moment boundary impedances to the right end of the beam are the infinite beam impedance. The impedances to the left end of the beam are (a) free; (b) pinned; (c) fixed; (d) as Figure 3.3, $\kappa = 0.2$; (e) $\kappa = 0.5$; (f) $\kappa = 1.0$; (g) $\kappa = 2.0$. ——— controlled; uncontrolled.

Figure 3.10—continued



3.4 Summary

Acceleration amplitude for both a finite and an infinite beam can be calculated using a propagating wave model with the supports treated as boundary impedances. If the boundary impedances of a finite beam are changed to values which represent no reflections from the ends, the characteristic standing wave distribution of acceleration amplitude flattens. This confirms that infinite beam behavior is accurately modeled. For the range of boundary impedances, representing both finite and infinite beams, the extent of control which is theoretically achievable with a feed-forward controller is found to be strongly dependent upon control force location, error sensor location and excitation frequency.

1. The maximum acceleration attenuation, upstream of the primary force and downstream of the error sensor, is achieved if the separation between the primary and control forces is an integer multiple of the half flexural wavelength. The minima occur as the control force is located at a node of the standing wave. These are true with the exception that the acceleration attenuation downstream of the error sensor is a constant for the infinite and semi-infinite beams. Increasing the separation between the primary and control forces does not improve the attenuation.
2. For error sensor locations outside the control force near field, the attenuation of acceleration upstream of the primary force does not depend on error sensor location. The attenuation of acceleration downstream of the error sensor increases with increasing separation between the error sensor and control force because of the existence of a small remaining near field effect.
3. Good harmonic acceleration control can be achieved over a relative large range of frequencies with a single control force and a single error sensor provided that the error sensor is in the far field of the control force.
4. The use of the second error sensor generally eases and in some cases even eliminates the minima in attenuation that occur when the first error sensor is located at a standing wave node.

Chapter 4

Minimizing acceleration and power transmission in a semi-infinite plate

4.1 Introduction

An extension of the work done on the minimization of power transmission in an infinite beam (Chapter 2) and acceleration amplitude in a finite beam (Chapter 3), is the minimization of acceleration and power transmission in a plate. This chapter is concerned with the theoretical analysis of the control of power transmission in a semi-infinite plate using a row of control forces and a row of error sensors. The work outlined here examines the extent of control which is achievable for a realistic control force configuration.

The model considered here is a semi-infinite plate, free at one end, anechoically terminated at the other end and simply supported along the other two sides. The analysis describes the vibration in terms of flexural waves propagating from the free end to the anechoically terminated end. The geometry of the semi-infinite plate and the alignment of the coordinate system are shown in Figure 4.1. The plate is assumed to be excited by either a single point primary force or an array of point primary forces arranged in a line across the plate parallel to the y -axis. Two alternative configurations of the control forces are considered. One configuration includes either a single point control force or a line of in-phase point control forces, and the other configuration includes a line of three independently controlled point forces. In each case, the line of control forces is arranged parallel to

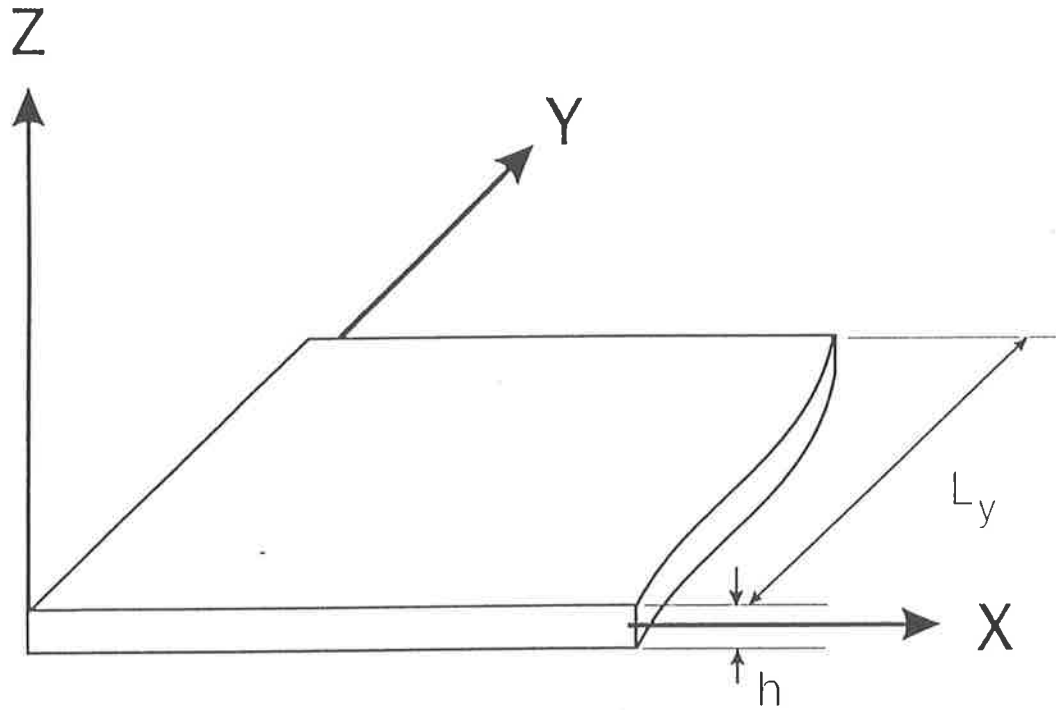


Figure 4.1: Semi-infinite plate model.

the line of primary forces. Optimal control forces required to minimize average acceleration across the plate at a specified axial location, the error sensor location, are compared to those required to minimize total power transmission along the plate for the two alternative control force configurations. As it is difficult to measure power transmission in practice, it is of interest to examine theoretically the effectiveness of minimizing acceleration at error sensors in reducing power transmission along the plate. This is done for various axial locations and numbers of error sensors.

4.2 Theory

4.2.1 Minimization of acceleration with a line of in-phase control forces

If the plate is excited by a line of in-phase primary point forces of complex amplitude F_p located at $x = x_p$, the plate response $w(x, y)$ at any location (x, y) is found using

equations (C.25) and (C.27) in Appendix C and is

$$w(x, y) = F_p w_{p-f}(x, y) = F_p \sum_{n=1}^{\infty} \frac{2}{L_y D_h} \left(\sum_{i=1}^{m_p} \sin \frac{n\pi y_i}{L_y} \right) ([\alpha_p]^{-1})_{i,6}^T [\mathbf{E}_n] \sin \frac{n\pi y}{L_y} \quad (4.1)$$

where m_p is the number of primary forces, and $[\alpha_p]$ is similar to $[\alpha]$ with F_0 replaced by F_p and x_0 replaced by x_p . Similarly, if a line of control forces of complex amplitude F_c is placed at $x = x_c$, the plate response due to these acting alone is

$$w(x, y) = F_c w_{c-f}(x, y) = F_c \sum_{n=1}^{\infty} \frac{2}{L_y D_h} \left(\sum_{i=1}^{m_c} \sin \frac{n\pi y_i}{L_y} \right) ([\alpha_c]^{-1})_{i,6}^T [\mathbf{E}_n] \sin \frac{n\pi y}{L_y} \quad (4.2)$$

where m_c is the number of control forces. The total plate response due to primary and control forces acting together is then

$$w = w_p + w_c = F_p w_{p-f} + F_c w_{c-f}. \quad (4.3)$$

The optimal control force F_c for minimizing the acceleration along the width of the plate at a constant x may be found by integrating (across the plate) the mean square of the displacement defined in equation (4.3), and setting the partial derivatives of the integration with respect to the real and imaginary components of the control force equal to zero. The result is

$$F_c = -F_p \frac{\int_0^{L_y} w_{p-f} w_{c-f}^* dy}{\int_0^{L_y} |w_{c-f}|^2 dy} \quad (4.4)$$

4.2.2 Minimization of acceleration with a line of three independently driven control forces

If the plate is driven by an array of in-phase primary point forces in a line at $x = x_p$ and three independent control point forces in a line at $x = x_c$, the total plate response may be written as

$$w = w_p + w_c = F_p w_{p-f} + F_{c1} w_{c-f1} + F_{c2} w_{c-f2} + F_{c3} w_{c-f3}. \quad (4.5)$$

The quantities w_{c-f1} , w_{c-f2} and w_{c-f3} are each calculated in a similar way to w_{c-f} in Section 4.2.1.

The optimal control forces for minimizing acceleration may be found by integrating (across the plate) the mean square of the displacement defined in equation (4.5) and setting

the partial derivatives of the integration with respect to each of the real and imaginary components of the control forces equal to zero. The result is an optimal set of control forces as follows

$$\begin{bmatrix} F_{c1} \\ F_{c2} \\ F_{c3} \end{bmatrix} = - \begin{bmatrix} \int_0^{L_y} |w_{c-f1}|^2 dy & \int_0^{L_y} w_{c-f1}^* w_{c-f2} dy & \int_0^{L_y} w_{c-f1}^* w_{c-f3} dy \\ \int_0^{L_y} w_{c-f1} w_{c-f2}^* dy & \int_0^{L_y} |w_{c-f2}|^2 dy & \int_0^{L_y} w_{c-f2}^* w_{c-f3} dy \\ \int_0^{L_y} w_{c-f1} w_{c-f3}^* dy & \int_0^{L_y} w_{c-f2} w_{c-f3}^* dy & \int_0^{L_y} |w_{c-f3}|^2 dy \end{bmatrix}^{-1} \begin{bmatrix} \int_0^{L_y} w_{p-f} w_{c-f1}^* dy \\ \int_0^{L_y} w_{p-f} w_{c-f2}^* dy \\ \int_0^{L_y} w_{p-f} w_{c-f3}^* dy \end{bmatrix} F_p. \quad (4.6)$$

The procedure can be extended to any number of independently controlled forces.

4.2.3 Power transmission

The expression given by Romano (1990) for the x component of vibration intensity (or power transmission per unit width) in a plate is

$$P_x(t) = -[\dot{w}Q_x - \frac{\partial \dot{w}}{\partial x} M_x - \frac{\partial \dot{w}}{\partial y} M_{xy} + \dot{\xi}_x N_x + \dot{\xi}_y N_{xy}] \quad (4.7)$$

where $\dot{\xi}_x N_x$ and $\dot{\xi}_y N_{xy}$ are associated with longitudinal and shear wave propagation. Each force in equation (4.7) is "per unit width" and for this study, the contribution of longitudinal and shear waves is assumed to be zero. The total instantaneous flexural wave power transmission through a section at constant x is then given by

$$P_x(t) = - \int_0^{L_y} \left[\dot{w}(x, y, t) Q_x(x, y, t) - \frac{\partial \dot{w}(x, y, t)}{\partial x} M_x(x, y, t) - \frac{\partial \dot{w}(x, y, t)}{\partial y} M_{xy}(x, y, t) \right] dy \quad (4.8)$$

or, for a single frequency

$$P_x(t) = - \int_0^{L_y} \left[j\omega w(x, y, t) Q_x(x, y, t) - j\omega \frac{\partial w(x, y, t)}{\partial x} M_x(x, y, t) - j\omega \frac{\partial w(x, y, t)}{\partial y} M_{xy}(x, y, t) \right] dy. \quad (4.9)$$

Adopting the approach of Skudrzyk (1965), the real (or active) part of power transmission along the plate is calculated as the product of real part of the force term with the real part

of the velocity term for each pair of terms in equation (4.9) and the result is time averaged. Thus the active power transmission is given by

$$P_{xa} = -\frac{1}{2} \int_0^{L_y} \text{Re} \left\{ [j\omega w(x, y)]^* Q_x(x, y) - \left[j\omega \frac{\partial w(x, y)}{\partial x} \right]^* M_x(x, y) - \left[j\omega \frac{\partial w(x, y)}{\partial y} \right]^* M_{xy}(x, y) \right\} dy \quad (4.10)$$

where, according to Leissa (1969)

$$M_x = -D_h \left(\frac{\partial^2 w}{\partial x^2} + \nu \frac{\partial^2 w}{\partial y^2} \right), \quad (4.11)$$

$$M_{xy} = -D_h (1 - \nu) \frac{\partial^2 w}{\partial x \partial y} \quad (4.12)$$

and

$$Q_x = -D_h \left(\frac{\partial^3 w}{\partial x^3} + \frac{\partial^3 w}{\partial x \partial y^2} \right). \quad (4.13)$$

For one line of primary forces and a second line of control forces parallel to the y-axis, the resulting total power transmission can be expressed in terms of the primary and control forces, using superposition. Thus power transmission corresponding to equation (4.4) (representing optimal control of acceleration) is obtained by substituting equation (4.4) into (4.3) and the result into equations (4.10) to (4.13). The power transmission corresponding to equation (4.6) can be obtained in a similar way.

It is assumed for convenience here that it is possible in practice to actually measure the total power transmission through a particular plate cross section.

4.2.4 Minimization of power transmission with a line of in-phase point control forces

The total power transmission resulting from a line of in-phase point primary forces and a line of in-phase point control forces acting together can be found by substituting equations (4.1) and (4.2) into (4.3) and the result into equations (4.10) to (4.13). Carrying out the indicated substitutions in equations (4.11) to (4.13) gives the following expressions for the bending moment, twisting moment and shear force respectively.

$$M_x = -D_h \left[F_p \frac{\partial^2 w_{p-f}}{\partial x^2} + F_c \frac{\partial^2 w_{c-f}}{\partial x^2} + \nu \left(F_p \frac{\partial^2 w_{p-f}}{\partial y^2} + F_c \frac{\partial^2 w_{c-f}}{\partial y^2} \right) \right], \quad (4.14)$$

$$M_{xy} = -D_h(1 - \nu) \left(F_p \frac{\partial^2 w_{p-f}}{\partial x \partial y} + F_c \frac{\partial^2 w_{c-f}}{\partial x \partial y} \right) \quad (4.15)$$

and

$$Q_x = \frac{\partial M_x}{\partial x} - \frac{\partial M_{xy}}{\partial y} = -D_h \left(F_p \frac{\partial^3 w_{p-f}}{\partial x^3} + F_c \frac{\partial^3 w_{c-f}}{\partial x^3} + F_p \frac{\partial^3 w_{p-f}}{\partial x \partial y^2} + F_c \frac{\partial^3 w_{c-f}}{\partial x \partial y^2} \right). \quad (4.16)$$

These and equation (4.3) can be substituted into the expression for the power transmission through any plate cross section at axial location x (equation (4.10)) to produce,

$$P_{xa} = \frac{1}{2} \int_0^{L_y} \text{Re}[F_c F_c^* A + F_c B F_p^* + F_c^* C F_p + F_p F_p^* D] dy \quad (4.17)$$

where

$$A = j\omega D_h \left[- \left(\frac{\partial^3 w_{c-f}}{\partial x^3} + \frac{\partial^3 w_{c-f}}{\partial x \partial y^2} \right) w_{c-f}^* + \left(\frac{\partial^2 w_{c-f}}{\partial x^2} + \nu \frac{\partial^2 w_{c-f}}{\partial y^2} \right) \frac{\partial w_{c-f}^*}{\partial x} + (1 - \nu) \frac{\partial^2 w_{c-f}}{\partial x \partial y} \frac{\partial w_{c-f}^*}{\partial y} \right], \quad (4.18)$$

$$B = j\omega D_h \left[- \left(\frac{\partial^3 w_{c-f}}{\partial x^3} + \frac{\partial^3 w_{c-f}}{\partial x \partial y^2} \right) w_{p-f}^* + \left(\frac{\partial^2 w_{c-f}}{\partial x^2} + \nu \frac{\partial^2 w_{c-f}}{\partial y^2} \right) \frac{\partial w_{p-f}^*}{\partial x} + (1 - \nu) \frac{\partial^2 w_{c-f}}{\partial x \partial y} \frac{\partial w_{p-f}^*}{\partial y} \right], \quad (4.19)$$

$$C = j\omega D_h \left[- \left(\frac{\partial^3 w_{p-f}}{\partial x^3} + \frac{\partial^3 w_{p-f}}{\partial x \partial y^2} \right) w_{c-f}^* + \left(\frac{\partial^2 w_{p-f}}{\partial x^2} + \nu \frac{\partial^2 w_{p-f}}{\partial y^2} \right) \frac{\partial w_{c-f}^*}{\partial x} + (1 - \nu) \frac{\partial^2 w_{p-f}}{\partial x \partial y} \frac{\partial w_{c-f}^*}{\partial y} \right] \quad (4.20)$$

and

$$D = j\omega D_h \left[- \left(\frac{\partial^3 w_{p-f}}{\partial x^3} + \frac{\partial^3 w_{p-f}}{\partial x \partial y^2} \right) w_{p-f}^* + \left(\frac{\partial^2 w_{p-f}}{\partial x^2} + \nu \frac{\partial^2 w_{p-f}}{\partial y^2} \right) \frac{\partial w_{p-f}^*}{\partial x} + (1 - \nu) \frac{\partial^2 w_{p-f}}{\partial x \partial y} \frac{\partial w_{p-f}^*}{\partial y} \right]. \quad (4.21)$$

Numerically, the coefficients B and C are equal if the error sensors are in the far field of the primary and control forces. The optimal control force corresponding to minimum power transmission is obtained by determining derivatives of equation (4.17) with respect to the real and imaginary components of the control force and setting the derivatives equal to zero. Then the optimal control force is

$$F_c^{opt} = - \frac{\int_0^{L_y} B^* dy + \int_0^{L_y} C dy}{2 \int_0^{L_y} \text{Re}[A] dy} F_p. \quad (4.22)$$

4.2.5 Minimization of power transmission with a line of three independently driven point control forces

For this case, the plate response given by equation (4.5) can be substituted into equations (4.10) to (4.13) to give an expression for the total power transmitted past a line across the plate at an axial location x , which can be written in matrix form as:

$$P_{xa} = \frac{1}{2} \int_0^{L_y} \text{Re}[\mathbf{F}^H \mathbf{A} \mathbf{F}] dy \quad (4.23)$$

where

$$\mathbf{F} = [F_p, F_{c1}, F_{c2}, F_{c3}]^T \quad (4.24)$$

and

$$\mathbf{A} = \begin{bmatrix} A(1,1) & A(1,2) & A(1,3) & A(1,4) \\ A(2,1) & A(2,2) & A(2,3) & A(2,4) \\ A(3,1) & A(3,2) & A(3,3) & A(3,4) \\ A(4,1) & A(4,2) & A(4,3) & A(4,4) \end{bmatrix}. \quad (4.25)$$

The coefficients $A(i, j)$ ($i = 1, 4, j = 1, 4$) of matrix \mathbf{A} result from the product of terms in equation (4.10) which each contain contributions from the four different force elements of equation (4.24). Thus $A(i, j)$ is the product of the contribution to the first part of each term in equation (4.10) due to the i th element of \mathbf{F} with the contribution to the second part of each term due to the j th element of \mathbf{F} . For example

$$A(1,1) = j\omega D_h \left[-\left(\frac{\partial^3 w_{p-f}}{\partial x^3} + \frac{\partial^3 w_{p-f}}{\partial x \partial y^2} \right) w_{p-f}^* + \left(\frac{\partial^2 w_{p-f}}{\partial x^2} + \nu \frac{\partial^2 w_{p-f}}{\partial y^2} \right) \frac{\partial w_{p-f}^*}{\partial x} + (1 - \nu) \frac{\partial^2 w_{p-f}}{\partial x \partial y} \frac{\partial w_{p-f}^*}{\partial y} \right], \quad (4.26)$$

$$A(2,1) = j\omega D_h \left[-\left(\frac{\partial^3 w_{p-f}}{\partial x^3} + \frac{\partial^3 w_{p-f}}{\partial x \partial y^2} \right) w_{c-f1}^* + \left(\frac{\partial^2 w_{p-f}}{\partial x^2} + \nu \frac{\partial^2 w_{p-f}}{\partial y^2} \right) \frac{\partial w_{c-f1}^*}{\partial x} + (1 - \nu) \frac{\partial^2 w_{p-f}}{\partial x \partial y} \frac{\partial w_{c-f1}^*}{\partial y} \right], \quad (4.27)$$

$$A(4,1) = j\omega D_h \left[-\left(\frac{\partial^3 w_{p-f}}{\partial x^3} + \frac{\partial^3 w_{p-f}}{\partial x \partial y^2} \right) w_{c-f3}^* + \left(\frac{\partial^2 w_{p-f}}{\partial x^2} + \nu \frac{\partial^2 w_{p-f}}{\partial y^2} \right) \frac{\partial w_{c-f3}^*}{\partial x} + (1 - \nu) \frac{\partial^2 w_{p-f}}{\partial x \partial y} \frac{\partial w_{c-f3}^*}{\partial y} \right]. \quad (4.28)$$

An optimum set of control forces corresponding to minimum power transmission is obtained by determining derivatives of equation (4.23) with respect to the real and imaginary components of each control force and setting the derivatives equal to zero. An optimum set of control forces corresponding to a minimum power transmission due to three independently driven control forces is

$$\begin{bmatrix} F_{c1} \\ F_{c2} \\ F_{c3} \end{bmatrix} = - \begin{bmatrix} \int_0^{L_y} (A^*(2,2) + A(2,2))dy & \int_0^{L_y} (A^*(3,2) + A(2,3))dy \\ \int_0^{L_y} (A^*(2,3) + A(3,2))dy & \int_0^{L_y} (A^*(3,3) + A(3,3))dy \\ \int_0^{L_y} (A^*(2,4) + A(4,2))dy & \int_0^{L_y} (A^*(3,4) + A(4,3))dy \end{bmatrix}^{-1} \left(\begin{bmatrix} \int_0^{L_y} A^*(1,2)dy \\ \int_0^{L_y} A^*(1,3)dy \\ \int_0^{L_y} A^*(1,4)dy \end{bmatrix} + \begin{bmatrix} \int_0^{L_y} A(2,1)dy \\ \int_0^{L_y} A(3,1)dy \\ \int_0^{L_y} A(4,1)dy \end{bmatrix} \right) F_p. \quad (4.29)$$

The procedure can be extended for any number of independently controlled forces. By comparing equations (4.17) with (4.23) and (4.22) with (4.29), it can be seen that the single force changes to a force vector when in-phase force control changes to independent force control. The expression for power transmission given by equation (4.23) not only includes each force term, but also includes coupling force terms, which makes independent force control much more complex than in-phase force control to analyze.

The matrix which must be inverted in equation (4.29) is ill-conditioned for the case where only one or two modes are propagating and three independent control forces are used. This is because the control system is under determined and thus ill-conditioned (Nelson and Elliott, 1993). In this case, the use of one or two control forces respectively would be expected to achieve good performance.

4.3 Numerical results

The numerical results presented here have been calculated for a steel plate with Young's modulus $E = 207$ GPa, density $\rho = 7700$ kg/m³, Poisson's ratio $\nu = 0.3$, length 1.4 m, thickness $h = 0.003$ m and width $L_y = 0.5$ m. One end of the plate was terminated anechoically. The sides adjacent to the anechoically terminated end were simply supported and the remaining edge was free. In the following figures except Figure 4.9 in this chapter,

the x location of the primary force is at $x_p = 0.025 \text{ m}$ and the error sensor is at $x_e = 0.565 \text{ m}$. When a row of control forces appear, these forces are equally spaced in a row across the plate, parallel to the y -axis, so that the distance between any two control forces is twice the distance from the outermost control force to the edge of the plate. When an equal number (3, 6, 12 or 24) of primary and control forces appear, each primary force shares an identical Y -coordinate location with one control force. The locations of primary forces, control forces and error sensors are adhered to unless otherwise stated. Theoretical cut-on frequencies for the first five modes are listed in Table 4.1.

Table 4.1: Calculated cut-on frequencies for the first five modes

Plate mode	Cut-on frequency (Hz)
First mode	30
Second mode	118
Third mode	266
Fourth mode	473
Fifth mode	739

In many of the calculations for the plate, rounding errors became a problem when the calculated attenuation due to active control exceeded 120 dB and values shown higher than this can be quite inaccurate. However this is not considered to be a serious problem as, in practice active control systems will be limited to achieve a maximum of about 50 dB attenuation.

4.3.1 One primary and one control force

In this section it is assumed that an ideal feed-forward controller is available and that it is possible to obtain a measure of power transmission along the plate to be used as the controller error input.

Figure 4.2(a) is a contour map, calculated using the theory of Section 4.2.4, of the maximum achievable reduction (in dB) in active power transmitted along the plate to the

anechoic end as a function of the location (x_c, y_c) of a single control force. The frequency of 210 Hz ($\lambda_f = 0.3752m$) was chosen to begin with as it is well above the cut-on frequency of the second propagating mode and well below the cut-on frequency of the third propagating mode. The control force locations corresponding to local power transmission minima listed in Table 4.2 were found by using optimization software to process the data used for generating the contour plot and are also shown in the figure as asterisks (*). The optimal control force and resulting power transmission for the control force in this location were then calculated using the analysis of the previous sections and the results are recorded in Table 4.2. Figure 4.2(a) demonstrates the important result that for any control force location there is always a control force amplitude which does not increase the power transmission downstream of the control force, including the degenerate case of $F_c = 0$. The map clearly has several local minima, a fact which makes the search for the optimal control force location very time consuming.

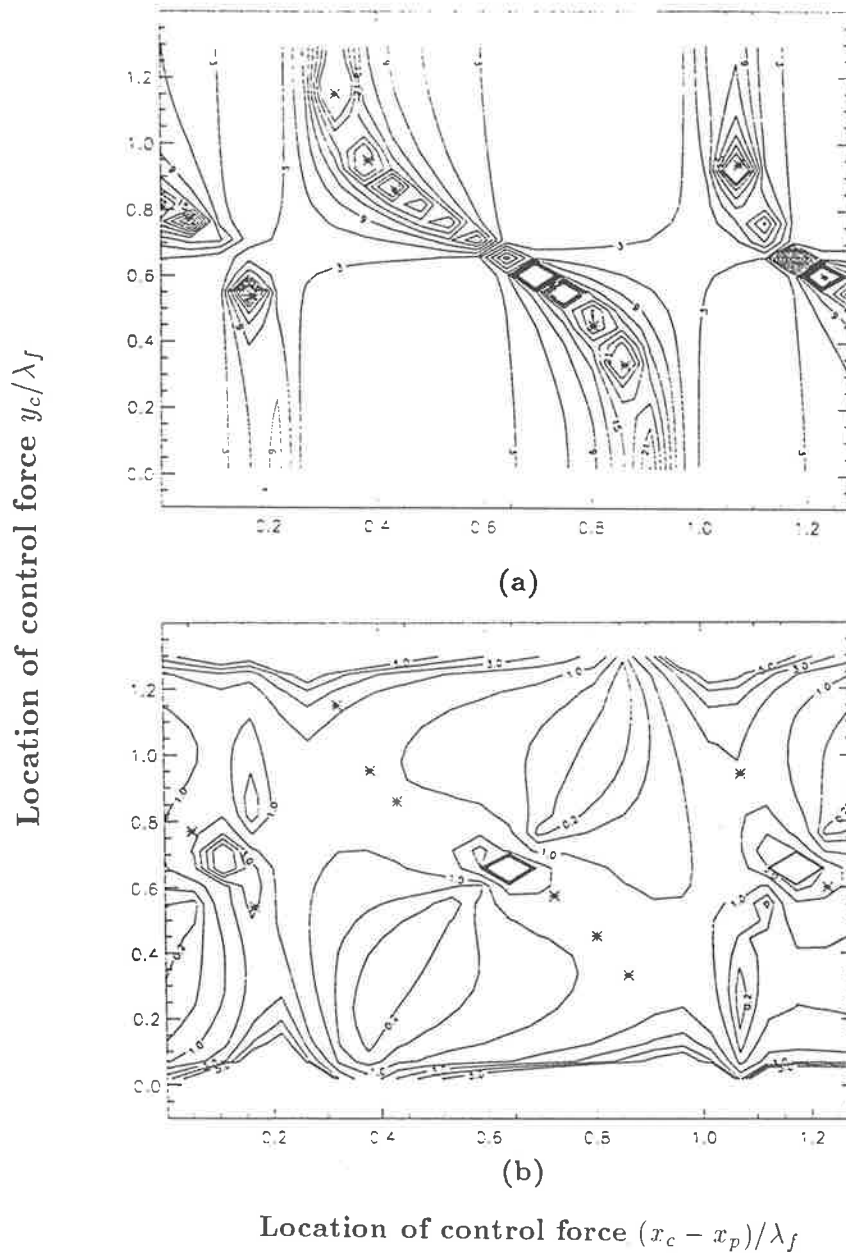


Figure 4.2: (a) Maximum achievable reduction of power transmission (dB) due to one primary force and one control force as a function of control force location. The primary force is located at $(x_p, y_p)/\lambda_f = (0.07, 0.80)$, the error sensor is located at $(x_e - x_p)/\lambda_f = 1.43$ and the forcing frequency is 210 Hz ($\lambda_f = 0.3752m$). (b) Optimal control force amplitude relative to the primary force to achieve the maximum power transmission reduction of (a).

Table 4.2: Control force locations for power transmission minima at 210 Hz

$(x_c - x_p)/\lambda_f$	y_c/λ_f	$\frac{ F_c }{ F_p }$	$\phi_c - \phi_p$ radians	P.T.reduction(dB)
0.00	0.80	1.00	$-\pi$	∞
0.05	0.77	1.70	$-\pi$	25
0.17	0.53	3.15	0	30
0.32	1.15	2.24	0	45
0.38	0.95	1.12	0	40
0.43	0.86	1.08	0	36
0.72	0.57	1.66	$-\pi$	43
0.80	0.45	1.11	$-\pi$	26
0.86	0.33	1.25	π	50
1.07	0.94	1.94	π	28
1.23	0.60	2.39	0	40

From Figure 4.2(a), it can be seen that there are two relatively large regions in which a single control force can be located to achieve a power transmission attenuation of more than 15 dB. These regions extend from the top mid-left of the contour map (at $(x_c - x_p, y_c)/\lambda_f = (0.30, 1.3)$) to the bottom mid-right (at $(x_c - x_p, y_c)/\lambda_f = (0.95, 0.0)$). As these regions are so large, there appears to be a reasonable prospect of achieving a useful experimental result with this plate and force arrangement. Figure 4.2(b) shows the optimal control force amplitude required to produce the attenuation given in Figure 4.2(a) (for unit amplitude primary force). In regions where good attenuation is obtained, the required optimal control force varies considerably, with minimum values of about 1.1 times the primary force amplitude or greater. If both the maximum achievable attenuation value and the desire to minimize the control force amplitude are taken into consideration, the optimal control force location seems to be $(x_c - x_p, y_c)/\lambda_f = (0.32, 1.15)$ with 45 dB maximum achievable power transmission reduction or $(x_c - x_p, y_c)/\lambda_f = (0.86, 0.33)$ with 50 dB maximum achievable power transmission reduction.

Figure 4.3 shows the result of repeating the calculation displayed in Figure 4.2, but for

a higher frequency of 510 Hz ($\lambda_f = 0.2408m$). As before, the local power transmission minima (*) are listed in Table 4.3. In practice, the best result would probably be achieved by placing a control force of amplitude 1.0 at $(x_c - x_p, y_c)/\lambda_f = (1.85, 1.88)$ to produce a maximum power transmission reduction of 15 dB. The peak in Figure 4.3(a) is relatively flat and occupies a relatively large region and, so the result is not very sensitive to variations in control force location.

Both Figures 4.2(a) and Figure 4.3(a) show that the maximum achievable reduction in power transmission depends strongly on the location of control forces. If the control force location is not chosen correctly, it is quite likely that the maximum achievable power transmission reduction will be negligible. It is also noted that a single control force location will be ineffective over a range of frequencies. Figure 4.3(a) indicates that there are several regions near the edge of the plate where a theoretical attenuation of more than 6 dB can be produced, but in practice it may not be possible to generate the large control forces which would be required. Note that Figures 4.2 and 4.3 do not extend to the plate boundaries as it is clear that optimal control forces on the boundaries would tend to infinity and power transmission reduction would tend to zero.

Results which are not shown here to conserve space and which are similar to those of Figure 4.2 and 4.3 have been produced for the frequencies 310 Hz, 410 Hz and 610 Hz. The number of frequencies examined was limited by the computation time (approximately 90 hours for the UNIX machine SUN/4) required to produce each map. From these examples, it can be observed that optimum control force location and power transmission attenuation are strong functions of the excitation frequency. One trend with increasing excitation frequency is that the number of local minima increases because the complexity of the vibration pattern increases.

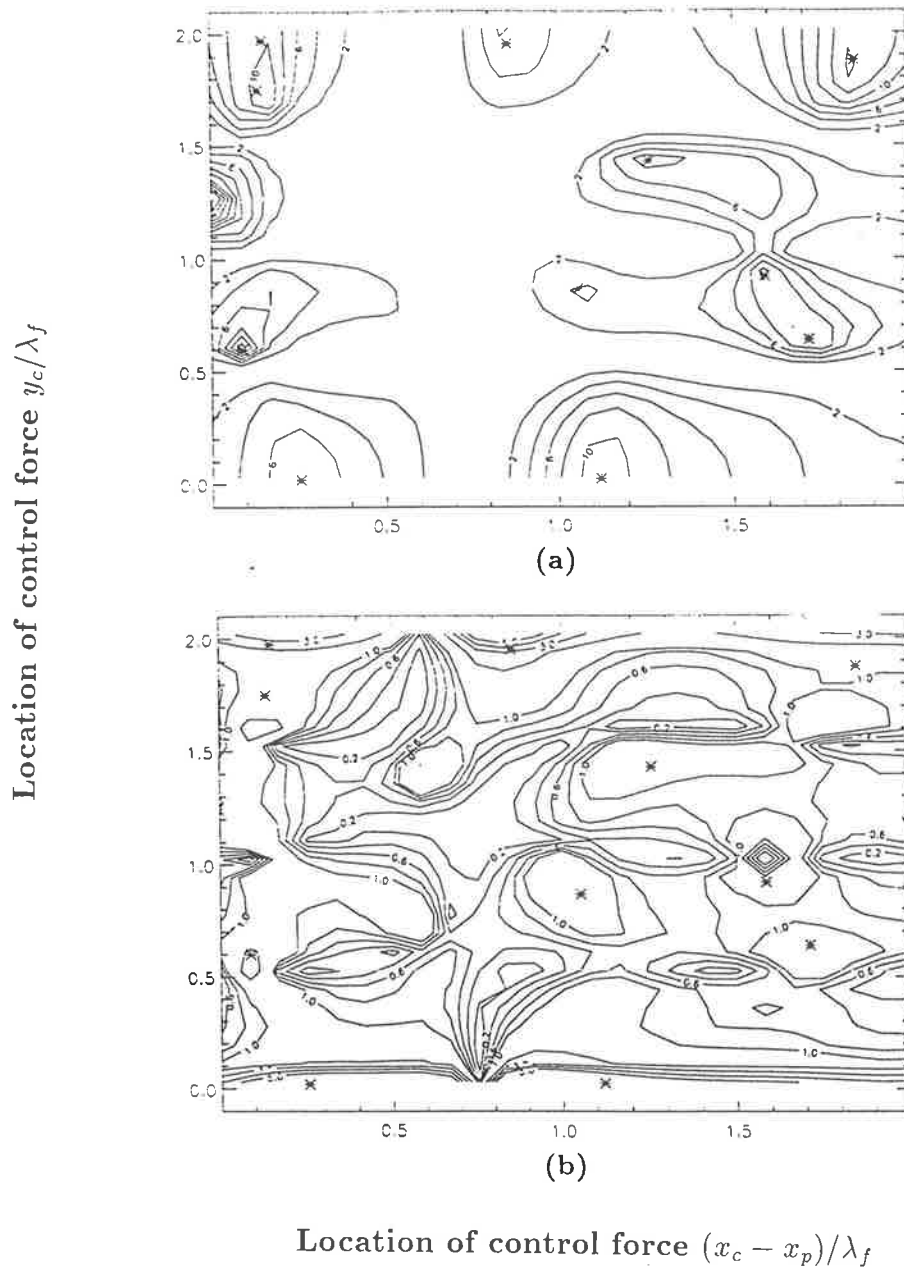


Figure 4.3: (a) Maximum achievable reduction of power transmission (dB) due to one primary force and one control force as a function of control force location. The primary force is located at $(x_p, y_p)/\lambda_f = (0.10, 1.25)$, the error sensor is located at $(x_e - x_p)/\lambda_f = 2.24$ and the forcing frequency is 510 Hz ($\lambda_f = 0.2408m$). (b) Optimal control force amplitude relative to the primary force to achieve the maximum power transmission reduction of (a).

Table 4.3: Control force locations for power transmission minima at 510 Hz

$(x_c - x_p)/\lambda_f$	y_c/λ_f	$\frac{ F_c }{ F_p }$	$\phi_c - \phi_p$ radians	P.T.reduction(dB)
0.00	1.24	1.00	$-\pi$	∞
0.08	0.60	2.40	0	14
0.13	1.75	1.32	0	14
0.14	1.97	2.10	0	10
0.25	0.02	11.55	$-\pi$	7
0.86	1.95	3.18	$-\pi$	6
1.06	0.87	1.40	π	4
1.12	0.02	9.50	0	11
1.26	1.43	1.39	0	9
1.59	0.92	1.49	$-\pi$	10
1.71	0.64	1.35	π	11
1.85	1.88	1.07	$-\pi$	15
2.18	1.21	1.31	0	5

The maximum practical achievable reductions of real power transmission corresponding to the optimal control force location at each of the frequencies analyzed are presented in Table 4.4, which shows that increasing the excitation frequency generally decreases the maximum achievable power transmission reduction. It is also of interest to note that the number of complex modal wavenumbers k_{in} (equation (C.8)) shown in Appendix C) increases as the excitation frequency is increased — for example, there are 2 at 210 Hz, 4 at 510 Hz and 5 at 1000 Hz. Thus, as waves represented by imaginary exponents in equation (C.4) in Appendix C (where k_{3m} and k_{4m} are imaginary if using the condition of equation (C.10)) represent propagation of power along the plate, there will be more modes propagating at high frequencies, making active control with a single control force more difficult.

Table 4.4: Effect of forcing frequency on the maximum achievable power transmission reduction for a single primary force and a single control force (at best practical locations)

Freq (Hz)	$(x_c - x_p)/\lambda_f$	y_c/λ_f	$\frac{ F_c }{ F_p }$	$\phi_c - \phi_p$ radians	P.T. reduction (dB)
210	0.32	1.15	2.24	0	45
210	0.86	0.33	1.25	π	50
310	0.90	1.22	1.04	π	30
410	0.83	1.37	0.89	π	16
510	1.85	1.88	1.07	$-\pi$	15
610	0.72	1.96	1.02	$-\pi$	20

4.3.2 A row of in-phase, uniform amplitude control forces and a single primary force

In this case, the single primary force is driven with unit amplitude near the free end of the plate at $x_p = 0.025$ and $y_p = 0.25$, which is at the same y -coordinate location as the central control force. At an excitation frequency of 210 Hz (Figure 4.4(a)), more than 50 dB reduction is obtained over a large area of control force location. At frequencies of 410 Hz (Figure 4.4(b)), 510 Hz (Figure 4.4(c)) and 610 Hz (Figure 4.4(d)), a maximum achievable power transmission reduction greater than 20 dB is observed for a few control force locations. However, the areas of these locations are so small that it is unlikely that this level of control could be realized in practice.

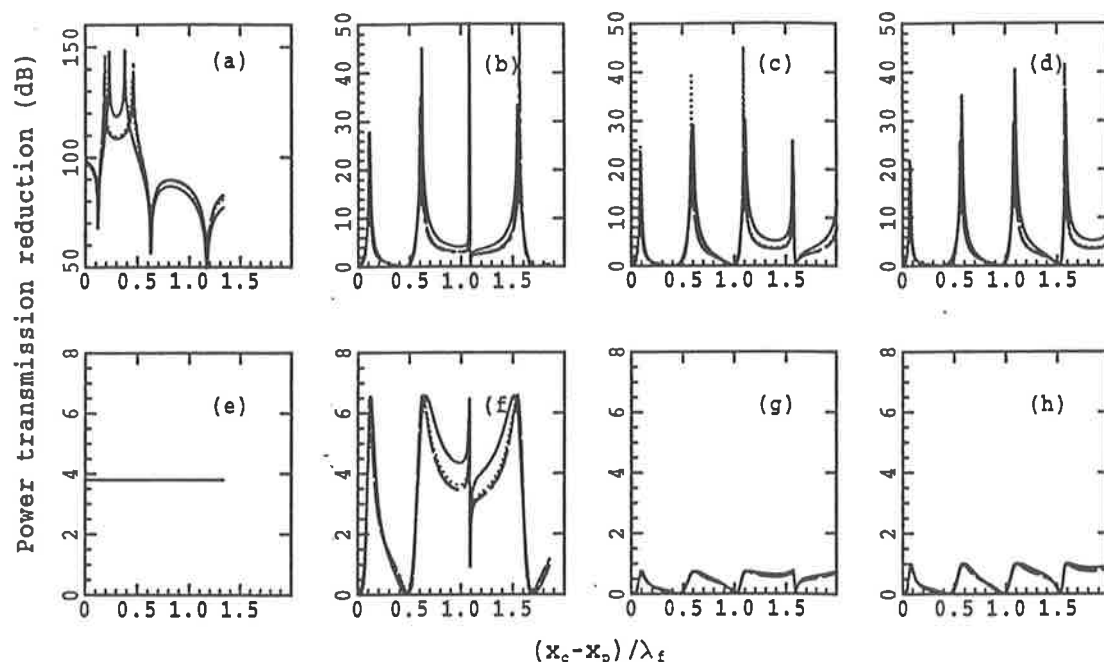


Figure 4.4: Power transmission reduction for a line of in-phase, uniform amplitude control forces and a single primary force. (a) “central” primary force (in (a) to (d), $y_p = 0.25$) located at $(x_p, y_p)/\lambda_f = (0.07, 0.67)$, error sensor located at $(x_e - x_p)/\lambda_f = 1.43$ and excitation frequency 210 Hz; (b) $(x_p, y_p)/\lambda_f = (0.09, 0.93)$, $(x_e - x_p)/\lambda_f = 2.01$ and excitation frequency 410 Hz; (c) $(x_p, y_p)/\lambda_f = (0.10, 1.04)$, $(x_e - x_p)/\lambda_f = 2.24$ and excitation frequency 510 Hz; (d) $(x_p, y_p)/\lambda_f = (0.11, 1.14)$, $(x_e - x_p)/\lambda_f = 2.45$ and excitation frequency 610 Hz; (e) off-center primary force (in (e) to (h), $y_p = 0.3$) located at $(x_p, y_p)/\lambda_f = (0.07, 0.80)$, $(x_e - x_p)/\lambda_f = 1.43$ and excitation frequency 210 Hz; (f) $(x_p, y_p)/\lambda_f = (0.09, 1.12)$, $(x_e - x_p)/\lambda_f = 2.01$ and excitation frequency 410 Hz; (g) $(x_p, y_p)/\lambda_f = (0.10, 1.25)$, $(x_e - x_p)/\lambda_f = 2.24$ and excitation frequency 510 Hz; (h) $(x_p, y_p)/\lambda_f = (0.11, 1.36)$, $(x_e - x_p)/\lambda_f = 2.45$ and excitation frequency 610 Hz. — 1 primary force and 3 control forces; 1 primary force and 6 control forces; - - - 1 primary force and 12 control forces; - · - · - 1 primary force and 24 control forces.

Figures 4.4(e) to 4.4(h) show the results of repeating the calculation displayed in Figures 4.4(a) to 4.4(d), but with the primary force located off the mid point of the plate y-axis, as for Section 4.3.1. At an excitation frequency of 210 Hz (Figure 4.4(e)), the maximum achievable power transmission reduction is approximately 4 dB for 3, 6, 12 or 24 control forces over a wide range of locations of the row of control forces. The performance of the row of control forces for the off-center primary force (Figure 4.4(e)) is much poorer than when the primary force is located centrally (Figure 4.4(a)) for a frequency of 210 Hz, which shows that the symmetric control force distribution will not control the anti-symmetric component of primary vibration. At a frequency of 410 Hz (Figure 4.4(f)), the maximum achievable power transmission reduction of 6 dB for the off-center primary force can be obtained by choosing appropriate control force locations. However for excitation frequencies of 510 Hz (Figure 4.4(g)) and 610 Hz (Figure 4.4(h)), the maximum achievable reduction is only 1dB. In all of the cases shown in Figure 4.4, increasing the number of control forces above three does not increase the maximum achievable power transmission reduction.

4.3.3 A row of in-phase, uniform amplitude control forces and a row of in-phase, uniform amplitude primary forces

Figure 4.5 shows power transmission reduction corresponding to an equal number (3, 6, 12, 24) of primary and control forces. The results shown in Figure 4.5(a) to 4.5(d) are similar to the results shown in corresponding Figures 4.4(a) to 4.4(d). This is probably because the symmetric control forces control symmetric components of primary vibration in these two cases. At a frequency of 210 Hz, and an equal number of primary and control forces (Figure 4.5(a)), the maximum achievable power transmission reduction is slightly less than that achievable for a row of control forces and a single central primary force (Figure 4.4(a)). At excitation frequencies of 410 Hz, 510 Hz and 610 Hz, it can be seen that the achievable reduction in power transmission is critically dependent upon the axial location of the row of control forces with this optimal location being frequency dependent as well.

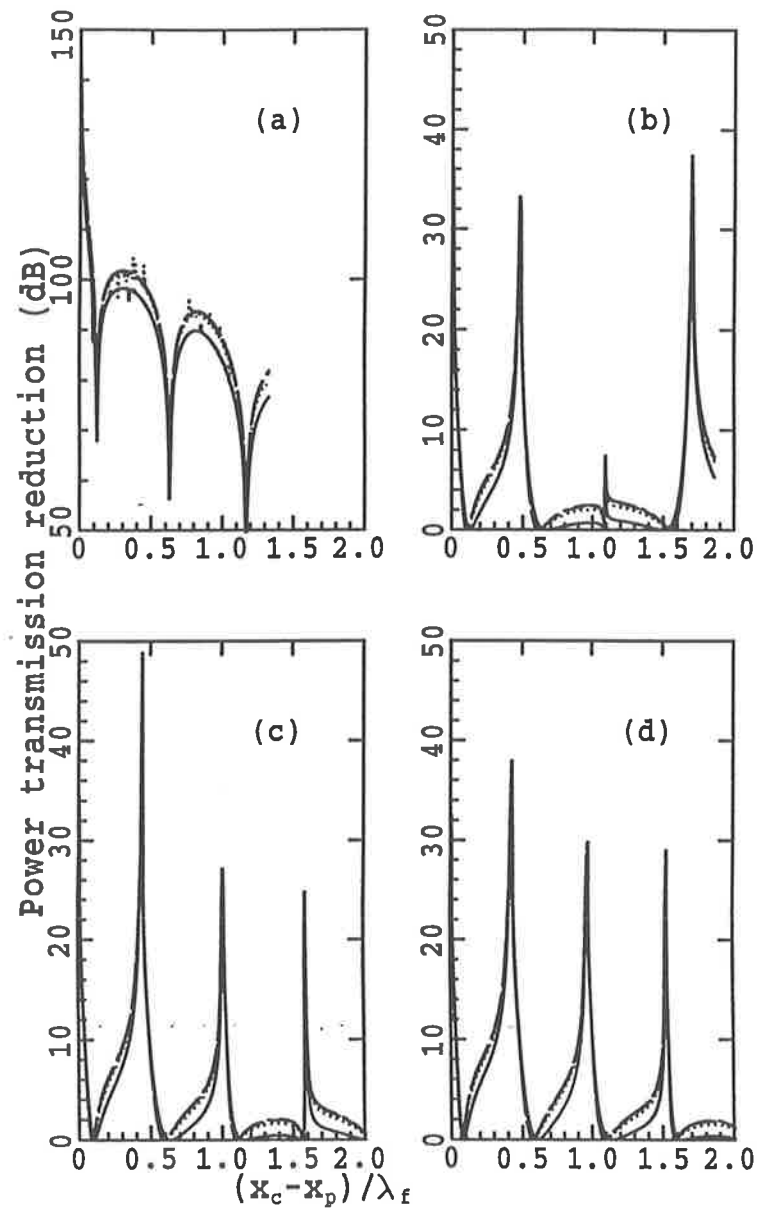


Figure 4.5: Power transmission reduction for the same number of in-phase, uniform-amplitude primary and control forces. (a) excitation frequency 210Hz; (b) excitation frequency 410Hz; (c) excitation frequency 510Hz; (d) excitation frequency 610Hz. — 3 primary forces and 3 control forces; 6 primary forces and 6 control forces; --- 12 primary forces and 12 control forces; -.-.- 24 primary forces and 24 control forces.

4.3.4 Effect of forcing frequency on performance with in-phase control forces

In practice, the location of each control force is fixed and it is of interest to observe the frequency range over which control can be achieved for a control force configuration optimized for a particular frequency. Figure 4.6(a) shows the maximum power transmission reduction which can be obtained with a fixed control force location as a function of frequency for a single off-center primary force as for Figure 4.2 and a single control force located at the optimum position for an excitation frequency of 210 Hz ($(x_c - x_p, y_c)/\lambda_f = (0.38, 0.91)$). It can be seen from the figure that power transmission reduction at frequencies higher than the cut-on frequency (266 Hz) of the third mode is either very small or zero.

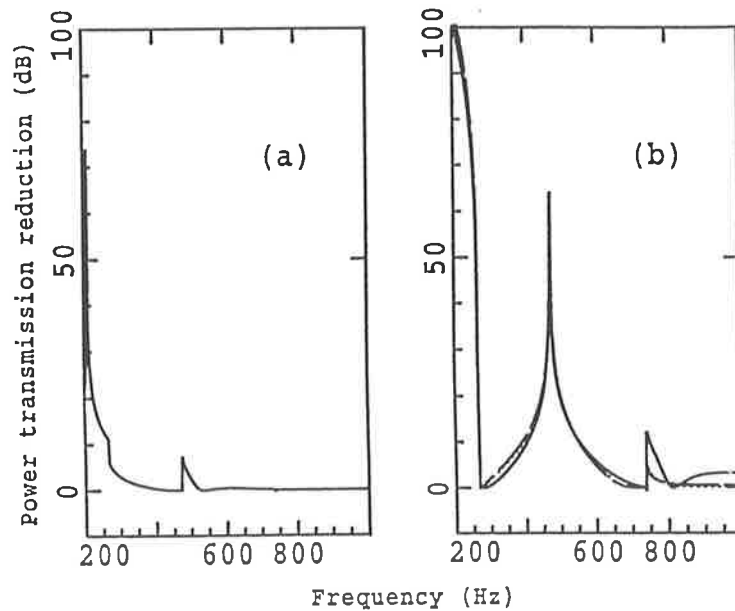


Figure 4.6: Power transmission reduction as a function of frequency with the control forces located at the optimum location for 210 Hz. (a) a single off-center primary and control forces; (b) equal numbers of primary and control forces with the control forces driven in phase. — a single primary force with a single control force in (a) and 3 primary forces with 3 control forces in (b); 6 primary forces and 6 control forces; - - - 12 primary forces and 12 control forces; - · - · 24 primary forces and 24 control forces.

Figure 4.6(b) shows the performance for an equal number of primary and control forces,

with the row of control forces at the optimum location of $(x_c - x_p)/\lambda_f = 0.30$ for 210 Hz (shown in Figure 4.5(a)). From this figure, it can be seen that power transmission reduction decreases as the frequency increases from 200 Hz to 266 Hz (the cut-on frequency of the third mode). At 266 Hz the reduction is zero. At the cut-on frequencies of the fourth and fifth modes (473 Hz and 739 Hz), significant levels of power transmission reduction are also obtained. Increasing the number of primary and control forces equally above three does not significantly affect the maximum achievable power transmission reduction. In general, the control performance for an equal number of primary and control forces is better than that for a single off-center primary force and a number of control forces. This is probably because the symmetric control force arrangement effectively controls the symmetric but not the anti-symmetric components of vibration generated by the primary forces.

It seems from these results that the maximum reduction in power transmission is achieved when only one or two modes are propagating, which is as expected. However, the reason for the increase in performance close to the cut-on frequencies of the fourth and fifth modes is that at resonance the system response is dominated by one mode thus one control force can achieve good performance.

4.3.5 A row of three in-phase primary forces and a row of three independently driven control forces

For this case, at an excitation frequency of 210 Hz (Figure 4.7(a)) with both independent and in-phase control forces, more than 50 dB of reduction is obtained at all but a few discrete control force locations. Power transmission reduction with three independent control forces is not presented in Figure 4.7(a). This is because at 210 Hz there are only two waves cut-on and there are three independent control forces so the control system is under determined (Nelson and Elliott, 1993), thus the matrix in equation (4.29) is too ill-conditioned to be inverted to obtain a valid solution. Reducing the number of control forces to two would fix this problem. At frequencies of 410 Hz, 510 Hz and 610 Hz (Figures 4.7(b), (c) and (d) respectively), power transmission reductions achieved with independently driven control forces are more than 50 dB greater than with in-phase control forces. Thus, for these cases there is a considerable advantage in using independently driven control forces.

The continuous line in Figure 4.8 shows the effect of changing the excitation frequency on power transmission reduction when the three control forces are driven independently, with the row of control forces at the optimal location of $(x_c - x_p)/\lambda_f = 0.30$ for 210 Hz. The result with three independent control forces for frequencies less than 266 Hz is omitted because of numerical difficulties associated with the ill-conditioning of the matrix in equation (4.29). As for Figure 4.6, the control forces are optimally located for a 210 Hz primary excitation. For comparison, the result for three in-phase forces (from Figure 4.6(b)) is shown as a dotted line. In Figure 4.8, it can be seen that the theoretically achievable power transmission reduction achieved by driving the control forces independently is more than 50 dB for all frequencies lower than the cut-on frequency of the fifth mode (that is, 739 Hz), and well in excess of the reduction achieved by driving the forces in-phase. It is interesting to note that at the cut-on frequency of the fourth mode (473 Hz), the three independent optimal control force amplitudes and phases are the same as the three in-phase optimal control forces, and similar maximum power transmission reductions are achieved for both in-phase control and independent control cases. The difference in the calculated reductions between the two cases is a result of rounding errors in the calculations. As the frequency is further increased to 816 Hz, the maximum achievable reduction decreases rapidly to zero (dB). Between 816 Hz and 1000 Hz, the reduction increases slowly again to about 4 dB, but in this region use of independent rather than in-phase control forces produces no significant advantage.

Figure 4.7 demonstrates the important result that, in contrast with a row of in-phase control forces, it is possible to achieve a large reduction in power transmission by driving the control forces independently. Such results can be obtained by placing the row of control forces at any except a few discrete distances downstream of the primary forces. Figure 4.8 shows that with three independently driven control forces, good control can be achieved over the frequency range for which only the first five modes are propagating.

The results given so far, indicate that there are some control force locations where significantly less attenuation in power transmission can be obtained. However, a second line of control forces may be used to overcome the difficulty in controlling power transmission when the first line of control forces is located at a nodal line in a standing wave (see the examples for vibration control, Young, 1995).

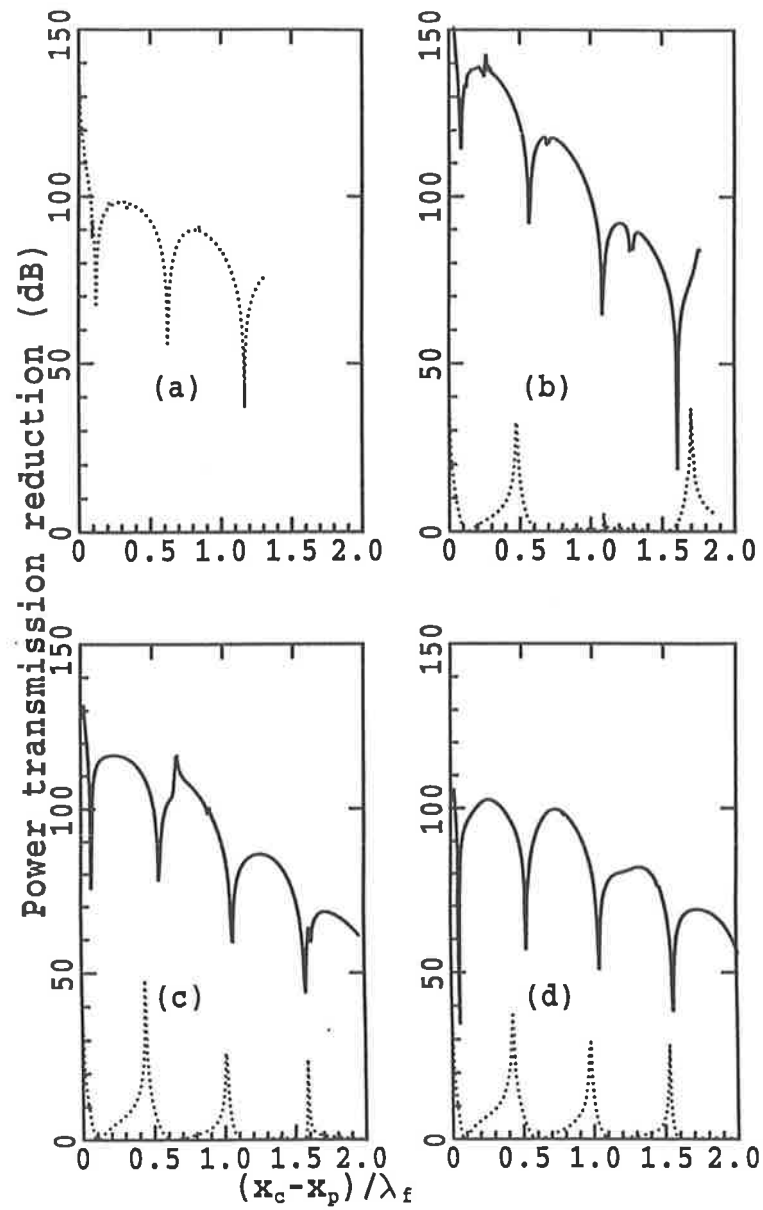


Figure 4.7: Power transmission reduction for three-in-phase, uniform-amplitude primary forces with three independent control forces. (a) Excitation frequency 210Hz; (b) excitation frequency 410Hz; (c) excitation frequency 510Hz; (d) excitation frequency 610Hz. 3 primary forces and 3 control forces driven in phase; ——— 3 primary forces driven in phase and 3 control forces driven independently.

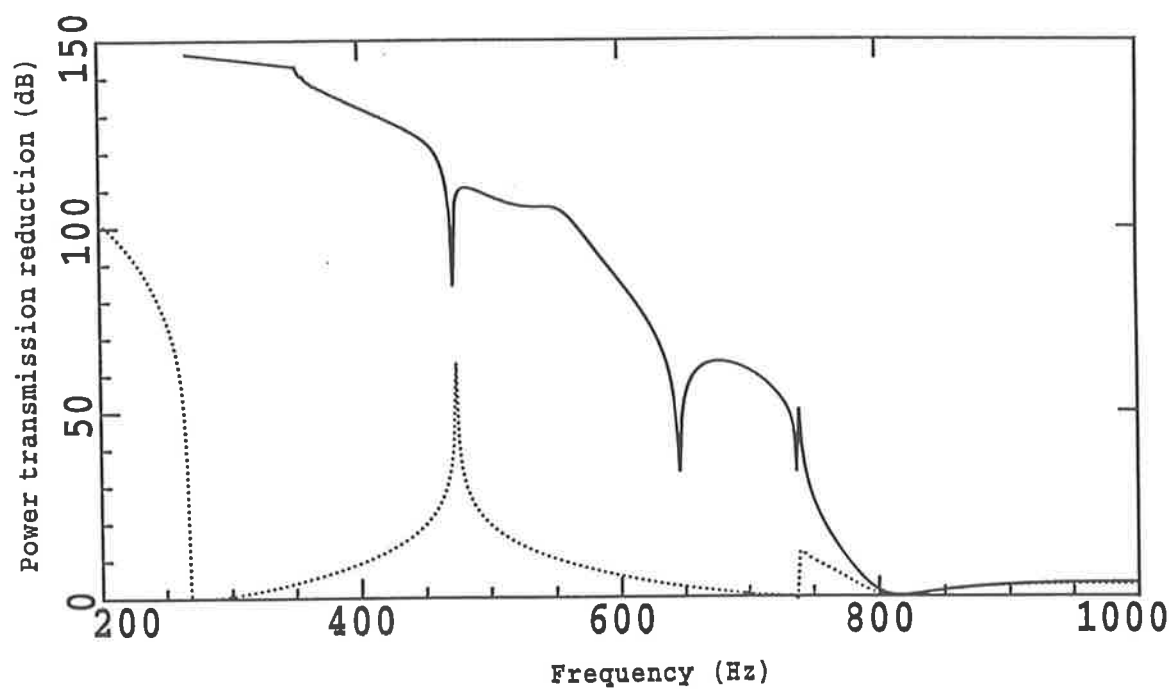


Figure 4.8: Power transmission reduction for three in-phase, uniform-amplitude primary forces and three independent control forces, as a function of frequency with the control forces located at the optimum location for 210 Hz. 3 primary forces and 3 control forces driven in phase; — 3 primary forces driven in phase and 3 control forces driven independently.

4.3.6 Effect of error sensor type and location

In the examples discussed so far, the cost function which has been minimized is intensity integrated across the width of the plate at some axial location x_e . This quantity, referred to as power transmission, is not easily measured in practice. Thus the purpose of this section is to examine an alternative cost function which could be used to supply the error input to a feed-forward controller on the total power transmission reduction.

First of all, the effect on power transmission reduction of using flexural acceleration amplitude averaged over the width of the plate is examined. Two axial locations are assumed for the error sensor location, one in the near field of the control force (at $(x_e - x_c)/\lambda_f = 0.1$) and one in the far field of the control force (at $(x_e - x_c)/\lambda_f = 2.0$), with control forces located at the optimal location of $(x_c - x_p)/\lambda_f = 0.30$ for 210 Hz. Maximum achievable power transmission reductions for three in-phase primary forces and three in-phase control forces are listed in Table 4.5 for both types of error signal measured at locations in both the near and far field of the forces, for a range of excitation frequencies. As three control forces are driven symmetrically, the first and the third force are the same. Only the first and second control forces are shown in Table 4.5 and 4.6. Except at 210 Hz where the wavelength is relatively large, results for maximum power transmission reduction are independent of whether or not the power transmission error sensor is in the near or far field of the control force. On the other hand, the influence of the near field on the maximum achievable power transmission reduction is very significant when acceleration amplitude is used as the cost function. However, if the acceleration sensor is in the far field of the control force, the results obtained are similar to those obtained using a power transmission sensor. Similar conclusions may be drawn for the case where the three control forces are driven independently, the results for which are shown in Table 4.6. The unexpected effect of the near field on the results corresponding to the use of power transmission as the cost function is because the near field reactive power fluctuations affect the ability of the error sensors properly to observe the power transmission.

Table 4.5: Error sensor type and location for three in-phase control forces

Freq (Hz)	$(x_e - x_c)/\lambda_f$	Acc. control $ F_c $	$\phi_c - \phi_p$ radian	P.T. reduction (dB)	P.T. control $ F_c $	$\phi_c - \phi_p$ radian	P.T. reduction (dB)
210	0.1	0.78	0.31	9	1.02	0	73
	2.0	1.02	0	129	1.02	0	123
310	0.1	0.17	0.57	0.44	0.56	0	1
	2.0	0.22	0	0.71	0.56	0	1
410	0.1	0.79	0.10	9	1.02	0	11
	2.0	1.09	0	11	1.02	0	11
510	0.1	0.69	0	9	1.03	0	17
	2.0	1.01	0	17	1.03	0	17
610	0.1	0.27	0	2	0.94	0	5
	2.0	0.91	0	5	0.94	0	5

Note: “Freq” refers to frequency, “Acc. control” refers to use acceleration amplitude cost function, and “P.T. control” refers to use power transmission cost function.

Table 4.6: Error sensor type and location for three independent control forces

Freq (Hz)	$(x_e - x_c)/\lambda_f$	Acc. control $ F_c $	$\phi_c - \phi_p$ radian	P.T. reduction (dB)	P.T. control $ F_c $	$\phi_c - \phi_p$ radian	P.T. reduction (dB)
210	0.1	0.39	0.46	11	16.50	-1.54	32
		1.45	0.24		16.51	1.47	
	2.0	0.49	0	121	0.49	-0.16	122
		1.56	0		1.57	0	
310	0.1	0.55	3.02	13	0.62	π	54
		1.83	0		2.26	0	
	2.0	0.62	π	122	0.62	$-\pi$	180
		2.26	0		2.26	0	
410	0.1	1.00	0.13	12	1.13	0	63
		0.21	-0.18		0.61	0	
	2.0	1.13	0	119	1.13	0	147
		0.61	0		0.61	0	
510	0.1	0.65	0	8	1.12	0	62
		0.44	-0.18		1.33	0	
	2.0	1.12	0	114	1.12	0	118
		1.33	0		1.33	0	
610	0.1	0.19	-0.17	3	2.91	0	44
		0.37	-0.27		5.01	0	
	2.0	2.91	0	64	2.92	0	83
		5.02	0		5.03	0	

Note: "Freq" refers to frequency, "Acc. control" refers to use acceleration amplitude cost function, and "P.T. control" refers to use power transmission cost function.

In practice, it is not possible to integrate intensity over the width of the plate experimentally, although it is possible to integrate flexural acceleration which is proportional to surface strain measured by using a PVDF film sensor (Gibbs and Fuller, 1990). However in some instances, even acceleration will be measured by a number of accelerometers at discrete points so it is of interest to examine the effect on the maximum achievable reduction in power transmission of deriving the cost function by averaging over a fixed number of sensors rather than integrating over the full width of the plate.

Figure 4.9 demonstrates the effect of changing the number of numerical integration subinterval for error sensors located in the far field of the control forces. This is done to simulate the effect of changing the number of error sensors (accelerometers for acceleration and accelerometer pairs for power transmission (Appendix H)) spaced uniformly in a line across the plate. Figures 4.9(a) and (b) show the results for three in-phase control forces, with acceleration and power transmission as cost functions respectively. In the same way Figures 4.9(c) and (d) present the results for three independent control forces. For power transmission reduction values of 180 dB in the figures, the calculation actually produced minimum power transmissions slightly less than zero. In Figure 4.9, the reduction sometimes gets worse with increasing number of error sensors. This is because the reduction exceeds 120 dB. As indicated in the beginning of Section 4.3, rounding errors become significant when the calculated attenuation due to active control exceeded 120 dB. Generally, the performance is seen to improve as the number of error sensors is increased, but significant improvements are not evident once the number of sensors exceeds seven. The propagating waves in the plate below 800 Hz are carried by the first five modal components. The selection of seven sensors with spacing less than half of the wavelength of the highest mode will ensure the satisfaction of the spatial Nyquist criterion for resolving the 5th modal component and sufficient number of equations (see Eq. (D.3)) for the determination of the modal components in the propagating waves.

The figure shows that to obtain the best results with a minimum number of error sensors, the control forces should be driven independently. In such cases, the power transmission reduction is almost always larger than 40 dB, even if only three error sensors are used.

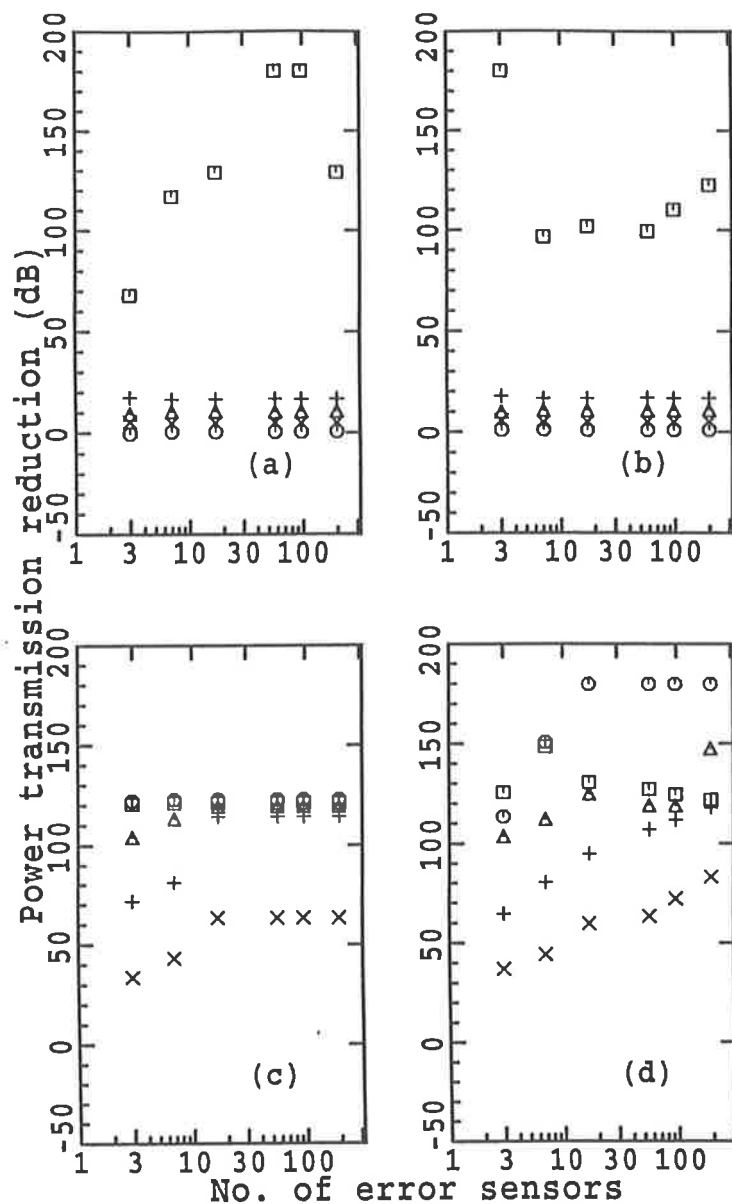


Figure 4.9: Maximum achievable power transmission reductions for three in-phase, uniform amplitude primary forces, as a function of the number of error sensors. The primary and control force locations are as for Figure 4.8 and the error sensors are at $(x_e - x_c)/\lambda_f = 2.0$. (a) Three in-phase control forces and acceleration as the cost function; (b) three in-phase control forces and power transmission as the cost function; (c) three independent control forces and acceleration as the cost function; (d) three independent control forces and power transmission as the cost function. \square \square \square excitation frequency 210 Hz; \circ \circ \circ \circ excitation frequency 310 Hz; \triangle \triangle \triangle excitation frequency 410 Hz; $+$ $+$ $+$ excitation frequency 510 Hz; \times \times \times excitation frequency 610 Hz.

4.4 Summary

Power transmission in a semi-infinite plate can be significantly reduced by using an array of independently driven control forces placed in a row across the plate. For three or more control forces it is possible to achieve levels of power transmission reduction in excess of 50 dB over a frequency range (0-750 Hz), provided that power transmission is used as the error sensor cost function to be minimized. Use of acceleration as the error sensor cost function in power transmission reduction can be equally effective, provided that the error sensors are in the far field of the control forces. For the plate tested here a minimum of seven acceleration or power transmission error sensors spaced evenly in a line across the plate were found to be necessary if the error sensors are in the far field of the control forces for the frequency range; however, results improve slightly if the number of error sensors is increased further.

Compared with independently driven control forces, a row of control forces driven with uniform amplitude and in-phase, is less effective in power transmission reduction, except at plate resonance frequencies. However, even at plate resonance frequencies, there is an optimum axial location of the control force array, and performance falls off rapidly as the control force location varies from the optimum location.

For a single point control force, a reduction in power transmission in excess of 15 dB is possible over the frequency range if the control force is located optimally. However, once again the optimal control force location is strongly frequency dependent, and the reduction falls off rapidly as the control force location varies from the optimum location. It should be noted that with increasing frequency more waves cut-on and thus (more likely) more control forces and error sensors are required.

Chapter 5

An experimental study of active control of power transmission characteristics in a semi-infinite plate

5.1 Introduction

Controlling vibratory power transmission and intensity distribution in large plate-like structures is one way of minimizing the transmission of vibrational energy between two items of equipment mounted on the same structure. To evaluate the effectiveness of a control system built for this purpose, it is useful to measure residual structural intensity distribution in the plate structure.

In Chapter 4, power transmission in a semi-infinite plate was analyzed theoretically. This chapter is concerned with an experimental investigation of power transmission and intensity distribution in a semi-infinite plate excited by a pair of piezoelectric ceramic actuators. The two crystals are attached at the same location but on opposite surfaces of the plate. The intensity, modal amplitude and reflection coefficient measurements are used to evaluate the effectiveness of an active control system driving three control actuator pairs. The control system is designed to reduce power transmission using a cost function consisting of the sum

of the squared outputs of eight accelerometers arranged in a single row across the width of the plate in the far field of the control and primary sources (actuators).

In this chapter, the experimental results are compared to theoretical predictions and in addition intensity distributions before and after control are investigated. These distributions and the associated intensity vortices are of considerable interest as will become apparent in the following discussion.

5.2 Experimental arrangement

One end of a steel test plate (Figure 5.1) with a working length of 1.4 m, thickness of 0.003 m and width of 0.5 m was mounted in a sand filled triangular box (1 m in length) in an attempt to provide a semi-anechoic termination. The sides normal to the anechoically terminated end were simply supported using thin steel strips. One edge of each strip was attached to the plate by epoxy and small set screws while the other edge was bolted to the heavy steel frame. The remaining edge of the plate, opposite the anechoically terminated end was free.

The power transmission was investigated experimentally on the test plate which was excited near the free end using a pair of piezoelectric ceramic actuators (one primary source) driven out of phase and with the same amplitude, with the idea of introducing pure bending excitation. Active control was implemented using a second row of three piezoceramic actuator pairs (three control sources) bonded on each of two opposite surfaces of the plate nearer to the anechoic end with each piezoelectric ceramic pair driven independently. Eight accelerometers mounted in single row across the plate between the control sources and the anechoic end acted as error sensors. The source signal from an HP spectrum analyzer was passed through a power amplifier into a primary transformer and then into the primary piezoceramic actuator pair. Error signals from the eight accelerometers and the source signal (as a reference) were passed by way of amplifiers and filters to the feed-forward controller which generated the driving signal for the control sources. Using a T800 transputer as the central processor, the primary controller includes a FIR (finite impulse response) filter, a filtered-x LMS algorithm for the cancellation of plate vibration at the error sensors and a LMS algorithm for the identification of the secondary path. Up to three control signals were used to drive up to three independent control sources. The arrangement is shown in Figure 5.2(a) and a block diagram is shown in Figure 5.2(b).

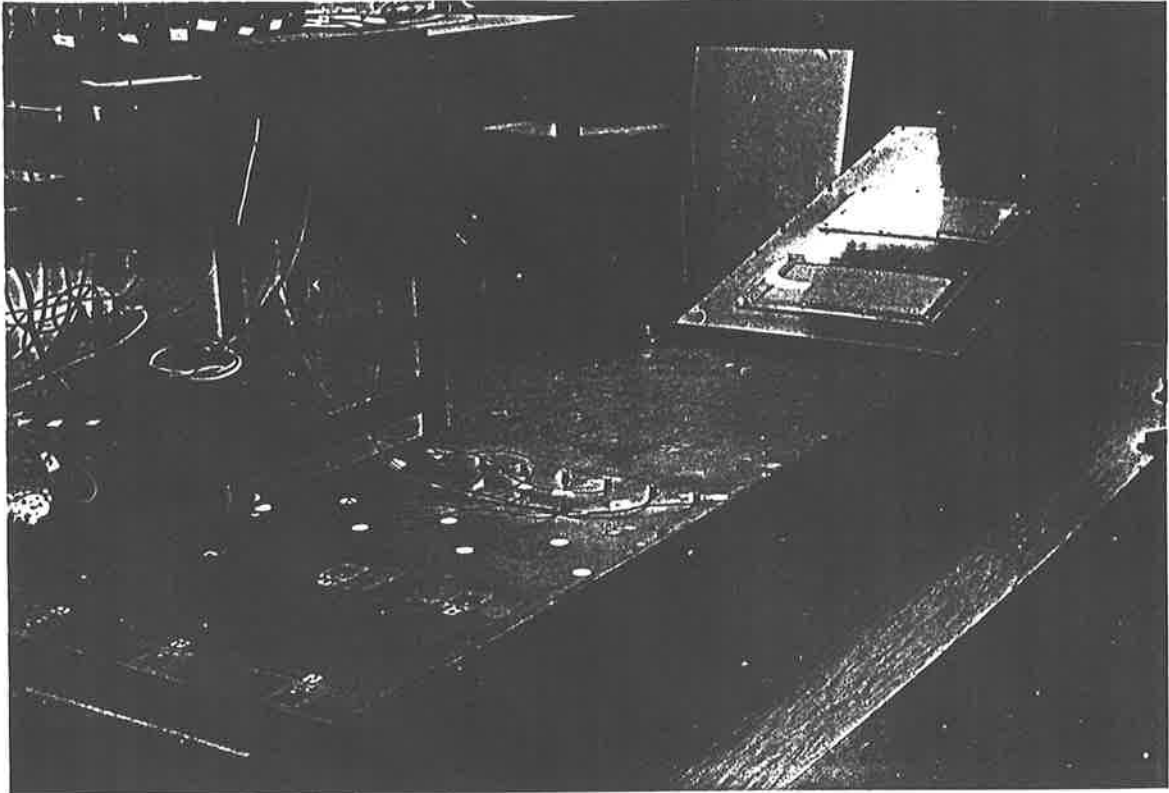
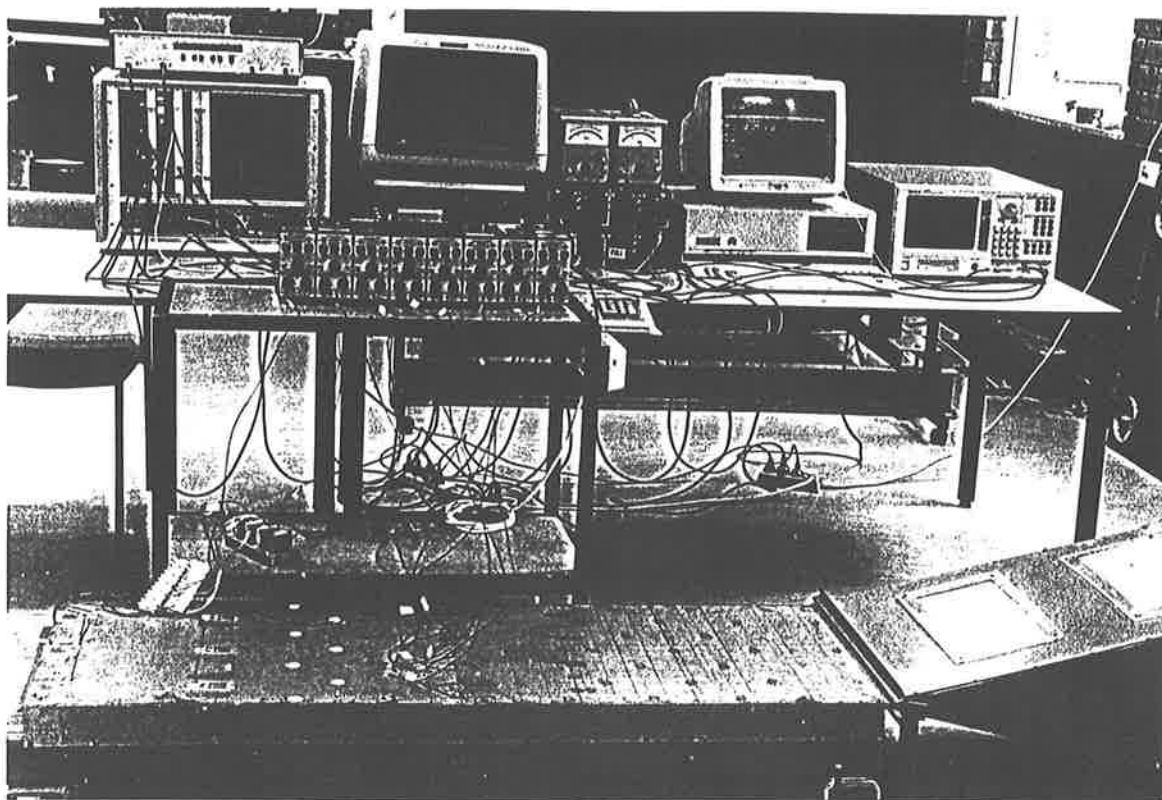


Figure 5.1: Experimental semi-infinite plate model.

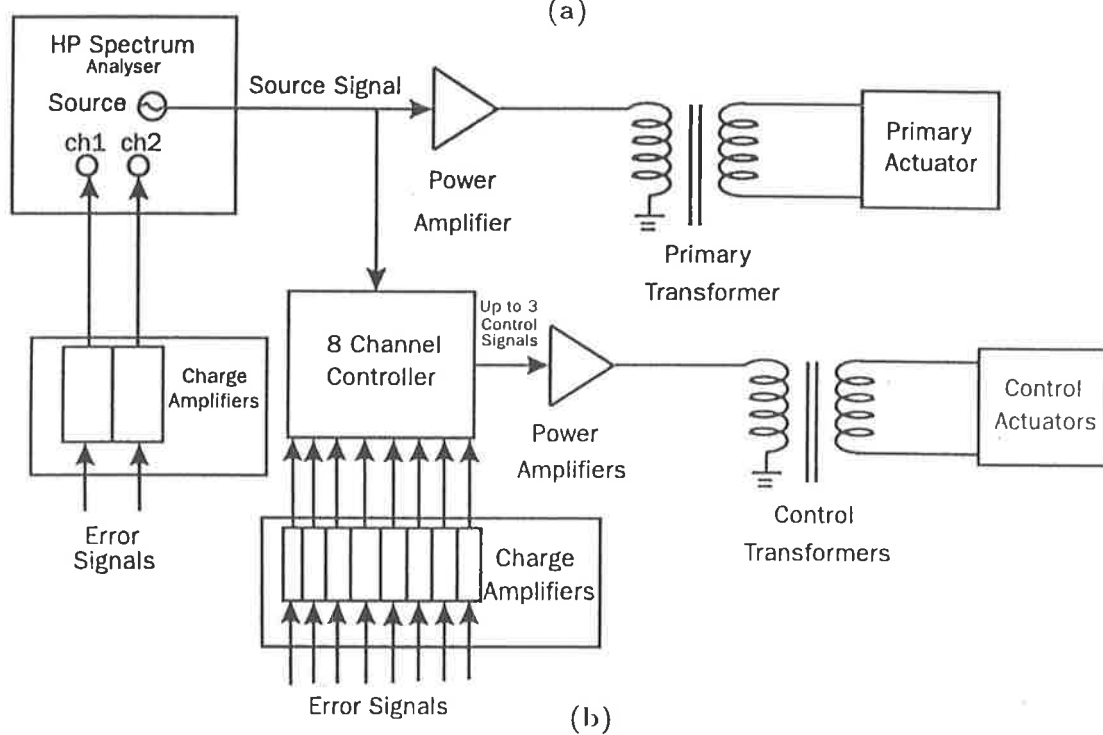
5.3 Test procedure

Modal amplitudes were obtained by measuring acceleration across the plate at fifteen points in a row parallel to the free end and, then by using the analysis described in Appendix D. Using the theoretical analysis, it was found that a minimum of fifteen measurement points were necessary to provide a reasonable degree of accuracy. Displacement amplitude reflection coefficients were determined by measuring, in the far field of the control sources, acceleration at five points in each of two rows parallel to the free end and, by using the analysis described in Appendix E.

Intensity (in one direction) was measured as described in Appendix H where the intensity is proportional to the product of the outputs of two closely spaced accelerometers. The accelerometers were mounted in a hard plastic template and attached to the plate with small permanent magnets, so that the distance between the two accelerometers was always



(a)



(b)

Figure 5.2: Experimental arrangement: (a) general set up; (b) block diagram.

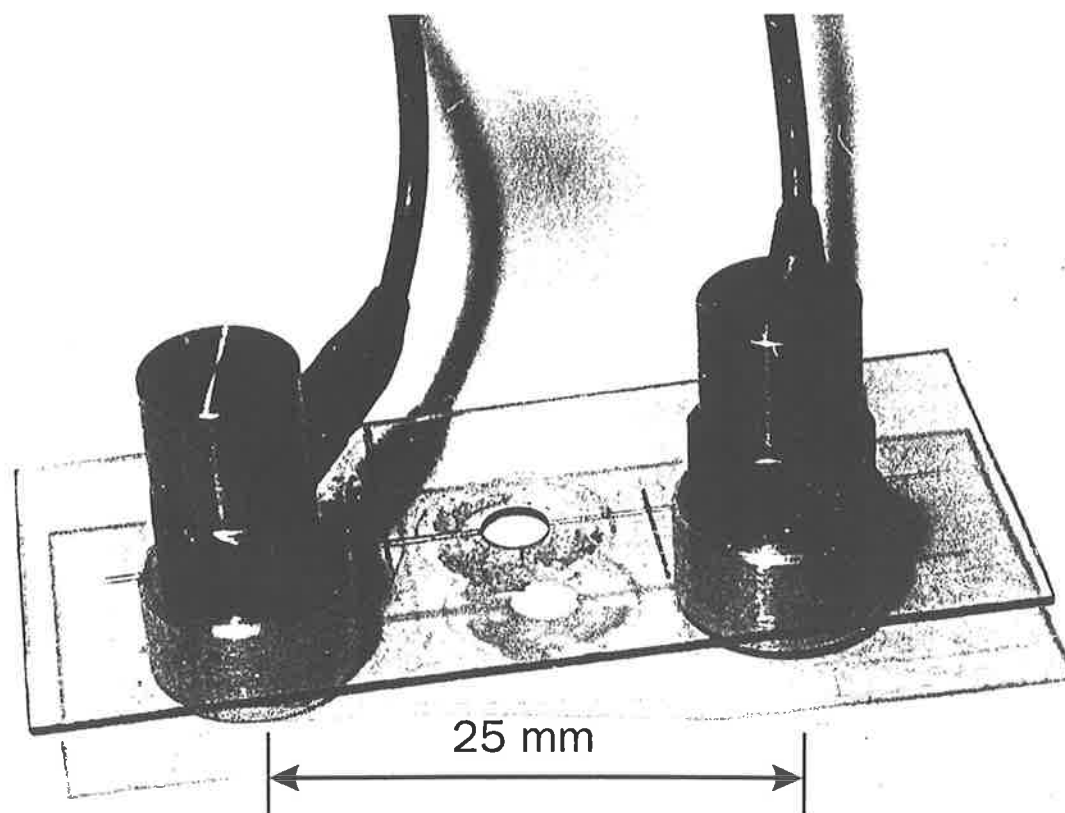


Figure 5.3: A structural intensity measuring set.

25 mm (Figure 5.3). The x (axial) component of the intensity was measured by setting the line joining the accelerometer centers parallel to the x-axis and the y component of the intensity measured by turning the template by 90° . Acceleration amplitudes were determined by multiplying the auto spectrum of each signal by an appropriate factor (see Appendix H), and the phase difference was obtained by taking the transfer function between the two signals. Acceleration values so obtained were then used to calculate the intensity as shown in Appendix H.

5.4 Numerical and experimental results

The results presented in this chapter are for the locations of sources, error sensors and intensity measurements illustrated in Figure 5.4. These locations are adhered to unless otherwise stated.

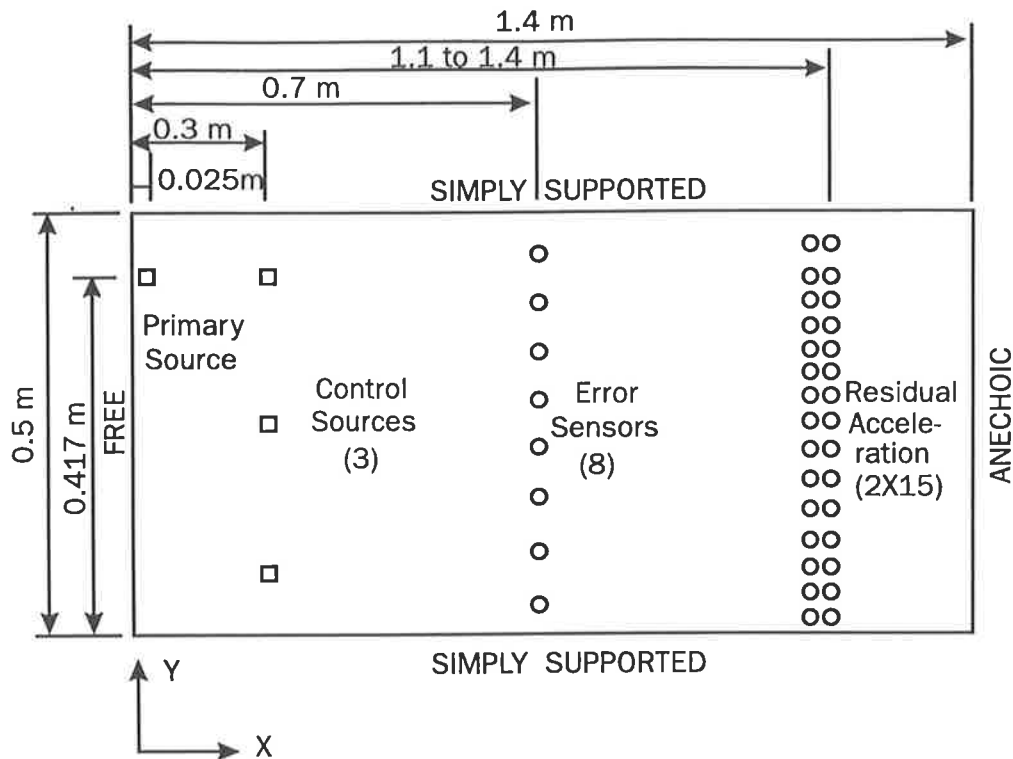


Figure 5.4: Block diagram of the vibration control system

There was some difficulty in experimentally simulating the analytical semi-infinite model. Slightly different boundary conditions between the experimental and analytical models resulted in different resonance frequencies, a problem which was compensated for by slightly changing the thickness of the the plate to 2.9 mm (from 3 mm) in the analytical model. The measured (using random noise) and adjusted theoretical frequency responses are shown in Figure 5.5.

As can be seen from the figure, the two frequency responses are very different at all frequencies except in the 260 Hz region. This is due to the inability of the plate termination to simulate an infinite plate by preventing waves from being reflected. To evaluate the effectiveness of the termination, displacement amplitude reflection coefficients were determined as a function of frequency for each mode propagating along the plate. Figure 5.6 shows the measured reflection coefficients from the anechoically terminated end of the semi-infinite plate for the first three modes in the frequency range of 200–400 Hz, determined as described in Appendix E.

Figure 5.6(a) shows the reflection coefficient determined using 5 pairs of measurement points in two rows parallel to the y-axis. Each pair of measurement points were equally

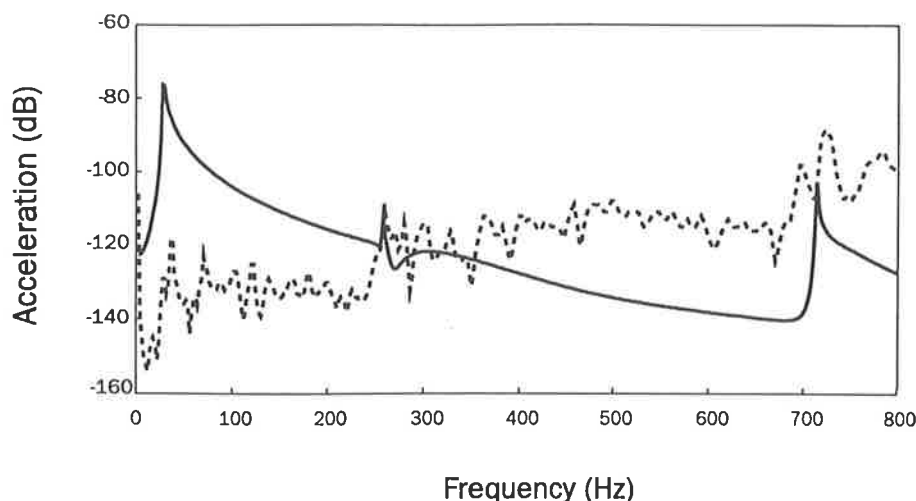


Figure 5.5: Experimental and theoretical acceleration as a function of frequency at $(x, y) = (0.875, 0.175)$ with adjusted plate thickness. \cdots measurement; — theory.

spaced at a distance of 0.05 m apart. From Figure 5.6(a), it can be seen that experimental reflection coefficients of more than 0.2 are obtained for the first three modes at some frequencies, indicating large reflections from the anechoically terminated end, thus explaining the discrepancies between theoretical and experimental frequency responses. The measured reflection coefficient for the third mode (dotted line) at frequencies of less than 259 Hz (third modal cut-on frequency) is zero which indicates that there is no third mode excitation in this region. At 259 Hz, minimum reflection coefficients are achieved for the first three modes and, thus at this frequency the experimental model best approximates the theoretical model.

Figure 5.6(b) shows the result for the same configuration as represented in Figure 5.6(a), except for the different location of the second row of measurement points. It can be seen that the general shapes of the reflection coefficient curves for each mode are similar in both Figures 5.6(a) and (b), although it can be seen that at some frequencies (but not at 259 Hz) large differences exist, indicating that in general more measurement points should be used, because the results should be independent of small changes in accelerometer spacing. Figure 5.6(c) shows the result for the same configuration as represented in Figure 5.6(a), except only the first three pairs of measurement points were used. Comparing Figures 5.6(a) and (c), it can be seen that the general shapes of the reflection coefficient curves are similar for corresponding modes but at some frequencies (not 259 Hz) large dis-

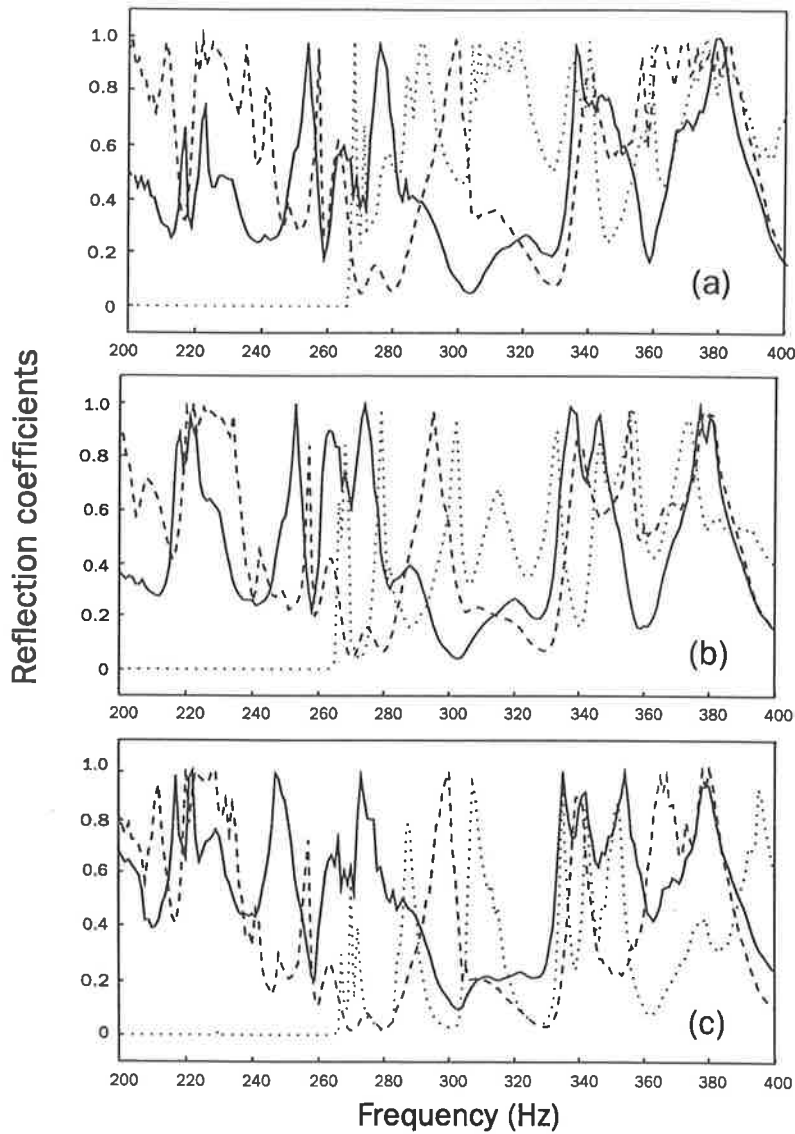


Figure 5.6: Experimental amplitude reflection coefficients measured at $x = \frac{x_2 - x_1}{2}$. (a) 5 pairs of measurement points with $x_1 = 1.2m$ and $x_2 = 1.23m$; (b) 5 pairs of measurement points with $x_1 = 1.2m$ and $x_2 = 1.25m$; (c) 3 pairs of measurement points with $x_1 = 1.2m$ and $x_2 = 1.23m$. — first mode; - - - second mode; third mode.

crepancies exist which clearly indicate that at these frequencies more measurement points should be used. Table 5.1 lists the reflection coefficients measured for the first three modes at 259 Hz as shown in Figure 5.6. From the table it can be seen that at this frequency 5 pairs of measurement points appear adequate for determining the reflection coefficient.

Table 5.1: Measured amplitude reflection coefficients at the third mode cut-on frequency of 259 Hz

	First mode	Second mode	Third mode
5 pairs of measurement points $x_1 = 1.2m, x_2 = 1.23m$	0.2178	0.2656	0
5 pairs of measurement points $x_1 = 1.2m, x_2 = 1.25m$	0.2795	0.2013	0
3 pairs of measurement points $x_1 = 1.2m, x_2 = 1.23m$	0.2069	0.1378	0

From the above analysis, it can be seen that the experimental plate was not anechoically terminated at the sand box and, as a result there were waves traveling in two directions (the incident wave along the plate to the termination and the reflected wave back along the plate to the free end). However, the numerical simulation demonstrates that the reduction in both power transmission and intensity distribution is independent of the reflection coefficient. This means that experimentally determined values of power reduction are valid even if there is large reflection from the anechoic termination. For the experiment conducted, a determination was made of the net total energy produced by the incident and reflected waves by using two rows of accelerometers. It was not necessary to determine the separate intensities of the incident and reflected waves in the experiment.

5.4.1 Active control of power transmission

To investigate the potential for actively controlling power transmission, the plate was excited at the third modal “cut-on” frequency (259 Hz for experiment and 257 Hz for theory).

An estimate of power transmission was obtained by using the procedure outlined in Appendix H which included averaging the intensity measured by each of 15 accelerometer pairs arranged in two rows across the plate parallel to the free edge and in the far field of the control sources. The measured and theoretical power transmission reductions are shown in Table 5.2. The measured power transmission reductions were determined from intensity measurements at $x = 1.20$ m. An acceleration amplitude cost function was used for both theory and experiment. The results presented in this table show that significant power transmission reductions for either measured or theoretical cases cannot be achieved with only one control source. However, significant power transmission reductions can be obtained (68 dB theoretical and 14 dB measured) by using three independent control sources. The difference between theoretical and measured reductions for the latter case can be attributed to the difficulty in obtaining identical output force amplitudes from each element of the piezoceramic control actuators and the limitations in the controller capability. The measured reduction would be expected to increase when a new type of controller, such as EZ-ANC controller, is used (see the examples for the measurement of power transmission in a cylinder (Section 8.4)). Table 5.2 also shows that in practice, the achievable power transmission reduction generally increases as the separation between the error sensors and control sources increases. However, the theoretical power transmission reduction is virtually independent of the error sensor location when $(x_e - x_c)/\lambda_f > 1.0$. Although the measured power transmission reduction was not as great as that predicted theoretically, a value of 14 dB does show that the approach described here could be a feasible way of controlling vibration transmission in large structures.

Table 5.2: Measured and theoretical power transmission reductions with acceleration amplitude as the cost function

$(x_e - x_c)/\lambda_f$	Measured P.T. redu.(dB) with one F_c	Measured P.T. redu.(dB) with three F_c	Theoretical P.T. redu.(dB) with one F_c	Theoretical P.T. redu.(dB) with three F_c
1.36	-1	7	0	68
1.51	-1	7	0	68
1.66	0	7	0	68
1.82	-2	3	0	68
1.97	-2	1	0	68
2.12	-2	4	0	68
2.27	-1	6	0	68
2.45	3	11	0	68
2.54	2	11	0	68
2.63	2	10	0	68
2.73	2	11	0	68
2.82	0	10	0	68
2.91	0	11	0	68
3.00	0	11	0	68
3.09	0	12	0	68
3.18	1	13	0	68
3.27	0	14	0	68

Note: “one F_c ” represents one control source (sharing the same y-location as the primary source) and “three F_c ” represents three independent control sources.

5.4.2 Intensity vortices

An interesting aspect to the results for the reduction in power transmission obtained from active control is the observation of intensity vortices. The presence of such vortices had been reported previously by Tanaka et al. (1993) for a harmonically excited simply supported plate. These authors demonstrated that for vortices to appear, at least two excitation sources were needed or if only a single source was used, then at least two modes had to be excited at a similar amplitude and, at a frequency close to their resonance frequencies. This means that the resonance frequencies of the two modes have to be close together if a vortex is to be obtained with a single harmonic excitation source.

It is interesting to note that when one side of the plate is approximately anechoically terminated (as for the case considered here) such that the traveling wave field dominates the standing wave field, strictly speaking no resonant modes exist; rather, the vibration field is made up of "cut-on" traveling modes, in much the same way as occurs in an anechoically terminated duct. Thus at any frequency above the second modal cut-on frequency there will usually be two or more modes propagating and in most cases there will be sufficient energy in at least two modes for intensity vortices to be generated.

For intensity results presented here, the applied frequencies are the same as for Section 5.4.1. Measured and theoretical intensity vectors were determined as a function of location on the plate as described in Appendix H. Figure 5.7(a) shows the distribution of the measured uncontrolled intensity and Figure 5.8(a) shows the corresponding theoretical result. Figures 5.7(a) and 5.8(a) essentially indicate one major vortex. This is due to the fact that the path of power transmission in the plate is a combination of transmission and rotation, the latter being induced by the interference of two modes that produces a "vortex generating block". The theoretical and experimental results are slightly different because the experimental model was characterized by some reflection from the "infinite end" of the experimental plate as shown in the beginning of Section 5.4 where the reflection coefficients were about 0.2 for the first and second modes at the test cut-on frequency of 259 Hz. Also, the method of measuring intensity as described in Appendix H assumes the absence of near field effects and thus gives only approximate results. On the other hand, the theoretical model makes no such assumption. Nevertheless, it is encouraging to see that the vortex

trends are similar for the theoretical and experimental models.

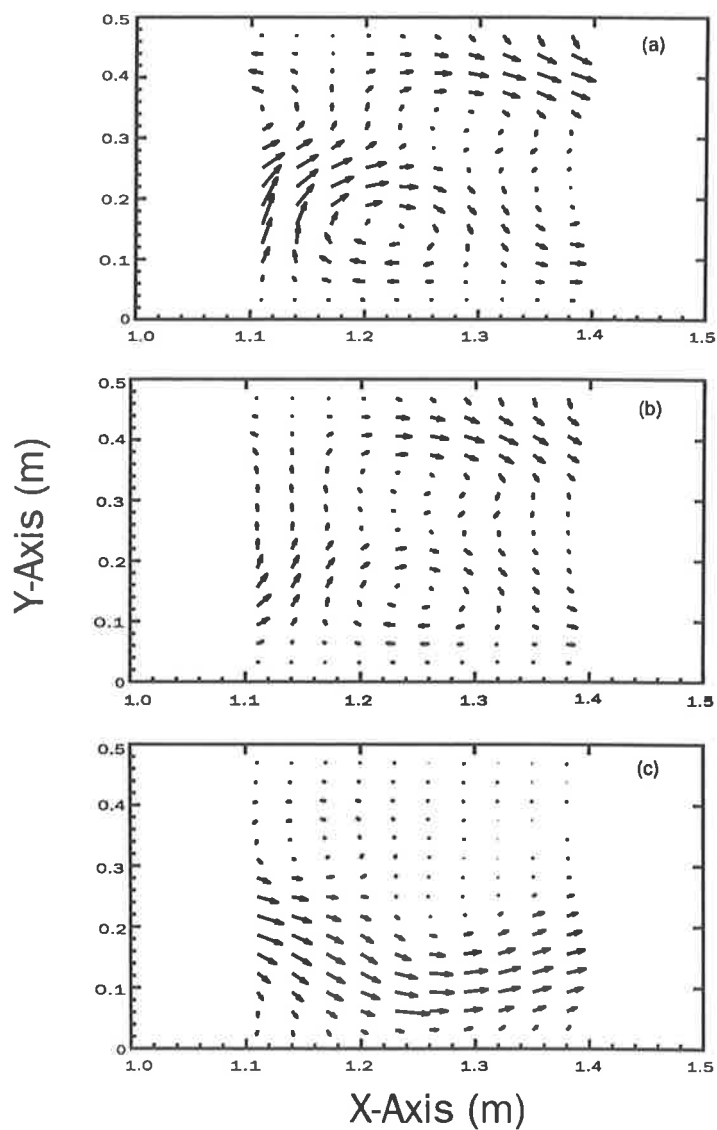


Figure 5.7: Measured intensity distribution. (a) with one primary source; (b) with one primary source and one control source; (c) with one primary source and three independent control sources.

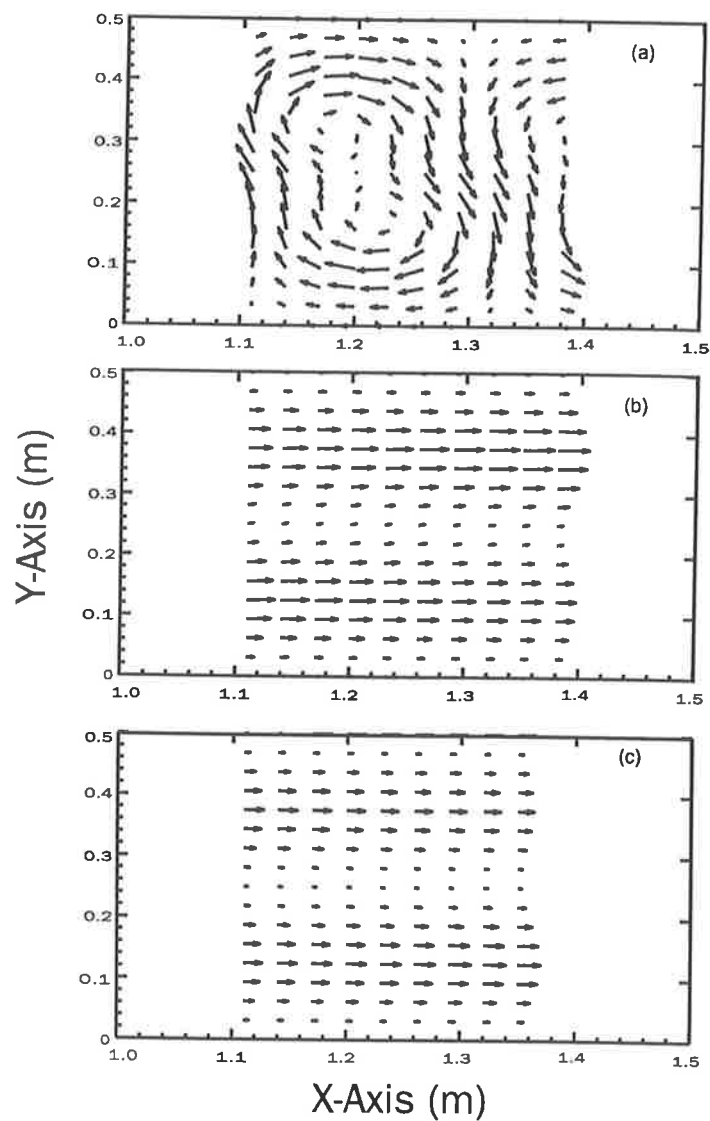


Figure 5.8: Theoretical intensity distribution. (a) with one primary source; (b) with one primary source and one control source; (c) with one primary source and three independent control sources.

Figure 5.7(b) shows a measured intensity distribution with one primary source and one control source, and Figure 5.7(c) shows a measured intensity distribution with one primary source and three control sources driven independently. Figures 5.8(b) and (c) present corresponding theoretical results. Comparing Figures 5.7(b) and (c) with Figures 5.8(b) and (c), it can be seen that the theoretical intensity vectors are orientated almost entirely in one direction, whereas the measured intensity vectors include some vortices. This difference is probably due to the difficulty in ensuring that each element in each actuator pair produces the same force. Any differences in the properties of the two piezoelectric ceramics, such as differences in their sizes, their locations or their bonding layer thicknesses would cause differences in their force output.

In an attempt to explain the presence of observed intensity vortices, a modal decomposition of the plate response was undertaken to determine the relative amplitudes of the contributing modes (“cut-on” traveling modes as described earlier in this section). The modal decomposition technique is explained in Appendix D and results are given in Figures 5.9 (measured) and 5.10 (theoretical) for the amplitudes of the first three modes. For the uncontrolled case, the measured modal amplitude (black columns in Figure 5.9) increases as the modal number increases, with the third mode being the dominant mode. The theoretical modal amplitude (black columns in Figure 5.10) follows the same tendency as the measured modal amplitude. Experimentally, the third with first mode produces a major vortex, while the third with second mode produces a minor vortex. In contrast, theoretically, the third with the other two modes produces two minor vortices included in a major vortex. However in both cases, the intensity pattern is dominated by a single major vortex corresponding to the dominant third mode.

For the experimentally controlled cases, with one control source (grey columns in Figure 5.9) the modal amplitudes are not significantly altered. However, with three independently driven control sources (hatched columns in Figure 5.9) the third modal amplitude is significantly decreased although the first modal amplitude is increased. In contrast, using one control source (grey columns in Figure 5.10) in the theoretical calculation reduces the third modal amplitude and using three independently driven control sources (hatched columns in Figure 5.10) decreases the first three modal amplitudes, resulting in a significant reduction in overall vibration levels. The numerical results shown in Figure 5.10 indicate

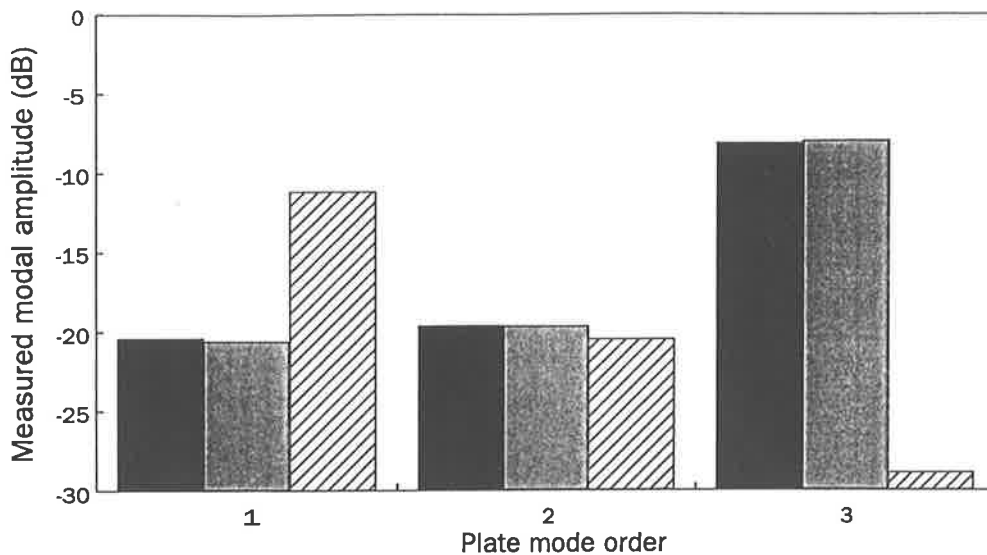





Figure 5.9: Measured modal amplitudes. The measurement points for determining modal amplitudes are at $x = 1.2$.  with one primary source;  with one primary source and one control source;  with one primary source and three independent control sources.

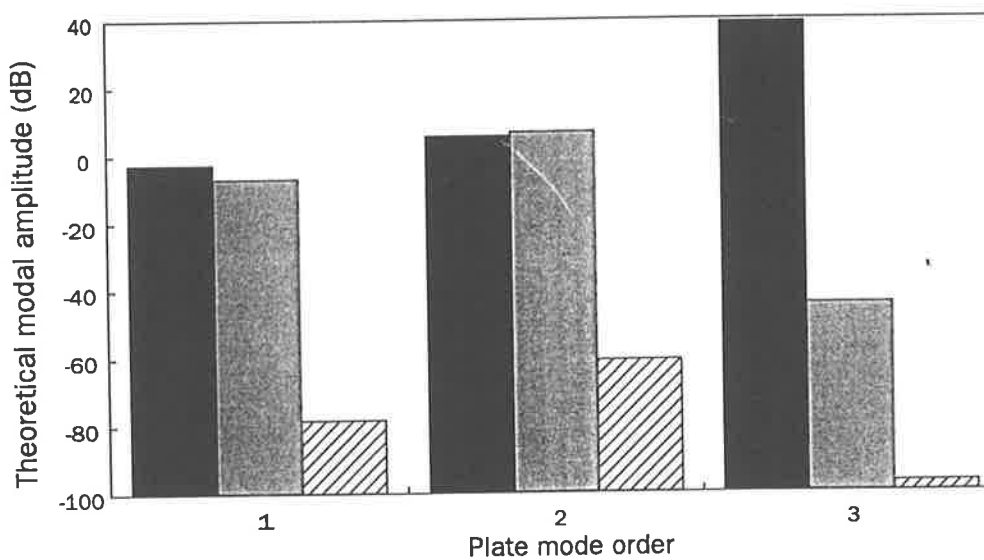


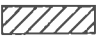


Figure 5.10: Theoretical modal amplitudes.  with one primary source;  with one primary source and one control source;  with one primary source and three independent control sources.

that the second mode is the dominant mode for the two controlled cases. Therefore the distribution of the theoretical intensity vector is orientated almost entirely in one direction (Figures 5.8(b) and (c)) as the response is dominated by the second mode, whereas the distribution of the measured intensity vector includes some vortices (Figures 5.7(b) and (c)) due to the interaction of the first three modes. From the above analysis it can be seen that relative modal amplitudes significantly affect the intensity distribution.

5.5 Discussion and summary

In practice, power transmission in a semi-infinite plate can be significantly reduced by driving an array of independent control sources, placed in a row, across the plate. With three controlled piezoceramic actuator pairs it is possible to achieve experimentally maximum levels of power transmission reduction of 14 dB at the “cut-on” frequency of the third mode. Acceleration amplitude only may be used as the error sensor cost function to be minimized, provided that the error sensors are in the far field of the control sources. For the test plate, a minimum of eight acceleration error sensors spaced evenly in a line across the plate are necessary; however, it is expected that results would improve further if the number of error sensors were increased.

Measurements of intensity on the semi-infinite plate, under primary excitation only, frequently show a vortex pattern which changes as the number and location of the primary sources change. It was found that the addition of control sources driven to minimize power transmission, also largely eliminates the vortex pattern. In future studies, it may be possible to drive control sources to create intensity vortices around points where sensitive items of equipment are attached to effectively isolate these from the plate vibration.

The theoretical results presented in this chapter, show that the experimental results are broadly true for power transmission and intensity distribution, except that the theoretically predicted reduction in power transmission is higher than that which could be measured. This is due to the difficulty in obtaining identical output force amplitudes from each element of each pair of piezoceramic control actuators and limitations in the controller capability. Also, highly reflective or reverberant fields may make measurement of intensity difficult and inaccurate. Thus improving the termination is likely to vastly improve the agreement

between theory and experiment.

Chapter 6

Piezoelectric actuator vs point force excitation of a beam and a plate

6.1 Introduction

In calculating the optimal control force for feed-forward active control of a vibrating structure, it is simplest to model the control force as point force (Chapters 2 to 4). When the control force is applied by a shaker attached to the structure by way of a thin rod then the point force model is adequate. However, when the structure is excited by piezoelectric actuators (Chapter 5), the point force model may no longer be sufficiently accurate. In many applications, piezoelectric actuator pairs are placed on parts of the structure in configurations which induce pure bending only. For a rectangular section beam or a thin plate this is achieved by placing one actuator on each of two opposite surfaces. For modeling, one alternative is to consider the actuator pair, in the case of beams (Clark et al. 1991) as point moments (Figure 6.1) and, in the cases of plates (Dimitriadis et al. 1991) as line moments acting along the edge of each actuator (Figure 6.2). A second alternative is to explore the conditions under which the actuator pair can be considered as a point force applied to one surface of the structure in the center of the actuator. The purpose of this chapter is to undertake this latter task for a beam and a semi-infinite plate excited by a piezoelectric actuator pair, as a result of application of active vibration control. Thus in the following analysis, expressions for the point force equivalent of a pair of applied mo-

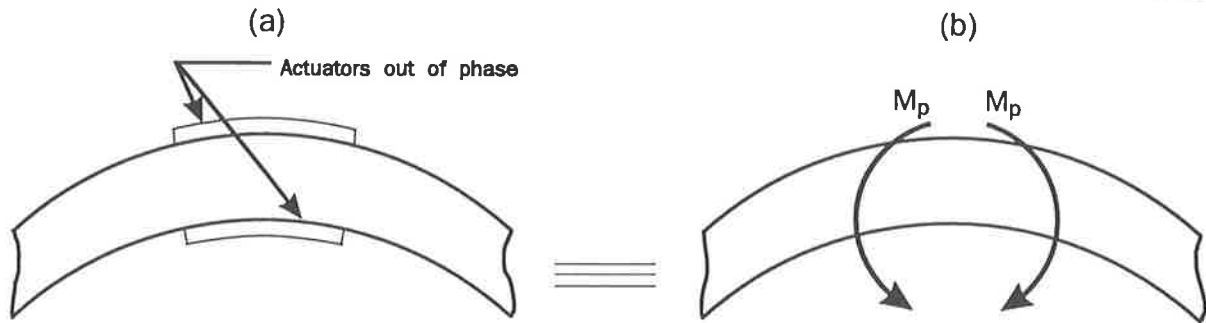


Figure 6.1: Infinite beam with a pair of piezo actuators bonded to it: (a) physical system; (b) equivalent dynamic system showing applied bending moments.

ments (for a beam) and two pairs of line moments (for a plate) are derived. The effect of piezoelectric actuator size, location and excitation frequency are also investigated. The derivation of expressions relating the applied moment to piezoelectric driving voltage has been considered elsewhere (Kim and Jones, 1991) and will not be considered further here.

6.2 Response of infinite beam excited by a pair of piezoelectric actuators

The flexural wave response of an infinite beam, to an applied normal force F_p and an applied moment M_p as shown in Figure 6.3 (with displacement $w(x)$ in the Z direction), is given by Pan and Hansen (1990) as

$$w(x) = \frac{1}{4EI_{yy}k_f^3} F_p \beta_f + \frac{1}{4EI_{yy}k_f^2} M_p \beta_m. \quad (6.1)$$

The subscripts f and m refer to the applied forces and applied moments respectively, and the factors β_f and β_m are defined as

$$\beta_f(x, x_0) = -(j e^{-jk_f|x-x_0|} + e^{-k_f|x-x_0|}) \quad (6.2)$$

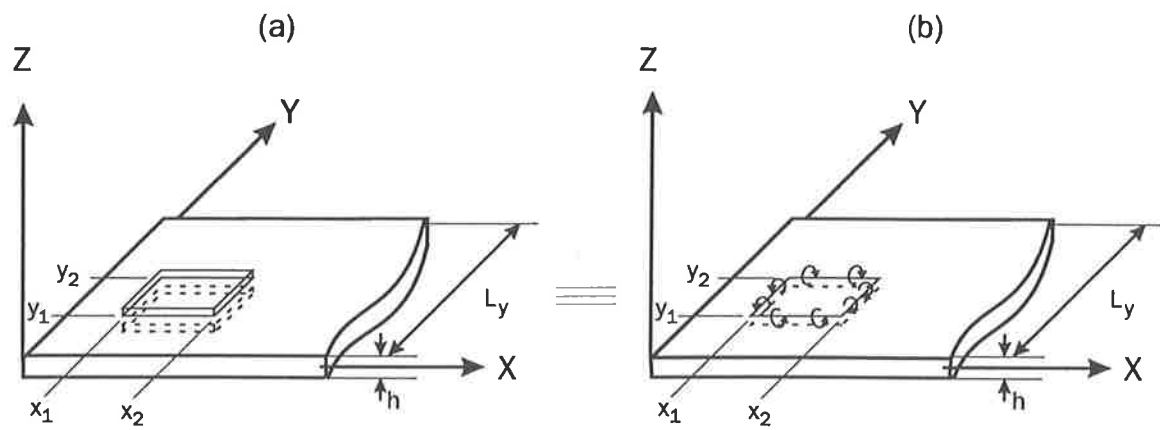


Figure 6.2: Semi-infinite plate with a pair of piezo actuators bonded to it: (a) coordinate system; (b) equivalent dynamic system showing applied bending moments.

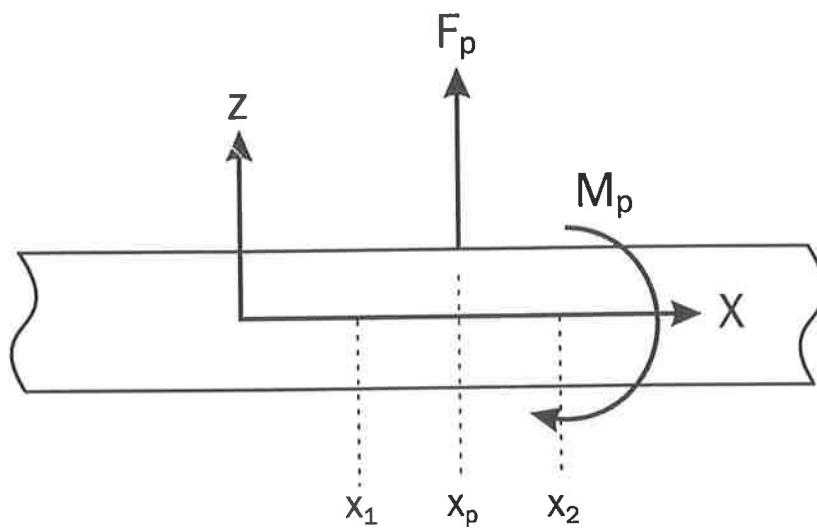


Figure 6.3: Infinite beam model.

and

$$\beta_m(x, x_0) = \frac{x_0 - x}{|x - x_0|} (e^{-jk_f|x-x_0|} - e^{-k_f|x-x_0|}) \quad (6.3)$$

where x_0 is an excitation location.

If only an excitation force is applied at $x = x_p$,

$$w_f(x) = \frac{1}{4EI_{yy}k_f^3} F_p \beta_f(x, x_p). \quad (6.4)$$

If only a pair of counteracting moments of equal amplitude M_p are located at $x = x_1$ and $x = x_2$ (Figure 6.1(b))

$$w_m(x) = \frac{1}{4EI_{yy}k_f^2} M_p [\beta_m(x, x_1) - \beta_m(x, x_2)]. \quad (6.5)$$

The ratio of amplitudes of the applied moment and force which is required to produce equal vibration amplitudes at some location downstream of the source can be obtained by writing

$$|w_f(x)| = |w_m(x)|. \quad (6.6)$$

From this equation, the moment/force amplitude “equivalence ratio” at any location x is

$$\frac{|M_p|}{|F_p|} = \frac{|\beta_f(x, x_p)|}{|[\beta_m(x, x_1) - \beta_m(x, x_2)]k_f|}. \quad (6.7)$$

As defined in Chapter 2, the near field extends up to a distance of approximately 0.73 wavelengths from the source. At this distance, the “equivalence ratio” has converged to within 2% of its final far field value. An example for an aluminum infinite beam, 50mm × 25mm in cross section is shown in Figure 6.4 for two actuator sizes and two excitation frequencies. The actuator width has no effect on the results. Similar results of independence of location x are obtained for a range of actuator sizes, locations and excitation frequencies. Thus in the far field, equation (6.7) is independent of location x but not independent of excitation frequency and actuator size.

As shown in Chapter 2, the power transmission is proportional to the displacement magnitude square in an infinite beam. This ratio is the same as the power transmission equivalence ratio in the infinite beam.

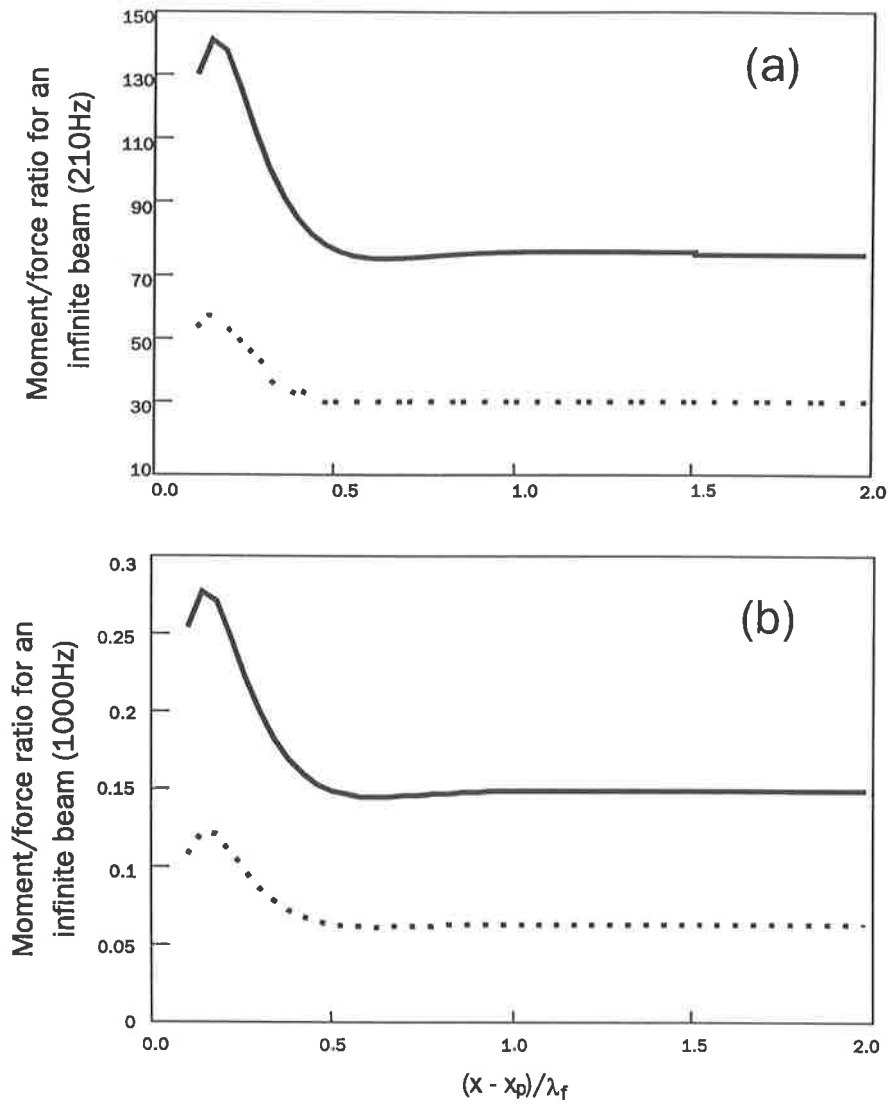


Figure 6.4: Moment/force amplitude “equivalence ratio” for an infinite beam shown as a function of $(x - x_p)/\lambda_f$. $(x - x_p)$ is the distance of the measurement point from the center of the actuators. (a) Excitation frequency 210 Hz ($\lambda_f = 10.9383m$); (b) excitation frequency 1000 Hz ($\lambda_f = 0.4823m$). — actuator length 40mm; actuator length 100mm.

6.3 Response of semi-infinite plate driven by a pair of piezoelectric actuators

Theory

In this section, the concept of moment/force “equivalence ratio” for an infinite beam is extended to the vibration of a semi-infinite plate.

The equation of motion for a plate given by Graff (1975) is

$$\rho h \ddot{w}(x, y, t) + D_h \nabla^4 w(x, y) = q(x, y), \quad (6.8)$$

where $\nabla^4 = \nabla^2 \nabla^2$ is the square of the Laplacian operator, and $q = F_0 \delta(x - x_0) \delta(y - y_0)$ is the force per unit area, where F_0 is the point force applied at (x_0, y_0) perpendicular to the plate. If the edges of the plate at $(y = 0, y = L_y)$ are simply supported, the following harmonic series solution in y can be assumed for the vibrational displacement (Appendix C)

$$w_f(x, y) = \sum_{n=1}^{\infty} w_{fn}(x) \sin \frac{n\pi y}{L_y}. \quad (6.9)$$

Each force eigenfunction $w_{fn}(x)$ can be expressed in terms of modal wavenumbers k_{in} as follows

$$w_{fn}(x) = A_{fn} e^{k_{1n}x} + B_{fn} e^{k_{2n}x} + C_{fn} e^{k_{3n}x} + D_{fn} e^{k_{4n}x}. \quad (6.10)$$

If the excitation applied to the plate is a pair of counteracting line moments acting about a line parallel to the y -axis from (x_1, y_1) to (x_1, y_2) and from (x_2, y_1) to (x_2, y_2) , the applied force term $q(x, y)$ in equation (6.8) becomes $\partial M_x / \partial x$, where the applied moment per unit area, M_x , is given by Dimitriadis et al. (1991)

$$M_x = M_{x1} + M_{x2} = M_{px} [\delta(x - x_1) - \delta(x - x_2)] [h(y - y_1) - h(y - y_2)] \quad (6.11)$$

where $h(\bullet)$ is the unit step function. Equation (6.8) becomes

$$\rho h \ddot{w}(x, y) + D_h \nabla^4 w(x, y) = \frac{\partial M_x}{\partial x}, \quad (6.12)$$

and the displacement (replacing the applied force with the applied moment in Appendix C) is

$$w_m(x, y) = \sum_{n=1}^{\infty} w_{mn}(x) \sin \frac{n\pi y}{L_y} \quad (6.13)$$

with a corresponding moment eigenfunction

$$w_{mn}(x) = A_{mn}e^{k_1nx} + B_{mn}e^{k_2nx} + C_{mn}e^{k_3nx} + D_{mn}e^{k_4nx}. \quad (6.14)$$

For the case where the excitation consists of a pair of counteracting line moments acting about a line parallel to the x-axis applied from (x_1, y_1) to (x_2, y_1) and from (x_1, y_2) to (x_2, y_2) , the applied force term $q(x, y)$ in equation (6.8) becomes $\partial M_y / \partial y$, where (Dimi-triadis et al. 1991)

$$M_y = M_{py}[\delta(y - y_1) - \delta(y - y_2)][h(x - x_1) - h(x - x_2)]. \quad (6.15)$$

To be compatible with the use of primary point forces in the analysis, it is necessary to replace the step function $[h(x - x_1) - h(x - x_2)]$ with a sequence of adjacent δ functions, so that

$$M_y = M_{py}[\delta(y - y_1) - \delta(y - y_2)] \frac{\sum_{i=1}^k \delta(x - x_i)}{k} (x_k - x_1). \quad (6.16)$$

That is, the line moments are transformed into sequences of point moments, and k is the number of point moments. Equation (6.8) then becomes

$$\rho h \ddot{w}(x, y, t) + D_h \nabla^4 w(x, y) = \frac{\partial M_y}{\partial y}. \quad (6.17)$$

To allow for different actuator sensitivities in the x and y directions to an applied electric field, we define $M_{px} = M_p$ and $M_{py} = \alpha M_p$ in the following analysis. The total plate response at any location (x, y) due to a pair of counteracting line moments M_x , and a pair of counteracting line moments M_y modeled as a series of point moments (Figure 6.2) is

$$w_m(x, y) = w_{mx1} + w_{mx2} + \sum_{i=1}^k w_{mi} = M_p(w_{x1} - w_{x2} + \alpha \sum_{i=1}^k w_i), \quad (6.18)$$

where w_{mx1} and w_{mx2} are the responses due to each of the two line moments M_{x1} and M_{x2} , w_{mi} ($i = 1, 2 \dots k$) is the response due to a pair of counteracting point moments at (x_i, y_1) and (x_i, y_2) . w_{x1} , w_{x2} , w_i ($i = 1, 2 \dots k$) are the plate responses to the respective unit applied moments (obtained by replacing the applied force with the applied moment in Appendix C).

The moment/force "equivalence ratio" for the plate can be obtained by equating the spatially averaged vibration amplitude produced by a point force actuator and spatially

averaged vibration amplitude produced by a pair of piezoelectric actuators, which can be obtained by writing

$$\int_0^{L_y} |F_p w_{f-p}(x, y)|^2 dy = \int_0^{L_y} |M_p [w_{x1}(x, y) - w_{x2}(x, y) + \alpha \sum_{i=1}^k w_i(x, y)]|^2 dy, \quad (6.19)$$

where w_{f-p} is the unit primary force response. Note that the spatially averaged values are calculated along a transverse plate section (from $y = 0$ to $y = L_y$). Thus, the moment/force amplitude "equivalence ratio" at any location x is

$$\frac{|M_p|}{|F_p|} = \frac{\sqrt{\int_0^{L_y} |w_{f-p}(x, y)|^2 dy}}{\sqrt{\int_0^{L_y} |w_{x1}(x, y) - w_{x2}(x, y) + \alpha \sum_{i=1}^k w_i(x, y)|^2 dy}}. \quad (6.20)$$

An alternative method of analysis utilizing separation of variables which was employed by Dimitriadis et al. (1991) can only be used if the plate is of finite size.

Results

Before presenting detailed results obtained by evaluating equation (6.20), it is necessary to determine the minimum number k of point moments into which the line moment M_y should be divided. Table 6.1 presents the moment/force "equivalence ratio" (calculated by applying $\alpha = 1$ in equation (6.20)) as a function of the number of point moments k applied along each actuator edge parallel to the x-axis and as a function of the distance $(x - x_p)/\lambda_f$ from the center of the piezoelectric actuators. For the results presented in this table, the analytical model is a 0.003 m thick and 0.5 m wide semi-infinite steel plate excited by a piezoelectric actuator pair and simply supported along the infinite length sides and free at the other side. The center of the square piezoelectric actuators (one on each side of the plate) is located at $(x, y) = (0.06, 0.3)$.

It can be seen from the table that varying the number of point moments k produces only very small changes in the "equivalence ratio". The loss of accuracy caused by using only one point moment along each side of the actuator parallel to x-axis is only about 0.04%. The effect of varying k has been tested for a number of different piezoelectric actuator sizes, a number of different actuator locations, and a range of excitation frequencies. A result very similar to that shown in Table 6.1 was obtained in every case. Therefore, each of the line moments M_{y1} and M_{y2} can be replaced by an equivalent point moment applied

Table 6.1: Moment/force amplitude “equivalence ratio” of a semi-infinite plate for varying numbers k of point moments used to characterize the line moment. The actuator size is $40 \text{ mm} \times 40 \text{ mm}$ and the excitation frequency is 210 Hz (wavelength $\lambda_f = 0.3752m$).

$(x - x_p)/\lambda_f$	$k = 1$	$k = 3$	$k = 8$	$k = 18$	$k = 38$	$k = 78$
0.1	2.30	2.30	2.30	2.30	2.30	2.30
0.3	2.51	2.50	2.50	2.50	2.50	2.50
0.5	2.95	2.93	2.95	2.95	2.95	2.95
0.7	3.15	3.15	3.15	3.15	3.15	3.15
0.9	3.25	3.22	3.22	3.22	3.22	3.22
1.1	3.24	3.24	3.24	3.24	3.24	3.24
1.3	3.25	3.25	3.25	3.25	3.25	3.25
1.5	3.25	3.25	3.25	3.25	3.25	3.25
1.7	3.25	3.25	3.25	3.25	3.25	3.25
1.9	3.25	3.25	3.25	3.25	3.25	3.25

at the midpoint of the actuator edge. Equation (6.16) can then be simplified to

$$M_y = \alpha M_p [\delta(y - y_1) - \delta(y - y_2)] \delta(x - \bar{x}) (x_k - x_1), \quad (6.21)$$

where $\bar{x} = \frac{x_k + x_1}{2}$. The total plate response at any location (x, y) due to a pair of piezo-electric actuators given by equation (6.18) becomes

$$w_m(x, y) = M_p (w_{x_1} - w_{x_2} + \alpha w_y), \quad (6.22)$$

where w_{x_1} and w_{x_2} are the unit responses due to M_{x_1} and M_{x_2} respectively and w_y is the unit response due to M_y applied at $x = \bar{x}$. The “equivalence ratio” given by equation (6.20) can then be written as

$$\frac{|M_p|}{|F_p|} = \frac{\sqrt{\int_0^{L_y} |w_{f-p}(x, y)|^2 dy}}{\sqrt{\int_0^{L_y} |w_{x_1}(x, y) - w_{x_2}(x, y) + \alpha w_y(x, y)|^2 dy}}. \quad (6.23)$$

If the actuator is placed near the free edge of the plate, the response due to M_x is very small and the response due to M_y dominates the vibration. As the distance between the free

edge and the actuator increases, the response due to M_x increases and eventually becomes the dominant source of vibration, and also the “equivalence ratio” changes slightly for the semi-infinite plate.

Tests have shown that the amplitude of the plate’s response to applied moment pairs M_x and M_y increases and so the “equivalence ratio” decreases as the size of the actuator or the excitation frequency increases. These tests have been performed with piezoelectric actuators up to 100 mm × 100 mm square and with an excitation frequency of up to 5000 Hz.

If the same definition for the extent of a near field is used as in a beam, Figure 6.5 shows that at the boundary of near field (0.73 wavelengths from the source) the “equivalence ratio” converges to within 2% of the final far field value for a range of actuator sizes and frequencies. Thus in the far field, equation (6.23) is independent of location x but not independent of excitation frequency and actuator size.

6.4 Power transmission along a semi-infinite plate excited by a pair of piezoelectric actuators

A different “equivalence ratio” is obtained if the criterion for selecting the applied moment is equal power transmission rather than equal displacement amplitude downstream of the source.

The active power transmission through the plate section at a constant location x , with only two point forces acting (i.e. a primary force and a control force), has been given in Chapter 4 as

$$P_{fx} = \frac{1}{2} \int_0^{L_y} \text{Re}[F_c F_c^* A_f + F_c F_p^* B_f + F_c^* F_p C_f + F_p F_p^* D_f] dy. \quad (6.24)$$

If a pair of piezoelectric actuators is used as a single moment actuator, the total plate response at any location (x, y) is given by equation (6.22). The corresponding power transmission is given as

$$P_{mx} = \frac{1}{2} M_p M_p^* \int_0^{L_y} \text{Re}[A_m + B_m + C_m] dy, \quad (6.25)$$

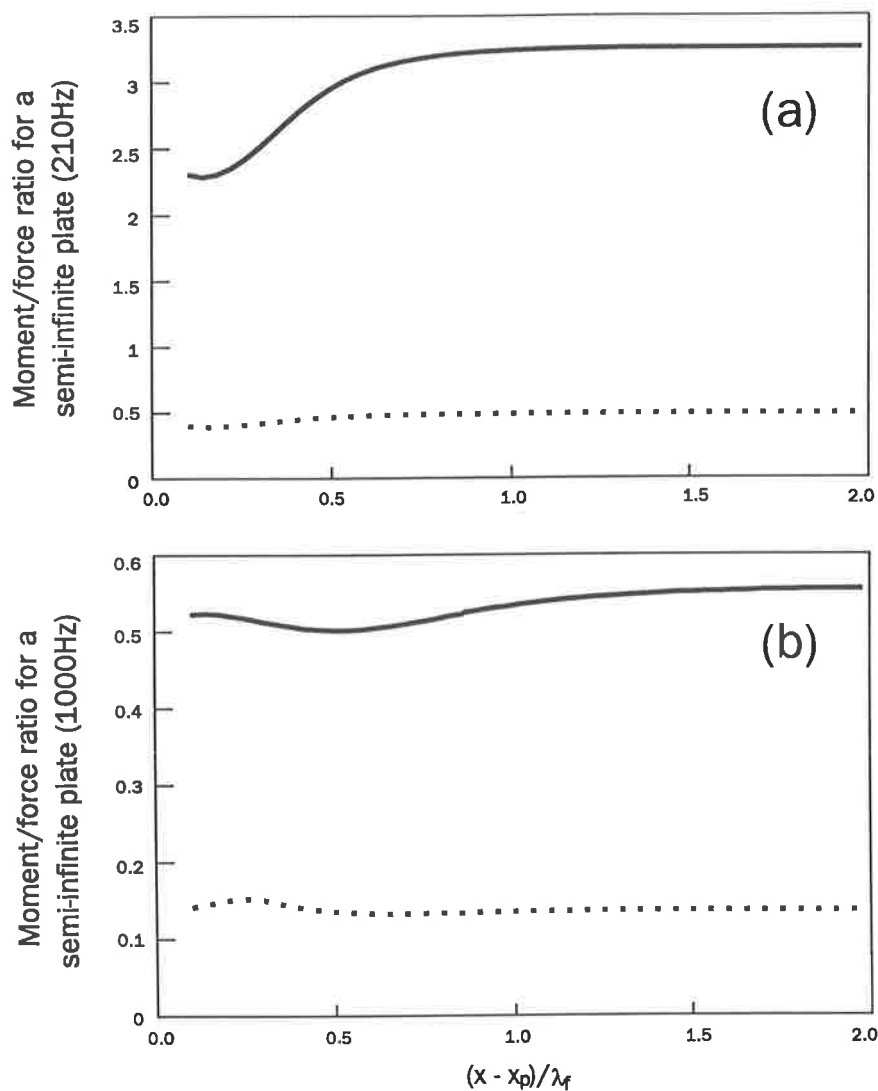


Figure 6.5: Moment/force amplitude “equivalence ratio” for a semi-infinite plate shown as a function of $(x - x_p)/\lambda_f$. (a) Excitation frequency 210 Hz ($\lambda_f = 0.3752m$); (b) excitation frequency 1000 Hz ($\lambda_f = 0.1719m$). — actuator size $40mm \times 40mm$; actuator size $100mm \times 100mm$.

where

$$A_m = -j\omega D_h \left(\frac{\partial^3 w_{x1}}{\partial x^3} + \alpha \frac{\partial^3 w_y}{\partial x^3} - \frac{\partial^3 w_{x2}}{\partial x^3} + \frac{\partial^3 w_{x1}}{\partial x \partial y^2} + \alpha \frac{\partial^3 w_y}{\partial x \partial y^2} - \frac{\partial^3 w_{x2}}{\partial x \partial y^2} \right) (w_{x1} + \alpha w_y - w_{x2})^*, \quad (6.26)$$

$$B_m = j\omega D_h \left[\frac{\partial^2 w_{x1}}{\partial x^2} + \alpha \frac{\partial^2 w_y}{\partial x^2} - \frac{\partial^2 w_{x2}}{\partial x^2} + \nu \left(\frac{\partial^2 w_{x1}}{\partial y^2} + \alpha \frac{\partial^2 w_y}{\partial y^2} - \frac{\partial^2 w_{x2}}{\partial y^2} \right) \left(\frac{\partial w_{x1}}{\partial x} + \alpha \frac{\partial w_y}{\partial x} - \frac{\partial w_{x2}}{\partial x} \right)^* \right] \quad (6.27)$$

and

$$C_m = j\omega D_h (1 - \nu) \left(\frac{\partial^2 w_{x1}}{\partial x \partial y} + \alpha \frac{\partial^2 w_y}{\partial x \partial y} - \frac{\partial^2 w_{x2}}{\partial x \partial y} \right) \left(\frac{\partial w_{x1}}{\partial y} + \alpha \frac{\partial w_y}{\partial y} - \frac{\partial w_{x2}}{\partial y} \right)^*. \quad (6.28)$$

The ratio of applied moment and force amplitudes, which is required to produce equal active power transmission through a plate cross-section can be obtained by writing

$$P_{fx} = P_{mx}. \quad (6.29)$$

The result of solving this equation is the “equivalence ratio”

$$\frac{|M_p|}{|F_p|} = \frac{\sqrt{\int_0^{L_y} \text{Re}[D_f] dy}}{\sqrt{\int_0^{L_y} \text{Re}[A_m + B_m + C_m] dy}}. \quad (6.30)$$

As power transmission is independent of location x , the value obtained for this ratio must also be independent of x .

The relative importance of M_x and M_y in determining the overall “equivalence ratio” for power transmission follows the same trends with changing actuator size, location and excitation frequency as those described for the displacement “equivalence ratio” in Section 6.3.

6.5 Discussion and summary

For an infinite beam or a semi-infinite plate, the point force amplitude which is equivalent to a pair of piezoelectric actuators has been expressed in terms of a ratio of applied moment to

applied force which has been called an “equivalence ratio”. This ratio may be calculated on the basis of equal spatially averaged displacement amplitude or on the basis of equal power transmission at some location x downstream of the actuators. It has been shown that for a beam and semi-infinite plate over a large range of actuator sizes, locations and excitation frequencies, the power transmission equivalence ratio is independent of measurement location for each case. The displacement equivalence ratio however, is only independent of measurement location provided that the location is in the far field of the source (the actuators). Calculations have been made for the controlled case where a control source is used which consists of a pair of secondary piezoelectric control actuators attached to the beam or semi-infinite plate. In this case, it is shown that for the primary source, a pair of piezoelectric actuators will result in the same acceleration *reduction* as an equivalent point force, provided that the measurement location is in the far field of the primary and control sources. This result is independent of the actuator sizes, locations and excitation frequencies. A very similar result is obtained if power transmission rather than acceleration is measured. Therefore, it is possible to calculate the achievable *reduction* in the far field of the primary and control sources produced by a piezoelectric actuator pair, by simulating the actuators with a single applied point force for an infinite beam and a semi-infinite plate.

Numerical results show that the phenomenon of the displacement “equivalence ratio” for a finite beam is similar to that for the infinite beam. However, similar analyses, for plates with all sides simply supported and plates with two opposite sides simply supported and remaining two sides free, show that an effective displacement “equivalence ratio”, independent of measurement location, only exists if the plates are excited at a resonance frequency.

Chapter 7

Minimizing acceleration and power transmission in a semi-infinite cylinder

7.1 Introduction

An extension of the minimization of acceleration and power transmission in an infinite beam (Chapter 2) and in a semi-infinite plate (Chapter 4), is the minimization in a cylinder. This chapter is concerned with the theoretical analysis of control of power transmission in a semi-infinite cylinder using a circumferential array of radial control forces and a circumferential array of radial error sensors. This study examines the extent of control which is achievable for a realistic control force configuration.

The work outlined here examines the extent of control of flexural, extensional and torsional waves which is achievable for a circumferential array of control forces on a semi-infinite cylinder, simply supported at one end, anechoically terminated at the other end and excited by an array of in-phase harmonic primary forces arranged in a line around its circumference. The geometry of the cylinder and coordinates are shown in Figure 7.1(a) and the sign conventions are shown in Figure 7.1(b). The total power transmission reduction is calculated for different wave type acceleration and different wave type power transmission cost functions. In addition, the effect of error sensor type and location, control force

type and location, cylinder thickness, radius and excitation frequency is investigated and discussed in detail.

7.2 Theory

7.2.1 Minimization of acceleration with a line of in-phase control forces

If the cylinder is excited by an array of in-phase radial primary forces of complex amplitude F_p located at $x = x_p$, the flexural displacement $w(x, \phi)$ at any location (x, ϕ) is discussed in Appendix F and is found by using equations (F.48) in Appendix F as follows

$$w(x, \phi) = F_p w_{p-f}(x, \phi). \quad (7.1)$$

Similarly, if an array of radial control forces of complex amplitude F_c are placed at $x = x_c$, the flexural displacement due to this acting alone is

$$w(x, \phi) = F_c w_{c-f}(x, \phi). \quad (7.2)$$

The total flexural displacement response at location (x, ϕ) due to the primary and control forces acting together is then

$$w(x, \phi) = F_p w_{p-f}(x, \phi) + F_c w_{c-f}(x, \phi). \quad (7.3)$$

The optimal control force F_c for minimizing the flexural acceleration (and the flexural displacement) around the circumference of the cylinder at a constant axial location x may be found by integrating the sum of the squares of the flexural displacement defined in equation (7.3) around the circumference of the cylinder, and setting the partial derivatives of the integration with respect to the real and imaginary components of the control force equal to zero. The partial derivatives are

$$\frac{\partial \int_0^{2\pi} |w|^2 d\phi}{\partial F_{rel}} = \int_0^{2\pi} (F_p w_{p-f} w_{c-f}^* + F_p^* w_{p-f}^* w_{c-f} + 2F_{rel} |w_{c-f}|^2) d\phi \quad (7.4)$$

and

$$\frac{\partial \int_0^{2\pi} |w|^2 d\phi}{\partial F_{img}} = \int_0^{2\pi} (-j F_p w_{p-f} w_{c-f}^* + j F_p^* w_{p-f}^* w_{c-f} + 2F_{img} |w_{c-f}|^2) d\phi \quad (7.5)$$

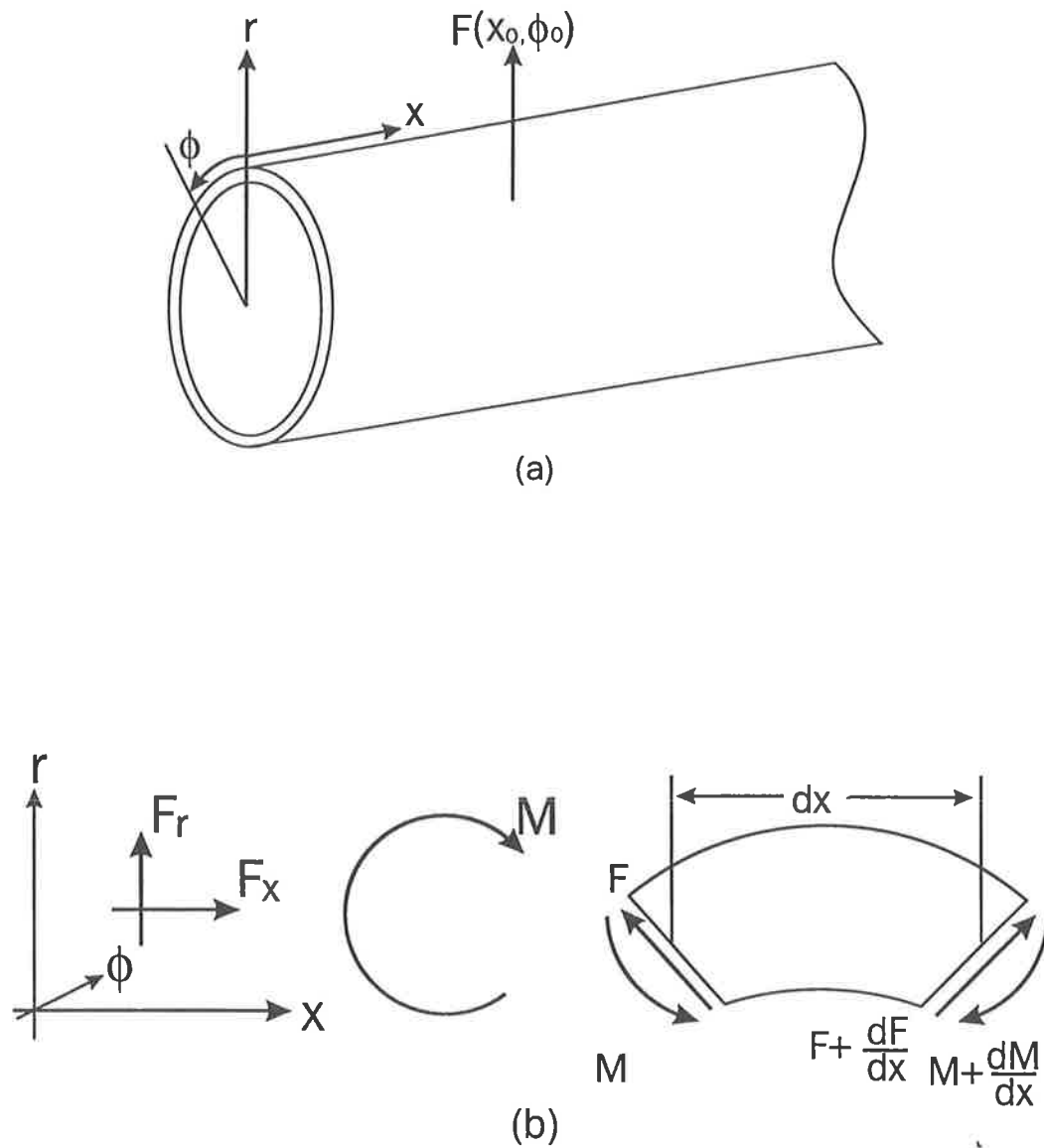


Figure 7.1: Semi-infinite cylinder model. (a) Cylinder with excitation F at location (x_0, ϕ_0) ; (b) Sign conventions for forces and moments (conventions for forces and moments in the ϕ -plane are similar).

respectively where $F_c = F_{rel} + jF_{img}$. The result is

$$F_c = -F_p \frac{\int_0^{2\pi} w_{p-f} w_{c-f}^* d\phi}{\int_0^{2\pi} |w_{c-f}|^2 d\phi}. \quad (7.6)$$

The superscript asterisk * represents the complex conjugate.

The axial and tangential displacement due to the radial primary and radial control forces are

$$u(x, \phi) = F_p u_{p-f}(x, \phi) + F_c u_{c-f}(x, \phi) \quad (7.7)$$

and

$$v(x, \phi) = F_p v_{p-f}(x, \phi) + F_c v_{c-f}(x, \phi) \quad (7.8)$$

respectively.

7.2.2 Minimization of acceleration with a line of three independently driven control forces

If the cylinder is driven by an array of in-phase radial primary point forces around one circumference of the cylinder at $x = x_p$ and three independent radial control point forces around the other circumference at $x = x_c$, the total radial displacement response may be written as

$$w = w_p + w_c = F_p w_{p-f} + F_{c1} w_{c-f1} + F_{c2} w_{c-f2} + F_{c3} w_{c-f3}. \quad (7.9)$$

The quantities w_{c-f1} , w_{c-f2} and w_{c-f3} are each calculated in a similar way to w_{c-f} in Appendix F. The optimal control forces for minimizing the flexural acceleration or displacement at any axial location x may be found by integrating the sum of the squares of the flexural displacement defined in equation (7.9) around the circumference of the cylinder and setting the partial derivatives of the integration with respect to each of the real and imaginary components of the control forces equal to zero. The result is an optimal set of control forces as follows

$$\begin{bmatrix} F_{c1} \\ F_{c2} \\ F_{c3} \end{bmatrix} = - \begin{bmatrix} \int_0^{2\pi} |w_{c-f1}|^2 d\phi & \int_0^{2\pi} w_{c-f1}^* w_{c-f2} d\phi & \int_0^{2\pi} w_{c-f1}^* w_{c-f3} d\phi \\ \int_0^{2\pi} w_{c-f1} w_{c-f2}^* d\phi & \int_0^{2\pi} |w_{c-f2}|^2 d\phi & \int_0^{2\pi} w_{c-f2}^* w_{c-f3} d\phi \\ \int_0^{2\pi} w_{c-f1} w_{c-f3}^* d\phi & \int_0^{2\pi} w_{c-f2} w_{c-f3}^* d\phi & \int_0^{2\pi} |w_{c-f3}|^2 d\phi \end{bmatrix}^{-1}$$

$$\times \begin{bmatrix} \int_0^{2\pi} w_{p-f} w_{c-f1}^* d\phi \\ \int_0^{2\pi} w_{p-f} w_{c-f2}^* d\phi \\ \int_0^{2\pi} w_{p-f} w_{c-f3}^* d\phi \end{bmatrix} F_p. \quad (7.10)$$

The procedure can be extended to any number of independently controlled forces.

7.2.3 Power transmission

The vibratory power transmission is a result of three wave motions, and is given by Fuller (1981), as

$$P_s = P_f + P_e + P_t \quad (7.11)$$

where the subscript refers to the shell motion: i.e. either flexure, extension or torsion respectively. The quantity P_f consists of two parts contributed by rotation of the cylindrical element as well as radial flexure. Thus

$$P_f = \frac{1}{T} \int_0^T \int_0^{2\pi} [M_x \frac{\partial \theta_x}{\partial t} + Q_x \frac{\partial w}{\partial t}] r d\phi dt, \quad (7.12)$$

$$P_e = \frac{1}{T} \int_0^T \int_0^{2\pi} N_x \frac{\partial u}{\partial t} r d\phi dt \quad (7.13)$$

and

$$P_t = \frac{1}{T} \int_0^T \int_0^{2\pi} N_{x\phi} \frac{\partial v}{\partial t} r d\phi dt \quad (7.14)$$

where T is the period of vibration and θ_x is angular rotation of the cylindrical element about the ϕ axis. Substituting equations (7.12), (7.13) and (7.14) into (7.11), equation (7.11) can be written as

$$P_s = \frac{1}{T} \int_0^T \int_0^{2\pi} [M_x \frac{\partial \theta_x}{\partial t} + Q_x \frac{\partial w}{\partial t} + N_x \frac{\partial u}{\partial t} + N_{x\phi} \frac{\partial v}{\partial t}] r d\phi dt. \quad (7.15)$$

Adopting the approach of Skudrzyk (1965), the real (or active) part of the power transmission along the cylinder for harmonic excitation is calculated as the product of the real part of the force term with the real part of the velocity term for each pair of terms in equation (7.15) and the result is time averaged. Thus the active power transmission is given by

$$P_s = \frac{r}{2} \int_0^{2\pi} \text{Re} [M_x \frac{\partial \theta_x^*}{\partial t} + Q_x \frac{\partial w^*}{\partial t} + N_x \frac{\partial u^*}{\partial t} + N_{x\phi} \frac{\partial v^*}{\partial t}] d\phi \quad (7.16)$$

where, according to Flügge (1973), the bending moment about the ϕ axis is as shown in equation (F.26) (in Appendix F), the axial force is given by

$$N_x = \frac{D_e}{r}(u' + \nu v' + \nu w) - \frac{K}{r^3}w'', \quad (7.17)$$

the tangential shear force is given by

$$N_{x\phi} = \frac{D_e}{r} \frac{1-\nu}{2}(u' + v') + \frac{K}{r^3} \frac{1-\nu}{2}(v' - w') \quad (7.18)$$

and the transverse shear force is given by

$$Q_x = \frac{K}{r^3}[(w'''' + \nu w'''' - u'' - \nu v'') + (1-\nu)(w'''' + \frac{1}{2}u'' - \frac{1}{2}v'')] \quad (7.19)$$

where $D_e = \frac{Eh}{1-\nu^2}$.

For one line of primary actuators around one circumference of the cylinder and a second line of control actuators around the other, the resulting total power transmission along the cylinder can be expressed in terms of the primary and control forces, using superposition. Thus the power transmission corresponding to equation (7.6) (representing optimal control of flexural acceleration) is obtained by substituting equation (7.6) into (7.3), (7.7) and (7.8), then into equations (F.26), (7.17) to (7.19), and the results into equation (7.16). The power transmission corresponding to equation (7.10) can be obtained in a similar way.

7.2.4 Minimization of power transmission with a line of in-phase point control forces

The total power transmission resulting from a line of in-phase radial primary forces and a line of in-phase radial control forces acting together can be found by substituting equation (7.3), (7.7) and (7.8) into (F.26), (7.17) to (7.19) and the results into equation (7.16). Carrying out the indicated substitutions in equations (F.26), (7.17) to (7.19) gives the following expressions for the bending moment, axial force, tangential force and transverse shear force respectively.

$$M_x = \frac{K}{r^2} \left[\left(F_p \frac{\partial^2 w_{p-f}}{\partial x^2} + F_c \frac{\partial^2 w_{c-f}}{\partial x^2} \right) + \nu \left(F_p \frac{\partial^2 w_{p-f}}{\partial \phi^2} + F_c \frac{\partial^2 w_{c-f}}{\partial \phi^2} \right) - \left(F_p \frac{\partial u_{p-f}}{\partial x} + F_c \frac{\partial u_{c-f}}{\partial x} \right) - \nu \left(F_p \frac{\partial v_{p-f}}{\partial \phi} + F_c \frac{\partial v_{c-f}}{\partial \phi} \right) \right], \quad (7.20)$$

$$N_x = \frac{D_e}{r} \left[\left(F_p \frac{\partial u_{p-f}}{\partial x} + F_c \frac{\partial u_{c-f}}{\partial x} \right) + \nu \left(F_p \frac{\partial v_{p-f}}{\partial \phi} + F_c \frac{\partial v_{c-f}}{\partial \phi} \right) \right. \\ \left. + \nu (F_p w_{p-f} + F_c w_{c-f}) \right] - \frac{K}{r^3} \left(F_p \frac{\partial^2 w_{p-f}}{\partial x^2} + F_c \frac{\partial^2 w_{c-f}}{\partial x^2} \right), \quad (7.21)$$

$$N_{x\phi} = \frac{D_e}{r} \frac{1-\nu}{2} \left[\left(F_p \frac{\partial u_{p-f}}{\partial \phi} + F_c \frac{\partial u_{c-f}}{\partial \phi} \right) + \left(F_p \frac{\partial v_{p-f}}{\partial x} + F_c \frac{\partial v_{c-f}}{\partial x} \right) \right] \\ \frac{K}{r^3} \frac{1-\nu}{2} \left[\left(F_p \frac{\partial v_{p-f}}{\partial x} + F_c \frac{\partial v_{c-f}}{\partial x} \right) - \left(F_p \frac{\partial^2 w_{p-f}}{\partial x \partial \phi} + F_c \frac{\partial^2 w_{c-f}}{\partial x \partial \phi} \right) \right] \quad (7.22)$$

and

$$Q_x = \frac{K}{r^3} \left\{ \left[\left(F_p \frac{\partial^3 w_{p-f}}{\partial x^3} + F_c \frac{\partial^3 w_{c-f}}{\partial x^3} \right) + \nu \left(F_p \frac{\partial^3 w_{p-f}}{\partial x \partial \phi^2} + F_c \frac{\partial^3 w_{c-f}}{\partial x \partial \phi^2} \right) \right. \right. \\ \left. \left. - \left(F_p \frac{\partial^2 u_{p-f}}{\partial x^2} + F_c \frac{\partial^2 u_{c-f}}{\partial x^2} \right) - \nu \left(F_p \frac{\partial^2 v_{p-f}}{\partial x \partial \phi} + F_c \frac{\partial^2 v_{c-f}}{\partial x \partial \phi} \right) \right] \right. \\ \left. + (1-\nu) \left[\left(F_p \frac{\partial^3 w_{p-f}}{\partial x \partial \phi^2} + F_c \frac{\partial^3 w_{c-f}}{\partial x \partial \phi^2} \right) + \frac{1}{2} \left(F_p \frac{\partial^2 u_{p-f}}{\partial \phi^2} + F_c \frac{\partial^2 u_{c-f}}{\partial \phi^2} \right) \right. \right. \\ \left. \left. - \frac{1}{2} \left(F_p \frac{\partial^2 v_{p-f}}{\partial x \partial \phi} + F_c \frac{\partial^2 v_{c-f}}{\partial x \partial \phi} \right) \right] \right\}. \quad (7.23)$$

These and equations (7.3), (7.7) and (7.8) can be substituted into the expression for the power transmission (equation (7.16)) through any cylinder cross section at axial location x to produce

$$P_{xa} = \frac{r}{2} \int_0^{2\pi} \text{Re}[F_c F_c^* A + F_c F_p^* B + F_p F_c^* C + F_p F_p^* D] d\phi \quad (7.24)$$

where

$$A = -\frac{K}{r^3} \left(\frac{\partial^2 w_{c-f}}{\partial x^2} + \nu \frac{\partial^2 w_{c-f}}{\partial \phi^2} - \frac{\partial u_{c-f}}{\partial x} - \nu \frac{\partial v_{c-f}}{\partial \phi} \right) \frac{\partial^2 w_{c-f}^*}{\partial x \partial t} \\ + \frac{K}{r^3} \left[\frac{\partial^3 w_{c-f}}{\partial x^3} + \nu \frac{\partial^3 w_{c-f}}{\partial x \partial \phi^2} - \frac{\partial^2 u_{c-f}}{\partial x^2} - \nu \frac{\partial^2 v_{c-f}}{\partial x \partial \phi} \right. \\ \left. + (1-\nu) \left(\frac{\partial^3 w_{c-f}}{\partial x \partial \phi^2} + \frac{1}{2} \frac{\partial^2 u_{c-f}}{\partial \phi^2} - \frac{1}{2} \frac{\partial^2 v_{c-f}}{\partial x \partial \phi} \right) \right] \frac{\partial w_{c-f}^*}{\partial t} \\ + \left(\frac{D_e}{r} \frac{\partial u_{c-f}}{\partial x} + \nu \frac{D_e}{r} \frac{\partial v_{c-f}}{\partial \phi} + \nu \frac{D_e}{r} w_{c-f} - \frac{K}{r^3} \frac{\partial^2 w_{c-f}}{\partial x^2} \right) \frac{\partial u_{c-f}^*}{\partial t} \\ + \left(\frac{D_e}{r} \frac{1-\nu}{2} \frac{\partial u_{c-f}}{\partial \phi} + \frac{D_e}{r} \frac{1-\nu}{2} \frac{\partial v_{c-f}}{\partial x} \right. \\ \left. + \frac{K}{r^3} \frac{1-\nu}{2} \frac{\partial v_{c-f}}{\partial x} - \frac{K}{r^3} \frac{1-\nu}{2} \frac{\partial^2 w_{c-f}}{\partial x \partial \phi} \right) \frac{\partial v_{c-f}^*}{\partial t}. \quad (7.25)$$

The expressions for B , C and D are very similar to above expression for A . For example: to obtain B , replace c by p in the conjugate part of each term; to obtain C , replace c

by p in the non-conjugate part of each term; and to obtain D , replace c by p in both the conjugate and non-conjugate part of each term.

The optimal control force corresponding to minimum power transmission is obtained by determining derivatives of equation (7.24) with respect to the real and imaginary components of the control force and setting the derivatives equal to zero. The result is

$$F_c^{opt} = -\frac{\int_0^{2\pi} B^* d\phi + \int_0^{2\pi} C d\phi}{2 \int_0^{2\pi} \text{Re}[A] d\phi} F_p. \quad (7.26)$$

7.2.5 Minimization of power transmission with a line of three independently driven point control forces

For this case, the cylindrical displacements w (obtained from equation (7.3)), u (obtained by replacing w with u in equation (7.3)) and v (obtained by replacing w with v in equation (7.3)) can be substituted into equations (F.26), (7.17) to (7.19). The results from these equations can then be substituted into equation (7.16), to give an expression for the total power transmission. The total power transmission can be written in matrix form as:

$$P_{xa} = \frac{r}{2} \int_0^{2\pi} \text{Re}[\mathbf{F}^H \mathbf{A} \mathbf{F}] d\phi \quad (7.27)$$

where

$$\mathbf{F} = [F_p, F_{c1}, F_{c2}, F_{c3}]^T \quad (7.28)$$

and

$$\mathbf{A} = \begin{bmatrix} A(1,1) & A(1,2) & A(1,3) & A(1,4) \\ A(2,1) & A(2,2) & A(2,3) & A(2,4) \\ A(3,1) & A(3,2) & A(3,3) & A(3,4) \\ A(4,1) & A(4,2) & A(4,3) & A(4,4) \end{bmatrix} \quad (7.29)$$

and the superscript H is the complex conjugate and transpose of a matrix. The coefficients $A(i, j)$ ($i = 1, 4, j = 1, 4$) of matrix \mathbf{A} result from the product of terms in equation (7.16), each of which contains contributions from the four different force elements of equation (7.28). The expressions for $A(i, j)$ ($i = 1, 4, j = 1, 4$) are very similar to the above expression for A in equation (7.25). There is only one change to the expression in each case. For example: to obtain $A(1, 1)$, replace c by p in both the conjugate and

non-conjugate parts of each term; to obtain $A(2, 1)$, replace p by $c1$ in the non-conjugate part of each term.

An optimal set of control forces corresponding to minimum power transmission is obtained by determining derivatives of equation (7.27) with respect to the real and imaginary components of each control force and setting the derivatives equal to zero. An optimum set of control forces corresponding to a minimum power transmission due to three independent radial control forces is

$$\begin{bmatrix} F_{c1} \\ F_{c2} \\ F_{c3} \end{bmatrix} = - \begin{bmatrix} \int_0^{2\pi} (A^*(2, 2) + A(2, 2))d\phi & \int_0^{2\pi} (A^*(3, 2) + A(2, 3))d\phi \\ \int_0^{2\pi} (A^*(2, 3) + A(3, 2))d\phi & \int_0^{2\pi} (A^*(3, 3) + A(3, 3))d\phi \\ \int_0^{2\pi} (A^*(2, 4) + A(4, 2))d\phi & \int_0^{2\pi} (A^*(3, 4) + A(4, 3))d\phi \end{bmatrix}^{-1} \left(\begin{bmatrix} \int_0^{2\pi} A^*(1, 2)d\phi \\ \int_0^{2\pi} A^*(1, 3)d\phi \\ \int_0^{2\pi} A^*(1, 4)d\phi \end{bmatrix} + \begin{bmatrix} \int_0^{2\pi} A(2, 1)d\phi \\ \int_0^{2\pi} A(3, 1)d\phi \\ \int_0^{2\pi} A(4, 1)d\phi \end{bmatrix} \right) F_p \quad (7.30)$$

By comparing equations (7.26) with (7.30) and (7.24) with (7.27), it can be seen that the single force changes to a force vector when in-phase force control changes to independent force control. The expression for the power transmission given by equation (7.27) not only includes each force term, but also includes coupling force terms, which makes independent force control much more complex than in-phase force control to analyze.

The procedure can be used for any number of independently controlled forces. For six control sources, the corresponding (7×1) force matrix is:

$$\mathbf{F} = \begin{bmatrix} F_p \\ F_{c1} \\ F_{c2} \\ F_{c3} \\ F_{c4} \\ F_{c5} \\ F_{c6} \end{bmatrix} \quad (7.31)$$

The analysis shown in Section 7.2 is for radial forces. Similar analyses can be applied to axial and tangential forces, and also to corresponding acceleration amplitude and power transmission cost functions.

7.3 Numerical results

The numerical results presented in this section have been calculated for a steel cylinder with Young's modulus $E = 207$ GPa, density $\rho = 7700$ kg/m³ and Poisson's ratio $\nu = 0.3$. With the exception of Section 7.3.5, the radius, thickness and excitation frequency are held constant at $r = 0.25$ m, $h = 0.003$ m and $f = 510$ Hz. By way of example, the frequency of 510 Hz is selected which is well below the ring frequency (3310 Hz). The investigation of a range of frequencies will be shown in Appendix H.3. One end of the cylinder is assumed to be terminated anechoically and the other is simply supported. Based on experience with semi-infinite plates, three independent control forces are expected to give better power transmission reduction (when three in-phase primary forces are used) than either single or multiple in-phase control forces and, are therefore used in the following analysis. In Section 7.3.5, results are given for varying radii, thicknesses and excitation frequencies.

7.3.1 Definition of the near field

The near field of a vibration source in free field is the region near the source in which the amplitude of the amplitude of reactive power fluctuation is not negligible. The boundary between near and far fields is defined for convenience to be the point at which the reactive power fluctuation is 20 dB less than than the corresponding active power. At and below this level the effects of reactive power fluctuation are considered to be relatively insignificant. The radius of the near field is then $x/\lambda_f = 0.73$ m ($\lambda_f = 0.9632$ m is the flexural wavelength calculated from equation (F.24), see Appendix F). That is, points further than $0.73\lambda_f$ from the source are considered to be in the far field of the source. It should be noted that the transition from near to far fields is gradual, and a fixed location is chosen here only for convenience.

The definition of the near field can be used to define the near field of the extensional and torsional waves, because the extensional and torsional wave displacement has similar far field terms (Appendix F).

7.3.2 Power transmission reduction

In this section it is assumed that an ideal feed-forward controller is available. It is also assumed that it is possible to obtain a measure of the vibratory power transmission along the cylinder, to be used as the controller error input.

The three radial primary actuators are all located at the same distance from the simply supported end of the cylinder. They are arranged around the circumference of the cylinder in ϕ -coordinate locations of $2\pi/3$, $(4\pi/3) \times 1.05$ and 2π . For each primary actuator there is a corresponding radial control actuator sharing an identical ϕ -coordinate location. The second (primary and control) actuators have been moved slightly from a symmetric position on the circumference. This is because the matrix which must be inverted in equation (7.30) is ill-conditioned if symmetric forces are applied. Two axial locations are used as examples for the radial control force locations, at $(x_c - x_p) = 0$ m and at $(x_c - x_p) = 0.05$ m. The effect of the locations of error sensors and control forces will be discussed below. The primary forces are at $x_p = 0.025$ m, the error sensors are at $x_e = 0.565$ m at which the error sensors are close to the far field of the primary forces and the measurement points are at $x_{meas} = 2.1$ m. The cost function is the power transmitted past the error sensors.

Table 7.1 lists the different wave type power transmission reductions for three independently driven radial control forces, with the power transmitted by either the combined or individual wave types used for the cost function. The relative amplitudes and phases of the three control forces are also shown in the table for each error sensor case. In the first row of Table 7.1, "three waves" refers to flexural, extensional and torsional. In the three rows below, the individual wave types are considered separately. For the power transmission reduction values of 180 dB in this and following tables, the calculated power transmission should theoretically be zero. However numerical inaccuracies resulted in values which were only in the vicinity of zero and not exactly zero, thus limiting the calculated reduction to 180 dB when in fact it should have been ∞ dB. Thus a reduction of 180 dB may be considered to be the calculation "noise floor".

Table 7.1: Power transmission reduction for three independently driven radial control forces and, for either combined or individual wave type power transmission cost function

Wave type	$x_c - x_p$ (m)	$\frac{ F_c }{ F_p }$	$\phi_c - \phi_p$ radian	P_{un} (W)	P_{co} (W)	P.T.reduction (dB)
Three waves combined	0.00	1.00	$-\pi$	0.19E-07	-0.66E-23	180
		1.00	π			
		1.00	π			
	0.05	0.74	3.11	0.19E-7	0.20E-10	30
		0.55	3.13			
		0.66	3.12			
Flexural wave	0.00	1.00	$-\pi$	0.57E-09	-0.31E-24	180
		1.00	π			
		1.00	π			
	0.05	0.75	3.13	0.50E-09	0.57E-13	40
		0.55	3.13			
		0.67	3.13			
Extensional wave	0.00	1.00	$-\pi$	0.18E-07	-0.33E-23	180
		1.00	π			
		1.00	π			
	0.05	0.74	3.11	0.18E-07	0.19E-10	30
		0.55	3.13			
		0.66	3.12			
Torsional wave	0.00	0.99	π	0.71E-10	0.15E-24	146
		1.00	$-\pi$			
		1.00	$-\pi$			
	0.05	0.71	-3.10	0.71E-10	0.10E-11	18
		0.55	3.04			
		0.64	3.10			

This table shows that a total power transmission reduction of more than 30 dB can be achieved when the power transmitted by all three wave types is used as the cost function. It is possible to achieve a flexural wave power transmission reduction of more than 40 dB when only flexural wave power is used as the cost function, an extensional wave power transmission reduction of more than 30 dB when only extensional wave power is used as the cost function and a torsional wave power transmission reduction of more than 18 dB when only torsional wave power is used as the cost function. It can be seen that the reduction of the total power transmission is the same as that of the extensional wave power.

Comparing the uncontrolled power transmission P_{un} due to different wave types, it is found that the major contribution to power transmission is from extensional waves. The power transmission contribution due to flexural waves is small while for torsional waves it is negligible as the excitation of the cylindrical shell is relatively axisymmetric. This is because the axial force N_x shown in equation (7.17) is relatively large so that extensional wave power transmission P_e is greater than flexural wave power transmission P_f , even though the amplitude of the displacement of the extensional waves is smaller than that of the flexural waves.

7.3.3 Effect of error sensor type, location and number

In the examples discussed so far, the cost function which has been minimized is the vibratory intensity integrated around the circumference of the cylinder at some axial location x_e . This quantity is referred to as power transmission. Individual intensity measurements are used to supply the error input to a feed-forward controller. However, vibratory intensity is not easily measured in practice. Thus the purpose of this section is to examine the effectiveness of using acceleration, which is more easily measured in practice, as the cost function. A theoretical comparison will be made of the total power transmission reduction obtained while using seven alternative cost functions including different wave type acceleration and different wave type power transmission. The different wave types include the three individual wave types and, in the case of power transmission, three waves combined.

The primary radial actuator locations are the same as shown above in Section 7.3.2 and

the control radial actuator locations are at $(x_c - x_p) = 0.05$ m. For acceleration control of individual wave types, the cost function to be minimized is the sum of the squares of the wave acceleration amplitudes integrated around the circumference of the cylinder. Table 7.2 shows the effect of cost function for either acceleration amplitude or power transmission, with different wave types either combined or individually. Data for three waves combined acceleration amplitude cost function has not been obtained, partly because of the complexity of calculation and partly because of the complexity of measurement in practice. The results show that, except for torsional wave cases, a similar reduction in total power transmission is obtained when the cost function uses acceleration amplitude or power transmission for different wave types. Thus, either flexural or axial acceleration amplitude cost functions can be considered to be alternatives to the total power transmission cost function. In practice, flexural acceleration amplitude as the cost function is considered to be more easily measured. Therefore, the flexural acceleration amplitude cost function can be used as a suitable alternative to the total power transmission cost function. In the following analysis, both the flexural wave acceleration cost function and the total power transmission cost function are included.

Table 7.2: Effect of different wave type cost functions on total power transmission reduction

Wave types	Acc. control $\frac{ F_c }{ F_p }$	$\phi_c - \phi_p$ radian	total P.T. red.(dB)	P.T. control $\frac{ F_c }{ F_p }$	$\phi_c - \phi_p$ radian	Total P.T. red.(dB)
Three waves combined				0.74	3.11	30
				0.55	3.13	
				0.66	3.12	
Flexural wave	0.75	3.10	30	0.75	3.13	31
	0.56	3.13		0.55	3.13	
	0.67	3.11		0.67	3.13	
Extensional wave	0.73	-3.12	29	0.74	3.11	30
	0.55	3.13		0.55	3.13	
	0.65	-3.13		0.66	3.12	
Torsional wave	0.56	3.06	14	0.71	-3.10	23
	0.72	3.00		0.55	3.04	
	0.68	3.06		0.64	3.10	

Note: "Acc. control" refers to acceleration amplitude cost function and "P.T. control" refers to power transmission cost function, corresponding to the wave type shown in the first column.

In Table 7.3, four different axial locations are tried for the error sensor locations. The calculated power transmission reduction corresponding to each axial location of the error sensors using flexural acceleration amplitude as the cost function, is then compared with that found using total power transmission as the cost function. The total power transmission reduction is dependent on the error sensor locations for both cost functions. The reduction increases when the error sensor/control source axial separation ($x_e - x_c$) increases. However, the reduction does not continue to increase significantly when $(x_e - x_c) > 0.49$ m at which point the error sensors are close to the far field of the primary forces. The reduction is a constant when $(x_e - x_c) > 0.69$ m at which point the error sensors are in the far field of the control forces. The reduced reduction in total power transmission when the error sensors are in the near field of the control forces, i.e. when $(x_e - x_c) < 0.69$ m, is due to the fact that the near field reactive power fluctuations affect the ability of the error sensors properly to observe the power transmission. The results further show that the total reduction resulting from using the flexural acceleration amplitude cost function is approximately the same as that obtained by using total power transmission as the cost function. This applies for each of four error sensor locations.

Table 7.3: Effect of error sensor type and location on total power transmission reduction

Location ($x_e - x_c$) (m)	Acc.control $\frac{ F_c }{ F_p }$	$\phi_c - \phi_p$ radian	Total P.T. red.(dB)	P.T.control $\frac{ F_c }{ F_p }$	$\phi_c - \phi_p$ radian	Total P.T. red.(dB)
0.29	0.71	3.11	25	0.71	-3.11	25
	0.54	3.12		0.54	3.13	
	0.64	3.12		0.64	-3.13	
0.49	0.75	3.10	30	0.74	3.11	30
	0.56	3.13		0.55	3.13	
	0.67	3.11		0.66	3.12	
0.69	0.77	3.12	31	0.76	3.11	31
	0.56	3.14		0.56	3.14	
	0.68	3.13		0.68	3.13	
0.89	0.77	-3.14	31	0.77	3.13	31
	0.55	-3.14		0.55	-3.13	
	0.68	-3.14		0.68	-3.13	

In practice, it is not possible to integrate the vibratory intensity around the circumference of the cylinder, although it is possible to integrate strain (which is proportional to normal acceleration) by using a PVDF film sensor. However in some instances, the acceleration will be measured by a number of accelerometers at discrete points. It is of interest to examine the effect on the maximum achievable reduction in power transmission of deriving the cost functions by averaging over a fixed number of sensors rather than integrating around the full circumference of the cylinder.

Table 7.4 shows results which demonstrate the effect of changing within the range of 3 to 199 the number of error sensors (accelerometers for acceleration and accelerometer pairs for power transmission, see Appendix F), for locations at $(x_e - x_c) = 0.49$ m. The error sensors are spaced in a line around the circumference of the cylinder. Two important results are obtained. The power transmission reduction is constant for error sensor numbers in the range of 9 to 199. Also the power transmission reduction is equal both for the acceleration amplitude cost function and for the total power transmission cost function in the range of 9 to 199. From this table, it can be seen that only 3 flexural acceleration error sensors are necessary, because the results are similar to those obtained when using power transmission cost function with 199 error sensors. Only three accelerometers needed because only the first three circumferential modes are significant. For three and seven error sensors, the reduction obtained by using power transmission as the cost function are not presented in this table. This is because the expression for power transmission given by equation (7.27) is inaccurate when less than nine power transmission error sensors are used. Use of less than three error sensors results in an under-determined system which causes one of the three control forces to be redundant and this is not analyzable. As the computer program used for calculations is only applicable when there is an odd number of error sensors, the results for even numbers of error sensors are not presented in this table. Note that the error sensors should not be spaced evenly, otherwise all of the error sensors might be located at vibrational nodes for some of the modes.

Table 7.4: Effect of number of error sensors in a ring at a single axial location on total power transmission reduction

No. error sensors	Acc.control $\frac{ F_c }{ F_p }$	$\phi_c - \phi_p$ radian	Total P.T. red.(dB)	P.T.control $\frac{ F_c }{ F_p }$	$\phi_c - \phi_p$ radian	Total P.T. red.(dB)
3	0.76	3.10	29	0.74	3.10	
	0.55	3.13		0.56	3.11	
	0.67	3.11		0.65	3.10	
7	0.75	3.11	29	0.75	3.12	
	0.56	3.14		0.55	-3.13	
	0.67	3.11		0.66	3.10	
9	0.75	3.10	30	0.74	3.12	30
	0.56	3.13		0.55	3.11	
	0.67	3.11		0.66	3.12	
19	0.75	3.10	30	0.74	3.11	30
	0.56	3.13		0.55	3.13	
	0.67	3.11		0.66	3.12	
39	0.75	3.10	30	0.74	3.11	30
	0.56	3.13		0.55	3.12	
	0.67	3.11		0.66	3.12	
199	0.75	3.10	30	0.74	3.11	30
	0.56	3.13		0.55	3.12	
	0.67	3.11		0.66	3.12	

7.3.4 Effect of control force type and location

In the examples discussed so far, the primary and control force types are all radial forces. In the example in this section, consideration is given to the following alternative primary and control force types: application of radial forces only; application of axial forces only or application of tangential forces only. For each of these cases the primary and control forces are of the same type, and the cost function to be minimized is the sum of the squares of the flexural acceleration amplitudes at the error sensors. For each case, three different control force locations were analyzed, and the primary actuator and error sensor locations were the same as those used in the earlier analysis outlined in Section 7.3.2. Results are shown in Table 7.5. It is concluded that the radial force is more effective than the axial force and the tangential force. The results also show that the reduction of power transmission decreases when the control actuators are located at some distance downstream from the primary actuators. Therefore, it can be concluded that for optimal control, the control actuators should be placed as close as possible to the axial location of the primary excitation force. Although theoretically, a reduction of 180 dB can be obtained for $(x_c - x_p) = 0$ m, in practice the minimum achievable separation will probably be $(x_c - x_p) \geq 0.05$ m. Theoretical results from Table 7.5 show that a reduction of 30 dB is achievable for $(x_c - x_p) = 0.05$ m when flexural wave acceleration control and radial forces are used.

Note that some of the results for tangential force $|F_c|/|F_p|$ are very large in Table 7.5 which shows that the tangential force is not effective in the control of power transmission.

As mentioned above, the results in Table 7.5 refer only to the use of flexural acceleration amplitude as the cost function. Similar analyses for alternative cost functions, using either flexural, extensional or total power transmission as the cost function, result in similar conclusions to those presented above. An example is shown in Table 7.2.

Table 7.5: Effect of control force type and location on total power transmission reduction for flexural acceleration amplitude as the cost function

Control force type	Location ($x_c - x_p$) (m)	Acc.control $\frac{ F_c }{ F_p }$	$\phi_c - \phi_p$ radians	Total P.T. red. (dB)
radial	0.00	1.00	$-\pi$	180
		1.00	π	
		1.00	$-\pi$	
	0.05	0.75	3.10	30
		0.56	3.13	
		0.67	3.11	
	0.20	2.87	0.72	27
		3.82	1.82	
		4.41	1.21	
axial	0.00	1.00	$-\pi$	147
		1.00	π	
		1.00	π	
	0.05	0.11	0.81E-2	15
		0.34E-2	0.29E+1	
		0.19E-1	0.25E-1	
	0.20	0.28E-1	0.49E-1	13
		0.14E-1	-0.19E-1	
		0.48E-2	0.64E-1	
tangential	0.00	1.00	$-\pi$	159
		1.00	$-\pi$	
		1.10E+5	0.61	
	0.05	0.46	3.12	27
		0.46	3.12	
		0.56E+13	-0.53	
	0.2	0.92	0.20E+1	0
		0.79	0.19E+1	
		0.49E+15	0.31E+1	

7.3.5 Effect of thickness, radius and frequency

It is known that measurement of power transmission is easier for flexural waves than for extensional waves. In Section 7.3.2, it was shown that for the cases considered, extensional waves produced the major contribution to power transmission. The purpose of this section is to examine the effect of cylinder thickness, radius and excitation frequency on the relative importance of flexural waves to the total power.

Table 7.6 shows uncontrolled power transmission as a function of the thickness h . The locations of the primary actuators and the error sensors are the same as shown in Table 7.4 and the cost function is flexural acceleration amplitude. Radial forces only are used as the primary forces. The results show that generally the ratio $\frac{P_f}{P_s}$, of flexural wave power transmission P_f to the total power transmission P_s , increases as h increases. Table 7.7 presents the uncontrolled power transmission as a function of the radius r which shows a trend of increasing ratio $\frac{P_f}{P_s}$ as r increases. Table 7.8 presents the uncontrolled power transmission as a function of the excitation frequency f and shows a trend of increasing ratio $\frac{P_f}{P_s}$ as f increases. More discussion of effect of excitation frequency will be shown in Appendix H.3.

Table 7.6: Effect of cylinder thickness on the ratio of flexural to total power transmission

Thickness h (m)	Radius r (m)	Frequency f (Hz)	Flexural P.T. P_f (W)	Total P.T. P_s (W)	$\frac{P_f}{P_s}$
0.001	0.5	510	0.2192E-9	0.3773E-6	0.00058097
0.008	0.5	510	0.5646E-9	0.1821E-7	0.03100494
0.010	0.5	510	0.5880E-9	0.1351E-7	0.04352331
0.040	0.5	510	0.3263E-9	0.2643E-8	0.12345819
0.050	1.0	510	0.7737E-8	0.9059E-8	0.85406777
0.060	1.0	510	0.6010E-8	0.6949E-8	0.86487264

Comparing Table 7.6, 7.7 and 7.8, it can be seen that cylinder thickness has a

Table 7.7: Effect of cylinder radius on the ratio of flexural to total power transmission

Thickness h (m)	Radius r (m)	Frequency f (Hz)	Flexural P.T. P_f (W)	Total P.T. P_s (W)	$\frac{P_f}{P_s}$
0.003	0.1	510	0.8529E-14	0.4074E-11	0.00209351
0.003	0.3	510	0.1710E-09	0.2772E-07	0.00616883
0.003	0.5	510	0.1213E-08	0.7764E-07	0.01562339

Table 7.8: Effect of excitation frequency on the ratio of flexural to total power transmission

Thickness h (m)	Radius r (m)	Frequency f (Hz)	Flexural P.T. P_f (W)	Total P.T. P_s (W)	$\frac{P_f}{P_s}$
0.003	0.5	110	0.4168E-10	0.3856E-7	0.00108091
0.003	0.5	210	0.9335E-10	0.5924E-7	0.00157579
0.003	0.5	430	0.2807E-09	0.7732E-7	0.00363036
0.003	0.5	510	0.4032E-09	0.7764E-7	0.00519319
0.003	0.5	610	0.6414E-09	0.7525E-7	0.00852358

more significant effect on the ratio $\frac{P_f}{P_s}$ than radius or excitation frequency. However, the assumption in the analysis is that $\frac{r}{h} > 16$, so there is a limit as to how much h can be increased without increasing r . It is concluded that a very large diameter and very thick cylinder is necessary to obtain the flexural waves as the dominant waves in producing power transmission under the assumption of $\frac{r}{h} > 16$. The extensional waves remain the major factor in producing power transmission for most cylinders of a practical size. It is also concluded that in the most cases, the extensional wave power transmission gives a good approximation of the total power transmission. This conclusion provides an opportunity for simplification of power transmission measurement methods in experimental work involving error sensors either in or close to the far field of the control sources as will be discussed further in Chapter 8 and Appendix H.

7.4 Summary

Harmonic power transmission in a semi-infinite cylinder can be reduced significantly by using an array of independently driven control forces around the circumference of the cylinder. For three or more radial control forces it is theoretically possible to achieve levels of power transmission reduction in excess of 30 dB for both acceleration amplitude and power transmission cost functions, under certain conditions. To achieve this reduction, it is necessary that the error sensors are either in or close to the flexural wave far field of the primary and control forces. It is also necessary that the control sources should be very close to the primary sources and that the modeling conditions for the point forces can be achieved in practice. For the test cylinder, only three flexural acceleration error sensors are necessary if the error sensors are in the far field of the primary and control forces. It is concluded that, in general, the radial control force is more effective than the axial force or the tangential force in controlling total power transmission. It is suggested that use of either the flexural or the axial acceleration cost function can be an alternative to the total power transmission cost function.

It is interesting to note that only one type of cost function can be effective on its own. This is because the flexural, extensional and torsional waves in the cylinders are strongly coupled.

The study has also indicated that in the test frequency range (well below the ring frequency) the extensional wave power transmission gives a good approximation of the total power transmission. This finding provides an opportunity for simplification of total power transmission measurement methods in experimental work. However, for frequencies from approximately half the ring frequency and up, this conclusion may become increasingly incorrect.

Chapter 8

An experimental study of active control of power transmission in a semi-infinite cylinder

8.1 Introduction

This chapter is concerned with experimental investigation of vibratory power transmission in a semi-infinite cylinder and its active control. A numerical study of the experimental method used is included in Appendix H. This study indicates that the measurement of vibratory intensity at a point on a cylinder requires the use of only two accelerometers for the test frequencies (well below the ring frequency). This finding is similar to that for plates which were discussed earlier in Chapter 5. This is notwithstanding the greater complexity in the theoretical analysis of cylinders compared with plates. This chapter will present some experimental results using the two accelerometer method to compare with the theoretical results.

8.2 Experimental arrangement

Vibratory power transmission was investigated experimentally by measuring intensity on a steel test cylinder with a working length of 1 m, thickness of 0.003 m and radius of 0.25 m.

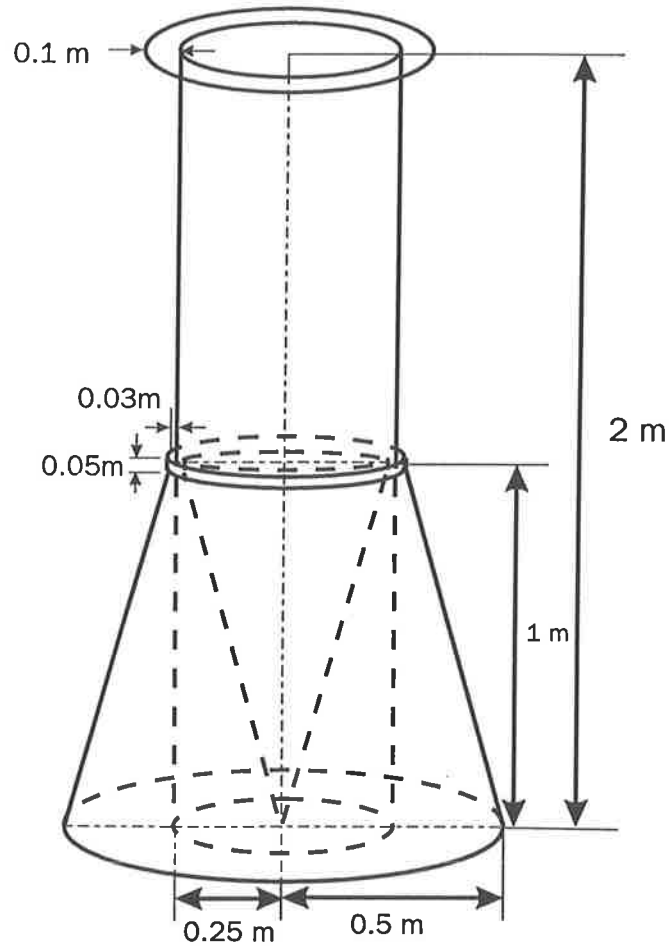


Figure 8.1: Schematic diagram of the semi-infinite cylinder model

There are three types of wave power transmission: flexural, extensional and torsional, which couple together to produce the total power transmission along the cylinder. The total intensity is actually approximated by the extensional wave intensity, an approximation which is shown to be valid by the analysis in Appendix H.3. A schematic diagram of the semi-infinite cylinder model is shown in Figure 8.1 and the experimental semi-infinite cylinder model is shown in Figure 8.2. The cylinder was mounted vertically in a sand filled box (1 m in height) in an attempt to provide a semi-anechoic termination at one end. The other end was simply supported using a thick steel ring.

The test cylinder was excited near the simply supported end using an electrodynamic primary shaker (see Figure 8.3). Control was implemented using three electrodynamic

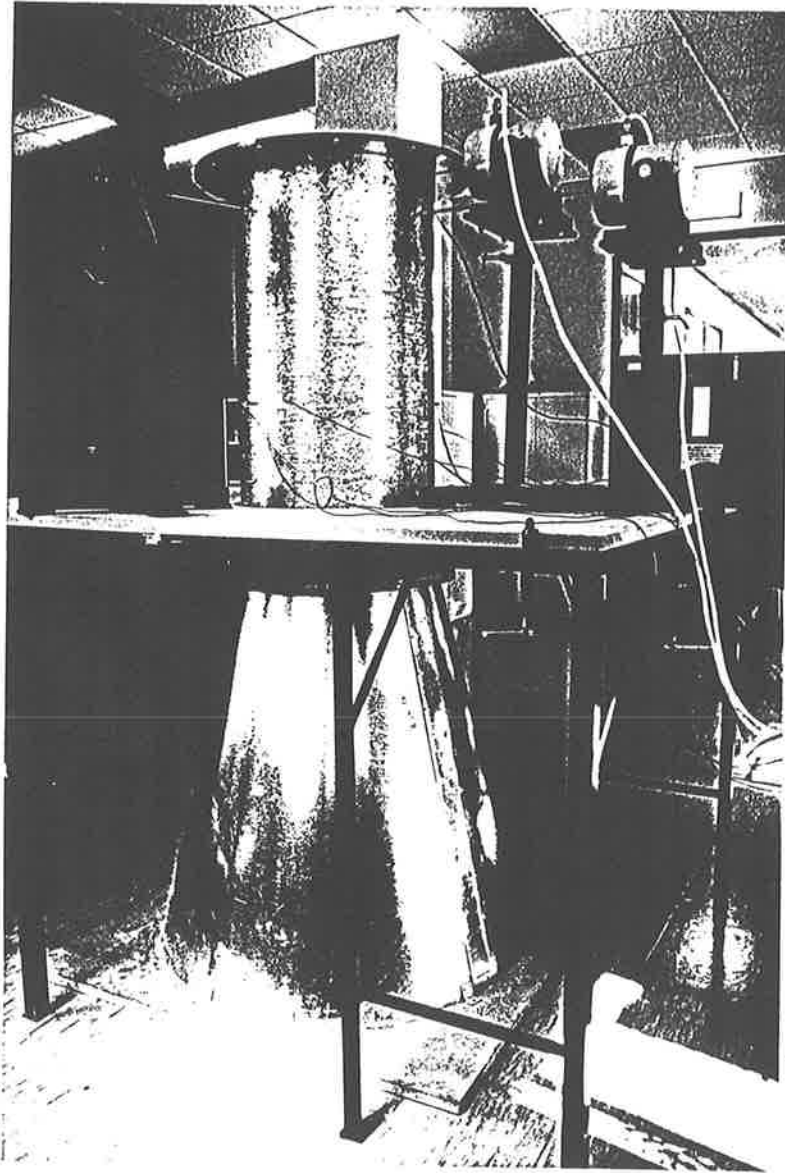


Figure 8.2: Experimental semi-infinite cylinder model.

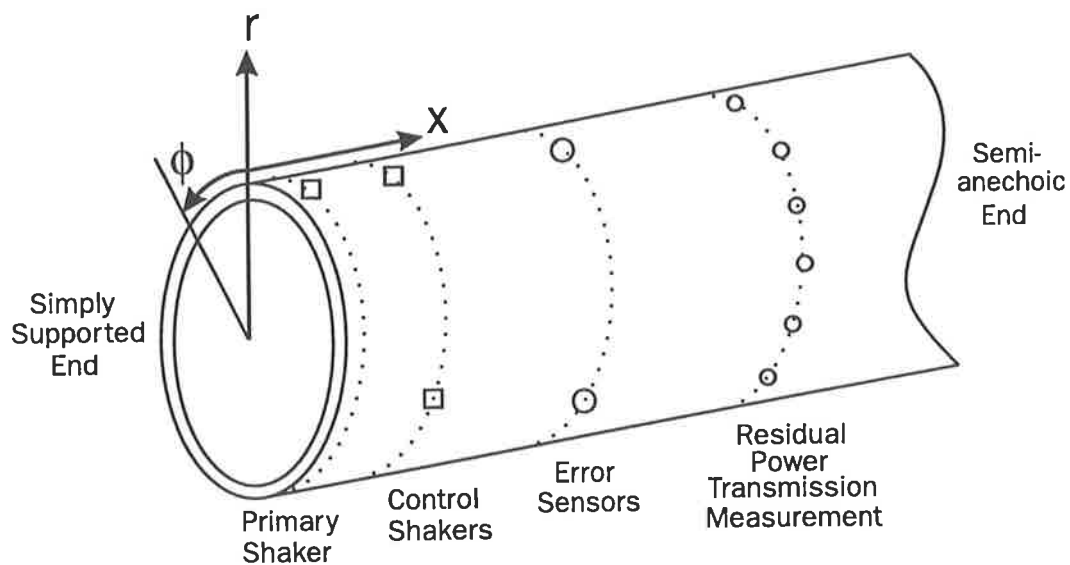
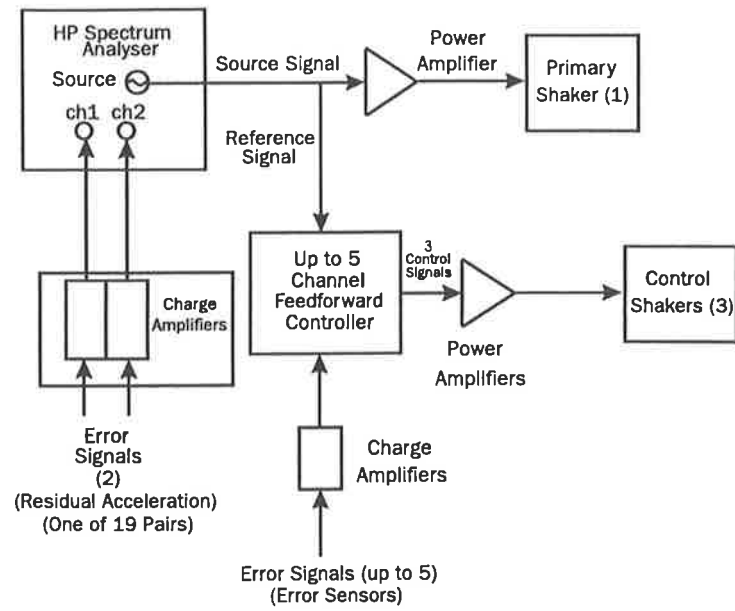


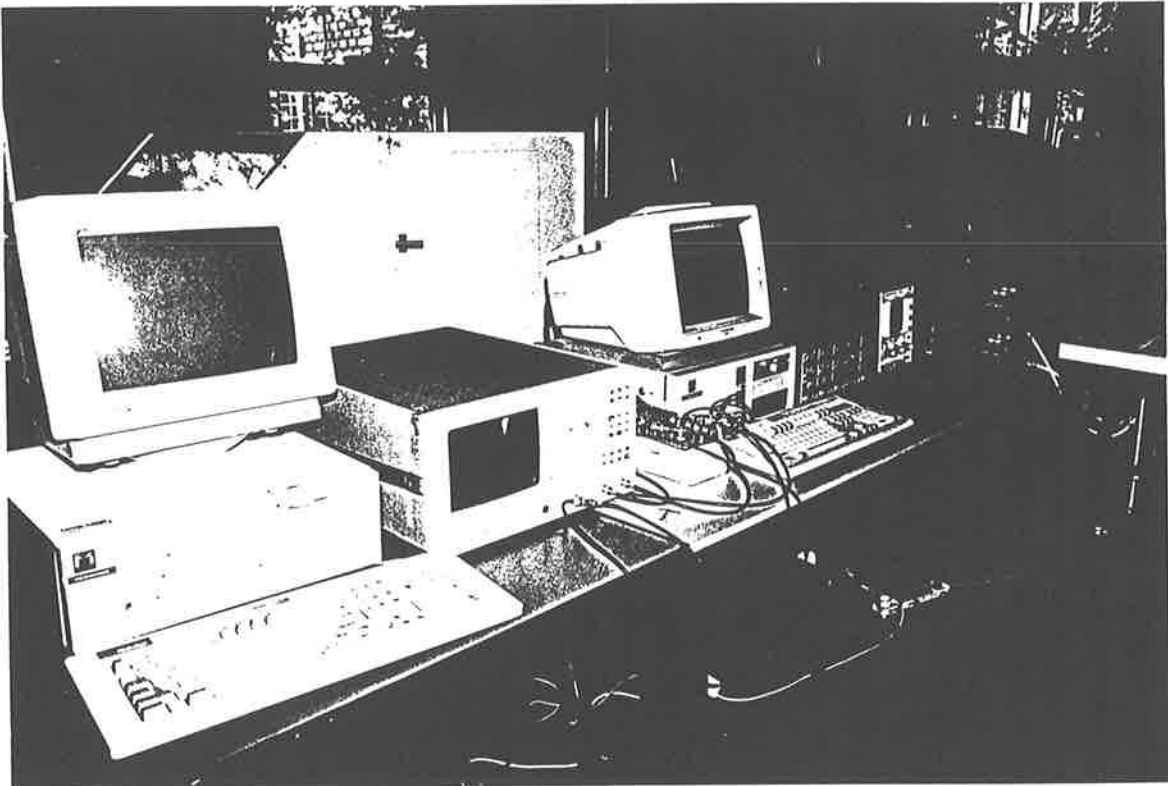
Figure 8.3: Vibration control system physical layout.

control shakers in locations around a circumference on the surface of the cylinder further from the simply supported end. Each control shaker was driven independently. Up to five accelerometers, mounted around the circumference and located between the control shakers and the semi-anechoic end, acted as error sensors. The control shakers were operated to minimize power transmission using an acceleration amplitude cost function consisting of the sum of squared outputs of the error sensors. Up to five error sensors could be used because the controller (EZ-ANC controller) had five available channels and the theoretical analysis indicated that this number was sufficient.

A block diagram of the vibration control system is shown in Figure 8.4(a). A source signal from an HP spectrum analyzer was passed through a power amplifier into the primary shaker. The source signal (as reference) and error signals from the error sensors were passed by way of amplifiers to a feed-forward controller. This controller generated three control signals which were used to drive independently the three control shakers. The experimental vibration control system is illustrated in Figure 8.4(b).



(a)



(b)

Figure 8.4: (a) Block diagram of the vibration control system; (b) experimental equipment.

8.3 Test procedure

To compare the characteristics of the experimental cylinder and the theoretical model, the circumferential modal amplitude was determined by undertaking a modal decomposition of the flexural cylinder displacement with the cylinder excited by electrodynamic shakers. This is because in the semi-infinite cylinder there is no axial mode, and the circumferential modes are the only modes available to be considered. The circumferential modal amplitudes were obtained by measuring the flexural displacement at 19 points around the circumference of the cylinder in the locations which will be described later with the residual power transmission measurements. The modal decomposition method is shown Appendix G.

The residual power transmission was measured on the cylinder downstream of the error sensors by measuring the intensity at nineteen measurement points, each comprising a pair of accelerometers located in a line around the circumference of the cylinder (Appendix H). The results of the numerical analysis indicated that a minimum of 19 measurement points were necessary to provide a reasonable degree of accuracy (within 0.5% of the power transmission value compared with the value obtained from 199 measurement points). As described in Appendix H, the intensity is proportional to the product of the outputs of a pair of accelerometers. The pair of accelerometers was mounted on a small rectangular aluminum block as a measuring set (Figure 8.5). One of the accelerometers was directed perpendicularly to the cylinder and the other was directed in the axial direction along the cylinder. The surface of the block towards the cylinder was shaped to match the curvature of the cylinder and was attached to the cylinder with double sided adhesive tape. For the test frequency of 510 Hz, experiments showed that adhesive tape provided similar results to wax or glue but was much easier to clear from the surfaces after each test run. Excellent reproducibility of results was also obtained. The acceleration amplitudes were determined by multiplying the auto-spectrum (in the spectrum analyzer) of each signal by an appropriate factor (Appendix H). The phase difference between the two signals was obtained by using the transfer function in the spectrum analyzer. The acceleration amplitude and phase difference values so obtained were then used to calculate the intensity in accordance with the equations shown in Appendix H.

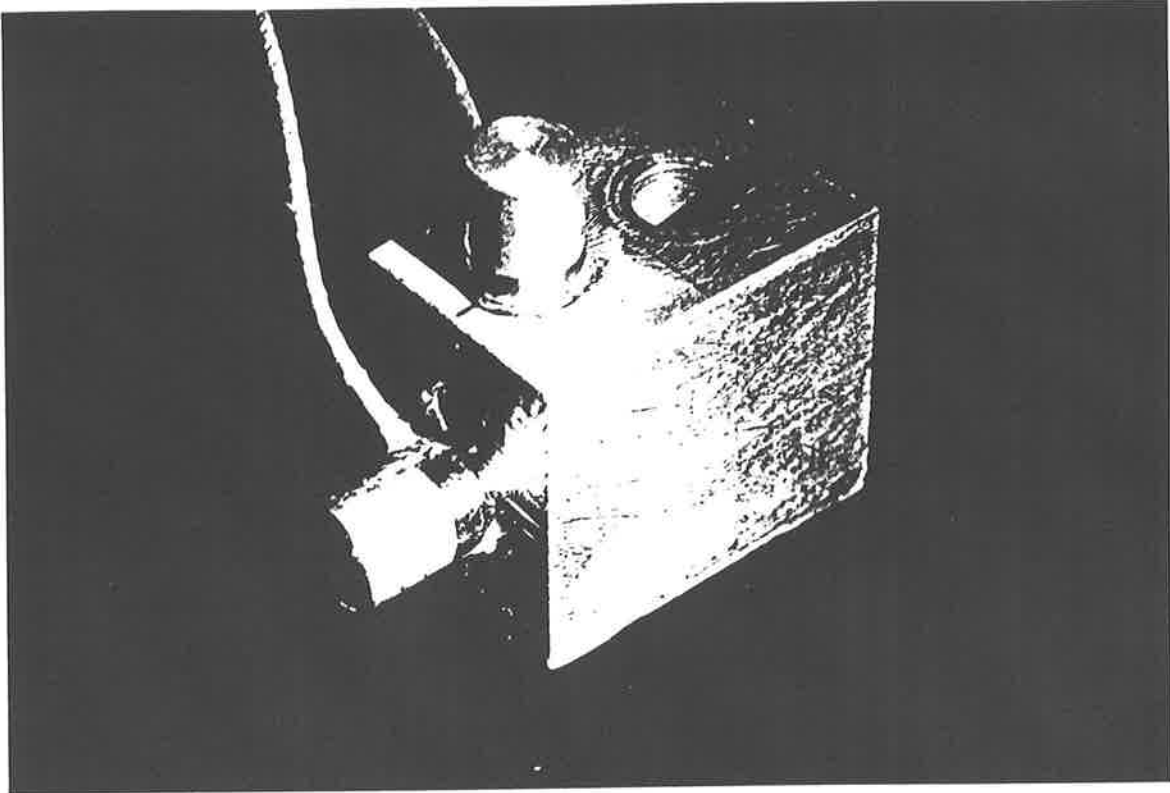


Figure 8.5: A cylindrical intensity measuring set.

8.4 Numerical and experimental results

To investigate the potential for actively controlling vibratory power transmission, the cylinder was excited at a frequency of 510 Hz. The primary shaker was located at 0.025 m in the x -direction and 2π in the ϕ -direction. The co-ordinate system is shown in Figure 8.3. Three control shakers were mounted around the circumference at 0.11 m in the x -direction, and spaced at $2\pi/3$, $4\pi/3 \times 1.05$ and 2π in the ϕ -direction respectively. Error sensors were arranged around the circumference at 0.566 m in the x -direction and spaced unequally in the ϕ -direction. The measurement points for circumferential modal amplitude and residual power transmission were arranged around the circumference at 0.965 m in the x -direction.

Circumferential modal amplitudes were obtained as described in Section 8.3. Numerical analysis showed that only the first three circumferential modes are significant for producing acceleration and power transmission. The first three circumferential modal shapes are shown in Figure 8.6. The circumferential modal amplitudes are presented in Figure 8.7(a) (measurement) and 8.7(b) (theory) for the first three modes. In Figure 8.7(a) (measurement), the controlled modal amplitude (grey or hatched columns) decreases for each mode. The

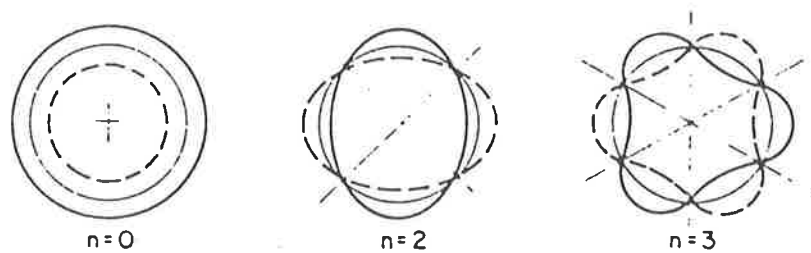


Figure 8.6: The first three circumferential modal shapes taken from Leissa (1973).

controlled modal amplitude trend (grey or hatched columns) is similar to the uncontrolled modal amplitude trend (black columns) in that the first mode dominates the response. In Figure 8.7(b) (theory), these phenomena are different to those found in the measurement. The amount of control is different to that shown in the measurement and the third mode dominates the response. This is due to the difficulty in ensuring that the locations of the primary and control shakers in the experiment are the same as the locations of the primary and control sources in the theory relative to the modal nodes and anti-nodes. The numerical simulation shows that the same modal amplitude trend as shown in Figure 8.7(a) can be obtained by moving the locations of the primary and control sources in the ϕ -direction. Also, the difference is probably because the experimental model was characterized by some reflection from the “infinite end” of the experimental cylinder. Figure 8.7 shows that reflection affects significantly the circumferential modal amplitudes.

To test the efficiency of the sand filled box which acted as an anechoic termination, a numerical simulation was carried out. It demonstrated that the reduction of power transmission is independent of the reflection coefficient. This means that experimentally determined values for the reduction of power transmission are valid even if there is large reflection from

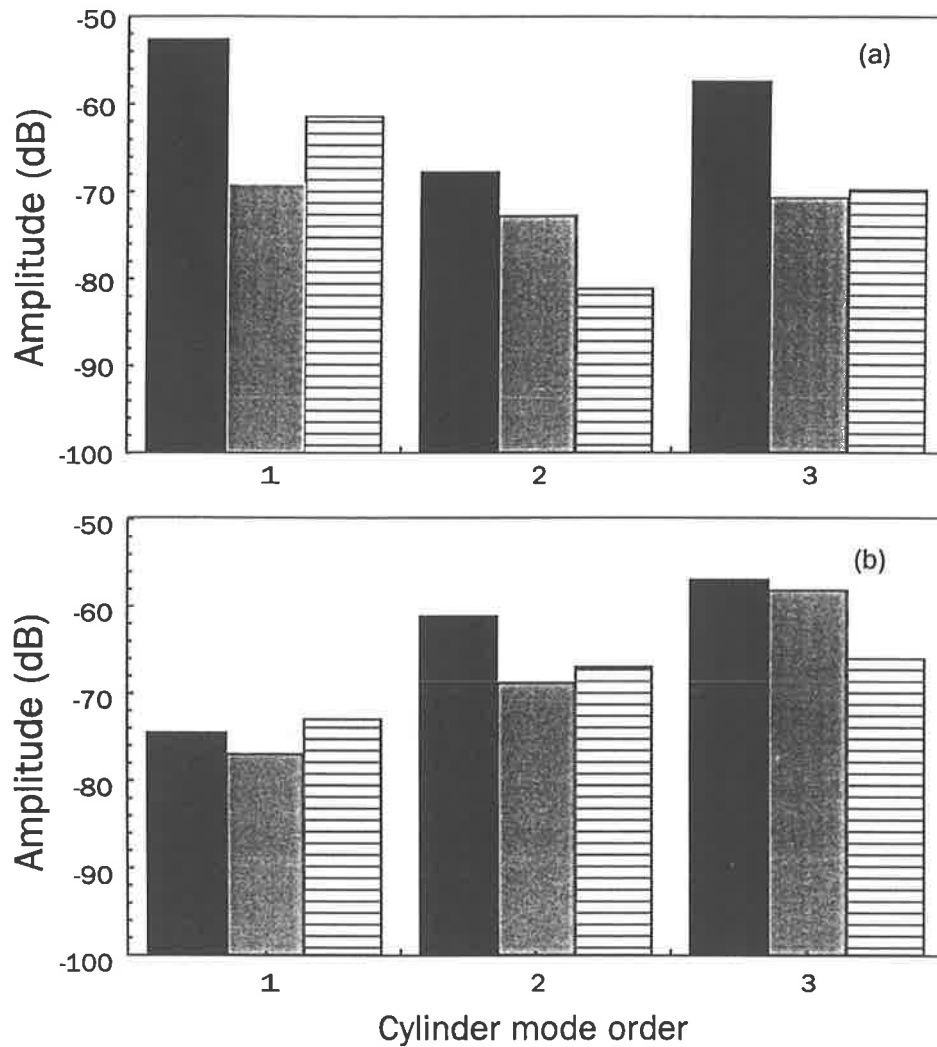


Figure 8.7: (a) Measured modal amplitudes; (b) theoretical modal amplitudes.
 for the uncontrolled case; for the controlled case and using three error sensors; for the controlled case and using five error sensors.

the anechoic termination. This finding is similar to that for plates which were discussed in Chapter 5.

Measured power transmission was obtained by averaging the intensity measured by each of 19 accelerometer pairs arranged around the circumference of the cylinder. The measured and theoretical power transmission reductions are shown in Table 8.1 with the range of 1, 3 and 5 error sensors.

Table 8.1: Experimental and theoretical power transmission

No. es.	Expt. $P_{un}(w)$	Expt. $P_{co}(w)$	Expt. $P_{red}(dB)$	Theo. $P_{un}(w)$	Theo. $P_{co}(w)$	Theo. $P_{red}(dB)$
1	0.68E-8	0.66E-8	0.1	0.59E-8	0.47E-8	0.9
3	0.68E-8	0.12E-8	7.2	0.59E-8	0.10E-8	7.4
5	0.68E-8	0.15E-8	6.4	0.59E-8	0.12E-8	6.8

Note: “No. es.” is the number of the error sensors, “Expt.” refers to the experimental results, “Theo.” refers to the theoretical results.

Table 8.1 shows that 7 dB power transmission reduction can be achieved by using three error sensors for the test cylinder in both experiment and theory. The reductions are similar for both experiment and theory for a particular number of error sensors. This further proves that the reduction of power transmission is independent of the reflection from the “infinite end”. The experimental results give approximate agreement with the numerical results which demonstrates the reliability of the experimental work. Most important is that the two accelerometer method is valid for the measurement of the intensity in a cylinder.

Table 8.1 also shows that use of one error sensor is insufficient. However, three error sensors provided a relatively good reduction. For the error sensor locations selected, the use of five error sensors did not increase the reduction. It is considered that the location of the error sensors in the ϕ -direction is very sensitive for the estimation of power transmission. The extra two accelerometers (error sensors) might have been either at or close to nodes where the error sensors cannot work effectively.

The amount of control shown in Table 8.1 is different from the amount shown in Figure 8.7. This is due to the fact that the intensity is proportional to the product of

flexural and extensional displacement amplitudes and their phase difference (Appendix H), but the circumferential modal amplitudes are dependent only on the flexural displacement.

Using a numerical simulation, it was found that the reduction in power transmission is similar for a range of excitation frequencies and a range of cylinder radii. It has also been found numerically that a greater reduction in power transmission is obtained when the cylinder working length is increased and/or when the separation distance between the primary and control shakers is decreased. It was found that for longer cylinders the improvement in power transmission reduction was due to less interference from the near field effects (from shakers) because of the increase in achievable distance between the control shakers and the error sensors and the increase in distance between the control shakers and the residual intensity measurement points. For example, it was found that up to 30 dB reduction (see Chapter 7) can be achieved for a semi-infinite cylinder with a 2.5 m working length (compared with 1 m used in the experimental work) and, with a separation distance between the primary and control shakers of 0.05 m (compared with 0.085 m used in the experimental work). The use of these physical specifications was not feasible for the current experimental work due, in part, to the excessive space requirement. For example, the total cylinder plus sand box length (equal to the working length of the cylinder) would be 5.0 m. Secondly, as each of the shaker bodies had a diameter of 0.16 m in practice the separation distance between the primary and control shakers could not be reduced to less than 0.085 m (see Figure 8.2).

8.5 Summary

Vibratory power transmission in a semi-infinite cylinder can be reduced by using an array of electrodynamic control shakers. For a semi-infinite cylinder having the physical characteristics described above, using three shakers and three error sensors, it is possible to achieve a 7 dB reduction in power transmission both experimentally and in theory for the test frequencies (well below the ring frequency). Although a 7 dB power reduction was the maximum which could be obtained for the particular experimental configuration investigated, numerical simulation showed that for a longer cylinder, a reduction of 30 dB could be obtained. This shows that the approach described here could be a feasible way of controlling vibra-

tion transmission in large cylindrical structures. Measurement of power transmission in a cylinder has been demonstrated by using two accelerometers for the test frequency range. This finding provides an opportunity for simplification of power transmission measurements in large cylindrical structures.

Chapter 9

Conclusions and recommendations

In this thesis, active control of harmonic vibratory power transmission in simple structures, including a beam, a plate and a cylinder, has been investigated. The results demonstrate that for a beam significant power transmission reduction can be obtained by the use of a single control source. For both the test plate and cylinder it was found that three independent control sources are required for the test low frequency range. It was found that for simple structures it is possible, with the use of acceleration amplitude as the cost function, to achieve satisfactory control of power transmission when the error sensors are in the far field of the control sources.

Increasing the separation between the error sensors and the control sources increases the maximum reduction in power transmission in each type of simple structure. Increasing the separation between the control sources and the primary sources does not significantly lower the amount of reduction in power transmission for a beam and a plate, but may produce a significantly lower reduction in the case of a cylinder.

It has been indicated that for the simple structures considered in this thesis, harmonic vibratory intensity in the far field of the primary and control sources can be measured by using a very limited number of accelerometers. For the measurement of the intensity, for a beam only one accelerometer located in the radial direction is required. For a plate two closely spaced accelerometers located in the radial direction are required for the test low frequency range. For a cylinder two accelerometers are required with one of the accelerometers directed perpendicularly to the cylinder and the other directed in the axial direction

along the cylinder for the test low frequency range. These findings provide an opportunity for simplification of harmonic vibratory power transmission measurements in large plate-like and cylindrical structures.

This study confirmed the existence of vibratory intensity vortices on a semi-infinite plate under primary excitation. It was also found that when control sources are added and are driven to minimize power transmission, the vortex pattern is largely eliminated.

The above results which apply to the use of point forces for the primary and control sources, can be achieved by using shakers. However, for a beam and a plate, it has also been shown that when piezoelectric actuators are used as an alternative to shakers for the primary and control sources, similar reductions in both acceleration and power transmission are obtained.

There are a number areas for further research based on this study. The theoretical analysis of the effect of boundary conditions on active control of acceleration in a beam (Chapter 3) can be extended to examine the effect on active control of power transmission in a plate and a cylinder. The use of piezoelectric actuators as an alternative to shakers (i.e. point force excitation) in a beam and a plate (Chapter 6) can be extended to a cylinder.

So far, to the author's knowledge, the experimental work has been carried out only on a single cylinder (Chapter 8). Further experimental studies could be conducted on vibratory intensity and vibratory power transmission on cylinders with different dimensions, physical conditions and therefore different boundary conditions. For example, an investigation using a longer cylinder may confirm the significant power transmission reduction as predicted by the theory.

Based on this research, analyses considering random vibration excitation, multiple lines of control sources and error sensors on a plate and multiple rings of control sources and error sensors on a cylinder can be developed. For example, the introduction of a second line of control sources/error sensors may overcome the difficulty in controlling power transmission when the first line of control sources/error sensors are located at a nodal line (see the cases for a beam in Chapter 3).

Investigations on plates could consider whether the use of a different cost function is more effective in reducing the intensity vortex pattern (see the examples for one particular cost function in Chapter 5). One possibility is to drive the control actuators to create in-

tensity vortices around points where sensitive items of equipment are attached to effectively isolate these from the plate vibration.

Appendix A

Classification of beam boundary conditions

The resonance frequencies (eigenvalues) and mode shapes (eigenvectors) of a finite beam are determined by the physical properties and geometry of the beam and the nature of the supports. In this study, the supports are only placed at the ends of the beam and are described in terms of their impedance. Therefore, this appendix is a mathematical classification of the various types of boundary impedance.

A.1 Beam boundary impedance

The flexural wave displacement amplitude of a finite beam (in the z direction shown in Figure 3.1(a)) at location x is defined by Fahy (1985), Fuller and Gonidou (1988)

$$w(x) = Ae^{k_f x} + Be^{-k_f x} + Ce^{jk_f x} + De^{-jk_f x} \quad (\text{A.1})$$

where A , B , C , D are constants. To describe the effect of boundaries upon beam vibration behavior in terms of boundary impedances (see Fuller et al. 1990), it is first necessary to find a suitable definition for such impedances. A correctly defined boundary impedance should express the internal beam moments and forces at the boundary as functions of the motion of the beam at the boundary. The motion of the beam can be described mathematically as a Taylor series containing *all* time and space derivatives of displacement. Fortunately, the time derivatives are not actually required in this sum, because the simple harmonic time dependence ensures that each time derivative simply results in multiplying the displacement

by $j\omega$ (The displacement w is assumed to have positive simple harmonic time dependence $e^{j\omega t}$). Also, from the general solution of equation (A.1), it can be seen that any space derivative of order greater than 4 can be written in terms of w , w' , w'' or w''' (where ' indicates partial derivative with respect to x). From this, the bending moment and shear force at any location in the beam (including the boundaries) are

$$M = m_1 w + m_2 w' + m_3 w'' + m_4 w''', \quad (\text{A.2})$$

$$Q = f_1 w + f_2 w' + f_3 w'' + f_4 w''' \quad (\text{A.3})$$

where m_1, \dots, m_4 and f_1, \dots, f_4 are all the required Taylor series coefficients. For the bending moment and shear force sign conventions illustrated in Figure 3.1(c),

$$M = -EI_{yy} w'' \quad (\text{A.4})$$

and

$$Q = EI_{yy} w''', \quad (\text{A.5})$$

so that equations (A.2) and (A.3) can be written as a matrix equation

$$\begin{bmatrix} M \\ Q \end{bmatrix} = \begin{bmatrix} m_1 & m_2 \\ f_1 & f_2 \end{bmatrix} \begin{bmatrix} w \\ w' \end{bmatrix} + \frac{1}{EI_{yy}} \begin{bmatrix} -m_3 & m_4 \\ -f_3 & f_4 \end{bmatrix} \begin{bmatrix} M \\ Q \end{bmatrix}, \quad (\text{A.6})$$

which can be written as

$$\begin{bmatrix} 1 + \frac{m_3}{EI_{yy}} & -\frac{m_4}{EI_{yy}} \\ \frac{f_3}{EI_{yy}} & 1 - \frac{f_4}{EI_{yy}} \end{bmatrix} \begin{bmatrix} M \\ Q \end{bmatrix} = \begin{bmatrix} m_1 & m_2 \\ f_1 & f_2 \end{bmatrix} \begin{bmatrix} w \\ w' \end{bmatrix}. \quad (\text{A.7})$$

Equation (A.7) can be inverted to give

$$\begin{bmatrix} M \\ Q \end{bmatrix} = \begin{bmatrix} 1 + \frac{m_3}{EI_{yy}} & -\frac{m_4}{EI_{yy}} \\ \frac{f_3}{EI_{yy}} & 1 - \frac{f_4}{EI_{yy}} \end{bmatrix}^{-1} \begin{bmatrix} m_1 & m_2 \\ f_1 & f_2 \end{bmatrix} \begin{bmatrix} w \\ w' \end{bmatrix}, \quad (\text{A.8})$$

or

$$\begin{bmatrix} M \\ Q \end{bmatrix} = [Z] \begin{bmatrix} \dot{w} \\ \dot{\theta} \end{bmatrix}, \quad (\text{A.9})$$

where $\dot{w} = j\omega w$ is velocity, and $\dot{\theta} = -j\omega w'$ is angular velocity, and

$$[Z] = \begin{bmatrix} Z_{m\dot{w}} & Z_{m\dot{\theta}} \\ Z_{f\dot{w}} & Z_{f\dot{\theta}} \end{bmatrix} \quad (\text{A.10})$$

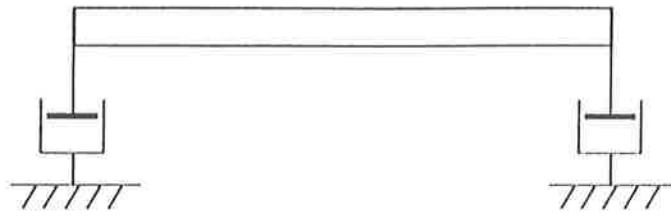
where $Z_{m\dot{w}}$, $Z_{m\dot{\theta}}$, $Z_{f\dot{w}}$ and $Z_{f\dot{\theta}}$ represent the impedance term due to the displacement on the moment, the rotation on the moment, the displacement on the shear force and the rotation on the shear force respectively. This 2×2 impedance matrix $[Z]$ is sufficiently general to describe any dependence of boundary forces (i.e. shear force and bending moment) upon the motion of a beam in simple flexure. This is in accordance with Cremer's (Cremer et. al, 1973) assertion that a 2×2 driving point force impedance matrix is required to describe the effect of a combined point force and moment excitation on the flexural motion of a beam.

The relationships between standard support types and corresponding left-hand boundary impedances are shown in Table A.1. For example, viscous damping (Figure A.1(a)) may be represented by a negative real boundary impedance, the simple spring support shown in Figure A.1(b) can be represented by a positive imaginary boundary impedance and a combined spring and dashpot can be represented as a complex impedance (Figure A.1(c)). Note that for all of these standard support conditions, the cross terms $Z_{m\dot{w}}$ and $Z_{f\dot{\theta}}$ of the impedance matrix are zero. Thus only two terms are shown for each end condition in Table A.1.

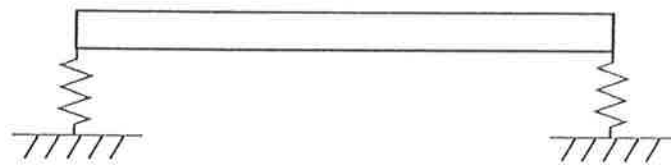
Table A.1: Standard support types and corresponding left-hand boundary impedance

End Condition Type		Boundary Condition	Impedance
Pinned		$w(-\frac{L}{2}, t) = 0$ $\frac{\partial^2 w(-\frac{L}{2}, t)}{\partial x^2} = 0$	$Z_{f\dot{w}} = \infty$ $Z_{m\dot{\theta}} = 0$
Fixed		$w(-\frac{L}{2}, t) = 0$ $\frac{\partial w(-\frac{L}{2}, t)}{\partial x} = 0$	$Z_{f\dot{w}} = \infty$ $Z_{m\dot{\theta}} = \infty$
Free		$\frac{\partial^2 w(-\frac{L}{2}, t)}{\partial x^2} = 0$ $\frac{\partial^3 w(-\frac{L}{2}, t)}{\partial x^3} = 0$	$Z_{f\dot{w}} = 0$ $Z_{m\dot{\theta}} = 0$
Deflected Spring		$\frac{\partial^2 w(-\frac{L}{2}, t)}{\partial x^2} = 0$ $EI_{yy} \frac{\partial^3 w(-\frac{L}{2}, t)}{\partial x^3} = -K_D w(-\frac{L}{2}, t)$	$Z_{f\dot{w}} = j \frac{K_D}{\omega}$ $Z_{m\dot{\theta}} = 0$
Torsion Spring		$w(-\frac{L}{2}, t) = 0$ $EI_{yy} \frac{\partial^2 w(-\frac{L}{2}, t)}{\partial x^2} = K_T \frac{\partial w(-\frac{L}{2}, t)}{\partial x}$	$Z_{f\dot{w}} = \infty$ $Z_{m\dot{\theta}} = -j \frac{K_T}{\omega}$
Mass		$\frac{\partial^2 w(-\frac{L}{2}, t)}{\partial x^2} = 0$ $EI_{yy} \frac{\partial^3 w(-\frac{L}{2}, t)}{\partial x^3} = -m \frac{\partial^2 w(-\frac{L}{2}, t)}{\partial t^2}$	$Z_{f\dot{w}} = -j\omega m$ $Z_{m\dot{\theta}} = 0$
Dashpot		$\frac{\partial^2 w(-\frac{L}{2}, t)}{\partial x^2} = 0$ $EI_{yy} \frac{\partial^3 w(-\frac{L}{2}, t)}{\partial x^3} = -c \frac{\partial w(-\frac{L}{2}, t)}{\partial t}$	$Z_{f\dot{w}} = -c$ $Z_{m\dot{\theta}} = 0$

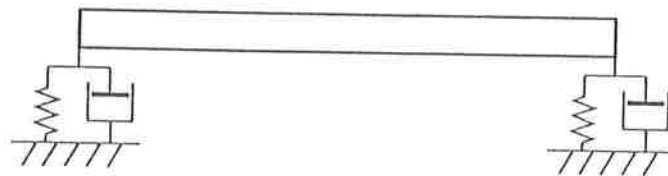
Note that at this stage the only energy dissipation which has been considered has been at the ends of the beam. However, there is also hysteresis loss in the beam itself which may be taken into account in this analysis by replacing Young's modulus E , with the complex modulus, $E(1 + j\eta)$.



(a)



(b)



(c)

Figure A.1: Physical meaning of boundary impedance: (a) real boundary impedance; (b) imaginary boundary impedance; (c) complex boundary impedances.

A.2 Equivalent boundary impedance of an infinite beam

If an infinite beam with a flexural wave traveling toward the right from a sole point force excitation, the displacement amplitude function can be written as

$$w(x) = Be^{-k_f x} + De^{-jk_f x}, \quad (\text{A.11})$$

so that

$$\dot{w}(x) = j\omega Be^{-k_f x} + j\omega De^{-jk_f x} \quad (\text{A.12})$$

and

$$\dot{\theta}(x) = j\omega k_f Be^{-k_f x} - \omega k_f De^{-jk_f x} \quad (\text{A.13})$$

Equations (A.12) and (A.13) can be written in a matrix form

$$\begin{bmatrix} \dot{w}(x) \\ \dot{\theta}(x) \end{bmatrix} = \begin{bmatrix} j\omega & j\omega \\ j\omega k_f & -\omega k_f \end{bmatrix} \begin{bmatrix} Be^{-k_f x} \\ De^{-jk_f x} \end{bmatrix} \quad (\text{A.14})$$

which can be inverted to give

$$\begin{bmatrix} Be^{-k_f x} \\ De^{-jk_f x} \end{bmatrix} = \begin{bmatrix} -\frac{1+j}{2\omega} & \frac{1-j}{2\omega k_f} \\ \frac{1-j}{2\omega} & -\frac{1-j}{2\omega k_f} \end{bmatrix} \begin{bmatrix} \dot{w}(x) \\ \dot{\theta}(x) \end{bmatrix}. \quad (\text{A.15})$$

Equation (A.11) can be differentiated two more times to give bending moment M and shear force Q and the result can be written in matrix form:

$$\begin{bmatrix} M(x) \\ Q(x) \end{bmatrix} = -EI_{yy} \begin{bmatrix} k_f^2 & -k_f^2 \\ k_f^3 & -jk_f^3 \end{bmatrix} \begin{bmatrix} Be^{-k_f x} \\ De^{-jk_f x} \end{bmatrix} \quad (\text{A.16})$$

The column vector on the right hand side of equation (A.16) can be replaced with the right hand side of equation (A.15). Thus,

$$\begin{bmatrix} M(x) \\ Q(x) \end{bmatrix} = [Z_{R,inf}] \begin{bmatrix} \dot{w}(x) \\ \dot{\theta}(x) \end{bmatrix} \quad (\text{A.17})$$

where

$$[Z_{R,inf}] = \begin{bmatrix} EI_{yy}k_f^2/\omega & -(1-j)EI_{yy}k_f/\omega \\ (1+j)EI_{yy}k_f^3/\omega & -EI_{yy}k_f^2/\omega \end{bmatrix} \quad (\text{A.18})$$

so that the boundary bending moment and shear force are expressed as the product of the 2×2 impedance matrix $[Z_{R,inf}]$ and a column vector containing the velocity and angular velocity of the beam. $[Z_{R,inf}]$ is the right infinite beam impedance matrix. By a similar process of considering a flexural wave traveling from a source toward the left in an infinite beam the left infinite beam impedance matrix is

$$[Z_{L,inf}] = \begin{bmatrix} EI_{yy}k_f^2/\omega & (1-j)EI_{yy}k_f/\omega \\ -(1+j)EI_{yy}k_f^3/\omega & -EI_{yy}k_f^2/\omega \end{bmatrix}. \quad (\text{A.19})$$

Note that $[Z_{R,inf}] \neq [Z_{L,inf}]$ and $[Z_{R,inf}] \neq -[Z_{L,inf}]$. By using the infinite beam impedance matrix $[Z_{R,inf}]$ (or $[Z_{L,inf}]$) as the right (or left) boundary impedance matrix in the finite beam model, the boundary is effectively removed and the beam becomes semi-infinite. An infinite beam can be modeled by using both the left and right infinite beam impedance matrices as boundary impedances at opposite ends of the beam. This use of infinite beam impedance matrices to model the termination of a finite length beam produces numerical results identical to those obtained by evaluating the expression derived from the analysis of an infinite beam.

Appendix B

Response of a finite beam to a point force

The purpose of this appendix is to determine the response to a simple harmonic point force excitation applied at $x = x_0$ of a finite beam with left and right boundary conditions specified as impedance matrices $[Z_L]$ and $[Z_R]$. The applied point force produces a discontinuity in the shear force function $Q(x)$ and so it is necessary to calculate two sets of constant coefficients A , B , C and D , one on the left

$$w_1(x) = A_1 e^{k_f x} + B_1 e^{-k_f x} + C_1 e^{jk_f x} + D_1 e^{-jk_f x} \quad (\text{B.1})$$

and one on the right of the applied force

$$w_2(x) = A_2 e^{k_f x} + B_2 e^{-k_f x} + C_2 e^{jk_f x} + D_2 e^{-jk_f x}. \quad (\text{B.2})$$

At the common boundary $x = x_0$,

$$w_1(x_0) = w_2(x_0) \quad (\text{B.3})$$

$$w'_1(x_0) = w'_2(x_0) \quad (\text{B.4})$$

$$w''_1(x_0) = w''_2(x_0) \quad (\text{B.5})$$

$$w'''_2(x_0) = w'''_1(x_0) + \frac{F_0}{EI_{yy}}. \quad (\text{B.6})$$

From equation (A.9) the left hand boundary condition of the beam at $x = x_L$ can be written as

$$\begin{bmatrix} M(x_L) \\ Q(x_L) \end{bmatrix} = \begin{bmatrix} Z_{Lm\dot{w}} & Z_{Lm\dot{\theta}} \\ Z_{Lf\dot{w}} & Z_{Lf\dot{\theta}} \end{bmatrix} \begin{bmatrix} \dot{w}_1(x_L) \\ \dot{\theta}_1(x_L) \end{bmatrix} \quad (\text{B.7})$$

By using equations (A.4) and (A.5) to replace the bending moment and shear force with a derivative of the displacement function, the following is obtained

$$\begin{bmatrix} Z_{Lm\dot{w}} & Z_{Lm\dot{\theta}} \\ Z_{Lf\dot{w}} & Z_{Lf\dot{\theta}} \end{bmatrix} \begin{bmatrix} \dot{w}_1(x_L) \\ \dot{\theta}_1(x_L) \end{bmatrix} + EI_{yy} \begin{bmatrix} w_1''(x_L) \\ -w_1'''(x_L) \end{bmatrix} = 0. \quad (\text{B.8})$$

Similarly, for the right hand boundary of the beam at $x = x_R$,

$$\begin{bmatrix} Z_{Rm\dot{w}} & Z_{Rm\dot{\theta}} \\ Z_{Rf\dot{w}} & Z_{Rf\dot{\theta}} \end{bmatrix} \begin{bmatrix} \dot{w}_2(x_R) \\ \dot{\theta}_2(x_R) \end{bmatrix} + EI_{yy} \begin{bmatrix} w_2''(x_R) \\ -w_2'''(x_R) \end{bmatrix} = 0. \quad (\text{B.9})$$

Equations (B.1) and (B.2) are then differentiated to produce expressions for \dot{w} , $\dot{\theta}$, w_1' , w_1'' , w_1''' , w_2' , w_2'' and w_2''' which contain the unknown coefficients A_1 , B_1 , C_1 , D_1 , A_2 , B_2 , C_2 and D_2 . These expressions can be substituted into equations (B.3), (B.4), (B.5), (B.6), (B.8) and (B.9) and the equations can be combined into a single 8×8 system of linear equations, to obtain

$$[\alpha][\mathbf{X}] = [\mathbf{F}] \quad (\text{B.10})$$

where

$$[\mathbf{X}] = [A_1, B_1, C_1, D_1, A_2, B_2, C_2, D_2]^T, \quad (\text{B.11})$$

$$[\mathbf{F}] = \left[0, 0, 0, 0, 0, 0, 0, \frac{F_0}{EI_{yy}k_f^3} \right]^T, \quad (\text{B.12})$$

and

$$\begin{bmatrix} \beta_L(Z_{Lm\dot{w}} - k_f Z_{Lm\dot{\theta}} + Q_2) & \frac{Z_{Lm\dot{w}} + k_f Z_{Lm\dot{\theta}} + Q_2}{\beta_L} & \beta_L^j (Z_{Lm\dot{w}} + \frac{k_f}{j} Z_{Lm\dot{\theta}} - Q_2) \\ \beta_L(Z_{Lf\dot{w}} - k_f Z_{Lf\dot{\theta}} - Q_1) & \frac{Z_{Lf\dot{w}} + k_f Z_{Lf\dot{\theta}} + Q_1}{\beta_L} & \beta_L^j (Z_{Lf\dot{w}} + \frac{k_f}{j} Z_{Lf\dot{\theta}} + jQ_1) \\ 0 & 0 & 0 \\ 0 & 0 & 0 \\ \beta_0 & 1/\beta_0 & \beta_0^j \\ \beta_0 & -1/\beta_0 & j\beta_0^j \\ \beta_0 & 1/\beta_0 & -\beta_0^j \\ -\beta_0 & 1/\beta_0 & j\beta_0^j \end{bmatrix}$$

$$\begin{array}{ccc}
\frac{Z_{Lm\dot{w}} - \frac{k_f}{j} Z_{Lm\dot{\theta}} - Q_2}{\beta_L^j} & 0 & 0 \\
\frac{Z_{Lf\dot{w}} - \frac{k_f}{j} Z_{Lf\dot{\theta}} - jQ_1}{\beta_L^j} & 0 & 0 \\
0 & \beta_R(Z_{Rm\dot{w}} - k_f Z_{Rm\dot{\theta}} + Q_2) & \frac{Z_{Rm\dot{w}} + k_f Z_{Rm\dot{\theta}} + Q_2}{\beta_R} \\
0 & \beta_R(Z_{Rf\dot{w}} - k_f Z_{Rf\dot{\theta}} - Q_1) & \frac{Z_{Rf\dot{w}} + k_f Z_{Rf\dot{\theta}} + Q_1}{\beta_R} \\
1/\beta_0^j & -\beta_0 & -1/\beta_0 \\
-j/\beta_0^j & -\beta_0 & 1/\beta_0 \\
-1/\beta_0^j & -\beta_0 & -1/\beta_0 \\
-j/\beta_0^j & \beta_0 & -1/\beta_0 \\
0 & 0 & 0 \\
0 & 0 & 0 \\
\beta_R^j(Z_{Rm\dot{w}} + \frac{k_f}{j} Z_{Rm\dot{\theta}} - Q_2) & \frac{Z_{Rm\dot{w}} - \frac{k_f}{j} Z_{Rm\dot{\theta}} - Q_2}{\beta_R^j} & \\
\beta_R^j(Z_{Rf\dot{w}} + \frac{k_f}{j} Z_{Rf\dot{\theta}} + jQ_1) & \frac{Z_{Rf\dot{w}} - \frac{k_f}{j} Z_{Rf\dot{\theta}} - jQ_1}{\beta_R^j} & \\
-\beta_0^j & -1/\beta_0^j & \\
-j\beta_0^j & j/\beta_0^j & \\
\beta_0^j & 1/\beta_0^j & \\
-j\beta_0^j & j/\beta_0^j &
\end{array} = [\alpha], \quad (\text{B.13})$$

where $\beta_R = e^{k_f x_R}$, $\beta_0 = e^{k_f x_0}$, $\beta_L = e^{k_f x_L}$, $\beta_R^j = e^{jk_f x_R}$, $\beta_0^j = e^{jk_f x_0}$, $\beta_L^j = e^{jk_f x_L}$, $Q_1 = \frac{EI_{yy} k_f^3}{j\omega}$ and $Q_2 = \frac{EI_{yy} k_f^2}{j\omega}$. The solution vector $[\mathbf{X}]$ characterizes the response of a finite-length beam to a point force simple harmonic excitation.

Appendix C

Response of a semi-infinite plate to a line of point forces driven in phase

The classical equation of motion for a plate given by Graff (1975) is

$$\rho h \frac{\partial^2 w(x, y, t)}{\partial t^2} + D_h \nabla^4 w(x, y, t) = q(x, y, t) \quad (\text{C.1})$$

where ρ is mass density per unit volume of the plate and $\nabla^4 = \nabla^2 \nabla^2$ is the square of the Laplacian operator. Note that the effects of transverse shear and rotary inertia have been ignored to simplify the analysis. The geometry of the plate and the alignment of the coordinate system are shown in Figure 4.1. The plate lies in the x - y plane with a free edge at $x = 0$ and simply supported edges at $y = 0$ and $y = L_y$. The external force per unit area excitation represented by q is an array of m equally spaced point forces spanning the plate along a line parallel to the y -axis. At this stage, all of these forces at locations $(x_0, y_i, i = 1, m)$, will be assumed to be driven in phase and with the same complex amplitude F_0 so that

$$q = F_0 \sum_{i=1}^m \delta(x - x_0) \delta(y - y_i). \quad (\text{C.2})$$

The two sides ($y = 0, y = L_y$) are simply supported and, so the following harmonic series solution in y can be assumed for the vibratory displacement

$$w(x, y, t) = \sum_{n=1}^{\infty} w_n(x) \sin \frac{n\pi y}{L_y} e^{j\omega t}. \quad (\text{C.3})$$

Each eigenfunction $w_n(x)$ can be expressed in terms of unknown constants A_1, A_2, A_3 and A_4 and modal wavenumbers k_{in} as follows

$$w_n(x) = A_1 e^{k_{1n}x} + A_2 e^{k_{2n}x} + A_3 e^{k_{3n}x} + A_4 e^{k_{4n}x}. \quad (\text{C.4})$$

To find the modal wavenumbers (i.e. eigenvalues), the homogeneous form of equation (C.1) is multiplied by $\sin \frac{n\pi y}{L_y}$ and integrated with respect to y over the width the plate (i.e. from 0 to L_y), to give

$$\frac{d^4 w_n(x)}{dx^4} - 2\left(\frac{n\pi}{L_y}\right)^2 \frac{d^2 w_n(x)}{dx^2} + \left(\left(\frac{n\pi}{L_y}\right)^4 - \frac{\rho h \omega^2}{D_h}\right) w_n(x) = 0. \quad (\text{C.5})$$

Solutions to this ordinary differential equation are assumed to be of the form $e^{k_n x}$, and its characteristic equation is

$$k_n^4 - 2\left(\frac{n\pi}{L_y}\right)^2 k_n^2 + \left(\frac{n\pi}{L_y}\right)^4 - \frac{\rho h \omega^2}{D_h} = 0, \quad (\text{C.6})$$

which has the roots

$$k_{1n,2n} = \pm \sqrt{\left(\frac{n\pi}{L_y}\right)^2 + \sqrt{\frac{\rho h \omega^2}{D_h}}}, \quad (\text{C.7})$$

$$k_{3n,4n} = \pm \sqrt{\left(\frac{n\pi}{L_y}\right)^2 - \sqrt{\frac{\rho h \omega^2}{D_h}}}. \quad (\text{C.8})$$

Using equations (C.8) it can be shown that if

$$\left(\frac{n\pi}{L_y}\right)^2 < \sqrt{\frac{\rho h \omega^2}{D_h}} \quad (\text{C.9})$$

or

$$\omega = 2\pi f > \left(\frac{n\pi}{L_y}\right)^2 \sqrt{\frac{D_h}{\rho h}}, \quad (\text{C.10})$$

then the wavenumber in equation (C.8) is imaginary. By substituting the mode number in n into equation (C.10), the cut-on frequency for mode n can be calculated. Calculated cut-on frequencies for the first five modes are listed in Table 4.1.

On each side of the applied force, the eigenfunction $w_n(x)$ is then a different linear combination of the terms $e^{k_{in}x}$ (with $i = 1, 2, 3, 4$). For $x < x_0$,

$$w_{1n}(x) = A_1 e^{k_{1n}x} + A_2 e^{k_{2n}x} + A_3 e^{k_{3n}x} + A_4 e^{k_{4n}x} \quad (\text{C.11})$$

and for $x > x_0$,

$$w_{2n}(x) = B_2 e^{k_{2n}x} + B_4 e^{k_{4n}x}. \quad (\text{C.12})$$

Note that in equation (C.12) the coefficients B_1 and B_3 have been omitted because, for a semi-infinite plate, there is no boundary to produce reflected waves with a negative horizontal velocity component. At the junction $x = x_0$, the following boundary conditions must be satisfied

$$w_{1n} = w_{2n}, \quad (\text{C.13})$$

$$\frac{\partial w_{1n}}{\partial x} = \frac{\partial w_{2n}}{\partial x}, \quad (\text{C.14})$$

$$\frac{\partial^2 w_{1n}}{\partial x^2} = \frac{\partial^2 w_{2n}}{\partial x^2} \quad (\text{C.15})$$

and

$$\frac{\partial^3 w_{1n}}{\partial x^3} - \frac{\partial^3 w_{2n}}{\partial x^3} = -\frac{2F_0}{L_y D_h} \sum_{i=1}^m \sin \frac{n\pi y_i}{L_y}. \quad (\text{C.16})$$

For the free edge at $x = 0$, the expression

$$-D_h \left(\frac{\partial^2 w}{\partial x^2} + \nu \frac{\partial^2 w}{\partial y^2} \right) \Big|_{x=0} = 0 \quad (\text{C.17})$$

given by Leissa (1969) (The coordinate system given by Graff (1975) is different from that given by Leissa (1969), therefore this chapter cited corresponding equations given by Leissa (1969) as the coordinate system in this chapter is the same as that given by Leissa (1969).) can be used to express the bending moment boundary condition

$$M_x(0, y) = 0 \quad (\text{C.18})$$

in terms of displacement, with the following result

$$\sum_{n=1}^{\infty} \left[k_{1n}^2 A_1 + k_{2n}^2 A_2 + k_{3n}^2 A_3 + k_{4n}^2 A_4 - \nu \left(\frac{n\pi}{L_y} \right)^2 (A_1 + A_2 + A_3 + A_4) \right] \sin \frac{n\pi y}{L_y} = 0. \quad (\text{C.19})$$

By again multiplying both sides by $\sin \frac{n\pi y}{L_y}$ and integrating from $y = 0$ to L_y , the following is obtained:

$$\left[k_{1n}^2 - \nu \left(\frac{n\pi}{L_y} \right)^2 \right] A_1 + \left[k_{2n}^2 - \nu \left(\frac{n\pi}{L_y} \right)^2 \right] A_2 + \left[k_{3n}^2 - \nu \left(\frac{n\pi}{L_y} \right)^2 \right] A_3 + \left[k_{4n}^2 - \nu \left(\frac{n\pi}{L_y} \right)^2 \right] A_4 = 0. \quad (\text{C.20})$$

The free edge condition also requires that the net vertical force at $x = 0$ be zero (Leissa, 1969). Thus,

$$V_x = Q_x + \frac{\partial M_{xy}}{\partial y} = 0 \quad (\text{C.21})$$

which can be expressed in terms of displacement as

$$V_x(x, y)|_{x=0} = -D_h \left[\frac{\partial^3 w}{\partial x^3} + (2 - \nu) \frac{\partial^3 w}{\partial x \partial y^2} \right] \Big|_{x=0} = 0 \quad (\text{C.22})$$

Thus,

$$\begin{aligned} & \left[k_{1n}^3 - (2 - \nu) \left(\frac{n\pi}{L_y} \right)^2 k_{1n} \right] A_1 + \left[k_{2n}^3 - (2 - \nu) \left(\frac{n\pi}{L_y} \right)^2 k_{2n} \right] A_2 + \\ & \left[k_{3n}^3 - (2 - \nu) \left(\frac{n\pi}{L_y} \right)^2 k_{3n} \right] A_3 + \left[k_{4n}^3 - (2 - \nu) \left(\frac{n\pi}{L_y} \right)^2 k_{4n} \right] A_4 = 0 \end{aligned} \quad (\text{C.23})$$

Equations (C.13) to (C.16), (C.20) and (C.23) can be written as a 6×6 matrix equation as

$$\begin{bmatrix} k_{1n}^2 - \frac{\nu H}{2-\nu} & k_{2n}^2 - \frac{\nu H}{2-\nu} & k_{3n}^2 - \frac{\nu H}{2-\nu} & k_{4n}^2 - \frac{\nu H}{2-\nu} \\ k_{1n}^3 - H k_{1n} & k_{2n}^3 - H k_{2n} & k_{3n}^3 - H k_{3n} & k_{4n}^3 - H k_{4n} \\ e^{k_{1n}x_0} & e^{k_{2n}x_0} & e^{k_{3n}x_0} & e^{k_{4n}x_0} \\ k_{1n} e^{k_{1n}x_0} & k_{2n} e^{k_{2n}x_0} & k_{3n} e^{k_{3n}x_0} & k_{4n} e^{k_{4n}x_0} \\ k_{1n}^2 e^{k_{1n}x_0} & k_{2n}^2 e^{k_{2n}x_0} & k_{3n}^2 e^{k_{3n}x_0} & k_{4n}^2 e^{k_{4n}x_0} \\ k_{1n}^3 e^{k_{1n}x_0} & k_{2n}^3 e^{k_{2n}x_0} & k_{3n}^3 e^{k_{3n}x_0} & k_{4n}^3 e^{k_{4n}x_0} \end{bmatrix} \begin{bmatrix} A_1 \\ A_2 \\ A_3 \\ A_4 \\ B_2 \\ B_4 \end{bmatrix} = \begin{bmatrix} 0 \\ 0 \\ 0 \\ 0 \\ 0 \\ -\frac{2F_0}{l_y D_h} \sum_{i=1}^m \sin \frac{n\pi y_i}{L_y} \end{bmatrix} \quad (\text{C.24})$$

which can be written as $[\alpha][\mathbf{X}] = [\mathbf{F}]$. For each value of n , the solution $[\mathbf{X}]$ of the 6×6 system of equations is an eigenvector which describes a traveling wave mode shape and amplitude. The modal wavenumbers k_{1n} , k_{2n} , k_{3n} and k_{4n} required by equation (C.24) are calculated from equations (C.7) and (C.8), and the quantity $H = (2 - \nu) \left(\frac{n\pi}{L_y} \right)^2$.

The plate response at any location (x, y) due to the row of in-phase point forces is

$$w = F_0 w_{0-f} \quad (\text{C.25})$$

where w_{0-f} is the response to unit force excitation which is obtained by solving equation (C.24) (with $F_0 = 1$) and substituting the results for A_1, A_2, A_3, A_4, B_2 and B_4 into equations (C.11) and (C.3) or equations (C.12) and (C.3), depending upon the location at which the plate response is to be evaluated. By expressing the solution for the eigenvectors as:

$$[\mathbf{X}] = [\alpha]^{-1}[\mathbf{F}], \quad (\text{C.26})$$

the response at (x, y) is:

$$w_{0-f}(x, y) = \sum_{n=1}^{\infty} \frac{2}{L_y D_h} \left(\sum_{i=1}^m \sin \frac{n\pi y_i}{L_y} \right) ([\alpha]^{-1})_{i,6}^T [\mathbf{E}_n] \sin \frac{n\pi y}{L_y} \quad (\text{C.27})$$

where $([\alpha]^{-1})_{i,6}^T$ is the sixth column of the inverse of the coefficient matrix $[\alpha]$ from equation (C.24). For $x < x_0$,

$$[\mathbf{E}_n] = \begin{bmatrix} e^{k_{1n}x} \\ e^{k_{2n}x} \\ e^{k_{3n}x} \\ e^{k_{4n}x} \\ 0 \\ 0 \end{bmatrix} \quad (\text{C.28})$$

and for $x > x_0$,

$$[\mathbf{E}_n] = \begin{bmatrix} 0 \\ 0 \\ 0 \\ 0 \\ e^{k_{2n}x} \\ e^{k_{4n}x} \end{bmatrix} \quad (\text{C.29})$$

Appendix D

Modal decomposition method in a semi-infinite plate

For a simply supported plate, a modal decomposition method was introduced by Fuller (1991). For the plate with one end terminated anechoically and the sides adjacent to the anechoically terminated end simply supported, the flexural plate displacement w , for a fixed frequency in equation (C.3), at a point (x, y) is given by

$$w(x, y) = \sum_{n=1}^{\infty} A_n(x) \sin \frac{n\pi y}{L_y} \quad (\text{D.1})$$

where n is the modal number in the y direction and A_n is the modal amplitude of the plate.

For a single frequency producing a low modal density, summation over a finite number of modes will achieve a reasonably accurate result,

$$w(x, y) = \sum_{n=1}^N A_n(x) \sin \frac{n\pi y}{L_y}. \quad (\text{D.2})$$

In practice, the (complex) plate displacement can be measured at a discrete number of randomly selected points N . These values are then used in equation (D.2) to form a set of simultaneous equations, which can be represented as an $N \times N$ matrix equation as follows

$$\begin{bmatrix} w_1 \\ w_2 \\ \vdots \\ w_N \end{bmatrix} = \begin{bmatrix} \sin \frac{1\pi y_1}{L_y} & \sin \frac{2\pi y_1}{L_y} & \dots & \sin \frac{N\pi y_1}{L_y} \\ \sin \frac{1\pi y_2}{L_y} & \sin \frac{2\pi y_2}{L_y} & \dots & \sin \frac{N\pi y_2}{L_y} \\ \vdots & \vdots & \vdots & \vdots \\ \sin \frac{1\pi y_N}{L_y} & \sin \frac{2\pi y_N}{L_y} & \dots & \sin \frac{N\pi y_N}{L_y} \end{bmatrix} \begin{bmatrix} A_1 \\ A_2 \\ \vdots \\ A_N \end{bmatrix} \quad (\text{D.3})$$

or

$$[\mathbf{w}] = [\textit{spatial coefficients}][\mathbf{A}]. \quad (\text{D.4})$$

With the displacement vector and spatial coefficient matrix known, the modal amplitude vector $[\mathbf{A}]$ can be determined.

Using numerical simulation it was found that the ill-conditioning of the inverse matrix $([\textit{spatial coefficients}]^{-1})$ significantly affects the accuracy of the measured modal amplitudes when only a small number of measurement points is used. To avoid using this inverse matrix and the associated ill-conditioning problems, the modal amplitude vector $[\mathbf{A}]$ can be expressed as:

$$[\mathbf{A}] = ([\mathbf{S}]^T[\mathbf{S}])^{-1}[\mathbf{S}]^T[[\mathbf{W}]] \quad (\text{D.5})$$

where $[\mathbf{S}] = [\textit{spatial coefficients}]$ and the matrix $([\mathbf{S}]^T[\mathbf{S}])$ is nonsingular and not ill-conditioned.

Appendix E

Measurement of amplitude reflection coefficient in a semi-infinite plate

Reflection coefficients have been measured by Taylor (1990b) for a beam and by Abom (1989) in a duct. However, the measurement of reflection coefficients in a plate has not been studied previously.

The measured modal amplitude for the n th mode $A_n(x)$ ($n = 1, \dots, N$) shown in equation (D.5) is a complex number which comprised contributions from the reflected wave and the incident wave. If the measurement location x is in the far field of excitation sources, then each $A_n(x)$ can be defined as:

$$A_n(x) = A_n^{ref} e^{k_f(3,n)x} + A_n^{in} e^{k_f(4,n)x}, \quad (\text{E.1})$$

where A_n^{ref} is the amplitude of the reflected wave for the n th mode, A_n^{in} is the amplitude of the incident wave for the n th mode, $k_f(3, n)$ is the wave number generated by the reflected wave and $k_f(4, n)$ is the wave number generated by the incident wave at the n th mode. These wavenumbers are defined in equation (C.8). This analysis is possible because the wave numbers are only a function of an excitation frequency and the properties of the plate.

Consider $A_n(x)$ ($n = 1, \dots, N$) at two different axial locations ($x = x_1$ and $x = x_2$), each of which has been obtained from equation (D.5). The modal amplitudes $A_n(x_1)$ and

$A_n(x_2)$ ($n = 1, \dots, N$) are

$$A_n(x_1) = A_n^{ref} e^{k_f(3,n)x_1} + A_n^{in} e^{k_f(4,n)x_1} \quad (\text{E.2})$$

and

$$A_n(x_2) = A_n^{ref} e^{k_f(3,n)x_2} + A_n^{in} e^{k_f(4,n)x_2}. \quad (\text{E.3})$$

The matrix form of the system of equations (E.2) and (E.3) is

$$\begin{bmatrix} A_n(x_1) \\ A_n(x_2) \end{bmatrix} = \begin{bmatrix} e^{k_f(3,n)x_1} & e^{k_f(4,n)x_1} \\ e^{k_f(3,n)x_2} & e^{k_f(4,n)x_2} \end{bmatrix} \begin{bmatrix} A_n^{ref} \\ A_n^{in} \end{bmatrix} \quad (\text{E.4})$$

Therefore the amplitude reflection coefficient ($|A_n^{ref}|/|A_n^{in}|$) for the n th mode at a location of $x = \frac{x_2 - x_1}{2}$ is obtained by inverting equation (E.4) to obtain the coefficients A_n^{ref} and A_n^{in} .

Appendix F

Response of a semi-infinite cylinder to a line of point forces driven in phase

The classical equations of motion for a cylinder given by Flügge (1973) are

$$u'' + \frac{1-\nu}{2}u'' + \frac{1+\nu}{2}v' + \nu w' + \xi\left[\frac{1-\nu}{2}u'' - w'' + \frac{1-\nu}{2}w''\right] - \gamma^2 \frac{\partial^2 u}{\partial t^2} = -\gamma^2 \frac{F_x}{\rho h}, \quad (\text{F.1})$$

$$\frac{1+\nu}{2}u' + v'' + \frac{1-\nu}{2}v'' + w' + \xi\left[\frac{3(1-\nu)}{2}v'' - \frac{3-\nu}{2}w''\right] - \gamma^2 \frac{\partial^2 v}{\partial t^2} = -\gamma^2 \frac{F_\phi}{\rho h} \quad (\text{F.2})$$

and

$$\nu u' + v' + w + \xi\left[\frac{1-\nu}{2}u'' - u''' - \frac{3-\nu}{2}v''\right] + w^{IV} + 2w''' + w'' + 2w' + w + \gamma^2 \frac{\partial^2 w}{\partial t^2} = \gamma^2 \frac{F_r}{\rho h} \quad (\text{F.3})$$

where the quantities $u = u(x, \phi, t)$, $v = v(x, \phi, t)$ and $w = w(x, \phi, t)$ are the displacements in the axial, tangential and radial directions respectively, and F_x , F_ϕ and F_r are the applied forces per unit surface area in each direction. The derivatives with respect to the dimensionless coordinates $\frac{x}{r}$ and ϕ will be indicated by primes and dots:

$$r \frac{\partial()}{\partial x} = ()', \quad \frac{\partial()}{\partial \phi} = ()'.$$

The geometry of the cylinder and coordinates are shown in Figure 7.1(a) and the sign conventions are shown in Figure 7.1(b). The cylinder is simply supported at $x = 0$ and infinity on the other end.

As the cylinder is closed, the following harmonic series solutions in ϕ can be assumed for cylinder vibrational displacement in the axial, tangential and radial directions (Flügge, 1973, Brevart and Fuller, 1993):

$$u(x, \phi, t) = \sum_{n=1}^{\infty} u_n(x) \cos n\phi e^{j\omega t}, \quad (\text{F.4})$$

$$v(x, \phi, t) = \sum_{n=1}^{\infty} v_n(x) \sin n\phi e^{j\omega t} \quad (\text{F.5})$$

and

$$w(x, \phi, t) = \sum_{n=1}^{\infty} w_n(x) \cos n\phi e^{j\omega t}. \quad (\text{F.6})$$

Each of the eigenfunctions $u_n(x)$, $v_n(x)$ and $w_n(x)$ can be expressed in terms of the modal wavenumbers k_{sn} as follows (Forsberg, 1964)

$$u_n(x) = \sum_{s=1}^8 \alpha_{sn} A_{sn} e^{k_{sn} \frac{x}{r}}, \quad (\text{F.7})$$

$$v_n(x) = \sum_{s=1}^8 \beta_{sn} A_{sn} e^{k_{sn} \frac{x}{r}} \quad (\text{F.8})$$

and

$$w_n(x) = \sum_{s=1}^8 A_{sn} e^{k_{sn} \frac{x}{r}} \quad (\text{F.9})$$

where A_{sn} , α_{sn} and β_{sn} are arbitrary constants.

F.1 Determining the wavenumbers and constants α and β

For each mode, the homogeneous form of equations (F.1), (F.2) and (F.3) must be satisfied. To find the modal wavenumbers (i.e. eigenvalues), we take the general term of equations (F.4), (F.5) and (F.6), put $u = u_n(x) \cos n\phi$, $v = v_n(x) \sin n\phi$ and $w = w_n(x) \cos n\phi$, and introduce this into the homogeneous form of equations (F.1), (F.2)

and (F.3). All the terms in each equation have a common factor $\sin n\phi$ or $\cos n\phi$, which cancels to give

$$u_n'' - \frac{1-\nu}{2}n^2u_n + \frac{1+\nu}{2}nv_n' + \nu w_n' - \xi\left[\frac{1-\nu}{2}n^2u_n + w_n'' + \frac{1-\nu}{2}n^2w_n'\right] + \omega^2\gamma^2u_n = 0, \quad (\text{F.10})$$

$$-\frac{1+\nu}{2}nu_n' - n^2v_n + \frac{1-\nu}{2}v_n'' - nw_n + \xi\left[\frac{3(1-\nu)}{2}v_n'' + \frac{3-\nu}{2}nw_n''\right] + \omega^2\gamma^2v_n = 0 \quad (\text{F.11})$$

and

$$\nu u_n' + nv_n + w_n + \xi\left[-\frac{1-\nu}{2}n^2u_n' - u_n''' - \frac{3-\nu}{2}nv_n'' + w_n^{IV} - 2n^2w_n'' + n^4w_n - 2n^2w_n + w_n\right] - \omega^2\gamma^2w_n = 0. \quad (\text{F.12})$$

Equations (F.10), (F.11) and (F.12) have constant coefficients and may be solved by exponential functions:

$$u_n = A_n e^{k_n \frac{z}{r}}, \quad v_n = B_n e^{k_n \frac{z}{r}} \quad \text{and} \quad w_n = C_n e^{k_n \frac{z}{r}}.$$

After introducing this into equations (F.10), (F.11) and (F.12), we may drop the exponential factor and then have three ordinary linear equations for the constants A_n , B_n and C_n :

$$\left[k_n^2 - \frac{1-\nu}{2}n^2(1+\xi) + \omega^2\gamma^2\right]A_n + \frac{1+\nu}{2}k_n n B_n + \left[\nu k_n - \xi(k_n^3 + \frac{1-\nu}{2}k_n n^2)\right]C_n = 0, \quad (\text{F.13})$$

$$\frac{1+\nu}{2}k_n n A_n + \left[-\frac{1-\nu}{2}k_n^2 + n^2 - \frac{3(1-\nu)}{2}\xi k_n^2 + \omega^2\gamma^2\right]B_n + \left[n - \frac{3-\nu}{2}\xi k_n^2 n\right]C_n = 0 \quad (\text{F.14})$$

and

$$\left[\nu k_n - \xi(k_n^3 + \frac{1-\nu}{2}k_n n^2)\right]A_n + \left[n - \frac{3-\nu}{2}\xi k_n^2 n\right]B_n + \left[1 + \xi(k_n^4 - 2k_n^2 n^2 + n^4 - 2n^2 + 1) - \omega^2\gamma^2\right]C_n = 0. \quad (\text{F.15})$$

Since these equations are homogeneous, they can have a solution A_n , B_n and C_n different from zero only if the determinant formed from their nine coefficients vanishes. This condition can be used to determine k_n . In general, the solution will usually have the form (Forsberg, 1964)

$$k_1 = -a, \quad k_5 = +a,$$

$$k_2 = -jb, \quad k_6 = +jb,$$

$$k_3 = -(c + jd), \quad k_7 = +(c + jd),$$

$$k_4 = -(c - jd), \quad k_8 = +(c - jd)$$

where a , b , c and d are real quantities. This is different to the form of the solutions given by Flügge (1973), because the inertia terms have been included here.

The constants α_n and β_n ($n = 1, \dots, \infty$) can now be found from any two of equations (F.13), (F.14) and (F.15). Using the definition of $A_n = \alpha_n C_n$ and $B_n = \beta_n C_n$ ($n = 1, \dots, \infty$), the complex numbers α_n and β_n can be determined by assuming $C_n = 1$ ($n = 1, \dots, \infty$) in equations (F.13), (F.14) and (F.15).

On each side of an applied force at $x = x_0$, each eigenfunction is a different linear combination of the terms $e^{k_{sn} \frac{x}{r}}$. For $x < x_0$,

$$u_{1n}(x) = \sum_{s=1}^8 \alpha_{sn} A_{1sn} e^{k_{sn} \frac{x}{r}}, \quad (\text{F.16})$$

$$v_{1n}(x) = \sum_{s=1}^8 \beta_{sn} A_{1sn} e^{k_{sn} \frac{x}{r}} \quad (\text{F.17})$$

and

$$w_{1n}(x) = \sum_{s=1}^8 A_{1sn} e^{k_{sn} \frac{x}{r}}. \quad (\text{F.18})$$

For $x > x_0$,

$$u_{2n}(x) = \sum_{s=1}^4 \alpha_{sn} A_{2sn} e^{k_{sn} \frac{x}{r}}, \quad (\text{F.19})$$

$$v_{2n}(x) = \sum_{s=1}^4 \beta_{sn} A_{2sn} e^{k_{sn} \frac{x}{r}} \quad (\text{F.20})$$

and

$$w_{2n}(x) = \sum_{s=1}^4 A_{2sn} e^{k_{sn} \frac{x}{r}}. \quad (\text{F.21})$$

Note that in equations (F.19), (F.20) and (F.21), A_{25n} to A_{28n} have been omitted because, for a semi-infinite cylinder, there is no boundary to produce reflected waves with a negative horizontal velocity component.

F.2 Determining the flexural wavelength

The flexural wavelength can be obtained from the homogeneous form of equation (F.3). The flexural wavelength can be obtained by dividing both sides of the homogeneous form of equation (F.3) by ξ , and using the definitions of ξ and γ^2 (see list of symbols) to obtain

$$\frac{1}{\xi}(\nu u' + v' + w) + \left[\frac{1-\nu}{2} u'' - u''' - \frac{3-\nu}{2} v'' + w^{IV} + 2w'''' + w'''' + 2w'' + w \right] - \frac{\omega^4}{\frac{\omega^2 E h^2}{12\rho(1-\nu^2)r^4}} w = 0. \quad (\text{F.22})$$

Following a similar procedure to that used for the calculation of the flexural wavelength in a flat plate, the coefficient of the last term in equation (F.22) may be expressed as

$$\frac{\omega^4}{\frac{\omega^2 E h^2}{12\rho(1-\nu^2)r^4}} = k_f^4. \quad (\text{F.23})$$

Equation (F.23) can also be written as

$$k_f = \frac{\omega}{c_f} = \frac{2\pi}{\lambda_f} \quad (\text{F.24})$$

and

$$c_f = \left(\sqrt{\frac{\omega^2 E h^2}{12\rho(1-\nu^2)r^4}} \right)^{\frac{1}{4}}, \quad (\text{F.25})$$

which is the expression for the frequency dependent flexural wave speed in the cylinder. Note that the flexural wave speed is the ratio of the flexural wave speed in a flat plate of thickness equal to that of the cylinder, to the radius of the cylinder.

F.3 Simply supported end conditions

The four boundary conditions corresponding to a simple support are $u = 0$, $v = 0$, $w = 0$ and $M_x = 0$ (Leissa, 1973), where M_x was given by Flügge (1973):

$$M_x = \frac{K}{r^2}(w'' + \nu w'' - u' - \nu v'). \quad (\text{F.26})$$

In terms of the displacement unknowns, these boundary conditions for a simply supported end at $x = 0$ are

$$\sum_{s=1}^8 \alpha_{sn} A_{1sn} = 0, \quad (\text{F.27})$$

$$\sum_{s=1}^8 \beta_{sn} A_{1sn} = 0, \quad (\text{F.28})$$

$$\sum_{s=1}^8 A_{1sn} = 0 \quad (\text{F.29})$$

and

$$\sum_{s=1}^8 (k_{sn}^2 - \nu n^2 - \alpha_{sn} k_{sn} - \nu n \beta_{sn}) A_{1sn} = 0. \quad (\text{F.30})$$

F.4 Equilibrium conditions at the point of an applied force

Requiring that the displacement and its gradient in each direction be continuous at any point in the cylinder wall, the first six equilibrium conditions at $x = x_0$ which must be satisfied are

$$u_{1n} = u_{2n}, \quad (\text{F.31})$$

$$u'_{1n} = u'_{2n}, \quad (\text{F.32})$$

$$v_{1n} = v_{2n}, \quad (\text{F.33})$$

$$v'_{1n} = v'_{2n}, \quad (\text{F.34})$$

$$w_{1n} = w_{2n} \quad (\text{F.35})$$

and

$$w'_{1n} = w'_{2n}. \quad (\text{F.36})$$

The form of the excitation F will affect the higher order equilibrium conditions at $x = x_0$.

The displacement response of the cylinder to an array of m equally spaced radial point forces around a circumference of the cylinder at positions $((x_0, \phi_i), i = 1, \dots, m)$ is considered. The radial force F_r in equation (F.3) is assumed to be driven in-phase and with the same complex amplitude F_0 so that

$$F_r = F_0 \sum_{i=1}^m \delta(x - x_0) \delta(\phi - \phi_i) e^{j\omega t}. \quad (\text{F.37})$$

Replacing u , v and w by equations (F.4) to (F.6), dividing by $e^{j\omega}$, multiplying by $\cos n\phi$ and taking integral from $-\pi$ to π with respect to ϕ , equation (F.3) can be written as

$$\begin{aligned} \nu u'_n(x) + nv_n(x) + w_n(x) + \xi \left[-\frac{1-\nu}{2} n^2 u'_n(x) - u'''_n(x) - \frac{3-\nu}{2} m v''_n(x) + \right. \\ \left. w_n^{IV}(x) - 2m^2 w''_n(x) + m^4 w_n(x) - 2m^2 w_n(x) + w_n(x) \right] - \gamma^2 \omega^2 w_n(x) = \\ \frac{\gamma^2 F_0 \delta(x-x_0)}{\pi \rho h} \sum_{i=1}^m \cos \phi_i. \end{aligned} \quad (\text{F.38})$$

Then taking integral from $x_0 - \delta$ to $x_0 + \delta$ with respect to x in this equation, using the conditions

$$\int_{x_0-\delta}^{x_0+\delta} w_n(x) dx \rightarrow 0, \quad (\text{F.39})$$

$$\int_{x_0-\delta}^{x_0+\delta} w'_n(x) dx \rightarrow 0 \quad (\text{F.40})$$

(similarly for $u_n(x)$, $v_n(x)$, $u'_n(x)$ and $v'_n(x)$) and

$$\int_{x_0-\delta}^{x_0+\delta} w''_n(x) dx \rightarrow 0 \quad (\text{F.41})$$

as $\delta \rightarrow 0$, we obtain

$$-\int_{x_0-\delta}^{x_0+\delta} u'''_n(x) dx + \int_{x_0-\delta}^{x_0+\delta} w_n^{IV}(x) dx = \frac{F_0 \gamma^2}{\pi \rho h \xi} \sum_{i=1}^m \cos \phi_i \int_{x_0-\delta}^{x_0+\delta} \delta(x-x_0) dx \quad (\text{F.42})$$

or

$$u''_{1n}(x_0) - u''_{2n}(x_0) + w'''_{2n}(x_0) - w'''_{1n}(x_0) = \frac{F_0 \gamma^2}{\pi \rho h \xi} \sum_{i=1}^m \cos \phi_i. \quad (\text{F.43})$$

Finally, taking integral from $x_0 - \delta$ to $x_0 + \delta$ with respect to x in equation (F.43), we get

$$w''_{1n}(x_0) = w''_{2n}(x_0). \quad (\text{F.44})$$

F.5 Determination of the eigenvector

For a semi-infinite cylinder with the end at $x = 0$ modeled as a simply supported, equations (F.27) to (F.36), (F.44) and (F.43) can be written as a 12×12 matrix equation. We use the definition of $M_i = k_{in}^2 - \nu n^2 - \alpha_{in} k_{in} - \nu n \beta_{in}$ ($i = 1, \dots, 8$) in equation (F.30). In terms of displacement unknowns, the coefficients in equation (F.43) can be written as $F_i = \alpha_{in} k_{in}^2 e^{k_{in} x_0} - k_{in}^3 e^{k_{in} x_0}$ ($i = 1, \dots, 8$) and

$F_i = k_{(i-8)n}^3 e^{k_{(i-8)n}x_0} - \alpha_{(i-8)n} k_{(i-8)n}^2 e^{k_{(i-8)n}x_0}$ ($i = 9, \dots, 12$). The 12×12 matrix equation can be written as

$$\begin{array}{ccccc}
 \alpha_{1n} & \alpha_{2n} & \alpha_{3n} & \alpha_{4n} & \alpha_{5n} \\
 \beta_{1n} & \beta_{2n} & \beta_{3n} & \beta_{4n} & \beta_{5n} \\
 1 & 1 & 1 & 1 & 1 \\
 M_1 & M_2 & M_3 & M_4 & M_5 \\
 \alpha_{1n} e^{k_{1n}x_0} & \alpha_{2n} e^{k_{2n}x_0} & \alpha_{3n} e^{k_{3n}x_0} & \alpha_{4n} e^{k_{4n}x_0} & \alpha_{5n} e^{k_{5n}x_0} \\
 \alpha_{1n} k_{1n} e^{k_{1n}x_0} & \alpha_{2n} k_{2n} e^{k_{2n}x_0} & \alpha_{3n} k_{3n} e^{k_{3n}x_0} & \alpha_{4n} k_{4n} e^{k_{4n}x_0} & \alpha_{5n} k_{5n} e^{k_{5n}x_0} \\
 \beta_{1n} e^{k_{1n}x_0} & \beta_{2n} e^{k_{2n}x_0} & \beta_{3n} e^{k_{3n}x_0} & \beta_{4n} e^{k_{4n}x_0} & \beta_{5n} e^{k_{5n}x_0} \\
 \beta_{1n} k_{1n} e^{k_{1n}x_0} & \beta_{2n} k_{2n} e^{k_{2n}x_0} & \beta_{3n} k_{3n} e^{k_{3n}x_0} & \beta_{4n} k_{4n} e^{k_{4n}x_0} & \beta_{5n} k_{5n} e^{k_{5n}x_0} \\
 e^{k_{1n}x_0} & e^{k_{2n}x_0} & e^{k_{3n}x_0} & e^{k_{4n}x_0} & e^{k_{5n}x_0} \\
 k_{1n} e^{k_{1n}x_0} & k_{2n} e^{k_{2n}x_0} & k_{3n} e^{k_{3n}x_0} & k_{4n} e^{k_{4n}x_0} & k_{5n} e^{k_{5n}x_0} \\
 k_{1n}^2 e^{k_{1n}x_0} & k_{2n}^2 e^{k_{2n}x_0} & k_{3n}^2 e^{k_{3n}x_0} & k_{4n}^2 e^{k_{4n}x_0} & k_{5n}^2 e^{k_{5n}x_0} \\
 F_1 & F_2 & F_3 & F_4 & F_5 \\
 \\
 \alpha_{6n} & \alpha_{7n} & \alpha_{8n} & 0 & 0 \\
 \beta_{6n} & \beta_{7n} & \beta_{8n} & 0 & 0 \\
 1 & 1 & 1 & 0 & 0 \\
 M_6 & M_7 & M_8 & 0 & 0 \\
 \alpha_{6n} e^{k_{6n}x_0} & \alpha_{7n} e^{k_{7n}x_0} & \alpha_{8n} e^{k_{8n}x_0} & -\alpha_{1n} e^{k_{1n}x_0} & -\alpha_{2n} e^{k_{2n}x_0} \\
 \alpha_{6n} k_{6n} e^{k_{6n}x_0} & \alpha_{7n} k_{7n} e^{k_{7n}x_0} & \alpha_{8n} k_{8n} e^{k_{8n}x_0} & -\alpha_{1n} k_{1n} e^{k_{1n}x_0} & -\alpha_{2n} k_{2n} e^{k_{2n}x_0} \\
 \beta_{6n} e^{k_{6n}x_0} & \beta_{7n} e^{k_{7n}x_0} & \beta_{8n} e^{k_{8n}x_0} & -\beta_{1n} e^{k_{1n}x_0} & -\beta_{2n} e^{k_{2n}x_0} \\
 \beta_{6n} k_{6n} e^{k_{6n}x_0} & \beta_{7n} k_{7n} e^{k_{7n}x_0} & \beta_{8n} k_{8n} e^{k_{8n}x_0} & -\beta_{1n} k_{1n} e^{k_{1n}x_0} & -\beta_{2n} k_{2n} e^{k_{2n}x_0} \\
 e^{k_{6n}x_0} & e^{k_{7n}x_0} & e^{k_{8n}x_0} & -e^{k_{1n}x_0} & -e^{k_{2n}x_0} \\
 k_{6n} e^{k_{6n}x_0} & k_{7n} e^{k_{7n}x_0} & k_{8n} e^{k_{8n}x_0} & -k_{1n} e^{k_{1n}x_0} & -k_{2n} e^{k_{2n}x_0} \\
 k_{6n}^2 e^{k_{6n}x_0} & k_{7n}^2 e^{k_{7n}x_0} & k_{8n}^2 e^{k_{8n}x_0} & -k_{1n}^2 e^{k_{1n}x_0} & -k_{2n}^2 e^{k_{2n}x_0} \\
 F_6 & F_7 & F_8 & F_9 & F_{10}
 \end{array}$$

$$\begin{bmatrix}
0 & 0 \\
0 & 0 \\
0 & 0 \\
0 & 0 \\
-\alpha_{3n}e^{k_{3n}x_0} & -\alpha_{4n}e^{k_{4n}x_0} \\
-\alpha_{3n}k_{3n}e^{k_{3n}x_0} & -\alpha_{4n}k_{4n}e^{k_{4n}x_0} \\
-\beta_{3n}e^{k_{3n}x_0} & -\beta_{4n}e^{k_{4n}x_0} \\
-\beta_{3n}k_{3n}e^{k_{3n}x_0} & -\beta_{4n}k_{4n}e^{k_{4n}x_0} \\
-e^{k_{3n}x_0} & -e^{k_{4n}x_0} \\
-k_{3n}e^{k_{3n}x_0} & -k_{4n}e^{k_{4n}x_0} \\
-k_{3n}^2e^{k_{3n}x_0} & -k_{4n}^2e^{k_{4n}x_0} \\
F_{11} & F_{12}
\end{bmatrix}
\begin{bmatrix}
A_{11n} \\
A_{12n} \\
A_{13n} \\
A_{14n} \\
A_{15n} \\
A_{16n} \\
A_{17n} \\
A_{18n} \\
A_{21n} \\
A_{22n} \\
A_{23n} \\
A_{24n}
\end{bmatrix}
=
\begin{bmatrix}
0 \\
0 \\
0 \\
0 \\
0 \\
0 \\
0 \\
0 \\
0 \\
0 \\
0 \\
\frac{F_0\gamma^2}{\pi\rho h\xi} \sum_{i=1}^m \cos \phi_i
\end{bmatrix}
\quad (\text{F.45})$$

which can be written as $[\alpha][\mathbf{X}] = [\mathbf{F}]$. For each value of n , the solution $[\mathbf{X}]$ of the 12×12 system of equations is an eigenvector which describes three wave type modal shapes and amplitudes.

The cylinder displacement at any location (x, ϕ) due to a line of in-phase radial point forces is

$$u = F_0 u_{0-f}, \quad (\text{F.46})$$

$$v = F_0 v_{0-f} \quad (\text{F.47})$$

and

$$w = F_0 w_{0-f}. \quad (\text{F.48})$$

where u_{0-f} , v_{0-f} and w_{0-f} are the displacements to unit radial force excitation which are obtained by solving equation (F.45) and substituting the results for A_{1sn} ($s = 1, \dots, 8$) and A_{2sn} ($s = 1, 2, 3, 4$) into equations (F.16) to (F.21) and (F.4) to (F.6). Similarly, the displacement responses due to unit axial force excitation or tangential force excitation can be obtained by using equation (F.1) or (F.2) correspondently.

Appendix G

Modal decomposition method in a semi-infinite cylinder

For a cylinder, the flexural displacement w to a fixed frequency in equation (F.6) at a point (x, ϕ) is given by

$$w(x, \phi) = \sum_{n=1}^{\infty} A_n(x) \cos n\phi. \quad (\text{G.1})$$

For a single frequency producing a low modal density, summation over a finite number of modes will achieve a reasonably accurate result,

$$w(x, \phi) = \sum_{n=1}^N A_n(x) \cos n\phi. \quad (\text{G.2})$$

In practice, the (complex) cylinder displacement can be measured at a discrete number of randomly selected points N . These values are then used in equation (G.2) to form a set of simultaneous equations, which can be represented as an $N \times N$ matrix equation as follows

$$\begin{bmatrix} w_1 \\ w_2 \\ \vdots \\ w_N \end{bmatrix} = \begin{bmatrix} \cos 1\phi_1 & \cos 2\phi_1 & \dots & \cos N\phi_1 \\ \cos 1\phi_2 & \cos 2\phi_2 & \dots & \cos N\phi_2 \\ \vdots & \vdots & \vdots & \vdots \\ \cos 1\phi_N & \cos 2\phi_N & \dots & \cos N\phi_N \end{bmatrix} \begin{bmatrix} A_1 \\ A_2 \\ \vdots \\ A_N \end{bmatrix}. \quad (\text{G.3})$$

As shown in Appendix D, the modal amplitude vector on the right hand side of equation (G.3) can be determined.

Appendix H

Measurement of vibratory intensity in simple structures

H.1 Measurement of vibratory intensity in an infinite beam

Considering only flexural vibration, which is the dominant wave vibration in the beam configurations investigated in this thesis, the intensity consists of two components. The first is associated with the product of the internal shear force and transverse velocity, and the second is associated with the product of the bending moment about the neutral axis and rotational velocity. By adopting the approach of Fahy (1989), the intensity of flexural wave is

$$I_a = -\frac{1}{2} \text{Re}[\bar{Q}^* \frac{\partial \bar{w}}{\partial t} + \bar{M}^* \frac{\partial \bar{\theta}}{\partial t}] \quad (\text{H.1})$$

where Q and M are calculated from equation (2.11).

The method of determining the intensity in a beam given by Pavic (1976) requires the use of four accelerometers (two for sinusoidal waves). Also, Fuller et al. (1990) used two laser vibrometers to measure the intensity in a mass loaded beam. However, for simple harmonic excitation and for an error sensor in a source far field, equation (H.1) can be simplified to

$$I_a = EI_{yy} k_f^3 \omega |\bar{w}|^2. \quad (\text{H.2})$$

Equation (H.2) shows that the intensity is proportional to the displacement magnitude

squared. This demonstrates that one can use one accelerometer to measure the displacement and use the displacement to determine the intensity in the beam.

H.2 Measurement of vibratory intensity in a semi-infinite plate

For flexural waves which are the dominant wave vibration in the semi-infinite plate considered in this thesis, the intensity in the axial direction is the quantity which is integrated across the plate to obtain power transmission (equation (4.10)) and is given by

$$I_{xa} = -\frac{1}{2} \text{Re} \left\{ [j\omega w(x, y)]^* Q_x(x, y) - \left[j\omega \frac{\partial w(x, y)}{\partial x} \right]^* M_x(x, y) - \left[j\omega \frac{\partial w(x, y)}{\partial y} \right]^* M_{xy}(x, y) \right\}, \quad (\text{H.3})$$

where Q_x , M_x and M_{xy} defined by equations (4.11)–(4.13). Similarly the intensity in the y-direction can be determined by interchanging the x for y derivatives and subscripts in equations (H.3) and (4.11)–(4.13). The total power transmission through a section at constant x can be obtained by integrating both sides of equation (H.3) over the width of the plate.

An exact means of determining the intensity in the x direction in a plate requires the use of eight accelerometers (for both the near and far fields of a source) to evaluate the derivatives in equation (H.3) and has been described by Pavic (1976). Further, Hirata et al. (1990) developed Pavic's method to use four accelerometers to measure plate intensity in the far field. However, it will be shown that at low frequencies in the far field of any source, it is possible to obtain reasonably accurate results using just two accelerometers.

Beginning with equation (H.3) and substituting equations (4.11) to (4.13) into it, we obtain for harmonic excitation

$$I_{xa} = \frac{1}{2} \omega D_h \text{Im} \left\{ -w^* \left(k_x^2 \frac{\partial w}{\partial x} + k_y^2 \frac{\partial w}{\partial x} \right) - (1 - \nu) \frac{\partial w^*}{\partial y} \frac{\partial^2 w}{\partial x \partial y} + \frac{\partial w^*}{\partial x} (k_x^2 w + \nu k_y^2 w) \right\} \quad (\text{H.4})$$

where k_x is the x component of the plate wave number and k_y is the y component of the plate wave number. The following general solution for waves propagating in the plate in

the far field of any source has been assumed

$$w = X(x)Y(y) = (A_1e^{-jk_x x} + A_2e^{jk_x x})(B_1e^{-jk_y y} + B_2e^{jk_y y}). \quad (\text{H.5})$$

If it is assumed that k_x and k_y are small, equation (H.4) can be further simplified to

$$I_{xa} = w D_h k_x^2 \text{Im} \left\{ \omega \frac{\partial w^*}{\partial x} \right\}. \quad (\text{H.6})$$

A similar expression can be written for the intensity in the y-direction by substituting y for x everywhere in equation (H.6).

If we make the low frequency approximation that

$$k_x^2 \approx k_y^2 \approx \omega \left(\frac{m}{D_h} \right)^{\frac{1}{2}} \quad (\text{H.7})$$

where m is the mass per unit area of the plate, and use two closely spaced accelerometers to measure accelerations at x_1 and x_2 , the terms in brackets in equation (H.6) can be approximated as

$$w \approx -\frac{1}{2\omega^2} \left[\frac{\partial^2 w(x_1, y)}{\partial t^2} + \frac{\partial^2 w(x_2, y)}{\partial t^2} \right], \quad (\text{H.8})$$

$$\frac{\partial w^*}{\partial x} \approx -\frac{1}{\omega^2 \Delta} \left[\frac{\partial^2 w(x_1, y)}{\partial t^2} - \frac{\partial^2 w(x_2, y)}{\partial t^2} \right]^*, \quad (\text{H.9})$$

where Δ is the distance between the two closely spaced accelerometers. Equation (H.6) can then be written as

$$\begin{aligned} I_{xa} &= \frac{(D_h m)^{\frac{1}{2}}}{2\Delta\omega^2} \text{Im} \left[\left(\frac{\partial^2 w(x_1, y)}{\partial t^2} + \frac{\partial^2 w(x_2, y)}{\partial t^2} \right) \left(\frac{\partial^2 w(x_1, y)}{\partial t^2} - \frac{\partial^2 w(x_2, y)}{\partial t^2} \right)^* \right] \\ &= \frac{(D_h m)^{\frac{1}{2}}}{\Delta\omega^2} \left| \frac{\partial^2 w(x_1, y)}{\partial t^2} \right| \left| \frac{\partial^2 w(x_2, y)}{\partial t^2} \right| \sin(\theta_1 - \theta_2) \end{aligned} \quad (\text{H.10})$$

where $(\theta_1 - \theta_2)$ is the phase by which the signal from accelerometer 1 leads that from accelerometer 2, and intensity transmission is positive from accelerometer 1 to 2.

Equation (H.10) can also be used to determine the intensity vector in the y-direction by replacing $w(x_1, y)$ and $w(x_2, y)$ with $w(x, y_1)$ and $w(x, y_2)$ respectively.

The total power transmission in the x-direction along the plate is then obtained by averaging the intensity (which is actually power per unit plate width) measured by each accelerometer pair and multiplying the result by the plate width. Thus,

$$P_a \approx \frac{2(D_h m)^{\frac{1}{2}}}{\Delta\omega^2} \frac{\sum_{i=1,3,5}^N \left| \frac{\partial^2 w(x_i, y)}{\partial t^2} \right| \left| \frac{\partial^2 w(x_{i+1}, y)}{\partial t^2} \right| \sin(\theta_i - \theta_{i+1})}{N} L_y \quad (\text{H.11})$$

where N is the number of measurement points. Numerically, it can be shown that equations (H.3) (by integrating it along the plate width) and (H.11) give very similar results for the semi-infinite plate considered here. These are listed in Table H.1 for one primary source, three independent control sources, nine measurement points and an excitation frequency of 257 Hz (theoretical cut-on frequency for the third mode). The locations of the primary source, control sources, error sensors and measurement points are as shown in Figure 5.4. Thus the two accelerometer method for plate intensity measurement can be considered valid for the cases considered here.

Table H.1: Estimated and theoretical power transmissions

	Estimation equation (H.11)	Theory equation (H.3)
Uncontrolled power transmission (W)	0.66E-3	0.61E-3
Controlled power transmission (W)	0.10E-9	0.99E-10
Power reduction ratio	6109472	6119250
Power reduction (dB)	67.86	67.86

H.3 Measurement of vibratory intensity in a semi-infinite cylinder

Measurement of intensity in a cylinder is more complex than measurement of intensity in a beam and a plate, intensity in a cylinder is a result of three types of wave motion and, is expressed as (Fuller, 1981)

$$I_a = I_f + I_e + I_t \quad (\text{H.12})$$

where the subscript refers to the shell motion: i.e. either flexure, extension or torsion respectively. For each wave type, the individual wave intensity was defined as (Fuller,

1981)

$$I_f = \frac{r}{2} \text{Re} \left[M_x \frac{\partial \theta_x^*}{\partial t} + Q_x \frac{\partial w^*}{\partial t} \right], \quad (\text{H.13})$$

$$I_e = \frac{r}{2} \text{Re} \left[N_x \frac{\partial u^*}{\partial t} \right] \quad (\text{H.14})$$

and

$$I_t = \frac{r}{2} \text{Re} \left[N_{x\phi} \frac{\partial v^*}{\partial t} \right] \quad (\text{H.15})$$

where M_x was defined in equation (F.26), Q_x , N_x and $N_{x\phi}$ were defined in equations (7.17) to (7.19) respectively. Then the total power transmission can be obtained by integrating the total intensity (equation (H.12)) around the circumference of the cylinder with respect to ϕ .

There is little discussion in other research about measuring the intensity in a cylinder, because it is too difficult to measure the derivatives which are included in the force terms (Q_x , N_x and $N_{x\phi}$). However, it will be shown how it is possible to simplify equation (H.12) to a form which can be measured in practice.

For wide range of semi-infinite cylinders, the extensional wave intensity gives a good approximation of the total intensity as shown in Section 7.3.2 for the test low frequency range. In this case, one can use the extensional wave intensity instead of the total intensity. Introducing equation (7.17) into (H.14), equation (H.14) can be written as

$$I_e = \frac{r}{2} \text{Re} \left[D_e \frac{\partial u}{\partial x} \frac{\partial u^*}{\partial t} + \frac{D_e \nu}{r} \frac{\partial v}{\partial \theta} \frac{\partial u^*}{\partial t} + \frac{D_e \nu}{r} w \frac{\partial u^*}{\partial t} - \frac{K}{r} \frac{\partial^2 w}{\partial x^2} \frac{\partial u^*}{\partial t} \right]. \quad (\text{H.16})$$

Using numerical simulation it was found that the third term in equation (H.16) dominates and by itself gives a close approximation of the extensional wave intensity. By omitting the remaining three terms, equation (H.16) can be written as

$$I_e \simeq \frac{D_e \nu}{2} \text{Re} \left[w \frac{\partial u^*}{\partial t} \right]. \quad (\text{H.17})$$

For measurements made with two accelerometers, equation (H.17) can also be written as

$$I_e \simeq -\frac{D_e \nu \omega}{2} \text{Im} [w u^*] = -\frac{D_e \nu}{2 \omega^3} \left| \frac{\partial^2 w}{\partial t^2} \right| \left| \frac{\partial^2 u}{\partial t^2} \right| \sin(\theta_w - \theta_u) \quad (\text{H.18})$$

where $(\theta_w - \theta_u)$ is the phase by which the signal from one accelerometer leads that from the other accelerometer. Therefore one of the accelerometers can be used to measure flexural acceleration $\frac{\partial^2 w}{\partial t^2}$ and the phase θ_w by locating the accelerometer perpendicular to

the cylinder. Also one can use the other accelerometer to measure extensional acceleration $\frac{\partial^2 u}{\partial t^2}$ and phase θ_u by locating the accelerometer in the x-direction along the cylinder.

Then the total extensional wave power transmission in the x-direction along the cylinder is obtained by averaging the intensity (which is just power per unit length of circumference) measured by each of the accelerometer pairs and multiplying the result by the length of the circumference of the cylinder. Thus an estimation of the extensional wave power transmission is

$$P_e \simeq -\frac{D_e r \nu \pi}{\omega^3} \sum_{i=1}^N \left| \frac{\partial^2 w_i}{\partial t^2} \right| \left| \frac{\partial^2 u_i}{\partial t^2} \right| \sin(\theta_{wi} - \theta_{ui}) / N \quad (\text{H.19})$$

where N is the number of measurement points (i.e. the number of accelerometer pairs).

Table H.2 lists the reduction of power transmission calculated from equation (H.19) (estimation) and from equation (H.12)(Fuller's theory) (by integrating it around the circumference of the cylinder), for three primary sources, three independent control sources, thirty-nine measurement points and excitation frequency of 510 Hz. The locations of the primary sources, control sources, error sensors and measurement points are the same as in Table 7.1.

Table H.2: Estimated and theoretical power transmission for the semi-infinite cylinder

	P_{un} (W)	P_{co} (W)	P.T.reduction (dB)
Estimation equation (H.19)	0.26E-7	0.26E-10	30
Fuller's theory equation (H.12)	0.19E-7	0.20E-10	30

Table H.2 demonstrates that the reduction of power transmission from estimating intensity using equation (H.19) and Fuller's theory are very similar. The results are similar for a range of excitation frequencies and a range of cylinder radii. In Table H.3, the reduction of estimated and theoretical power transmission is shown as a function of the excitation frequency. The results show that the estimation is the same as theory for each excitation frequency considered, except for the highest frequency of 610 Hz, where the power

transmission reduction from the estimation is 1 dB less than that from theory. Hence equation (H.19) can be considered to be a numerical study of the experimental method for measuring the total power transmission. Numerical simulation has shown that the expression for estimated power transmission (equation (H.19)) can be used for both near field and far field conditions. Therefore, the two accelerometer method for cylindrical intensity measurement can be considered valid for cases (the test low frequencies) considered here.

Table H.3: Effect of excitation frequency on the estimated and theoretical power transmission

Thickness h (m)	Radius r (m)	Frequency f (Hz)	Estimation P.T.red.(dB)	Theory P.T.red.(dB)
0.003	0.5	110	23	23
0.003	0.5	210	27	27
0.003	0.5	263	28	28
0.003	0.5	310	29	29
0.003	0.5	410	31	31
0.003	0.5	510	32	32
0.003	0.5	610	34	33

References

Abom, M. (1989), "Modal decomposition in ducts based on transfer function measurements between microphone pairs", *Journal of Sound and Vibration* **135**(1), 95–114.

Baz, A. and Poh, S. (1987), "Modified independent modal space control method for active control of flexible systems", *NASA Technical Report, Contract No. 30429-d*.

Baz, A. and Poh, S. (1988), "Performance of an active control system with piezoelectric actuators", *Journal of Sound and Vibration* **126**(2), 327–343.

Baz, A. and Poh, S. (1990), "Experimental implementation of the modified independent modal space control method", *Journal of Sound and Vibration* **139**(2), 133–149.

Brevart, B.J. and Fuller, C.R. (1993), "Effect of an internal flow on the distribution of vibrational energy in an infinite fluid-filled thin cylindrical elastic shell", *Journal of Sound and Vibration* **167**(1), 149–163.

Carniel, X. and Pascal, J.L. (1985), "Vibrational power flow measurement: structures characterization and wave reflection coefficient measurement", *Inter-Noise 1985*, Munchen, 613–616.

Clark, R.L., Fuller, C.R. and Wicks, Al. (1991), "Characterization of multiple piezoelectric actuators for structural excitation", *Journal of the Acoustical Society of America*, **90**(1), 346–357.

Crawley, E.F. and de Luis, J. (1987), "Use of piezoelectric actuators as elements of intelligent structures", *AIAA Journal*, **25**(10), 1373–1385.

Cremer, L., Heckl, M. and Ungar, E.E. (1973), "Structure Borne Sound", Springer-Verlag, Berlin.

Dimitriadis, E.K., Fuller, C.R. and Rogers, C.A. (1991), "Piezoelectric actuators for distributed vibration excitation of thin plates", *Journal of Vibration and Acoustics*, **113**, 100–107.

Elliott, S.J., Nelson, P.A., Stothers, I.M. and Boucher, C.C. (1989), "Preliminary results of in-flight experiments on the active control of propeller-induced cabin noise", *Journal of Sound and Vibration* **128**(2), 355–357.

Fahy, F. J. (1985), "Sound and Structural Vibration", London, Academic, 16–23. Press.

Fahy, F.J. (1989), "Sound Intensity", Elsevier Applied Science Publishing Company, 57–60,

Fansen, J.L. and Chen, J.C. (1986), "Structural control by the use of piezoelectric active members", *Proceedings of NASA/DOD Control-structures Interaction Conference*, NASA CP 2447, Part II.

Flügge, W. (1973), "Stresses in Shells", Springer-Verlag Berlin Heidelberg, New York Press, 204–259.

Forsberg, K. (1964), "Influence of boundary conditions on the modal characteristics of thin cylindrical shells", *AIAA Journal* **2**(12), 2150–2157.

Forsberg, K. (1966), "A review of analytical methods used to determine the modal characteristics of cylindrical shells", *NASA CR-613*.

Fuller, C.R. (1981), "The effects of wall discontinuities on the propagation of flexural waves in cylindrical shells", *Journal of Sound and Vibration* **75**(2), 207–228.

Fuller, C.R. (1990), "Active control of sound transmission/radiation from elastic plates by vibration inputs: I. analysis", *Journal of Sound and Vibration* **136**(1), 1–15.

Fuller, C.R. (1991), "Active control of sound radiation from a vibrating rectangular panel by sound sources and vibration inputs: an experimental comparison", *Journal of Sound and Vibration* **145**(2), 195–215.

Fuller, C.R. and Brevart, B.J. (1995), "Active control of coupled wave propagation and associated power in fluid-filled elastic long pipes", *Active*, 2–13.

Fuller, C.R. and Gonidou, L.O. (1988), "Active vibration control of flexural power flow in beams", *Journal of the Acoustical Society of America Supplement* **1** **84**, s47.

Fuller, C.R. and Jones, J.D. (1987), "Experiments on reduction of propeller induced interior noise by active control of cylinder vibration", *Journal of Sound and Vibration* **112**(2), 389–395.

Fuller, C.R., Gibbs, G.P. and Gonidou, L.O. (1990), "Application of power and impedance measurement techniques to the study of active control of flexural energy flow in beams", *Proceedings, International Congress on Intensity Techniques*, Senlis, France 27-29 April 1990, 389–396.

Gibbs, G.P. and Fuller, C.R. (1990), "Experiments on active control of vibrational power flow using piezoceramic actuators and sensors", *AIAM SDM Conference*, Long Beach, California, U.S.A., 2331–2339.

Gonidou, L.O. (1988), "Active control of flexural power flow in elastic thin beams", Master of science thesis, Virginia Polytechnic Institute and State University.

Graff, K. F. (1975), "Wave motion in elastic solids", Oxford, Clarendon Press, 229–255.

Hirata, T., Shimode, S., Mizuguchi, N. and Muramoto, Y. (1990), "Characteristics of vibration energy flow and in its error analysis", CETIM, *Senlis*, 1990, 331–336.

Jones, J.D. and Fuller, C.R. (1989), "Active control of sound fields in elastic cylinders by multicontrol forces", *AIAA Journal*, **27**(7), 845–852.

Junger, M.C. and Feit, D. (1972), "Sound, Structures, and Their Interaction", The MIT Press, 133–152.

Kim, S.J. and Jones, J.D. (1991), "Optimal design of piezo-actuators for active noise and vibration control", *AIAA 13th Aeroacoustics Conference* October 22-24, 1990, 2047–2053.

Leissa, A.W. (1969), "Vibration of Plates", NASA SD-160, 1–160.

Leissa, A. W. (1973), "Vibration of Shells", *NASA SP-288*.

Lester, H.C. and Lefebvre, S. (1993), "Piezoelectric actuator models for active sound and vibration control of cylinders", *Journal of Intelligent Material Systems and Structures*, **4**, 295–306.

Mace, B.R. (1987), "Active control of flexural vibration", *Journal of Sound and Vibration* **114**, 253–270.

Meirovitch, L., Baruh, H. and Oz, H. (1983), "A comparison of control techniques for large flexible systems", *J. Guidance, Control and Dynamics* **6**, 302–310.

Meirovitch, L. and Bennighof, J.K. (1986), "Modal control of traveling waves in flexible structures", *Journal of Sound and Vibration* **111**(1), 131–144.

Metcalf, V.L., Fuller, C.R., Silcox, R.J. and Brown, D.E. (1992), "Active control of sound transmission/radiation from elastic plate by vibration inputs, II: experiments", *Journal of Sound and Vibration* **153**(3), 387–402.

Nelson, P.A. and Elliott, S.J. (1993), "Active Control of Sound", London, Academic Press, 310–355.

Noiseux, D.U. (1970), "Measurement of power flow in uniform beams and plates", *J. Acoust. Soc. Amer.*, **47**, 238–247.

Pan, J. and Hansen, C. H. (1990), "Active control of total power flow along a beam", *International congress on recent developments in air and structure-borne sound and vibration, Auburn University, Alabama, U.S.A. 1990* 229–236.

Pavic, G. (1976), "Measurement of structure borne wave intensity, part I: Formulation of the methods", *Journal of Sound and Vibration* **49**(2), 221–230.

Pavic, G.(1986), "The influence of curvature on structure-borne acoustical power propagation in a cylindrical shell", Paper D6-6, 12th ICA-Congress, 1986, Toronto.

Pinnington, R.J. and Briscoe, A.R. (1994), "Externally applied sensor for axisymmetric waves in a fluid filled pipe", *Journal of Sound and Vibration* **173**(4), 503–516.

Rasmussen, G. (1985), "Intensity analysis of structures", *inter-noise 85*, Munchen, 673–676.

Rivory, J.F. (1992), "Dynamic Response of Simply Supported Beams Excited by Piezo-electric Actuators", *Master of Science Thesis, University of Adelaide*

Romano, A.J., Abraham, P.B. and Williams, E.G. (1990), "A Pointing vector formulation for thin shells and plates, and its application to structural intensity analysis and force localization Part I: Theory", *The Journal of the Acoustical Society of America*, 1166–1175.

Skudrzyk, E. (1965), "Simple and Complex Vibration Systems", The Pennsylvania State University Press, 3–9.

Tanaka, N., Kikushima, Y., Kuroda, M. and Snyder, S.D. (1993), "Structure-borne intensity characteristics of an actively controlled thin plate", *Proceedings, Fourth structural intensity conference, France*, 273–280.

Taylor, P.D. (1990a), "Nearfield structure borne power flow measurements", *International congress on recent developments in air and structure borne sound and vibration*, Auburn University, USA, 339–345.

Taylor, P.D. (1990b), "Measurement of structural intensity, reflection coefficient, and termination impedance for bending waves in beams", *CETIM, Senlis 1990*, 249–256.

Venkatraman, K. and Narayanan, S. (1990), "The optimal independent modal-space control of a flexible beam subjected to constant disturbance", *Journal of Sound and Vibration* **140**, 349–355.

von Flotow, A.H. (1986), "Traveling wave control for large spacecraft structures", *J. Guidance, Control and Dynamics* **9**, 462–468.

von Flotow, A.H. and Schafer, B. (1986), "Wave absorbing controllers for a flexural beam", *J. Guidance, Control and Dynamics* 9(6), 673–680.

Wagstaff, P.R., Luo, Q., Jin, M. and Chassignon, C. (1995), "Conditions for obtaining accurate measurements of structural power flow in multiple source situations", *inter-noise* 1995, Newport Beach, U.S.A., 583–586.

Williams, E.G. (1988), "Introduction and survey of recent developments in near acoustic holography", *inter-noise* 1988, Avignon, 203–208.

Young, A.J. (1995), "Active Control of Vibration in Stiffened Structures", Ph.D Thesis, University of Adelaide.

Publications originating from this thesis work

Journals

1. Pan, X. and Hansen, C.H. (1993), "Effect of error sensor location and type on the active control of beam vibration", *The Journal of Sound and Vibration* **165**(3), 497–510.
2. Pan, X. and Hansen, C.H. (1993), "Effect of end conditions on the active control of beam vibration", *The Journal of Sound and Vibration* **168**(3), 429–448.
3. Pan, X. and Hansen, C.H. (1994), "Piezoelectric crystal vs point force excitation of beams and plates", *Journal of Intelligent Material Systems and Structures*, **5**(3), 363–370.
4. Pan, X. and Hansen, C.H. (1995), "Active control of vibratory power transmission along a semi-infinite plate", *The Journal of Sound and Vibration*, **184**(4), 585–610.
5. Pan, X., Hansen, C.H. and Snyder, S.D. (1995), "Power transmission characteristics in an actively controlled semi-infinite plate", *International Journal of Active Control*, **1**(2), 145–166.

Papers currently under review for publication

1. Pan, X. and Hansen, C.H. (1996), "Active control of vibration transmission in a cylindrical shell", *The Journal of Sound and Vibration*.

Conference publications

1. Hansen, C.H., Young, A.J. and Pan, X. (1993), "Active control of harmonic vibration in beams with arbitrary end conditions", *Second Conference on Recent Advances in Active Control of Sound and Vibration*, April 1993, 897–908.
2. Pan, X. and Hansen, C.H. (1994), "Power transmission characteristics in an actively controlled semi-infinite plate", *Australian Acoustical Society Annual Conference*, November 1994, 113–119.
3. Pan, X. and Hansen, C.H. (1995), "Active control of harmonic power transmission in a cylindrical shell", *The 130th Meeting of the Acoustical Society of America*, St. Louis, U.S.A., November 1995.
4. Pan, X. and Hansen, C.H. (1996), "An experimental study of active control of vibration transmission in a cylindrical shell", *The 131st Meeting of the Acoustical Society of America*, Indianapolis, U.S.A., May 1996.